4 March 2005

Science

Vol. 307 No. 5714
Pages 1357–1516 $10

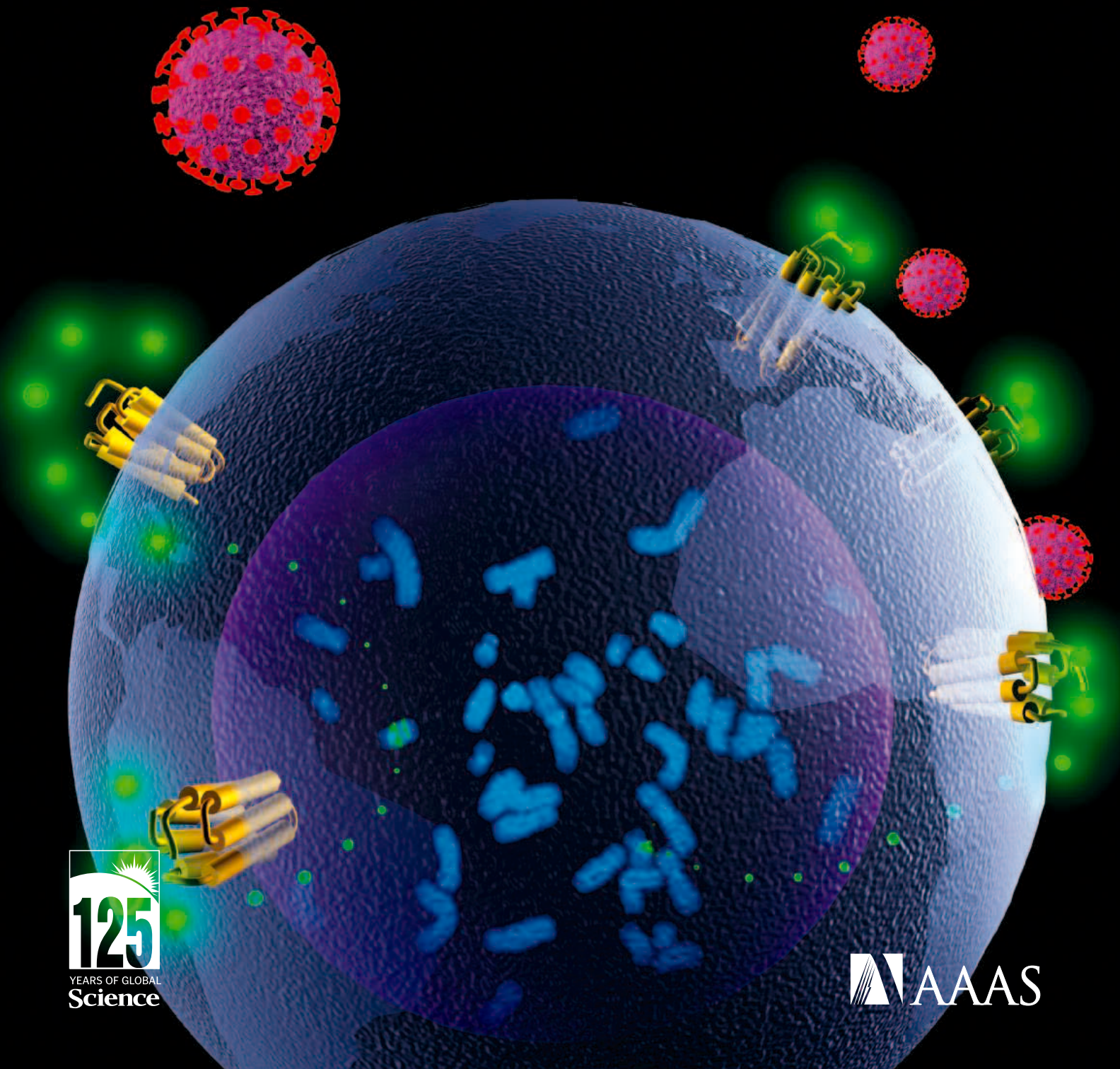

125 YEARS OF GLOBAL Science

AAAS

Science

Volume 307
4 March 2005
Number 5714

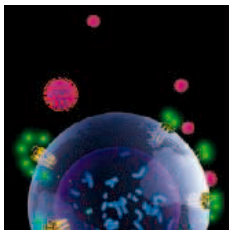

COVER Artist's view of a human T cell as a globe, with the chemokine CCL3L1 shielding the cell from infection by HIV-1 (circles with red spikes) by virtue of its interaction with the HIV coreceptor CCR5 (yellow). CCL3L1 is represented by green circles emanating from green bands on chromosome 17, with the intensity indicating differences in gene dose (fluorescence in situ hybridization courtesy of Robin Leach). See page 1434. [Image: S. K. Ahuja and D. Baker]

DEPARTMENTS

1369 *SCIENCE* ONLINE
1371 THIS WEEK IN *SCIENCE*
1375 EDITORIAL *by Donald Kennedy*
Bayh-Dole: Almost 25
1377 EDITORS' CHOICE
1382 CONTACT *SCIENCE*
1385 NETWATCH
1481 NEW PRODUCTS
1488 *SCIENCE* CAREERS

NEWS OF THE WEEK

1386 PALEOANTHROPOLOGY
Small but Smart? Flores Hominid Shows Signs of Advanced Brain
"Hobbit" Bones Go Home to Jakarta
related Science *Express Report by D. Falk* et al.

1387 PLANETARY SCIENCE
A Strange Little Saturnian Ice Ball Gets Stranger Still

1389 COMPUTER SECURITY
Flaw Found in Data-Protection Method

1389 SCIENCESCOPE

1390 PLANETARY SCIENCE
Ice or Lava Sea on Mars? A Transatlantic Debate Erupts

1390 CONFLICTS OF INTEREST
NIH Scientists Raise Fuss About Scope of New Rules

1391 FRENCH SCIENCE
Report Puts Pasteur Move on Hold

1392 INFECTIOUS DISEASES
Experts Dismiss Pig Flu Scare as Nonsense

1393 CANADA
Grants Councils Say More Isn't Nearly Enough to Keep Science Healthy

1393 HUMAN EMBRYONIC STEM CELLS
Getting the Mice out of ES Cell Cultures

1395 RETROVIRUS MEETING
Gut Assumes Sinister New Role in HIV Pathogenesis

NEWS FOCUS

1396 BIODEFENSE
Has Biodefense Spending Gone Overboard?
Microbiologist on a Mission
related Letter by S. Altman et al. *page 1409*

1396 & 1409

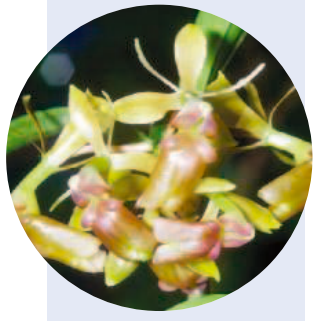

1399

1415

1399 CONSERVATION SCIENCE
What's in a Species' Name? More Than $450,000

1401 U.S. POLAR RESEARCH
Shift in Icebreaking Fleet Could Crunch NSF Budget

1402 MATHEMATICS
What in the Name of Euclid Is Going On Here?
Have a Coq and a Smile

1405 RANDOM SAMPLES

LETTERS

1409 **Retraction** *R. B. Case* et al. **An Open Letter to Elias Zerhouni** *S. Altman* et al. **A Small-Scale Foreign Aid Strategy** *U. Gerber*. **What Kind of Farming Works Best?** *A. A. Avery* et al. ***Response*** *D. Pimentel*. **An Explanation for the Placebo Effect?** *K. J. L. Irizarry and J. Licinio*
S. Altman et al.*: related News story page 1396*

BOOKS *ET AL.*

1413 HISTORY
Maps, Myths, and Men The Story of the Vinland Map
K. A. Seaver, reviewed by W. W. Fitzhugh

1414 BIOTECHNOLOGY
A Machine to Make a Future Biotech Chronicles
P. Rabinow and T. Dan-Cohen, reviewed by W. A. Haseltine

ESSAY

1415 GLOBAL VOICES OF SCIENCE
India's R&D: Reaching for the Top
R. A. Mashelkar

PERSPECTIVES

1419 MATERIALS SCIENCE
A Window on Biomineralization
A. Veis
related Report page 1450

1420 OCEAN SCIENCE
Lost City Life
A. Boetius
related Research Article page 1428

1422 HIV/AIDS
HIV: Experiencing the Pressures of Modern Life
D. Nolan, I. James, S. Mallal
related Research Article page 1434

1424 ASTRONOMY
Our Interstellar Neighborhood
J. R. Jokipii
related Report page 1447

1425 STRUCTURAL BIOLOGY
Membrane Protein Insertion and Stability
R. MacKinnon
related Brevia page 1427

Contents continued

SCIENCE EXPRESS www.sciencexpress.org

ANTHROPOLOGY: The Brain of LB1, *Homo floresiensis*

D. Falk et al.

A reconstruction of the external shape of the brain of *Homo floresiensis* resembles that of *Homo erectus*, but has some differences, including an expanded temporal lobe. *related News story page 1386*

PLANETARY SCIENCE: Supra-Canonical $^{26}Al/^{27}Al$ and the Residence Time of CAIs in the Solar Protoplanetary Disk

E. D. Young, J. I. Simon, A. Galy, S. S. Russell, E. Tonui, O. Lovera

An unexpected variation in the aluminum isotope ratio of early solar system condensates implies that they were reheated many times in a 300,000-year period after they formed.

ATMOSPHERIC SCIENCE: Extracting a Climate Signal from 169 Glacier Records

J. Oerlemans

A global temperature reconstruction based on records of glacier lengths chronicles the warming of the past 150 years.

BOTANY: Activation of a Phytopathogenic Bacterial Effector Protein by a Eukaryotic Cyclophilin

G. Coaker, A. Falick, B. Staskawicz

Plant and pathogen recognize each other through a cascade of protein processing and cleavage events that then set the plant's defense responses into action.

NEUROSCIENCE: Postsynaptic Receptor Trafficking Underlying a Form of Associative Learning

S. Rumpel, J. LeDoux, A. Zador, R. Malinow

Memory of the fear-conditioning response in mice depends on incorporation of AMPA receptors into synapses in a brain region called the amygdala.

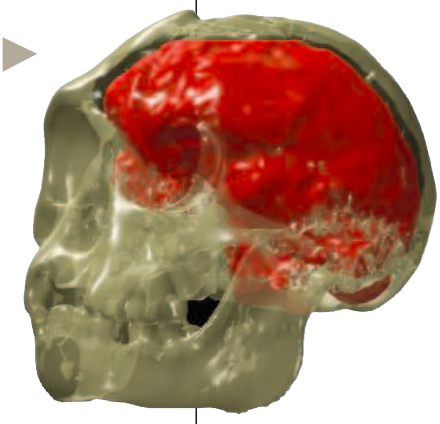

TECHNICAL COMMENT ABSTRACTS

1412 **OCEAN SCIENCE**

Comment on "Avian Extinction and Mammalian Introductions on Oceanic Islands"

R. K. Didham, R. M. Ewers, N. J. Gemmell

full text at www.sciencemag.org/cgi/content/full/307/5714/1412a

Response to Comment on "Avian Extinction and Mammalian Introductions on Oceanic Islands"

T. M. Blackburn, P. Cassey, R. P. Duncan, K. L. Evans, K. J. Gaston

full text at www.sciencemag.org/cgi/content/full/307/5714/1412b

BREVIA

1427 **BIOCHEMISTRY:** Membrane Insertion of a Potassium-Channel Voltage Sensor

T. Hessa, S. H. White, G. von Heijne

Even though it contains charged amino acids, the voltage-sensing portion of the potassium channel can spontaneously insert into a lipid bilayer as an isolated peptide. *related Perspective page 1425*

RESEARCH ARTICLES

1428 **OCEAN SCIENCE:** A Serpentinite-Hosted Ecosystem: The Lost City Hydrothermal Field

D. S. Kelley et al.

A hydrothermal vent system in the oceans, supported by heat from the reaction of seawater with rocks, hosts archaea methanogens within the vents and a diverse macrofauna. *related Perspective page 1420*

1434 **MEDICINE:** The Influence of *CCL3L1* Gene–Containing Segmental Duplications on HIV-1/AIDS Susceptibility

E. Gonzalez et al.

Analysis of gene numbers of an anti-HIV chemokine in people from many ethnic groups shows that individuals with more copies resist HIV infection more effectively. *related Perspective page 1422*

REPORTS

1440 **ASTRONOMY:** The Geometric Distance and Proper Motion of the Triangulum Galaxy (M33)

A. Brunthaler, M. J. Reid, H. Falcke, L. J. Greenhill, C. Henkel

An accurate distance to the nearby galaxy M33, determined by observing water masers, implies that the Andromeda galaxy has less dark matter than was presumed.

1443 **CHEMISTRY:** Laser-Initiated Shuttling of a Water Molecule Between H-Bonding Sites

J. R. Clarkson, E. Baquero, V. A. Shubert, E. M. Myshakin, K. D. Jordan, T. S. Zwier

Light energy is used to move a single water molecule between two binding sites on a single solute molecule, allowing detailed measurement of the binding energies.

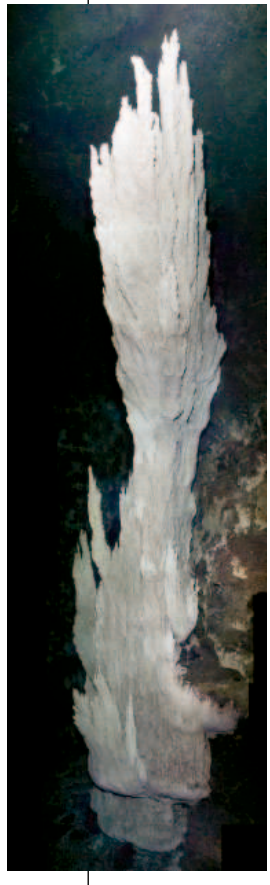

1420 & 1428

Contents continued

REPORTS CONTINUED

1447 **ASTRONOMY:** Deflection of the Interstellar Neutral Hydrogen Flow Across the Heliospheric Interface
R. Lallement, E. Quémerais, J. L. Bertaux, S. Ferron, D. Koutroumpa, R. Pellinen
Measurements from the SOHO satellite suggest that the shock boundary between the solar wind in our solar system and surrounding space is distorted, and Voyager 1 is still traveling in the distorted region. *related Perspective page 1424*

1450 **MATERIALS SCIENCE:** Supramolecular Assembly of Amelogenin Nanospheres into Birefringent Microribbons
C. Du, G. Falini, S. Fermani, C. Abbott, J. Moradian-Oldak
Tooth formation is guided by the protein amelogenin, which self-assembles into nanospheres and secondarily into microribbons that act as a framework for apatite crystal growth. *related Perspective page 1419*

1454 **ATMOSPHERIC SCIENCE:** Residential Biofuels in South Asia: Carbonaceous Aerosol Emissions and Climate Impacts
C. Venkataraman, G. Habib, A. Eiguren-Fernandez, A. H. Miguel, S. K. Friedlander
Burning of wood, agricultural waste, manure, and other biofuels for cooking and heat is the largest source of soot in South Asia.

1457 **ECOLOGY:** Nutritional Status and Diet Composition Affect the Value of Diatoms as Copepod Prey
R. H. Jones and K. J. Flynn
A diet of diatoms alone is nutritionally inadequate to sustain copepods in the pelagic ocean food chain, but is not toxic, as previously supposed.

1459 **GENETICS:** Life at Depth: *Photobacterium profundum* Genome Sequence and Expression Analysis
A. Vezzi et al.
The genome of a bacterium from the deep ocean reveals pressure-activated genes for alternative sources of carbon, and a stress response triggered by the relatively low pressure at the ocean's surface.

1461 **MICROBIOLOGY:** A Functional Dosage Compensation Complex Required for Male Killing in *Drosophila*
Z. Veneti, J. K. Bentley, T. Koana, H. R. Braig, G. D. D. Hurst
Bacteria that preferentially kill male flies do so by interfering with silencing of the extra X chromosome in males, which is necessary for male sex determination.

1463 **MICROBIOLOGY:** Extensive DNA Inversions in the *B. fragilis* Genome Control Variable Gene Expression
A. M. Cerdeño-Tárraga et al.
A bacterium from the human gut that can cause abscesses and blood infections has many inverted sequences in its genome, which may help it infect these diverse sites.

1465 **CELL SIGNALING:** Requirement for Caspase-8 in NF-κB Activation by Antigen Receptor
H. Su, N. Bidère, L. Zheng, A. Cubre, K. Sakai, J. Dale, L. Salmena, R. Hakem, S. Straus, M. Lenardo
A missing link in the pathway by which antigens activate the immune response is the full-length form of a protease, a fragment of which was known to trigger cell death.

1468 **CELL BIOLOGY:** Impaired Thermosensation in Mice Lacking TRPV3, a Heat and Camphor Sensor in the Skin
A. Moqrich et al.
A heat-sensitive receptor in skin cells contributes to the sense of warmth and painful heat and also mediates the sensation produced by camphor.

1472 **CELL SIGNALING:** OSBP Is a Cholesterol-Regulated Scaffolding Protein in Control of ERK1/2 Activation
P. Wang, J. Weng, R. G. W. Anderson
Cholesterol acts outside its usual location in the lipid bilayer to regulate the activity of a key signaling protein.

1476 **NEUROSCIENCE:** How Visual Stimuli Activate Dopaminergic Neurons at Short Latency
E. Dommett et al.
Dopamine-containing neurons, thought to be important in reward signals, respond to light via a direct pathway that bypasses the cortex and is independent of reward information.

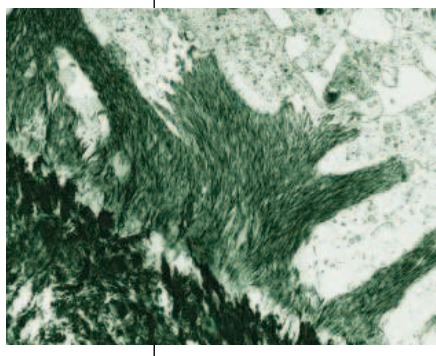

1419 & 1450

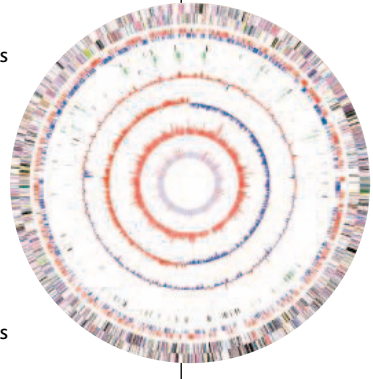

1459

ADVANCING SCIENCE, SERVING SOCIETY

SCIENCE (ISSN 0036-8075) is published weekly on Friday, except the last week in December, by the American Association for the Advancement of Science, 1200 New York Avenue, NW, Washington, DC 20005. Periodicals Mail postage (publication No. 484460) paid at Washington, DC, and additional mailing offices. Domestic individual membership and subscription (51 issues): $135 ($74 allocated to subscription). Domestic institutional subscription (51 issues): $550; Foreign postage extra: Mexico, Caribbean (surface mail) $55; other countries (air assist delivery) $85. First class, airmail, student, and emeritus rates on request. Canadian rates with GST available upon request, GST #1254 88122. Publications Mail Agreement Number 1069624. **Printed in the U.S.A.**

Change of address: allow 4 weeks, giving old and new addresses and 8-digit account number. **Postmaster:** Send change of address to *Science*, P.O. Box 1811, Danbury, CT 06813–1811. **Single copy sales:** $10.00 per issue prepaid includes surface postage; bulk rates on request. **Authorization to photocopy** material for internal or personal use under circumstances not falling within the fair use provisions of the Copyright Act is granted by AAAS to libraries and other users registered with the Copyright Clearance Center (CCC) Transactional Reporting Service, provided that $15.00 per article is paid directly to CCC, 222 Rosewood Drive, Danvers, MA 01923. The identification code for *Science* is 0036-8075/83 $15.00. *Science* is indexed in the *Reader's Guide to Periodical Literature* and in several specialized indexes.

Contents continued ▶

sciencenow www.sciencenow.org Daily News Coverage

Closing the Gender Gap
Training helps young female monkeys do as well as young males on tests of spatial memory.

Salt Packs a Punch
Crystals destroy stone by generating huge pressure from within.

Breathing Life into Dead Bones
Gene therapy resurrects bones from cadavers for use in transplants.

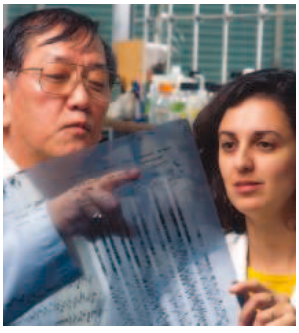

Few women at the top.

science's next wave www.nextwave.org Career Resources for Young Scientists

Postdoc Network: Gender and Scientific Achievement—Views from the Bench *B. Benderly*
Motherhood and discrimination are plausible explanations for the lack of top academic women scientists.

Canada: Canadian Budget Means Cuts for Early Career Scientists *W. Kondro*
Grant councils will have to scale back funding for postdocs and other training programs.

MiSciNet: Solving the Mysteries of Matter *V. Chase*
A physicist develops detectors and software to explore unanswered questions in particle physics.

MiSciNet: She's Come a Long Way on a B.A. *S. Lawrence*
Tania Ruiz's career has branched into research, science education, museum science communication, and program management.

GrantsNet: March 2005 Funding News *Edited by S. Otto*
Get the latest index of research funding, scholarships, fellowships, and internships.

science's sage ke www.sageke.org Science of Aging Knowledge Environment

Review: Oxidative Mutagenesis, Mismatch Repair, and Aging *A. M. Skinner and M. S. Turker*
Does oxidative stress both cause DNA damage and compromise mismatch repair?

News Focus: Will Humans Join the Club? *R. J. Davenport*
Changes in insulin-signaling genes might extend human longevity.

Genetic paths to longer life in people.

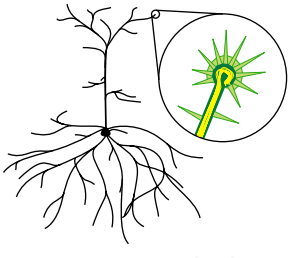

Dasm1 promotes dendritic branching.

science's stke www.stke.org Signal Transduction Knowledge Environment

Perspective: Progress from the Postsynaptic Side—Signaling in Synaptic Differentiation *T. Biederer*
Interactions between immobilized and soluble signals are likely involved in synaptic differentiation.

Perspective: Dasm1—A Receptor that Shapes Neuronal Dendrites and Turns On Silent Synapses? *D. L. Falls*
Dasm1 appears to both promote dendritic growth and activate glutamatergic synapses.

Teaching Resource: Protein Domains that Interact with Receptor Tyrosine Kinases—Structural Aspects *M.-M. Zhou*
Lecture notes and slides are provided for a graduate-level class.

Separate individual or institutional subscriptions to these products may be required for full-text access.

Hot Rocks, Lost City

Recently, a deep-ocean hydrothermal system was discovered in the Atlantic Ocean. The Lost City hydrothermal field is powered by sea water hydrating rocks in ocean crust to form the mineral serpentine, a process that releases heat. Because this reaction potentially occurs throughout the oceans, this type of system may be widespread. Detailed mapping of the system and chemical and microbial analyses by **Kelley *et al.*** (p. 1428; see the Perspective by **Boetius**) show that primarily archaea inhabit the vents living of methane. The surrounding diversity of marcofauna is high and comparable to that of mid-ocean ridge hydrothermal systems.

Water Shuffle

Solvation processes likely involve subtle rearrangements of the solvent molecules around the solute that vary only slightly in energy. **Clarkson *et al.*** (p. 1443, published online 3 February 2005) explore such processes in a model gas-phase system in which the organic molecule formanilide forms two different types of complexes with a water molecule via hydrogen bonds, either a donor link to the C=O group or an acceptor link to the NH group. A laser excitation scheme (stimulated emission pumping) boosts the vibrational energy of either isomer selectively. When sufficient energy is provided, the water can shift from one binding site to the other. The data support an energy difference of roughly 200 wavenumbers (cm^{-1}) or less between isomers, and lower bounds of 870 ± 120 cm^{-1} were extracted for the isomerization thresholds under experimental conditions.

Distorted Heliosphere

Measurements of the direction of neutral hydrogen flow as it enters the inner heliosphere from the Solar and Heliospheric Observatory (SOHO) by **Lallement *et al.*** (p. 1447; see the Perspective by **Jokipii**) show that the heliosphere is distorted. The distortion is probably caused by the interstellar magnetic field, which forces the termination shock to be more elongated with increasing ecliptic latitude. Voyager 1, which is at about 90 astronomical units from Earth, has sent back controversial signals that suggest it may have left the heliosphere. However, if the heliosphere is distorted, as suggested by the SOHO data, then Voyager 1 is still trapped within the elongated region of the heliosphere and has not crossed the termination shock.

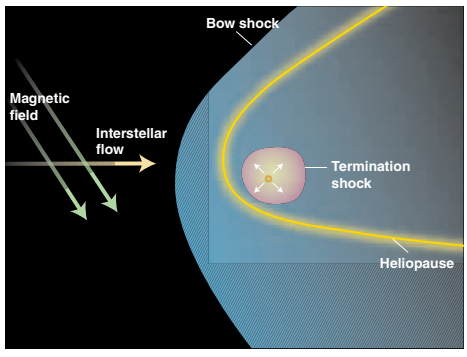

Maser Distance Markers

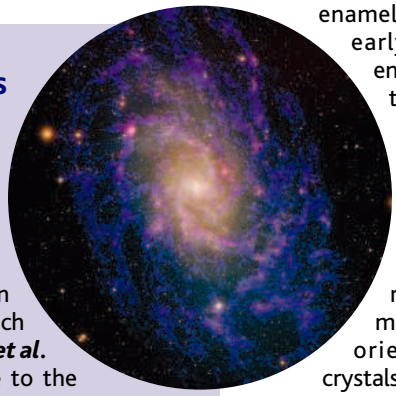

It is difficult to determine the distance to nearby galaxies in the Local Group of galaxies, but such data are needed in order to estimate the local distribution of matter and galactic dynamics, as well as to provide a calibration point for other distance scales, such as Cepheid variables. **Brunthaler *et al.*** (p. 1440) determined a distance to the Triangulum galaxy (M33) of 730 ± 168 kiloparsecs by observing two water masers with the Very Long Baseline Array (VLBA) of radio telescopes. This value agrees well with previous distance values, and their study also determined M33's angular rotation.

Organizing Enamel

Like bone, tooth enamel is composed of ordered carbonated apatite crystals, but unlike bone, enamel does not include collagen to direct crystallie growth, nor does enamel remodel like bone. At an early stage of development, enamel contains a large fraction of amelogenin proteins. **Du *et al.*** (p. 1450; see the Perspective by **Veis**) used in vitro studies to show that these proteins form nanospheres that subsequently organize into microribbons. These structures may control the subsequent oriented growth of apatite crystals during mineralization.

Doubling Resistance

Segmental duplications within the genome are fundamental to both human disease and evolution. Because certain duplications span genes involved in immune defense, some differences in the ability to fight infections can be attributable to dosage effects resulting from the number of copies of specific genes. **Gonzalez *et al.*** (p. 1434, published online 6 January 2005; see the cover and the Perspective by **Nolan *et al.***) noted differences in segmental duplications spanning the variant of the CCL3 chemokine, CCL3L1, in different ethnic and geographic populations. The CCL3 receptor, CCR5, is an important coreceptor for human immunodeficiency virus–1 (HIV-1) infection. The authors found that increased segmental duplications increased resistance to acquiring HIV-1 and progression to AIDS, and correlated with CCL3L1 expression, levels of CCR5, and reduced $CD4^+$ T cell decline. Similar duplications in chimpanzees suggest that some duplications may be an ancient adaptive response of the immune system to environmental pressures.

High-Pressure Existence

Despite the deep sea being the largest environment within the biosphere, adaptation to this habitat is still poorly understood. *Photobacterium profundum* has become a model for ocean depth adaptation, as it grows optimally at high hydrostatic pressure. In genome and expression analysis, **Vezzi *et al.*** (p. 1459) find hints of adaptations in metabolism and protein structure to high-pressure life. This bacterium apparently uses alternative carbon sources at these depths because enzymes for chitin, pullulan, and cellulose degradation are activated at 28 megapascals. This bacterium is so finely tuned to high-pressure life that atmospheric pressure triggers a stress response that activates distinct chaperones and DNA repair proteins.

CONTINUED ON PAGE 1373

CREDITS (TOP TO BOTTOM): BRUNTHALER *ET AL.*; JOKIPII

Dangers of an All-Diatom Diet

In the plankton food chains in the ocean, it has been believed that copepods primarily feed on diatoms. However, laboratory studies have indicated that copepods do not fare well with a pure diatom diet, and it has recently been suggested that diatoms may be toxic to copepods. **Jones and Flynn** (p. 1457) show that diatoms are not so much toxic to copepods as of poor nutritional value. In a series of feeding experiments, they show that copepods fed a mixed diet of diatoms and flagellates fare better than copepods fed a diet of diatoms alone, and also that the nutritional status of the diatoms themselves is important in determining the copepods' response.

To Kill a Male *Drosophila*

Certain cytoplasmically inherited microorganisms disturb the reproduction of their host to increase their own propagation. The mechanism by which host systems are affected are unclear. In particular, "male-killer" bacteria pass from a female insect to her daughters and sons, and selectively kill sons during embryogenesis. Around 20% of insect species may be afflicted in this way, but how do these bacteria kill just males? **Veneti *et al.*** (p. 1461) used the male-killer *Spiroplasma poulsonii*, which infects *Drosophila melanogaster*, to address this question. When male-killers were placed in flies carrying mutations within the gene dosage compensation system that is involved in male specification, any mutation in the dosage compensation complex increased the survival of male offspring.

Linking Caspase-8 and NF-κB Activation

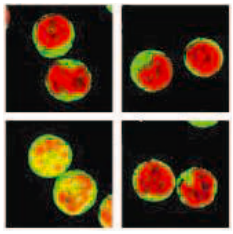

The protease caspase-8 functions in signaling from death-inducing receptors on the cell surface, but analysis of humans lacking the enzyme suggests that it must also play a role in signaling from antigen and Fc receptors on cells in the immune system. **Su *et al.*** (p. 1465) show that activation of nuclear factor κB (NF-κB, a key player in immune responses) is defective in cells lacking caspase-8. Antigen or Fc receptors stimulate NF-κB through a process mediated by a molecular complex that contains numerous signaling proteins, and caspase-8 physically interacts with adaptor proteins that aid in the formation of these signaling clusters. When it signals cell death, caspase-8 undergoes autoproteolysis that generates a fragment with strong protease activity. After activation of antigen receptors, however, catalytic activity of caspase-8 was still required for signaling, but the enzyme remained intact, perhaps in a conformation with a more moderate proteolytic activity. These results help explain the range of physiological effects seen in patients after loss of this single protein-degrading enzyme.

Skin Feels the Heat

Unlike other members of the transient receptor potential (TRP) family of ion channels that function as temperature sensors, TRPV3 is expressed in epithelial keratinocytes rather than sensory neurons in the skin. **Moqrich *et al.*** (p. 1468) generated a TRPV3 knockout mouse and found that the ion channel is required for animals to detect temperatures in the ambient range. Camphor potentiated the activation of TRPV3 by heat, and mice lacking TRPV3 could not respond to camphor. Once thought to be an exclusive function of neurons, the study extends thermosensation to keratinocytes.

Dopamine, Reward, and Attention

What is the functional significance of the fast burst firing of midbrain dopaminergic neurons, and what are the normal afferents projecting to these cells that carry the information to which the neurons respond? **Dommett *et al.*** (p. 1476) found that the superior colliculus is the major input source of short latency visual responses of dopaminergic neurons. The induction of visual responses in dopaminergic neurons leads to increase in dopamine release in the striatum. However, dopaminergic cells only responded to the novel visual stimuli when the colliculus was pharmacologically disinhibited.

CREDIT: SU *ET AL.*

Bayh-Dole: Almost 25

Now that we are firmly into 2005, the 1980 Bayh-Dole Act (hereafter, B-D) will soon graduate from adolescence to adulthood, having reached the quarter-century mark. This legislation has had a profound impact on science in the United States and, indirectly, in other nations as well. But the ratio of its benefits to its costs depends on one's view of what's important. To those who had worried about technology transfer, it's a huge success. To others, who expressed concern about university/corporate relations or mourn the enclosure of the scientific "knowledge commons," it looks more like a bad deal.

To review: Under B-D, the U.S. government renounced intellectual property claims on research supported by federal funds in universities or other nongovernment institutions. The argument in its favor went this way: Because few patents were being issued on government-funded work, scientists and their institutions needed an incentive to patent their discoveries and then license the new technology for development into useful products.

In response to B-D (and some favorable changes in the capital gains tax laws), universities grew offices of technology licensing and faculty members took a new interest in getting their discoveries patented. Venture capitalists, and venture funds in the universities' own endowment portfolios, were eager to help in the conversion of professor to entrepreneur, and pretty soon campus districts were peppered with commercial startups. For university administrators, this was a brand new problem. Should we co-invest with faculty members, linking endowment return to the work of those professors? Should graduate students be given offshore employment in their mentors' startups? Should the university be landlord, philanthropic beneficiary, and exclusive licensor to these entities all at once? We generally answered such questions in the negative in the 1980s, despite some intriguing offers.

The B-D cost/benefit ratio depends on one's view of what's important.

Hard questions soon emerged for others. When professors sent cell lines or reagents to other scientists, they now had to accompany them with a Material Transfer Agreement containing complex restrictions against further distribution. Has that custom evolved from merely annoying to mischievous? Has the developing thicket of patents and licenses created what Eisenberg and Heller called a "knowledge anti-commons," stifling communication among scientists? When those who make use of federally supported research add value, what is a legitimate return? B-D retained certain "march-in" rights for the government. But those are there to punish sloth, not greed: The National Institutes of Health (NIH) was recently asked to intervene in a case in which a drug manufacturer was making a hefty profit on an invention resulting from NIH-sponsored research. NIH refused (*Science*, 4 June 2004, p. 1427; and 13 August 2004, p. 926), supported by assertions from Senators Birch Bayh and Robert Dole themselves that price controls had not been contemplated in B-D.

That position follows a policy rationale used by the government ever since it entered basic research after World War II. Federal support of basic research was justified because it would generate good ideas; these would then attract private risk capital for development into products. It was assumed that those developers were entitled to a return on the value added, but that assumption may be unraveling. Drugs that generated large royalty payments to universities from domestic sales but were needed in poorer nations were natural targets for resentment: Students demonstrated over such cases. Meantime, Congress considered a bill to garnish royalty payments to universities for "blockbuster" drugs developed from a basic research idea. Scientific journals, including *Science* and other nonprofit society journals, were invited by Congress to make papers reporting government-sponsored research freely available and to find another way to finance the value added through editing, review, and evaluation.

Inconsistency and ambivalence prevail. We want technology transfer, but we resent those who take federally supported work, add some value, and receive a return on their investment. The same NIH that urges nonprofit publishers to give that value away properly declines to make drug manufacturers sell drugs cheaply if they were derived from NIH research. Some scientists resent any controls over material transfer; others insist that they're essential. Critics decry the "corporatization" of the university, yet academic/corporate collaborations flourish. B-D has neither a sunset nor a reauthorization requirement, but after a quarter-century it may be time to measure the innovation it has created and to balance that against the costs to universities, their faculties, and public trust in science.

Donald Kennedy
Editor-in-Chief

10.1126/science.1107581

EDITORS' CHOICE

edited by Gilbert Chin

CHEMISTRY

Reducing Nitrogen

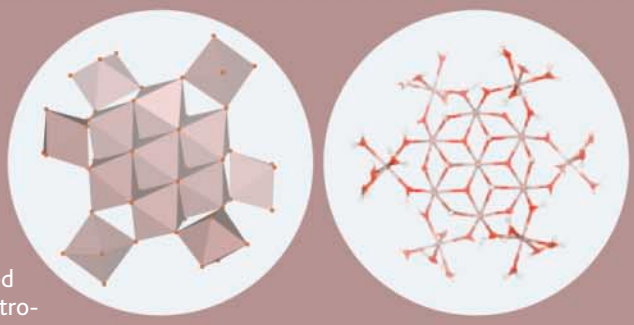

Polyhedral (left) and ball-and-stick (right) representations of the polycation (Ga atoms in pink, O atoms in red, and H atoms in white).

The formation of stable and well-defined inorganic clusters often requires the presence of chelating organic ligands. Rather *et al.* report using an organic reaction to drive the formation of a hydroxyl-bridged Ga_{13} cluster. The oxidation of nitrosobenzene to nitrobenzene can be coupled to the reduction of nitrate, and using $Ga(NO_3)_3$ as the source of nitrate yields as a product the compound $[Ga_{13}(\mu_3\text{-}OH)_6(\mu_2\text{-}OH)_{18}(H_2O)_{24}](NO_3)_{15}$, in which the N:Ga stoichiometry has been reduced from 3:1 to 15:13. Unlike related Al_{13} clusters, which have a modified Keggin ion structure, x-ray crystallography reveals that the Ga_{13} cluster is similar to ligand-stabilized clusters in that it has an octahedral Ga core, which is bridged by hydroxyl groups to six Ga cations that are, in turn, surrounded by six hydrated Ga ions. All together, this cluster forms a disklike structure about 1 nm thick and about 2 nm in diameter. — PDS

J. Am. Chem. Soc. 10.1021/ja043520t (2005).

VIROLOGY

Doubly Active Protease

Evasion of host immune responses is a common defensive strategy used by viruses and is clearly illustrated by the ability of hepatitis C virus (HCV) to cause chronic liver infection. HCV achieves evasion, in part, through expression of the NS3/4A protease, which interrupts the induction of α/β interferon (IFN) gene expression by interferon regulatory factor 3 (IRF3).

Two studies identify the targets of NS3/4A, and both pathways are shown to be pivotal in IRF3 induction. Li *et al.* observed that the Toll-like receptor 3 (TLR3) adapter protein TRIF was cleaved by NS3/4A in an in vitro assay system. This was sufficient to prevent the induction of IFN-β by an activating ligand of TLR3. Furthermore, compromising TLR3 signaling was found to be sufficient to permit the cellular replication of HCV RNA. Foy *et al.* determined that the retinoic acid–inducible gene I (RIG-I) signaling pathway was disrupted by NS3/4A, again leading to loss of IRF3 induction of IFN-β. The development of NS3/4A inhibitors may help guide improved therapeutic intervention in HCV infection. — SJS

Proc. Natl. Acad. Sci. U.S.A. **102**, 2992; 2986 (2005).

MOLECULAR BIOLOGY

A Fourth Musketeer

In eukaryotic cells, the enzymatic activities of RNA polymerases I, II, and III produce ribosomal RNA (rRNA), messenger RNA, and transfer RNA (and 5*S* rRNA), respectively. However, the genome sequence of *Arabidopsis thaliana* revealed that another RNA polymerase might exist, and Onodera *et al.* provide evidence for a functional RNA polymerase IV (Pol IV). Mutant plants lacking *RPD1* and *RPD2*, genes encoding the two largest subunits of the putative Pol IV, were still viable, but higher order heterochromatin assembly into centromeres was disrupted. Generally, an increase in cytosine methylation favors the formation of condensed heterochromatin. In *rpd2* plants, cytosine methylation of the pericentromeric 5*S* rRNA gene clusters was low, and these clusters did not cycle from a decondensed transcriptionally active state into inactive heterochromatin. Because small interfering RNAs (siRNAs) complementary to 5*S* rRNA genes were also reduced, the authors suggest that Pol IV affects amplification of siRNAs that direct DNA methylation (of their corresponding genes) and hence promote the organization of condensed nuclear chromocenters. — LDC

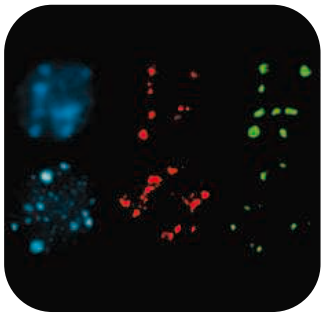

Centromeres (green) and 5*S* rRNA genes (red) in wild-type (upper) and *rpd2* (lower) plants.

Cell 10.1016/S0092867405001510 (2005).

CHEMISTRY

Fast and Accurate

Methods for detecting explosives in a range of settings, such as airports, should be highly sensitive, highly specific, and applicable to nonvolatile and thermally unstable substances. Furthermore, they should be fast and not require much sample preparation. Current methods do not measure up; they involve manual sample transfer and are not ideal for detecting nonvolatile or thermally unstable substances.

Takáts *et al.* show that the recently developed desorption electrospray ionization (DESI) method meets these requirements. An electrospray is directed onto a surface bearing the analyte, and the resulting secondary ions are collected and analyzed by mass spectrometry. Subnanogram amounts of several explosives, including TNT, can be detected on a variety of surfaces such as paper, skin, and metal. Analysis takes just a few seconds, and no sample preparation is required. — JFU

Chem. Commun. 10.1039/b418697d (2005).

BIOCHEMISTRY

Freedom to Associate

The power-generating capacity of mitochondria is based on redox reactions (in complexes I, II, III, and IV) that establish an electrochemical gradient of protons, which is used to make ATP (in complex V). The redox reactions utilize the mobile electron carriers ubiquinone and cytochrome C, and considerations of

CONTINUED ON PAGE 1379

catalytic flux as well as sequestration of reactive intermediates (not to mention membrane morphology and integrity) have led to the view that these complexes might associate into supercomplexes. Dudkina *et al.* provide electron microscopic evidence that in plant mitochondria, a 1.5-megadalton conglomerate of complex I and dimeric complex III exists. This observation fits nicely with recent human genetics studies that have linked mutations in genes coding subunits in one mitochondrial complex with functional or structural deficiencies in another. — GJC

Proc. Natl. Acad. Sci. U.S.A. 10.1073/pnas.0408870102 (2005).

MATERIALS SCIENCE

Greasing the Color Switch

Spirooxazine and chromene are photochromic dye molecules that undergo a reversible color change when subject to irradiation. Switching between clear and colored states requires that half of the molecule undergo an approximately 90° rotation. In solution, switching and unswitching are fast processes, but when these molecules are embedded in a host matrix, the unswitching or color fade times are significantly longer and are strongly influenced by the viscosity of the matrix. Although a matrix with a lower glass transition temperature could be used to mitigate this problem, this would then compromise other properties of the lens.

Evans *et al.* have come up with a solution that was inspired by drug and gene delivery, where sensitive peptides or oligonucleotides are protected by a polymer conjugate. In this application, they covalently linked their dye molecules to low–glass transition temperature oligomers, such as poly(dimethylsiloxane) and poly(ethyleneglycol), which then shield the dye from the lower-viscosity matrix material. The attached oligomers do not alter the electronic character of the dyes, but they do act to lubricate the twisting motion, so that the color fade times were reduced by 40 to 99%. — MSL

Nature Mater. 10.1038/nmat1326 (2005).

HIGHLIGHTED IN *SCIENCE*'S SIGNAL TRANSDUCTION KNOWLEDGE ENVIRONMENT

Science's stke www.stke.org

The Big Picture of Synaptic Phosphorylation

Collins *et al.* have used advances in mass spectrometry and strategies to enrich phosphopeptides in cell extracts to carry out a proteomic analysis of phosphorylation events in synaptosomes (synaptic terminals) from the mouse brain. Although phosphorylation events are known to be important in synaptic signaling and have been studied extensively, these results suggest that traditional studies have barely scratched the surface. Of the almost 300 phosphorylation sites identified, 92% had not been described previously. Many proteins exhibited multiple phosphorylation sites (as many as 30), so the 300 sites were distributed among only 79 proteins, half of which were not known to be phosphorylated before.

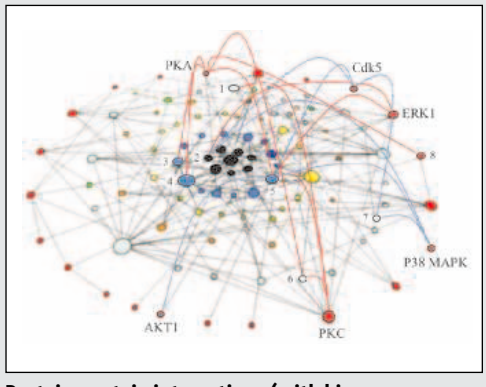

Protein-protein interactions (with kinase substrates connected by red and blue lines) in the NMDA receptor complex.

The authors used peptide arrays along with literature mining and bioinformatic analysis to assign kinases likely to target these sites. Most substrates appear to be targets of multiple kinases; one group of kinases appears to phosphorylate their target proteins at multiple sites, and another appears to hit just one site per substrate. A relatively small number of kinases appears to account for much of the phosphorylation observed. In fact, nine kinases appear to be responsible for more than 250 of the phosphorylation sites. — LBR

J. Biol. Chem. **280**, 5972 (2005).

CREDITS: COLLINS *ET AL.*, *J. BIOL. CHEM.* **280**, 5972 (2005)

www.sciencemag.org

Science

1200 New York Avenue, NW
Washington, DC 20005
Editorial: 202-326-6550, FAX 202-289-7562
News: 202-326-6500, FAX 202-371-9227

Bateman House, 82-88 Hills Road
Cambridge, UK CB2 1LQ
+44 (0) 1223 326500, FAX +44 (0) 1223 326501

Subscription Services For change of address, missing issues, new orders and renewals, and payment questions: 800-731-4939 or 202-326-6417, FAX 202-842-1065. Mailing addresses: AAAS, P.O. Box 1811, Danbury, CT 06813 or AAAS Member Services, 1200 New York Avenue, NW, Washington, DC 20005

Institutional Site Licences please call 202-326-6755 for any questions or information

Reprints Ordering/Billing/Status 800-635-7171; Corrections 202-326-6501

Permissions 202-326-7074, FAX 202-682-0816

Member Benefits Bookstore: AAAS/BarnesandNoble.com bookstore www.aaas.org/bn; Car purchase discount: Subaru VIP Program 202-326-6417; Credit Card: MBNA 800-847-7378; Car Rentals: Hertz 800-654-2200 CDP#343457, Dollar 800-800-4000 #AA1115; AAAS Travels: Betchart Expeditions 800-252-4910; Life Insurance: Seabury & Smith 800-424-9883; Other Benefits: AAAS Member Services 202-326-6417 or www.aaasmember.org.

science_editors@aaas.org (for general editorial queries)
science_letters@aaas.org (for queries about letters)
science_reviews@aaas.org (for returning manuscript reviews)
science_bookrevs@aaas.org (for book review queries)

Published by the American Association for the Advancement of Science (AAAS), *Science* serves its readers as a forum for the presentation and discussion of important issues related to the advancement of science, including the presentation of minority or conflicting points of view, rather than by publishing only material on which a consensus has been reached. Accordingly, all articles published in *Science*—including editorials, news and comment, and book reviews—are signed and reflect the individual views of the authors and not official points of view adopted by the AAAS or the institutions with which the authors are affiliated.

AAAS was founded in 1848 and incorporated in 1874. Its mission is to advance science and innovation throughout the world for the benefit of all people. The goals of the association are to: foster communication among scientists, engineers and the public; enhance international cooperation in science and its applications; promote the responsible conduct and use of science and technology; foster education in science and technology for everyone; enhance the science and technology workforce and infrastructure; increase public understanding and appreciation of science and technology; and strengthen support for the science and technology enterprise.

Information for Contributors

See pages 135 and 136 of the 7 January 2005 issue or access www.sciencemag.org/feature/contribinfo/home.shtml

NetWatch

edited by Mitch Leslie

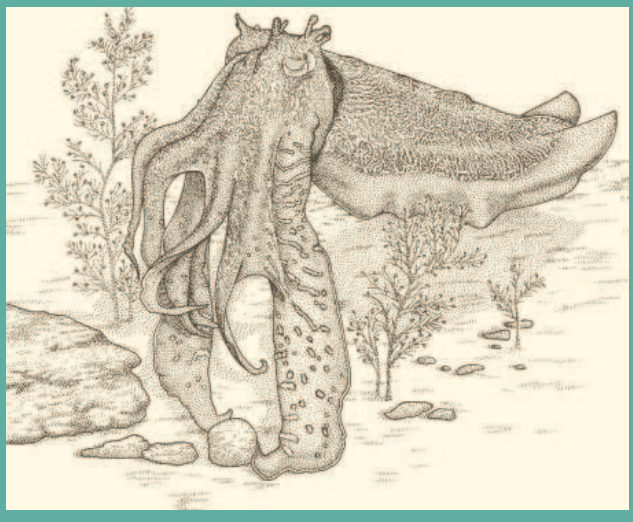

RESOURCES

Tallying Life Down Under

Home to egg-laying platypuses, tree-climbing kangaroos, and 2-meter-long lizards, Australia has more than its share of biological oddities. The country's estimated 2 million kinds of plants, animals, and other creatures include plenty of less spectacular species, too. The taxonomic catalogs at this site from the Australian government's Department of Environment and Heritage in Canberra can help researchers sort through this prodigious diversity. The Fauna Online page directs you to species descriptions for many animal groups, providing distribution maps, notes on ecology, key references, and other information about organisms such as the giant cuttlefish (*Sepia apama*; above), which lives along much of the country's coast. The listings will eventually cover all Aussie animal species. The Flora Online page lets you search a similar catalog of plants, algae, and lichens.

www.deh.gov.au/biodiversity/abrs/online-resources/index.html

DATABASE

Breaking Down Diabetes

The immune system runs amok in type I diabetes and rubs out insulin-making cells in the pancreas, sabotaging the body's ability to control glucose levels. The site T1DBase dispenses the latest information about genes implicated in this disease in rats, mice, and humans. Search the collection by chromosome or by name to dig up data about a particular gene. Plugging your selection into the tool Gbrowse lets you parse the gene's structure and see landmarks such as single nucleotide polymorphisms and repeated sequences. The entries also indicate which biochemical pathways the gene plays a role in and often provide measurements of its activity in different tissues. Another feature helps users sort through the sometimes-baffling genomic terminology by translating the various designations that different databases apply to the same genes. The site is sponsored by the Institute for Systems Biology in Seattle, Washington, and other organizations.

t1dbase.org

WEB PROJECTS

Catch a Gravity Wave

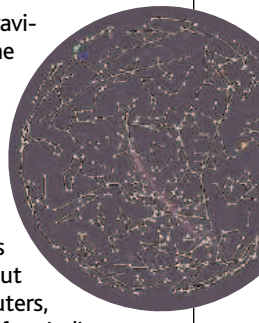

A new computer program allows you to discover gravitational waves from the comfort of your home. The program, called Einstein@Home, runs on idling personal computers and will analyze data from three observatories testing the central predictions of Albert Einstein's General Theory of Relativity.

The theory predicts that so-called gravitational waves should ripple outward from violent cosmic sources, such as colliding black holes. But the waves have never been detected directly. By parceling out the number crunching among participants' computers, Einstein@Home will search for a specific pattern of periodic gravitational waves produced by tiny spinning objects called neutron stars. Organizers hope to recruit at least 100,000 volunteers.

einstein.phys.uwm.edu

EDUCATION

Science Video Store

If you want to sit in on a lecture on buckyballs by chemist Harry Kroto or hear the late evolutionist John Maynard Smith's take on the origin of life, drop by this site from the Vega Science Trust, a nonprofit organization in the United Kingdom. Web viewers can screen more than 50 scientific programs—most aimed at college students or the general public—that range from interviews and lectures to roundtable discussions on issues such as the influence of genetics on personality. Visitors can also drop by a master class on states of matter or watch a documentary about a conference in which med students hobnob with Nobel laureates.

www.vega.org.uk

RESOURCES

Eye on Mesoamerica

You can keep a close watch on environmental changes in Central America at this new NASA Web site, created to inform researchers and the region's policymakers. SERVIR, based in the City of Knowledge, Panama, compiles satellite and other data to monitor weather, ocean conditions, and other variables. For instance, users can call up fresh measurements of ocean chlorophyll to check for the algal population explosions known as red tides. You can also pinpoint recent volcanic eruptions and earthquakes or track the latest fires. The image above shows fires erupting over the region during 2002.

servir.nsstc.nasa.gov/home.html

Send site suggestions to netwatch@aaas.org. Archive: www.sciencemag.org/netwatch

This Week

PAGE 1390
Martian ice, or lava?

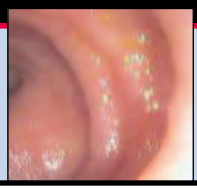

1395
The guts of HIV infections

PALEOANTHROPOLOGY

Small but Smart? Flores Hominid Shows Signs of Advanced Brain

The startling announcement last October of an 18,000-year-old skeleton of a new species of human posed a paradox: Despite having a brain no larger than a chimp's, the diminutive hominid from the Indonesian island of Flores showed signs of advanced intelligence, including hunting with sophisticated stone tools. That paradox may now be solved. A detailed study of the cranium of *Homo floresiensis*, published online this week by *Science* (www.sciencemag.org/cgi/content/abstract/1109727), reveals that the hominid apparently managed to pack a number of features of more advanced brains into its very small skull. Brain features preserved in its cranium suggest that the Flores hominid may have been able to perform advanced cognitive tasks, says lead author Dean Falk of Florida State University in Tallahassee.

That finding may overturn long-held ideas about the evolution of the human brain and also raises some provocative notions about how the Flores people evolved in the first place. "If they are correct, this is really a stunner," says anthropologist Leslie Aiello of University College London (UCL). Evolutionary anatomist Fred Spoor, also of UCL, adds that the new study "upsets one of our main concepts of human evolution, that brain size has to increase for humans to become clever." The work also undercuts the notion proposed by some critics that the Flores bones are those of a microcephalic modern human rather than of a new species.

To study the hominid's brain, Falk and colleagues, including anthropologist Charles Hildebolt of the Mallinckrodt Institute of Radiology in St. Louis, Missouri, analyzed a cast of the inner surface of its skull, or endocast, which preserves the surface features of the brain. Because the skull was too fragile for the usual method of pouring liquid rubber inside it, the team made a virtual endocast from computerized tomography scans. The original discovery team, including co-authors Michael Morwood and Peter Brown of the University of New England in Armidale, Australia, had the skull scanned at a hospital in the Indonesian capital of Jakarta before the bones were temporarily moved last fall to Yogyakarta (see sidebar).

The researchers compared the endocast to virtual endocasts of the skulls of a microcephalic modern human, a modern woman, a *Homo erectus*, a pygmy, and a chimpanzee, as well as latex endocasts of other humans, primates, and extinct hominids. They found that, relative to its overall size, the brain of *Homo floresiensis* has very large temporal lobes, brain regions associated in living people with understanding speech and hearing. Even more dramatically, the hominid has highly folded and convoluted frontal lobes, areas of the brain just under the forehead that are implicated in higher cognition. "There are two huge convolutions," Falk says. "I haven't seen swellings like this before in any [extinct] hominid endocasts," including those of *Homo erectus*. The most convoluted region is in the most forward-projecting part of the frontal lobe, called the frontal pole. Falk identifies this region as Brodmann's area 10, which is expanded in modern humans and is involved in undertaking initiatives and planning future actions—key components of higher cognition.

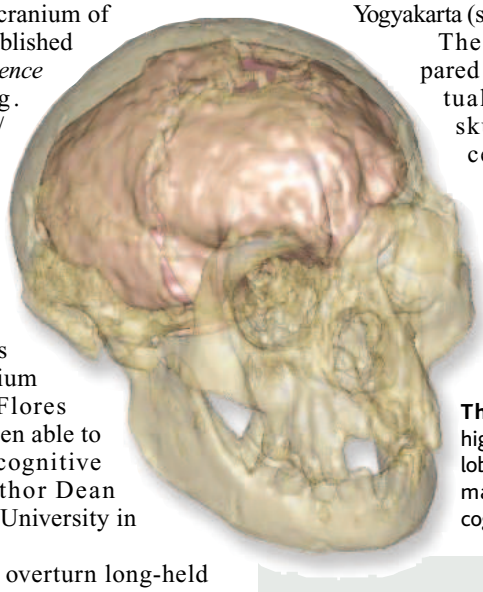

Thinking ahead? The highly convoluted frontal lobes of *Homo floresiensis* may indicate advanced cognition.

CREDIT: D. FALK *ET AL.*, *SCIENCE*

This enlarged area suggests that the little Flores people may well have been capable of creating the stone tools that were found near them, which are more typical of those made by prehistoric modern humans than earlier hominids including *Homo erectus*. "The real take-home message here is that advanced behaviors, like making sophisticated stone tools, do not necessarily require a large, modern, humanlike brain," says Spoor. "It can be done by reorganizing a small brain, with convolutions and rewiring, and this goes to the heart of our understanding of human evolution." ▶

"Hobbit" Bones Go Home to Jakarta

While scientists debate the evolutionary lessons to be drawn from the discovery of *Homo floresiensis* (see main text), a bitter custody battle over the tiny hominid's remains (*Science*, 25 February, p. 1179) may be almost over. Late last week, Indonesian paleoanthropologist Teuku Jacob gave most of the remains of up to eight individuals of the claimed new human species to members of the Center for Archaeology in Jakarta, the bones' official repository. Jacob had been studying the bones since November, when a center researcher helped him pack them into a leather bag and take them to his laboratory at Gadjah Mada University in the Indonesian city of Yogyakarta.

Some members of the original Australian-Indonesian team that discovered the hominid on the island of Flores protested loudly that the hominid had been in effect kidnapped, in violation of a memorandum of understanding between the Australian and Indonesian institutions involved. Jacob insisted that he had full permission from the archaeological center and in turn charged the Australians with interfering with long-standing arrangements among Indonesian laboratories.

According to center director Tony Djubiantono, Jacob has now returned all the hominid remains except two leg bones—a tibia and a femur—to Jakarta. Djubiantono says he is not sure when the rest of the bones will be reunited at their Jakarta home, but says that he will call Jacob "next week and every week" until they are returned.

–M.B.

Not everyone is ready to discard the importance of brain size, however. Anthropologist Katerina Semendeferi of the University of California, San Diego, who has studied area 10 extensively, cautions that "many would argue that absolute size is of paramount importance"; she adds that stronger evidence linking the stone tools with the small Flores people would strengthen the case for their cognitive abilities.

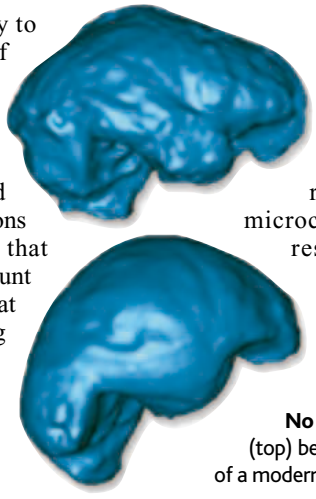

No match. The brain of *Homo floresiensis* (top) bears little resemblance in shape to that of a modern human microcephalic.

Whatever the hominid's capabilities, the endocast results argue against the notion that it was a pathological case of microcephaly, the authors say. In overall brain shape, the Flores hominid least resembles the microcephalic, and it also bears little resemblance to the pygmy. "The skull is totally the wrong shape" to be a microcephalic, Falk says. But anthropologist Alan Thorne of the Australian National University in Canberra counters that the single European microcephalic analyzed "tells us virtually nothing about the global range of microcephalic virtual endocasts." Others agree that the paper alone does not completely rule out microcephaly. "The case [against microcephaly] is increasingly less likely but not entirely closed," says Aiello. Spoor notes, however, that few researchers are convinced by the microcephaly argument at this point. "Colleagues advocating that [the Flores hominid] is a modern human microcephalic should start publishing hard evidence in peer-reviewed journals to underpin their claims," he says.

Assuming that *Homo floresiensis* is a ▶

CREDITS (TOP TO BOTTOM): D. FALK *ET AL.*, *SCIENCE*; JPL/NASA

PLANETARY SCIENCE

A Strange Little Saturnian Ice Ball Gets Stranger Still

When the Cassini spacecraft approached Saturn's icy-bright satellite Enceladus (en-SELL-uh-duss) last month, "we knew it was going to be weird," says camera team member Torrence Johnson. "We just didn't know how weird." The misfit satellite turned out to be even stranger than scientists thought in 1981, when Voyager 1 first visited. Voyager images showed the supposedly long-dead primordial ball of ice to have been geologically refreshed in recent times. Some unidentified geologic process had smoothed its battered surface in places. Now, says Johnson, it appears "some areas on Enceladus have to be very young, possibly younger than on Europa," the ice-covered ocean moon of Jupiter.

The Cassini camera, which returned 20 times the fine detail of Voyager images, imaged three sorts of terrain as it swept within 1180 kilometers of Enceladus, says Johnson, who works at the Jet Propulsion Laboratory in Pasadena, California. As seen in Voyager images, large parts of the 500-kilometer-diameter moon are cratered by comet impacts, although the craters appear "softened." Presumably, this geologically older surface ice has been warm enough to flow and "relax." A second sort of terrain that in Voyager images looked completely blank now appears to be fractured by repeated squeezing and stretching of a brittle crust.

A third terrain looks "scallopy, twisted, taffylike," says Johnson. Absent are the smooth plains formed by once-fluid water that were assumed to have spewed onto the surface in "cryovolcanic" eruptions. "You don't see the flat, flooded picture of cryovolcanism" discussed after Voyager, says Johnson. "Something flowed there, but it was very viscous." All in all, large parts of Enceladus have suffered "fairly energetic events fairly recently," perhaps less than 100 million years ago.

The missing piece of the puzzle is an energy source that could have warmed and melted ice as well as fueled tectonic forces on Enceladus. Cassini may have found one. As the spacecraft flew by, its radio signal's frequency shifted more than expected. That means the moon was gravitationally tugging on Cassini harder than a ball of pure ice would, says camera team member Joseph Veverka of Cornell University. "It's definitely got some rock in there," he says. And rock would carry radioactive elements such as potassium-40 whose decay would have heated the interior, perhaps melted ice with the help of some naturally occurring ammonia antifreeze, and churned the interior to deform the surface.

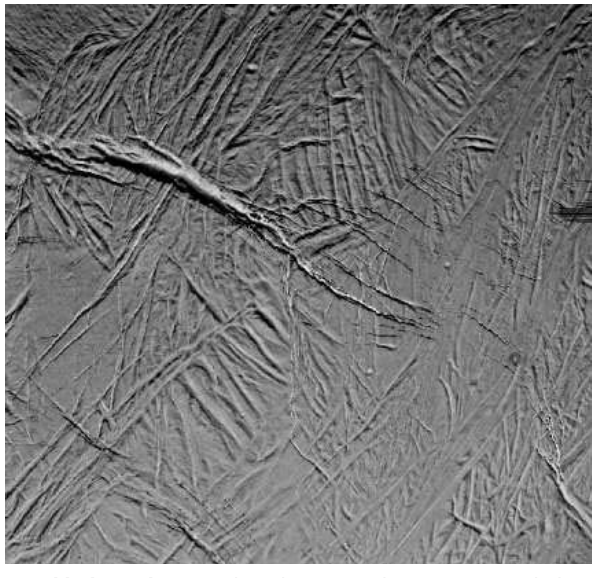

Wrinkled youth. Something has more than once crumpled this part of icy Enceladus. Judging by the dearth of impact craters, it happened in the geologically recent past.

Rock would help, notes planetary physicist David Stevenson of the California Institute of Technology in Pasadena, but, he adds, "I don't understand why Enceladus is doing something different from other moons." Neighboring Tethys, for example, is twice the diameter of Enceladus and has perhaps six times the mass, yet it is covered by ancient cratered terrain. Unlike watery Europa, Enceladus does not presently orbit in step with other moons, which could pump tidal energy to it from Saturn, although it might have done so in the past (*Science*, 29 July 1983, p. 449). More clues to Enceladus's energetic lifestyle could come next week (9 March), when Cassini makes an even closer pass. **–RICHARD A. KERR**

new hominid species, the question remains why its brain is so small. In the original *Nature* papers, Morwood, Brown, and their co-authors suggested that an ancestral population of larger *Homo erectus* shrank in body and brain, in the first case of island dwarfism seen in hominids. But the new paper urges reconsideration of an alternative hypothesis, that a small-brained, small-bodied, pre-*erectus* hominid managed to get to Flores in the distant past, and then, in a case of parallel evolution with modern humans, evolved a relatively advanced brain on its own. "Some of [the hominid's] traits indicate that the ancestral population may predate *Homo erectus*," says Morwood. He adds that his team is now preparing to look for just such an ancestor on the Indonesian islands of Java and Sulawesi. Says Falk: "Maybe there are even more surprises waiting out there."

–MICHAEL BALTER

COMPUTER SECURITY

Flaw Found in Data-Protection Method

Cryptographers are making a hash of things again. Last month three code breakers demonstrated a way to break the Secure Hash Algorithm (SHA-1), a government-approved standard cryptographic function crucial to many electronic transactions, including digital signature schemes and password verification. Although the finding doesn't mean that SHA-1 is unusable, it has prompted the cryptographic community to suggest finding more secure versions of SHA. "The research community is going to have to think very hard about this," says Massachusetts Institute of Technology cryptographer Ron Rivest. "We clearly have to replace SHA-1."

A hash function is a mathematical device that takes a chunk of text (which can be huge) and, through a series of arithmetic manipulations, turns that text into a number (which is small). Hash functions allow computer programs to verify that large blocks of text or data are unaltered without needing to store the large files themselves. For example, you might know that a particular hash function spits out the number 634,331,206 when given the authentic text of *War and Peace*. If someone gives you a file of text, you just run the hash function on it. If the number 634,331,206 doesn't come out, the file can't be an unaltered copy of *War and Peace*.

That is what many operating systems do with passwords: Rather than storing passwords in an easy-to-steal file, they store the passwords' hash values instead. Even if hackers get hold of the list of hash values, they don't know how to turn those values into valid passwords and get into the system. Of course, this is true only if the program can't be run backward. To guarantee a one-way hash function, the National Institute of Standards and Technology (NIST) in the early 1990s introduced SHA-1.

Now, more than a decade later, three researchers from China and the United States have devised the first successful attack on SHA-1. Although they don't force the algorithm to run backward, in an unpublished paper circulating among computer-security experts they show how to do a related trick. "What we have done is shown something called a collision," says Yiqun Lisa Yin, an independent consultant in Greenwich, Connecticut. "Two different messages map to the same outcome." In other words, Yin and her two colleagues, Xiaoyun Wang and Hongbo Yu of Shandong University in East China, came up with a way to find different blocks of text that have identical hash values. In theory, hackers could use the trick to forge stamps of authenticity for electronic documents.

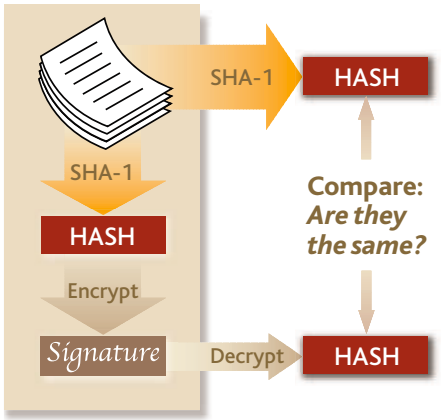

Hashed Hancock. A digital signature scheme using hash functions (such as SHA-1) and ciphers may be vulnerable to forgery.

An attacker, by pure brute force, would expect to find one such collision in 2^{80} attempts. The team shows how to reduce that value to 2^{69} tries—still out of the range of supercomputers, but close enough to worry experts. Rivest thinks NIST should hold a competition to design a next-generation hash algorithm. NIST has no plans for such a competition, says Edward Roback, chief of NIST's Computer Security Resource Center, but is encouraging users to switch to beefed-up versions of SHA: "It's not like SHA is completely broken, but any time the security of an algorithm is less than expected, it's a concern."

–CHARLES SEIFE

ScienceScope

Sri Lankan Disease Emerges

Sri Lankan and international health officials are warily eyeing the progress of a mysterious disease in that country. Over the past 3 weeks, 200 people have been hospitalized with chest pains, shortness of breath, and racing hearts. But there have been no deaths, despite media reports to the contrary. Sri Lankan health authorities have been unable to identify a causative agent in blood samples.

The outbreak has hit the region around Badulla, about 130 kilometers east of Colombo. The epicenter is some distance from the coast, and the outbreak is thought to be unrelated to the late December tsunami. Paba Palihawadana, deputy chief of epidemiology for the country's Ministry of Health, says that local hospitals are reporting five or six new cases a day. But she adds that concern about the disease's unknown cause is tempered by its apparent mildness. Patients are recovering quickly, and the disease does not seem to be highly contagious. "So far, we have not seen any clustering of cases," Palihawadana says.

Experts from the World Health Organization were due to arrive in Sri Lanka this week to help investigate the new disease.

–DENNIS NORMILE

Research Boost for Italy's South

ROME—Italy plans to spend $600 million over the next few years to strengthen research capacity in its underdeveloped southern region. The investment is large—the entire national research council budget for 2005 is about $1.2 billion—and will be divided between specific projects aimed at boosting the economy, such as a lagoon-monitoring system in Sardinia, and the creation of a dozen labs in areas from seismology to medical diagnostics.

"This is truly a first for the south," says Letizia Moratti, head of Italy's education and research ministry, who sees the initiative as an opportunity to attract scientists to the region.

However, critics argue that the money would be better spent in backing ongoing efforts that are underfunded. "Why not put resources into our existing labs, projects, and many excellent researchers?" asks medical researcher Gianluigi Giannelli of the University of Bari.

–SUSAN BIGGIN

PLANETARY SCIENCE

Ice or Lava Sea on Mars? A Transatlantic Debate Erupts

The déjà vu was palpable when U.S. planetary scientists heard the news last week that a frozen sea the size of the North Sea had been found on Mars. "We went through all this 7 years ago when [Mars Global Surveyor] first imaged these terrains," says planetary geologist Alfred McEwen of the University of Arizona, Tucson. "Our immediate reaction then was, 'Gosh, that looks like frozen ice.' But we quickly realized it had to be lava."

"It can't be lava," says volcanologist John Murray of the Open University in Milton Keynes, U.K. He and his teammates running the High Resolution Stereo Camera (HRSC) onboard the European Space Agency's Mars Express orbiter reported at the First Mars Express Science Conference last week that the "lava" is actually an ice floe–covered sea frozen in place. That would make the Elysium Plains a fetching place to land and look for microfossils of martian life, Murray notes.

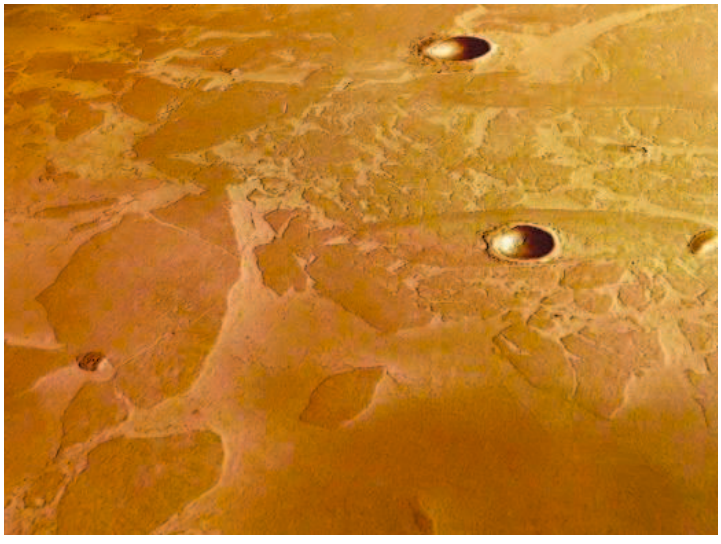

Sea ice or lava sea? No doubt parts of Mars look like a frozen sea off Antarctica, but looks can be deceiving, say many U.S. planetary scientists.

Everyone agrees that both water and lava have gushed from the ground in the vicinity of Elysium (*Science*, 30 November 2001, p. 1820). McEwen and others had traced lava and water flows back to the great ground cracks of the 1000-kilometer-long Cerberus Fossae. Apparently, rising magma intersected subterranean water and drove it through the cracks to the surface, carrying with it any debris of life past or present. Murray and his colleagues now see signs that about 5 million years ago such a gusher did not just seep into the ground but pooled to a depth of 45 meters over an area about 850 kilometers across. Once its surface froze, they say, the waters moved again, breaking the ice into floes now locked into a frozen sea that has become buried under a protective layer of volcanic ash and sediment.

In a paper to be published 17 March in *Nature*, Murray and his colleagues will detail the ice signs they see in the images, which are among the first European data returned from another planetary body. A pivotal claim is that the level of the putative sea has dropped since its surface froze. Mapping elevations using HRSC stereo imaging as well as laser altimetry from Mars Global Surveyor, they find that flood material inside as well as outside some craters has sunk about 15 meters below the crater rim. Floodwaters could have seeped or sublimated away, says Murray, but lava could not. In addition, "the edge [of the flow] ties in well with a sea rather than lava," says Murray. Where HRSC has looked, he sees a beach swept by turbulent flows, a high-water mark, and the final sunken level with pack ice at the bottom.

American Mars geologists, who have dominated the field by dint of returning almost all the previous data from Mars, aren't persuaded. "I think it's unlikely they're right," says Michael Carr, planetary geologist ▶

CONFLICTS OF INTEREST

NIH Scientists Raise Fuss About Scope of New Rules

Scientists at the National Institutes of Health (NIH) are rallying to challenge strict new ethics rules that many feel go much too far. A group of intramural leaders met with NIH Director Elias Zerhouni last week to air their concerns. Meanwhile, NIH officials say they have cleared many of those on a list of scientists who apparently had failed to report ties to drug companies.

The new ethics rules, imposed last month, came in response to revelations in the press and in Congress that some NIH scientists have had lucrative consulting deals that weren't always publicly disclosed or even reported to NIH. In addition to barring all consulting for industry and nonprofit health-related organizations, the regulations prohibit senior staff members and their families from owning stock in drug and biotech companies. Everyone else can own no more than $15,000 in holdings from any one company (*Science*, 11 February, p. 824).

The rules have outraged NIH scientists. Among their worries are their own stock portfolios and how the rules might affect the recruitment of fellows, who spend only a few years at NIH. Last week, a newly elected, 18-member executive committee of the Assembly of Scientists—a revival of a defunct body—shared their views with Zerhouni. He "clearly understand how difficult some of these issues are," says committee member Cynthia Dunbar of the National Heart, Lung, and Blood Institute. NIH officials were sympathetic to recommendations to craft exemptions for fellows and to extend the 150-day deadline for divesting stock, she says. But Zerhouni advised them to send their concerns to the Department of Health and Human Services, which developed the rule along with the Office of Government Ethics.

Dunbar says the Assembly of Scientists is now working on a set of proposals more in line with the recommendations of a blue-ribbon panel last year that urged Zerhouni to ban consulting by senior leaders but allow limited consulting by others (*Science*, 14 May 2004, p. 936). Other scientists are weighing a legal challenge to the stock ban, says Abner Notkins of the National Institute of Dental and Craniofacial Research.

Meanwhile, NIH clarified a press report regarding the status of about 100 scientists accused by a congressional committee of not telling NIH about their consulting activities. The committee compiled its list from information supplied by drug companies. As many as 80% of those on the list have been exonerated, according to a 23 February story in *The Washington Post*. But NIH Deputy Director Raynard Kington says only about half have been cleared, and investigations of the rest are still under way.

—JOCELYN KAISER

CREDIT: ESA/DLR/FU BERLIN (G. NEUKUM)

emeritus at the U.S. Geological Survey (USGS) in Menlo Park, California. McEwen and many others feel more strongly than Carr that they were right the first time. "We've been studying these lavas for 7 years," McEwen says. "Put aerial photos of Iceland [lava flows] side by side with Mars, and you can't tell the difference."

Martian lavas could look so much like sea ice because similar processes shape both. But on Mars, McEwen sees—among other volcanic features—small edifices that disgorged the lavas and steep-sided levees at the flow edges like the ones lavas form on Earth. "What we're talking about is a sea of lava," says planetary volcanologist Laszlo Keszthelyi of USGS in Flagstaff, Arizona. The apparently sunken lava may just be the result of lava withdrawing beneath a solid crust, he says.

Resolution of the matter will likely require targeting the exact areas HRSC imaged with the camera and ground-penetrating radar on Mars Reconnaissance Orbiter, due for launch this August. Until then, water or rock may remain in the eye of the beholder. **–Richard A. Kerr**

FRENCH SCIENCE

Report Puts Pasteur Move on Hold

Paris—Scientists at the Pasteur Institute here were elated last week after a report by British mediator John Skehel scuttled a controversial plan to move part of the lab to a commercial site outside Paris. But decisions about the Pasteur's future accommodation—and the fate of its embattled director, Philippe Kourilsky—are on hold until the election of a new board of directors in the next few weeks.

Loath to leave their historic campus in the heart of the city—the site of Louis Pasteur's original lab and now his resting place—the staff vehemently opposed moving several units to a building donated by Pfizer in the suburb of Fresnes. Kourilsky said the move was necessary to renovate key buildings on the Paris campus. Seeking to help resolve the crisis, Pasteur's board of directors resigned en masse on 12 January (*Science*, 21 January, p. 333).

But Skehel, director of the Medical Research Council's National Institute for Medical Research (NIMR) in London, has concluded that the building posing the biggest renovation problem, called Daclaux, can be upgraded in two stages, each taking about 6 months. Uprooted staff could be temporarily relocated to Biotop, an on-campus building that's now home to biotech start-ups. Biotop residents, in turn, should be offered temporary housing in a Paris science park, Skehel and NIMR assistant director John Wills conclude in their report.

The directors of Pasteur's 12 scientific departments, to whom Skehel presented his conclusions on 17 February, are generally "very pleased," says Brigitte Gicquel, director of the Microbial Pathogenesis department. "The recommendations are very precise, very clear, and they are feasible," she says.

Under fire. Philippe Kourilsky's abrasive style has angered Pasteur staff.

Some scientists say Kourilsky, already under fire for his abrasive management style, may have to step down. A Pasteur spokesperson says Kourilsky will not comment, but a short statement issued on his behalf says a study group would be formed soon to analyze the report and its consequences. Gicquel says it seems inconceivable that the recommendations would not be heeded. For the moment, however, all decisions are on hold until Pasteur's 100-strong General Meeting—made up of staff and outsiders—elects 16 new members to the 20-member board of directors on 15 March.

If the move to the 17,000-square-meter complex in Fresnes is abandoned, it's not clear how the building would be used. One option would be to rent it, a spokesperson says. Complicating matters further, the French government has recently floated yet another plan: to lure the entire Pasteur Institute to Palaiseau, 22 kilometers southwest of Paris. There, it would become part of a "Competitivity Pole"—regional centers of scientific expertise and innovation being promoted by the government—along with the prestigious École Polytechnique and other institutions.

This choice may be less controversial than Fresnes because the location is easier to reach, has more scientific prestige, and would not split the campus in two, notes Pasteur's Patrick Grimont. Although, as a private institution, Pasteur could not be forced to move, the spokesperson says the option is "being considered." **–Martin Enserink**

CREDITS (TOP TO BOTTOM): USC; GAILLARDE RAPHAEL/GAMMA

ScienceScope

Stem Cell Center Gets Head

Neurobiologist Zach Hall, medical research dean at the University of Southern California in Los Angeles, has been named interim president of the new California Institute for Regenerative Medicine (CIRM), the state agency set up by Proposition 71 to administer stem cell research. He was endorsed by the institute's board at a 1 March meeting held at Stanford University.

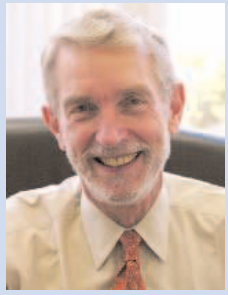

Hall, 67, seems to fill the bill admirably as a researcher, biotech entrepreneur, and former director of the National Institute of Neurological Disorders and Stroke at the National Institutes of Health. Hall is also relatively immune from conflict-of-interest charges because his work on cell surface receptors doesn't involve stem cells. A headhunting firm has been tapped to find a permanent director for CIRM by June.

–Constance Holden

New Buoys May Buoy Research

Ocean researchers hope the expanded U.S. tsunami warning system could offer new opportunities for basic science.

A shortfall in ship support from the National Science Foundation (NSF) is putting the squeeze on researchers. "The number of field programs at sea that NSF can actually support is going down," says Lynne Talley, a physical oceanographer with the Scripps Institution of Oceanography in La Jolla, California.

But marine scientists might find room aboard ships being deployed for the tsunami initiative. Managers from various seafaring government agencies met this week at the headquarters of the National Oceanic and Atmospheric Administration (NOAA) to discuss plans for, among other things, expanding the number of wave-detection buoys in its Pacific tsunami warning system from six to 24, plus a handful more in the Atlantic and Caribbean (*Science*, 21 January, p. 331). "Any other science mission we can do while we're out there we'll try to accommodate," a NOAA spokesperson says. Such missions could include bottom-mapping efforts and marine biology.

–Eli Kintisch

INFECTIOUS DISEASES

Experts Dismiss Pig Flu Scare as Nonsense

It could be the result of an embarrassing lab escape or a vaccine study gone awry; it could even be the smoking gun from a secret biowarfare program.

But then, it could be nothing at all.

For 4 months now, a series of strange influenza sequences has been sitting in GenBank, the U.S. National Institutes of Health's DNA database, that seems to suggest that pigs in South Korea have become infected with a flu strain used for research in labs around the world but not known to occur in nature. The World Health Organization (WHO) in Geneva has dismissed the snippets as the result of a lab error. But the Korean scientist who posted them insists they are real—and troubling—and he is hoping that two renowned flu labs will prove him right.

Meanwhile, speculation about the case has been fueled relentlessly on the Internet by an outsider to the influenza world. Henry Niman, the president of a Pittsburgh, Pennsylvania–based company called Recombinomics and the operator of a mailing list about flu, believes that the virus, called WSN/33, poses a grave danger to human health. Recently, his views have begun to draw attention—much to the chagrin of those scientists who think the whole story is nonsense.

The bizarre case started on 24 October when Sang Heui Seo, a researcher at Chungnam National University in Daejeon, deposited in GenBank partial RNA sequences from a series of viruses isolated from pigs. Niman, a molecular biologist and former Harvard surgery instructor with an intense interest in virus evolution, discovered them soon after they were made public in late November. He noticed that six of the viruses appeared to be hybrids; in addition to genes from H9N2, an avian flu virus that previously circulated in Korean pigs, they had between three and seven genes with WSN/33-like sequences.

WSN/33 was produced in 1940 by infecting mice with the first human flu virus ever isolated, in London in 1933. It's a mystery how it got into the pigs, says Niman, who proffers scenarios ranging from a lab accident to illicit experiments to create a deadly flu strain for biowarfare—neighboring North Korea comes to mind, he says. Niman believes the spread of the virus should be thoroughly investigated, because WSN/33, which infects mice's brains, is distantly related to the 1918 pandemic virus, and if it infects pigs, it may infect humans as well. That's why he immediately alerted WHO in December.

But WHO is unimpressed. The agency discussed Niman's claims by e-mail with its flu advisers in December, says Klaus Stöhr, WHO's global influenza coordinator. They quickly concluded that the results were lab contamination. Such mix-ups can happen easily when researchers use the polymerase chain reaction to amplify bits of genetic material, says Robert Webster of St. Jude Children's Research Hospital in Memphis, Tennessee, one of Stöhr's advisers. Contamination was likely, says Webster, because Seo had previously received WSN/33 from Webster's own lab. (Seo also worked at Webster's lab between 1999 and 2002, and the two published seven papers together.)

But in an interview, Seo denied ever having received the WSN/33 from Memphis or anywhere else. What's more, "I have many scientific data that can rebut WSN contamination," he wrote in a follow-up e-mail. But he declined further comment until his results are published. Seo says *Science* rejected his paper describing the discovery of WSN in pigs but may reconsider the manuscript if the findings are backed up by a well-established flu lab.

Seo hopes that Malik Peiris at the University of Hong Kong and Yoshi Kawaoka at the University of Wisconsin, Madison, who both have samples from Korea, can confirm WSN's presence. Both Peiris and Kawaoka declined to comment for this story, but Stöhr says the results from the Kawaoka lab will be out soon. The Korean National Veterinary and Quarantine Services also told *Science* it has been unable to replicate the findings, despite testing hundreds of pigs.

Molecular biologist and flu expert Ron Fouchier of Erasmus University Medical Center in Rotterdam, the Netherlands, says the sequences definitely contain WSN's genetic signature. But he says the fact that the six controversial isolates have varying numbers of WSN fragments points to lab contamination: "If this was an endemic pig virus, I'd expect all viruses to have the same WSN gene segments."

Even if WSN were circulating in Korean pigs, Stöhr says, that wouldn't spell disaster. There's no evidence that WSN is still dangerous to humans, he says; indeed, Fouchier adds, many labs use it without taking special safety precautions.

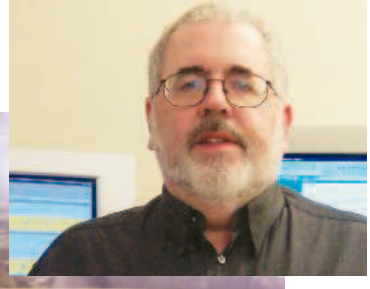

Agitator. Henry Niman (*top*) is worried that pigs on Korean farms (shown here being sanitized for foot-and-mouth disease) may harbor a strange flu virus, posing a threat to human health.

Determined to draw attention to the case, Niman, who has also criticized WHO extensively for its handling of the severe acute respiratory syndrome and avian influenza outbreaks, has posted more than 50 messages about the case on his site since December, with some success: Infectious-disease specialist Laurie Garrett of the Foreign Relations Council in New York City wrote about the case in an online article on 16 February—although she dismissed it as a "scary near-miss"—and last week, *Nature* reported Niman's claims.

That attention irks Stöhr, who points out that Niman has not published in the scientific literature since 1996 and is not a flu expert. WHO will not issue an official statement about the case, he says: "We're not going to bother 6.5 billion people with something that's of no public health importance." Webster, too, says any publicity is too much: "It's so easy these days for somebody with a Web site to create a lot of panic."

Being an expert doesn't always mean being right, counters Niman, who adds that when the truth comes out, "WHO and Webster will look very ridiculous."

—MARTIN ENSERINK

CREDITS: YUN SUK-BONG/REUTERS; (INSET) H. NIMAN

CANADA

Grants Councils Say More Isn't Nearly Enough to Keep Science Healthy

OTTAWA—Research no longer carries the political cachet it once did. That's the message Canadian science policy makers are taking from a new budget put forward last week. The Liberal Party's promise to double Canada's research effort by 2010 and put science at the top of its agenda has been undermined by disappointingly small increases for the country's three granting councils. The result, say the council chairs, is likely to be fewer grants, smaller awards, and less support for training the next generation of scientists.

"The problem is that the [political] winds are different," says Marc Renaud, head of the Social Sciences and Humanities Research Council (SSHRC). "Support for science and technology is not as strong as it used to be."

The minority government's blueprint for the fiscal year that begins on 1 April provides a little for everyone, although Prime Minister Paul Martin reserved the biggest increases for retooling the military and cutting taxes in an apparently successful bid to win over the opposition Conservative Party. Genome Canada gets $132 million over 2 years pending an assessment of long-term national genomics needs. The nonprofit agency had been due to expire this year after spending $300 million supporting genomics research of interest to industries such as agriculture, health, forestry, and fisheries (*Science*, 10 March 2000, p. 1732). Universities get a 6% boost in payments for indirect costs associated with research (*Science*, 27 October 2000, p. 687). And the government has reserved $24 million over 10 years for the new Canadian Academy of Sciences, once it becomes operational (*Science*, 22 October 2004, p. 589). The budget also provided $178 million over 5 years for the Vancouver-based TRI University Meson Facility (TRIUMF).

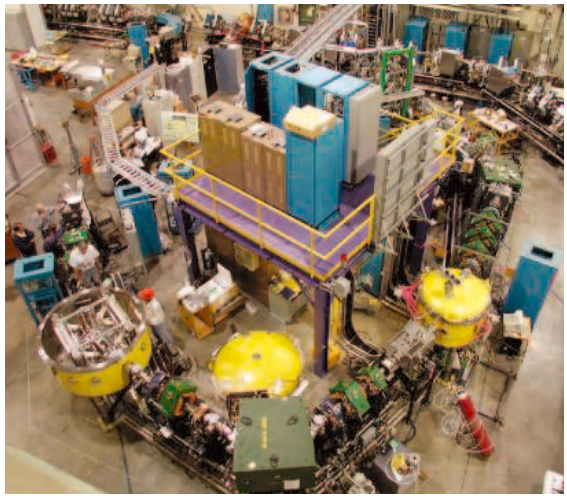

Mixed news. Canada's new budget contains upgrades to TRIUMF but not money to send scientists to CERN.

But Natural Sciences and Engineering Research Council president Thomas Brzustowski lamented his failure to obtain a larger increase. "I thought I made a good case" for a $64 million boost, he says; instead, the council received an increase of $18 million, or 3.3%, to its $522 million budget. That means Brzustowski will spend an unhappy last few months in office before retiring in July, trying to reconcile rising demand with few additional resources.

For SSHRC, Renaud says a 5% boost translates into a declining success rate for applicants. And Alan Bernstein, president of the Canadian Institutes of Health Research, says that a one-time, 5% hike could jeopardize a planned expansion of clinical trials and an initiative in regenerative medicine. "It's hard to be strategic when you get these increases 1 year at a time," he says.

TRIUMF also received $44 million less than requested. The gap, says Director Alan Shotter of the University of Alberta, means that TRIUMF won't be able to send Canadian scientists to international facilities such as CERN, Europe's high-energy particle physics lab near Geneva, although it will continue to host visiting scientists. Still, the government's continued investment in the lab was welcome news to foreign collaborators. "That facility is going to make significant contributions to science," says C. Konrad Gelbke, director of the National Superconducting Cyclotron Laboratory at Michigan State University in East Lansing.

–WAYNE KONDRO

Wayne Kondro is a freelance writer in Ottawa.

HUMAN EMBRYONIC STEM CELLS

Getting the Mice out of ES Cell Cultures

Researchers in Wisconsin have come a step closer to developing a culture for human embryonic stem (ES) cells that is free of animal products—a recipe that is essential for growing any cells that would be used for therapy in humans.

Human ES cells are tricky to grow, and many regard their culture more as an art than a science. "In general, we don't understand what is going on here," says stem cell researcher Ronald McKay of the National Institute of Neurological Disorders and Stroke in Bethesda, Maryland. But scientists have found that they need a combination of at least two animal-derived products: fetal bovine serum to nourish the cells and a layer of fetal mouse fibroblasts called feeder cells that inhibit differentiation into a variety of cell types.

Because of that, there is a risk of contamination from animal pathogens, a fact confirmed by a study published in the January issue of *Nature Medicine*. Physician Ajit Varki and colleagues at the University of California, San Diego, identified a substance on the surface of cultured human ES cells, *N*-glycolylneuraminic acid, that is taken up from animal products and that would probably cause them to be rejected if transplanted into a patient.

To circumvent such problems, many groups have been racing to develop stem cell culture media free of animal products—mouse feeder cells in particular—with some unreplicated reports of success. Now, a group led by developmental biologist Ren-He Xu of the WiCell Research Institute at the University of Wisconsin has found that in high doses, a synthetic human molecule known as fibroblast growth factor 2 (FGF2) can do what mouse feeder cells do: sustain stem cells in an undifferentiated—or pluripotent—state.

Xu says his team, which includes James Thomson, who first successfully derived human ES cells, discovered a few years ago that when the culture medium they normally use is not conditioned by mouse cells, it promotes stem cell differentiation, mimicking the activity of bone morphogenetic protein (BMP). That meant that there must be molecules in the feeder cells that suppress BMP activity. They have now determined that FGF2, a protein routinely used in human ES cell culture, will, if administered in high quantities in combination with BMP antagonists, inhibit BMP activity, preserving the cells in the undifferentiated state. The report appears in the March issue of *Nature Methods*.

Although Varki says the Wisconsin study is "a major step forward," he and others point to several issues that remain to be resolved—including finding ways to remove bovine serum, which also appears to be a major source of contamination.

–CONSTANCE HOLDEN

CREDIT: M. HAPKE/TRIUMF

RETROVIRUS MEETING

Gut Assumes Sinister New Role in HIV Pathogenesis

BOSTON—It's the gut, stupid.

That was one of the clearest take-home messages from the 12th Conference on Retroviruses and Opportunistic Infections, where 3900 researchers from 72 countries converged 22 to 25 February to discuss some of the most fundamental questions riddling the field. New insights emerged about everything from the forces behind Uganda's celebrated drop in HIV prevalence to the amount of benefit that anti-HIV drugs have provided. And on the basic research front, immunologist Daniel Douek of the Vaccine Research Center at the U.S. National Institutes of Health in Bethesda, Maryland, tied together new data with underappreciated older work that illuminate the guts of HIV pathogenesis.

Despite 20 years of research into HIV, debates still rage about the path from infection to immunological mayhem. There is abundant evidence that HIV preferentially infects and decimates CD4 white blood cells, and some researchers have long argued that direct killing alone causes the profound CD4 loss that is the hallmark of AIDS. That prompted David Ho, chair of this year's meeting, to once wear a button saying, "It's the virus, stupid." Another camp contends that HIV infects a relatively small number of CD4 cells and indirectly causes the massive death of uninfected "innocent bystanders" by activating them, a process that leads to their premature death.

Daniel Douek indicted both direct and indirect killing, with the infection of CD4 cells in the gut playing an especially sinister role. Building on previous work done in monkeys by Ronald Veazey and Andrew Lackner of the Tulane National Primate Research Center, Douek charted how HIV blazes through CD4 cells, starting in the gut and then moving into lymph nodes and the blood. Regardless of the route of transmission, at infection, HIV selects CD4s that also have surface receptors known as CCR5. The vast majority of CD4+/CCR5+ cells reside in the gut. Douek showed a startling photograph taken during colonoscopies. Whereas an uninfected person's ileum had mountains of lymphoid tissue that contained CD4+/CCR5+ cells, the landscape of the ileum of a person recently infected by HIV was scraped clean. "You have absolutely no lymphoid tissue at all—it's completely wiped out," noted Douek, who showed evidence that direct killing caused this loss.

As the disease progresses to a chronic infection, said Douek, indirect killing explains much of the CD4 loss. Douek focused on lymph nodes, which repopulate the body with new CD4s. He proposed that when HIV destroys gut immunity, other pathogens flourish, which, in turn, overactivates the lymph production of CD4s, many of which will soon die even though they are uninfected.

Just as the inflammation caused by hepatitis destroys the liver, chronic inflammation of lymph nodes—which Douek dubbed "immunitis"—destroys their architecture, leading to massive buildup of collagen, causing fibrosis. And his lab, working with a group headed by Timothy Schacker of the University of Minnesota, Twin Cities, indeed showed that the greater the amount of collagen in lymph nodes, the less able infected people were to respond to anti-HIV drugs. Douek says lymph node biopsies thus may help clarify differences in people's responses to treatment, and he suggests that antifibrotic agents like the cancer drug Gleevec might help HIV-infected people.

The most important ramifications of this improved understanding of how HIV causes disease could be in vaccine research, said Douek. A vaccine that triggers immune responses in the gut may best thwart the initial infection. Similarly, measuring gut immunity after vaccination—no easy feat—may also guide researchers to specific responses that correlate with protection.

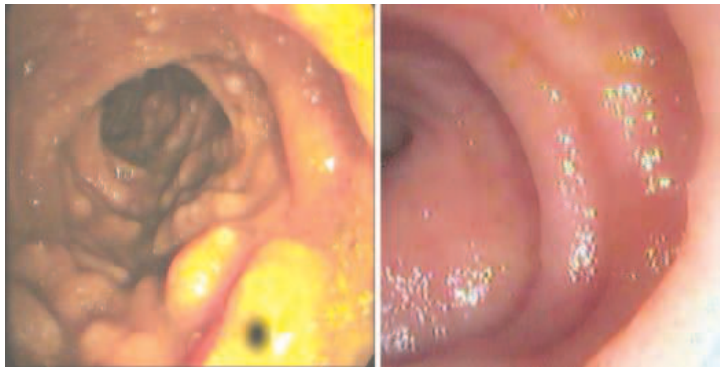

Before and after. An uninfected person's ileum contains mounds of protective immune cells (left); these are stripped bare after HIV infection.

Douek's presentation received rave reviews. "It made it worth my coming here," said Steven Deeks, a leading AIDS clinician at the University of California, San Francisco. "It's the best talk I heard," agreed AIDS vaccine researcher Ronald Desrosiers, who heads Harvard's primate research center.

Another highlight of the meeting was an epidemiologic study from Uganda. Maria Wawer of the Columbia University Mailman School of Public Health in New York City has led a study of HIV's spread in Uganda's Rakai district, conducting annual surveys of 10,000 people over the past 15 years. Uganda has been praised for its sharp declines in HIV prevalence, which some—including the Bush Administration—have attributed to increases in abstinence and monogamy. Wawer's new data challenge those assumptions, indicating that, at least in Rakai, drops in prevalence were due to deaths from HIV outnumbering new infections and an increase in condom use. Wawer noted that Uganda now has a shortage of condoms.

Off message. New data ascribe Uganda's AIDS "success" to condom use rather than the abstinence and faithfulness promoted on this Kampala billboard.

Kevin DeCock, an epidemiologist who heads the U.S. Centers for Disease Control and Prevention's efforts in Kenya, cautioned against pitting one prevention strategy against another and contended that one of the most effective approaches is often overlooked: HIV diagnosis, an opportune time to encourage people to reduce risky behaviors.

Diagnosis also frequently leads people to anti-HIV therapy, providing dramatic benefits that Rochelle Walensky, an infectious-disease specialist at Massachusetts General Hospital in Boston, has attempted to quantify. According to a mathematical model developed by Walensky, Kenneth Freedberg, and colleagues, anti-HIV drugs in the United States alone have saved over 2 million years of life. The model further shows that if a person starts potent treatment with an average of 87 CD4 cells—a state of destruction that typically occurs after about 11 years of untreated HIV infection—drugs available today will extend life by nearly 15 years. This "far exceeds the gains realized by many other disease interventions," including treatment for breast cancer and lymphoma, she said. Now the challenge is to get the drugs to the more than 4 million people who most need them but still have no access.

–JON COHEN

The 9/11 terrorist attacks and the anthrax letters triggered a vast program to protect the U.S. from bioterrorism. Three years later, some scientists complain that it is hurting basic microbiology—and ultimately, public health

Has Biodefense Gone Overboard?

Patricia Kiley is wondering whether to hop on the bandwagon.

As a young microbiologist at the University of Wisconsin, Madison, Kiley is making a name for herself studying some of the most basic life processes—for instance, how bacteria sense changing oxygen levels in their environment. But lately, she has felt the oxygen being sucked out of her own field, as funding has become increasingly scarce. Her dilemma: Should she trade her model organism, *Escherichia coli*, for a bioterrorism agent, to get a shot at the current U.S. biodefense bonanza? Scientifically speaking, switching would be "stupid," Kiley says; progress is much easier in *E. coli*, a well-known lab workhorse. But she worries that she may have little choice.

Kiley is not the only one who's concerned. More than 750 U.S. microbiologists—including the president-elect of the American Society for Microbiology in Washington, D.C., Stanley Maloy of San Diego State University, and seven past ASM presidents—sent an open letter to National Institutes of Health (NIH) Director Elias Zerhouni this week, complaining that the current spending spree in biodefense is threatening the very foundation of microbiology. While budgets have skyrocketed for exotic agents such as plague, anthrax, and tularemia—each of them negligible as human health threats—research on widespread and perhaps mundane pathogens is falling by the wayside, the letter says, as is work with traditional model organisms such as Kiley's *E. coli*.

The letter by S. Altman *et al*., published in this issue, has circulated among more than 1100 reviewers for, and beneficiaries of, two NIH study sections for microbiology, and it has become a hot topic in recent weeks. "Researchers should never whine about a lack of funding for their research," says David Walker of the University of Texas Medical Branch in Galveston, who did not sign it. "Biodefense is what Congress wants us to do," adds Walker, whose university has thrived thanks to the new money. Walker also notes that the main organizer of the letter, molecular biologist Richard Ebright of Rutgers University in Piscataway, New Jersey, has an agenda that goes beyond advocating for microbiology; Ebright has been an outspoken critic of the biodefense buildup, arguing that it is creating new risks (see sidebar, p. 1397).

Getting the boot? Biodefense grants have shot up but basic microbiology is suffering, the open letter complains.

NIH officials, meanwhile, say the numbers cited in the letter are misleading. Biodefense research spending—some $1.7 billion this year in NIH funding alone, almost entirely at the National Institute of Allergy and Infectious Diseases (NIAID)—has come on top of existing budgets, says NIAID Director Anthony Fauci, and nonbiodefense microbiology has fared no worse than NIH-supported research in general. "I wish those who signed it would take a careful look at the data," says Fauci. Moreover, studying biodefense agents is yielding valuable insights that will help fight other, more prominent diseases as well, Fauci says.

Even among those who did sign, opinions vary widely. Whereas some believe that the massive biodefense effort is unnecessary or even dangerous, others agree that it can help the fight against infectious disease—they just think the balance is skewed.

Windfall for science

Just how much money would go to biodefense was decided in the frantic months that followed 9/11 and the anthrax letters in 2001. Among several other measures aimed at protecting the nation from bioterrorism, the Bush Administration decided to radically ramp up research on biodefense. NIAID staff added up rough costs for new labs, put together a strategic plan, and persuaded the White House to propose $1.5 billion in new money for biodefense research and labs in NIH's 2003 budget.

Congress agreed, and NIAID's overall budget rose 47% in 1 year, leaving it with a portfolio divided evenly among AIDS, biodefense, and other infectious diseases. Although the new money helped complete a plan to double the NIH budget over 5 years, many institutes other than NIAID saw their budgets rise only about 85% to 90%.

Fauci takes pride in having made sure the research money landed at his institute. If two other contenders—the Department of Homeland Security, formed in 2002, and the Pentagon—had gotten their hands on the money, it would have been directed toward more concrete countermeasures, such as vaccines, drugs, and diagnostics, he says—giving the research community much more to grumble about.

In a vigorous defense of the program during an interview last week, Fauci said he was able to strike a "deal" with the Administration that allows NIAID to spend about one-third of the money on basic research and so-called emerging infectious diseases. That includes components such as a genomics initiative and an $85 million, 5-year program on innate immunity that "is totally non–organism specific," Fauci says.

CREDITS (TOP TO BOTTOM): KENNETH LAMBERT/AP; SOURCE: RICHARD EBRIGHT

Microbiologist on a Mission

The scientist who persuaded hundreds of his colleagues to sign a letter criticizing U.S. spending on biodefense research is not only worried about its impact on basic microbiology (see main text). Richard H. Ebright is also passionately opposed to the proposed expansion of biodefense labs. It might seem like a pacifist's argument, but far from it; as one former labmate puts it, Ebright is "complicated."

Ebright, 45, spent 6 years as an undergraduate and graduate student in the laboratory of Harvard geneticist Jon Beckwith, a left-leaning social activist on everything from the Vietnam War to genetic discrimination. As an outspoken conservative, Ebright "was unusual in my lab," says Beckwith; "we would get into lots of debates." Ebright held his own and also excelled academically, publishing his first paper in the *Proceedings of the National Academy of Sciences* while still in college. He is now a Howard Hughes Medical Institute investigator at Rutgers University in Piscataway, New Jersey, where he studies the initiation of DNA transcription.

Since 9/11 and the anthrax letters, Ebright, like his former adviser, has taken on a cause. When the National Institutes of Health proposed a massive new biodefense program, Ebright began to worry that vastly increasing the number of labs and people working on bioterror agents would only raise the risks that a pathogen would accidentally escape or be deliberately released by a "disturbed, disgruntled, or adversarial" scientist, he says. As he argued in a letter to *Nature* he co-authored in January 2002, a better strategy would be to expand research on related, less pathogenic agents, while limiting work on bioterrorism agents to a few strictly controlled labs. It's a view shared by "most policy experts on bioweapons outside the government," he contends. It also makes for some strange bedfellows: Ebright, still a registered Republican, shares information with Edward Hammond, a liberal Democrat and U.S. leader of the Sunshine Project, a weapons watchdog that is tracking the biodefense buildup (*Science*, 6 August 2004, p. 768). Hammond, who praises Ebright as "brave" for expressing what many scientists believe but don't say, calls it a "tactical alliance."

Speaking conservatively. Richard Ebright thinks the biodefense boom is making the country less safe.

Ebright's views have often made him a lone voice amid the many researchers who are benefiting from the biodefense boom. Some of these scientists have now added their signatures to the open letter, which the media-savvy Ebright sent to reporters at major newpapers and journals. The signers share a concern about preserving basic microbial science, even though they "have different views on other aspects of biodefense," Ebright says. **–J.K.**

A large chunk of the money has gone to building 14 new biosafety level 3 and BSL-4 labs that can handle the most dangerous pathogens—a source of much debate in local communities. Fauci points out that these labs can also be used to study emerging diseases such as avian flu or severe acute respiratory syndrome. Broader than the Category A, B, and C list of biodefense pathogens of the Centers for Disease Control and Prevention, the NIH list includes agents such as dengue, influenza, West Nile virus, and drug-resistant tuberculosis.

Besides, Fauci contends, even work on a potential bioterrorism agent can have broad applications—for instance, in the February issue of the *Journal of Clinical Investigation*, researchers report that mice can be partially protected from a poxvirus infection by a drug that targets a cell-signaling pathway needed by the virus, findings that could yield a new approach for antiviral drugs.

Dueling data

The current brouhaha hinges on two different analyses: one, by the letter writers, that suggests a steady erosion in funding for microbiology, and one from NIAID that purports to show that such support hasn't changed.

Ebright and his colleagues have several gripes. One is that many of the biodefense grants were initially awarded through special competitions with pots of money set aside specifically for a handful of high-priority Category A or B agents. Unlike investigator-initiated grants, which are assigned to NIH-wide review panels by topic and receive funding only if they meet a certain quality level, the "requests for applications" are reviewed by panels created just for that competition, and proposals that fall below the usual quality standard may still receive funding. So, like other targeted research, these grants can be easier to get.

The letter asserts that this funding strategy resulted in a steep decline in awards funded by the two main NIH study sections evaluating nonbiodefense, basic microbiology grants: Microbial Physiology and Genetics, and Bacteriology and Mycology. These two sections constitute the bulk of funding for basic microbiology, says Ebright, and are supported mostly by NIAID and the National Institute of General Medical Sciences (NIGMS). Ebright and his colleagues contend that in these two sections, the number of awards has fallen from 1117 between 1996 and 2000 to 746 since then, a drop of 33%. (The numbers come from CRISP, NIH's grants database.) In the same period, the number of grants for six bacterial diseases that are on the priority bioweapons list but are extremely rare in humans—tularemia, anthrax, plague, glanders, melioidosis, and brucellosis—shot up from 33 to 497. (The letter does not address viruses, but the developments in virology are similar, says Ebright.)

Enough for everyone. NIAID's Anthony Fauci, whose budget rose by 47% after 9/11, says biodefense hasn't come at the expense of other fields.

Data on success rates (the fraction of applications funded) provided by NIAID support the critics' contention that it has been harder to get grants for nonbiodefense work than for biodefense work (see table on p. 1396), although projections for 2006 suggest that the difference will disappear as biodefense funds get shunted from new grants into paying for existing grants and contracts.

Not only is less money going to research on bacteria that cause thousands of infections each

CREDITS (TOP TO BOTTOM): JENNIFER S. ALTMAN; GERALD HERBERT/AP

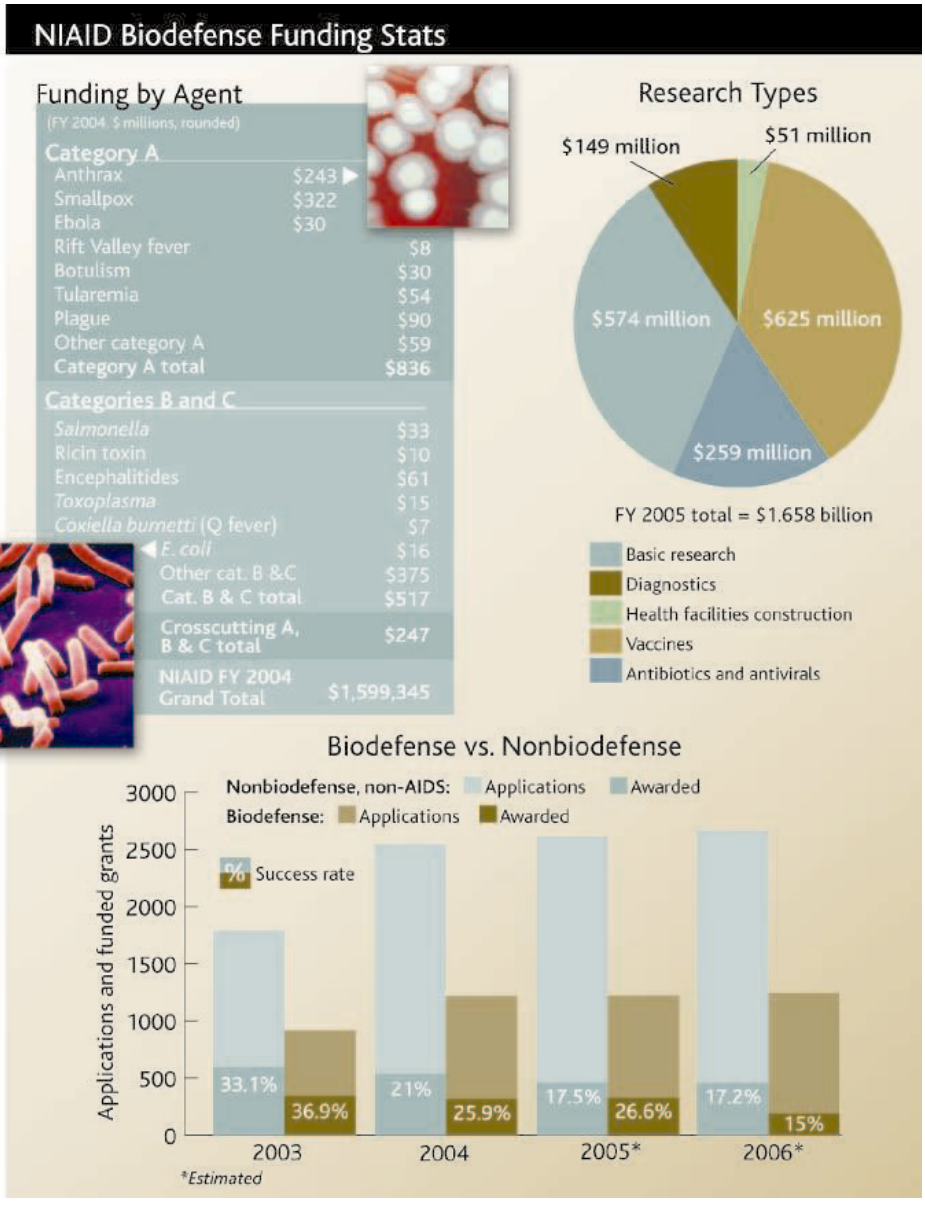

year, the protesters say, but fundamental research on model agents such as *E. coli*, *Bacillus subtilis*, and *Salmonella* is also in decline. Such basic work has led to vast advances in knowledge, paving the way for new antibiotics, says Stanley Falkow of Stanford University in California, who also signed the letter. "It will be very difficult to make the same basic discoveries working on the biothreat agents," he says—not just because researchers barely know them, but also because studying them is restricted to high-containment labs subject to strict and cumbersome security measures.

But Fauci counters with a different set of numbers. NIAID's analysis of nonbiodefense bacterial physiology grants since 2000—defined more broadly, not limited to two study sections—finds that the number of awards has been stable, hovering between about 120 and 150 per year since 2000. It's possible that the number of grants has fallen at NIGMS, Fauci says, but that could reflect tighter budgets at that institute: "If there wasn't biodefense money, they [investigators] would be suffering anyway." NIGMS program director James Anderson says the institute has not done an analysis of trends in microbiology funding, which are also affected by reviewers' own preferences; lately, they have preferred mechanistic studies, for example. But if the numbers of applications and awards have dropped, "NIGMS is interested in the reasons."

The letter urges NIH to add basic microbial research to its biodefense program and to assess proposals for biodefense side by side with basic microbial research, which would give nonbiodefense researchers a better chance at competing.

An exaggerated risk?

The nitty-gritty of grant numbers aside, the letter does raise a broader issue: Does biodefense deserve all this money? Apart from the five anthrax deaths in 2001, there have been no known bioterrorism deaths in the United States. Natural deaths from many other biodefense agents—such as smallpox, tularemia, and plague—are also low if not zero. Is it worth spending billions of dollars on these agents, when flu alone causes more than 30,000 deaths a year in the United States and food poisoning some 5000?

Countries other than the United States don't seem to think so. Although many European nations have taken some basic precautions, for instance, such as stocking up on smallpox vaccine, there isn't anywhere near the funding avalanche—nor the meetings, journals, and businesses—that have sprung up in the United States.

But Fauci says he's seen intelligence that convinces him that the threat is all too real. Some researchers are worried too, even if they're not privy to secret information. "I'm personally very concerned," says virologist Peter Palese of Mount Sinai School of Medicine in New York City, who considers the threat "underestimated." If anything, he adds, more money should be going to biodefense.

But Milton Leitenberg, an arms-control expert at the University of Maryland, College Park, couldn't disagree more. No evidence suggests that any terrorist organization is able to produce an effective bioweapon, he says, and some of the grim scenarios outlining a bioterror attack appear primarily designed to scare people. As an example, he cites Atlantic Storm, a recent exercise in which politicians simulated an international smallpox attack that takes thousands of lives (*Science*, 28 January, p. 513) Many of its premises—for instance, that an Al Qaeda splinter group could produce a smallpox powder in a "small brewery in Klagenfurt, Austria"—are wrong, Leitenberg says.

Abigail Salyers of the University of Illinois, Urbana-Champaign, who presided over ASM when the anthrax attacks occurred in 2001, also believes that much of the fear—and much of the research—is unnecessary. Public health officials know how to respond to crises, she says; even in 1947, when a smallpox case surfaced in New York City, millions were vaccinated against the disease almost without a wrinkle. The lesson: Dealing with a bioterror attack isn't rocket science, she says, and a powerful public health system and an effective communication strategy are the best preparation.

Mark Wheelis, a biological arms-control specialist at the University of California, Davis, says he's delighted to see the discussions unfurl. A few people have been critical of the biodefense boom, he notes, but by and large, the three-and-a-half years since 9/11 have passed without an informed debate about exactly what's threatening the U.S. population and how much should be invested to avert those dangers. "This letter finally opens the debate," he says. "We should welcome it."

–MARTIN ENSERINK AND JOCELYN KAISER

CREDITS (TOP TO BOTTOM): CDC/COURTESY OF LARRY STAUFFER MANFRED KAGE/PETER ARNOLD, INC.; SOURCE: NIAID

What's in a Species' Name? More Than $450,000

The German group BIOPAT has successfully raised funds for taxonomy and conservation science by selling the rights to name species

Everyone in Stan Vlasimsky's family has an alter ego in the animal kingdom. A dainty Bolivian orchid, *Epidendrum lezlieae*, is named for his wife Lezlie. For daughter Claudia and son Liam, there are frogs in Panama and Madagascar, respectively. Daughter Magdeline has a Filipino butterfly carrying her name. And for the newest addition, toddler Caiden, there is a Peruvian lizard, *Euspondylus caidenii*.

Vlasimsky is not a rugged biologist trudging through remote forests or swamps and naming newly discovered species. The business consultant was on a flight 5 years ago when he read about BIOPAT (Patrons for Biodiversity), a German nonprofit group offering naming rights to new species in exchange for donations to conservation science (*Science*, 21 January 2000, p. 421). "What a novel idea," says Vlasimsky, whose namesake, *Eupholus vlasimskyi*, is a belligerent-looking black beetle. "It was a great way to support not just the scientist's research but also the species. And at the end of the day, it was a lasting gift."

BIOPAT isn't the only game in town. This week the New York City–based Wildlife Conservation Society (WCS) held an online auction for the right to name a new species of titi monkey—a rare find from the jungles of Bolivia's Madidi National Park. "Bolivia is one of the poorest countries in South America, and it's hard to raise money to protect these places," says WCS primatologist Robert Wallace, the monkey's co-discoverer.

The WCS auction was, in part, inspired by BIOPAT's success. Born to some controversy in December 1999—critics called for the group to abandon its plan—BIOPAT has so far facilitated more than 100 species sponsorships and raised more than $450,000 for research and conservation. The cost of naming a species ranges from $3500 for various insects to $13,000 for a hummingbird; the more attractive or rare the species, the higher the price. The proceeds are split between the institution of the species' discoverer and field research projects in the country of the species' origin. BIOPAT-raised money, for instance, has funded surveys of bat populations in Sri Lanka, taxonomic training programs for locals in Myanmar, and an inventory of Bolivian orchids in the Tariquia conservation area.

Potential BIOPAT customers surf an online catalog of plants and creatures. About 40 species of slugs, bugs, flowers, frogs, and others are currently available. Customers can even request a species with specific traits—a yellow orchid with violet stripes, for example—and a call goes out to Germany's museums and institutions that are members of BIOPAT. The customer also works with scientists to craft an appropriate species name and publish its description, which brings official recognition.

"We can arrange virtually any sponsorship," says Claus Bätke, BIOPAT's president and an agrobiologist with German development agency Deutsche Gesellschaft für Technische Zusammenarbeit. Most large museums have drawers that have been stuffed for decades with species waiting for a taxonomist to describe, classify, and name them, Bätke explains. "We have several hundred unnamed insects here," adds Gerhard Haszprunar, a professor of systematic zoology at the University of Munich and director of the State Zoological Collection in Munich, who first came up with the naming idea. "We are always happy to give BIOPAT new species."

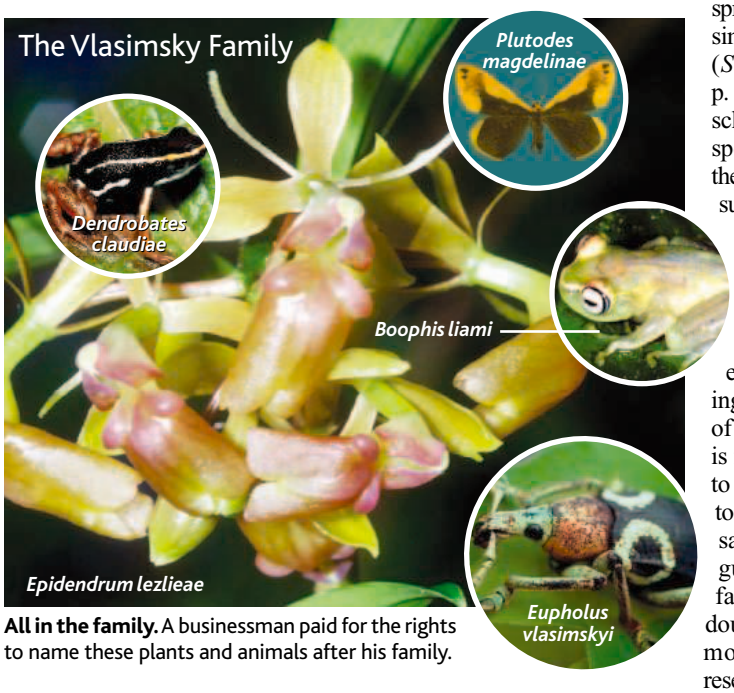

All in the family. A businessman paid for the rights to name these plants and animals after his family.

CREDIT: COURTESY OF BIOPAT

Most donors choose charismatic species—orchids and frogs account for about 50% of sponsorships. For example, BIOPAT enabled a friend of Mikhail Gorbachev to sponsor *Maxillaria gorbatchowii*, a Bolivian orchid. Insects and other arthropods seem to spark little interest. An "ugly" spider from China has remained unnamed for 2 years, says Bätke.

Corporations have gotten into the act. The German food company Vitaquell named a Columbian hummingbird *Thalurania vitaquelli* and plans to use it in ads for low-fat margarine. BIOPAT will veto requests that it deems inappropriate. One potential customer tried to name a particularly unattractive insect after his mother-in-law, and another wanted to memorialize Nazi propaganda filmmaker Leni Riefenstahl with an orchid.

Not every group selling species' names is as successful as BIOPAT. The Immortals Program of the Australian Museum in Sydney, which funds biodiversity research, has attracted only eight donors since its launch in the late 1990s, raising approximately $31,000.

BIOPAT itself got off to a rocky start, drawing fire from the U.K.'s International Commission on Zoological Nomenclature (ICZN), which suggested that "name selling would spread to those whose intention is simply their own financial gain" (*Science*, 18 February 2000, p. 1203). ICZN added that such a scheme could lead to fraudulent species descriptions and muddy the scientific naming system. No such abuses have arisen, however.

Still, Neal Evenhuis, the new president of ICZN, continues to share the concerns that his predecessors expressed. But he acknowledges that selling and auctioning species names is a symptom of how bad government funding is for taxonomy. "It's not as sexy to find a species anymore as it is to sequence its DNA," Evenhuis says. "BIOPAT are not the bad guys. Raising $450,000 in this fashion in 4 years is a tremendous result in their effort to promote and further taxonomic research and conservation."

For Vlasimsky, the eponymous flowers, frogs, lizards, and bugs instill in his family a value for research and biodiversity. "My kids know they each have an animal and that this is important. They talk about this with their friends," he says. Conservation scientists also hope that such personal links will spur donors to make sure their namesakes survive.

–Bijal P. Trivedi

Bijal P. Trivedi is a freelance writer in Washington, D.C.

Shift in Icebreaking Fleet Could Crunch NSF Budget

Plowing a path to polar research stations is no longer a core mission of the U.S. Coast Guard. But can the National Science Foundation afford to do the job?

Half a century after agreeing to help the National Science Foundation (NSF) serve up a banquet of polar research, the U.S. Coast Guard is getting up and walking away from the table. And NSF doesn't know if it can pay the bill.

NSF is responsible for U.S. science at the poles, which includes three stations in Antarctica and a growing presence in the Arctic. But it can't do its job without the Coast Guard's help in clearing the sea ice. That's a perennial need at McMurdo Station, the logistical hub for U.S. activities on the Antarctic continent. Although NSF pays for the fleet's deployment—some $12 million last year—the Coast Guard has shouldered the much greater cost of building and maintaining two aging heavy-duty icebreakers that focus on McMurdo and a newer, less powerful research icebreaker that spends most of its time in the Arctic.

But that relationship seems headed for the deep freeze. Last month the Bush Administration told Congress in its proposed 2006 budget submission that NSF would henceforth be responsible for the ships, two of which are desperately in need of major repairs or replacement after 30 years of ice-crunching. Officials at both the Coast Guard and NSF say the policy shift was presented as a fait accompli last fall during budget negotiations.

The White House has tried to sweeten the deal with a one-time transfer of $48 million to NSF from the Coast Guard. But that's less than two-thirds of the $75 million the Coast Guard estimates it will cost to maintain the ships this year. And it's little more than a down payment on a possible $600 million tab to retrofit the 30-year-old *Polar Sea* and *Polar Star*—and even more to replace them. (The *Sea* is now undergoing an extensive inspection to determine what repairs are needed, and the *Star* is slated for the same major overhaul after next winter.) Not surprisingly, NSF officials fear that the agency's new duties could eventually wreak havoc with its overall budget, which shrank by 3.2% this year and has little chance of growing significantly next year. Three panels have been convened to study the issue from all angles.

"We need to look at the whole system, both short-term and long-term, and figure out what makes the most sense," says Karl Erb, head of polar programs at NSF. But some things—none of them good—are already clear to Sridhar Anandakrishnan, a glaciologist at Pennsylvania State University, University Park, and past chair of NSF's polar science advisory committee. "It's a huge crisis," he says. "And I don't know how we can solve it without additional funding from Congress."

Cold welcome. *The Polar Sea* and *Polar Star* help an oil tanker reach McMurdo Station in Antarctica.

CREDIT: PETER WEST/NATIONAL SCIENCE FOUNDATION

The Administration says NSF should foot the bill because the icebreaking fleet mainly serves the academic scientific community. What's more, enabling science is a lower priority for the Coast Guard, now part of the Department of Homeland Security, than activities such as law enforcement, search and rescue, and fostering economic development. Accordingly, this year's 2006 budget request concludes that "it is unlikely that the Coast Guard could provide funding in future years for refurbishment or replacement of the icebreakers. That, in turn, threatens the research programs that depend on their services."

Indeed, funding lies at the heart of the problem. "We think that polar icebreaking is important," says Cmdr. Thomas Wojahn, ice operations program manager for the Coast Guard. "And we think we should continue to operate the ships. But icebreaking needs to be properly funded." Wojahn notes that soaring fuel bills, bigger repair bills, and recent extreme ice conditions in the Antarctic have boosted the cost of doing business without a commensurate rise in funding.

The new arrangement gives NSF a chance to break that vicious cycle, the White House says. Once the Coast Guard transfers responsibility for icebreaking, according to budget documents, "NSF will have flexibility to pursue alternatives to current operations." Those alternatives could include renting commercial or foreign icebreakers, as NSF did this winter to replace the *Polar Sea* (*Science*, 21 January, p. 338). A more radical approach would be to offload fuel, supplies, and other materials at a spot that remains ice-free throughout the year and then haul the material over land. But the savings in annual icebreaking might be swamped by the cost of building a new station and extending NSF's supply lines.

Anandakrishnan agrees that it makes sense for NSF to ensure access to its research assets. But he says nobody anticipated the "perfect storm" that has built up in the past few years. "We've known for a long time that it would eventually come to the point where the Coast Guard would say, 'You want us to do this? Then find the money!' But NSF is also in a bad way, financially."

Although Congress could reverse the policy and block the transfer of funds, both the Coast Guard and NSF are proceeding on the assumption that it will take effect next year. A joint working group is drawing up a new agreement on how the three ships will be operated and maintained over the next few years, says Erb. At the same time, the National Academies' National Research Council is beginning a study of how the country's polar icebreaking fleet should be deployed, "including scenarios for continuing those operations and alternative approaches." Although the $600,000 study will run until the end of 2006, Congress has asked for an interim report by September. Finally, Erb is assembling an NSF task force to weigh the agency's long-term prospects for operating in the polar regions. He hopes the panel will "at least start to narrow down the options" in time for NSF's 2007 budget submission to the White House in September.

—JEFFREY MERVIS

What in the Name of Euclid Is Going On Here?

Computer assistants may help mathematicians dot the i's and cross the t's of proofs so complex that they defy human comprehension

In 1998, a young University of Michigan mathematician named Thomas Hales solved a nearly 4-century-old problem called the Kepler conjecture. The task was to prove that the standard grocery-store arrangement of oranges is, in fact, the densest way to pack spheres together. The editor of *Annals of Mathematics*, one of the most prestigious journals in mathematics, invited him to submit his proof to *Annals*. Neither of them was prepared for what happened next.

Over a period of 4 years, a team of 12 referees wrestled with the lengthy paper and eventually raised a white flag. They informed the editor that they were only "99 percent" certain that it was correct. In particular, they could not vouch for the validity of the lengthy computer calculations that were essential to Hales's proof. The editor took the unprecedented step of publishing the article with a disclaimer that it could not be absolutely verified (*Science*, 7 March 2003, p. 1513).

It is a scenario that has repeated itself, with variations, several times in recent years: A high-profile problem is solved with an extraordinarily long and difficult megaproof, sometimes relying heavily on computer calculation and often leaving a miasma of doubt behind it. In 1976, the Four Color Theorem started the trend, with a proof based on computer calculations so lengthy that no human could hope to follow them. The classification of finite simple groups, a 10,000-page multiauthor project, was completed (sort of) in 1980 but had to be recompleted last year. "We've arrived at a strange place in mathematics," says David Goldschmidt of the Institute for Defense Analyses in Alexandria, Virginia, one of the collaborators on the finite simple group proof. "When is a proof really a proof? There's no absolute standard." Goldschmidt thinks the traditional criterion—review by a referee (or team of them)—breaks down when a paper reaches hundreds or thousands of pages.

The computer—which at first sight seems to be part of the problem—may also be the solution. In the past few months, software packages called "proof assistants," which go through every step of a carefully written argument and check that it follows from the axioms of mathematics, have served notice that they are no longer toys. Last fall, Jeremy Avigad, a professor of philosophy at Carnegie Mellon University, used a computer assistant called Isabelle to verify the Prime Number Theorem, which (roughly speaking) describes the probability that a randomly chosen number in any interval is prime. And in December, Georges Gonthier, a computer scientist at Microsoft Research Cambridge, announced a successful verification of the proof of the Four Color Theorem, using a proof assistant called Coq. "It's finally getting to the stage where you can do serious things with these programs," says Avigad.

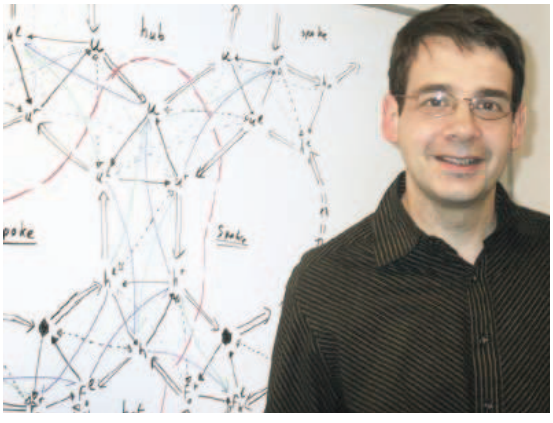

Mapping the way. Georges Gonthier's computer verified billions of calculations on "hypermaps" like the one shown.

Even Hales is getting into the action. Over the past 2 years, he has taught himself to use an assistant called HOL Light. In January, he became the first person to complete a computer verification of the Jordan Curve Theorem, first published in 1905, which says that any closed curve drawn in the plane without crossing itself separates the plane into two pieces.

For Hales, the motivation is obvious: He hopes, eventually, to vindicate his proof of the Kepler conjecture. In fact, three graduate students in Europe (not Hales's own) are already at work on separate parts of this project, two using Isabelle and one using Coq. Hales expects them to finish in about 7 years.

But Hales thinks that computer verifiers have implications far beyond the Kepler conjecture. "Suppose you could check a page a day," he says. "At that point it would make sense to devote the resources to put 100,000 pages of mathematics into one of these systems. Then the mathematical landscape is entirely changed." At present, computer assistants still take a lot of time to puzzle through some facts that even an advanced undergraduate would know or be able to figure out. With a large enough knowledge base, that particular time sink could be eliminated, and the programs might enable mathematicians to work more efficiently. "My own experience is that you spend a long time going over and going over a proof, making sure you haven't missed anything," says Carlos Simpson, an algebraic geometer and computer scientist at the University of Nice in France. "With the computer, once it's proved, it's proved. You only have to do it once, and the computer makes sure you get all the details."

In fact, computer proof assistants could change the whole concept of proof. Ever since Euclid, mathematical proofs have served a dual purpose: certifying *that* a statement is true, and explaining *why* it is

Have a Coq and a Smile

Why would hundreds of computer scientists devote more than 30 years to developing mathematical proof assistants that most mathematicians don't even want? The answer is that they are chasing an even more elusive grail: self-checking computer code.

In a sense, the statement "this program (or chip, or operating system) performs task *x* correctly" is a mathematical theorem, and programmers would love to have that kind of certainty. "Currently, people who have experience with programming 'know' that serious programs without bugs are impossible," Freek Wiedijk and Henk Barendregt, computer scientists at the University of Nijmegen in the Netherlands, wrote in 2003. "However, we think that eventually the technology of computer mathematics ... will change this perception."

Already, leading chip manufacturers use computer proof assistants to make sure their circuit designs are correct. Advanced Micro Devices uses a proof checker called ACL2, and Intel uses HOL Light. "When the division algorithm turned out to be wrong on the Pentium chip, that was a real wake-up call to Intel," says John Harrison, who designed HOL Light and was subsequently hired as a senior software engineer by Intel. **–D.M.**

CREDIT: COURTESY OF GEORGES GONTHIER

true. Now those two epistemological functions may be divorced. In the future, the computer assistant may take care of the certification and leave the mathematician to look for an explanation that humans can understand. "Just because a proof is explanatory doesn't mean it's certain," says Harvey Friedman, a logician at Ohio State University in Columbus. "Just because it is certain doesn't mean it's explanatory. They are two separate dimensions."

So far, Hales, Simpson, and Friedman are part of an extremely small minority: mathematicians who have taken the trouble to learn about proof assistants. "Mathematicians don't know about [computer proof verification], they're not interested in it, and they don't believe it," says Freek Wiedijk, a computer scientist at the University of Nijmegen in the Netherlands who specializes in proof verification. Simpson says much of the mistrust may stem from a misimpression that computerized proof checkers are trying to automate mathematical creativity.

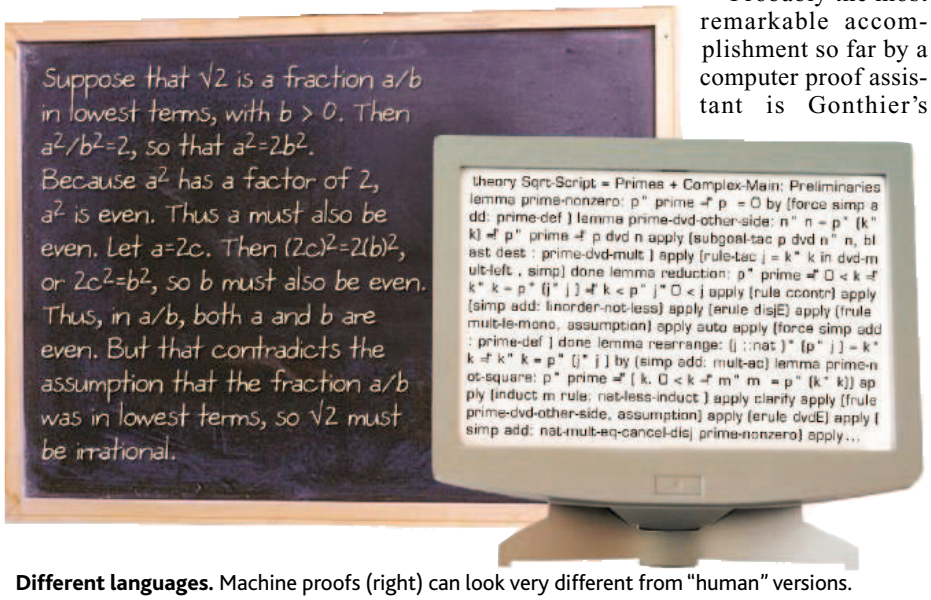

Different languages. Machine proofs (right) can look very different from "human" versions.

In fact, an assistant can no more prove the Four Color Theorem than an online thesaurus can write *Hamlet*. In a typical session with a proof verifier such as Isabelle or Coq, the mathematician enters the hypotheses at the top of the computer screen and the "proof obligation"—the conclusion—at the bottom. She decides on a "tactic" to simplify the proof obligation—for example, subdividing it into simpler cases, performing a calculation, or applying a previously known theorem. Each time the user enters a tactic, the computer program executes it and updates the proof obligation. When there are no more obligations left, the proof is verified.

One stumbling block is that published proofs never specify every step. Every math student is familiar with the dreaded words, "it is obvious that …" To the computer, *nothing* is obvious. It is up to the user to break the "obvious" step down into subtasks that the computer can check. Diagrams are particularly troublesome; the user must somehow parse the pictorial information into allowable tactics.

All in all, people who have used proof verifiers say they can formalize about a page of textbook mathematics in a week. Avigad says he reached a top speed of a page a day while working on the Prime Number Theorem—close to the break-even point at which it will be worth mathematicians' time. "When it becomes not too much harder to formally verify a proof than to write it up carefully, it starts looking like a win," he says.

Probably the most remarkable accomplishment so far by a computer proof assistant is Gonthier's recently completed verification of the Four Color Theorem. This theorem began as a conjecture in 1852, when a graduate student at University College London named Francis Guthrie asked his professor Augustus DeMorgan if he could prove that any map can be colored with four colors in such a way that no two adjacent countries have the same color. After more than a century of unsuccessful attempts, some by eminent mathematicians, two computer scientists, Kenneth Appel and Wolfgang Haken, finally proved it in 1976. Their computation-intensive argument raised an immediate furor. "Mathematicians over 40 years old couldn't be convinced that a proof by computer was correct, and those under 40 couldn't be convinced that a proof with 700 pages of hand calculations was correct," jokes Robin Wilson, a graph theorist at the Open University in Milton Keynes, U.K. Enough questions remained about its validity that another team of graph theorists, led by Paul Seymour of Princeton University and Neil Robertson of Ohio State University, published a revised proof in 1995. Even this streamlined proof relies on a case-by-case analysis of more than a billion different maps, far more work than a human mathematician could do in a lifetime. The computer did it in 3 hours.

Crunching through special cases also played a large role in checking the proof, Gonthier says. "From the point of view of someone using a formal computation system, those are really the easy parts. The hard part, in this case, was finding formal definitions that captured correctly the intuitions behind graph theory." Gonthier had to revamp Seymour and Robertson's approach considerably, so that the proof assistant would understand what elementary ideas such as "the next edge on the left" meant. In his final proof script, he estimates that 19,000 lines came directly out of the Robertson and Seymour paper, and 19,000 lines were his own work. (Another 22,000 lines are white space, comments, and "infrastructure.")

Specialists in computer verification give Gonthier's work very high marks. "That guy is amazing," says Wiedijk. "I can't compete with this kind of genius." Hales calls it "a magnificent piece of work. What this means is that the proof is finally self-checking. You don't have to worry about whether the programmers introduced bugs into the computer code." On the other hand, every graph theorist contacted for this article either had not heard of Gonthier's work or remained skeptical about it. "I have no serious doubts that computers have done their part flawlessly," says Bojan Mohar, a graph theorist at the University of Ljubljana, Slovenia. "[But] I cannot confirm that Gonthier has made the correct translation of the [human] proof into computer form." Others doubt the machines themselves. Coq may tell them that Gonthier's code is correct, but why should they trust Coq?

"It's reasonable to say [Coq's code] has been verified experimentally," Gonthier says. Coq is a program that has been developed (at INRIA in Paris) over a period of 20 years, boasts a community of about 100 active users, has source code that is open for inspection, and runs on several different computers and operating systems. Besides, he argues, "even traditional mathematical proofs use physical artifacts. You're relying on the fact that when you flip back to a previous page, the ink doesn't change. Your day-to-day experience is that the ink doesn't change. Similarly, our experience with computers is that once given a consistent set of instructions, they compute consistently. It's just hard to give them a consistent set. Proof-assistant technology makes sure that you do."

–DANA MACKENZIE

Dana Mackenzie is a freelance writer in Santa Cruz, California.

RANDOM SAMPLES

Edited by Constance Holden

Stonehenge for Southern Skies

A full-scale adaptation of Stonehenge is giving Southern Hemisphere stargazers a taste of ancient astronomical know-how.

Stonehenge Aotearoa, New Zealand's answer to the 4000-year-old stone circle on England's Salisbury Plain, is designed to illustrate how ancient cultures followed the movements of celestial bodies through the seasons. The henge, built on farmland on New Zealand's North Island, comprises a 30-meter-diameter stone circle that includes 24 pillars made of concrete and plaster joined by lintels, surrounded by six outer "heel" stones. When viewed from the center of the circle, the stones and arches mark the rising and setting positions of the sun and moon at different times of the year and of prominent stars and constellations. These include the star cluster Matariki (the Maori name for Pleiades), whose rising in June marks the start of the Maori year, and Capella, used for navigation by the Pacific Islanders who first settled New Zealand some 700 years ago.

Getting Buzzed out of Depression

A "pacemaker" for the brain? A Canadian-U.S. team has found that stimulation from electrodes placed deep in the brains of severely depressed patients has alleviated their misery when nothing else could.

Helen Mayberg of Emory University School of Medicine in Atlanta, Georgia, says this is the first depression study of "deep brain stimulation," which has been used with some success in Parkinson's patients.

The researchers targeted an area called the subgenual cingulate, a part of the emotional brain that is hyperactive in depression. The six patients had failed to benefit from any therapy, including shock treatments. But all had prompt reactions to the electrodes, reporting impressions such as "disappearance of the void."

The scientists followed patients for 6 months after implanting low-voltage pulse generators, attached to the electrodes, under their collarbones. In four of them, the depression mostly lifted, the scientists report in the March issue of *Neuron*. One woman started to relapse a couple of weeks after experimenters turned off the stimulator, but she quickly cheered up when the current was turned back on.

Mayberg says the brain area where the electrodes were inserted has "primary connections" with the frontal cortex as well as many areas in the limbic system that have been implicated in depression. Psychiatrist Husseini Manji of the National Institute of Mental Health says the technique "has a lot of potential" both for treating depression and for understanding the brain circuitry involved.

He Thinks He's Human ...

Animals' personalities are so complex that they can be measured along the same dimensions as human ones, says a University of Texas, Austin, researcher. At the AAAS annual meeting last week, psychologist Samuel Gosling reported that animal personality ratings are stable over time and "are as predictive in dogs as in humans."

Psychologists score humans on five major dimensions: conscientiousness, extraversion, neuroticism, openness, and agreeableness. After querying dog owners, Gosling created a four-factor dog inventory based on energy, affiliativeness, emotional reactivity, and competence. His team also created one for hyenas: assertiveness, excitability, human-directed agreeableness, sociability, and curiosity. Gosling, who reviewed the literature on 64 animal species including pigs and octopi, said basic personality traits are universal. For example, "openness" in humans is analogous to "curiosity" in animals. And he found that neuroticism (nervousness and fearfulness), agreeableness, and extroversion cut across all species.

Agreeable hyena?

Primatologist Stephen Suomi of the National Institute of Child Health and Human Development says that Gosling has gone beyond merely typing animals ("shy" or "aggressive") and is "the first to apply principles from personality and social psychology" to individual differences. Such work, Gosling noted, can aid the hunt for biological and evolutionary bases of human personality.

Seeing Stars Underground

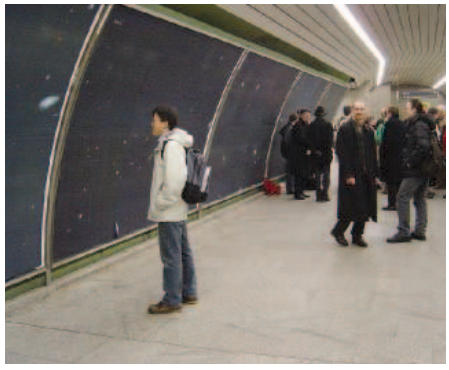

Munich subway riders have a monthlong chance to peer through the cosmos. Scientists from the Max Planck Institute for Astronomy in Heidelberg have put up six giant posters in a Munich subway station that together—at 120 square meters—make up one of the largest astronomical images ever printed. The display is a mosaic of Hubble Space Telescope pictures, taken of an area in the southern sky about the size of the full moon, that covers about 10,000 galaxies as far as 7 billion light-years away, halfway back to the big bang. It wows commuters and astronomers alike, says Jakob Staude of the Heidelberg institute: "It's so much data, on your screen you can never see it all together."

CREDITS (TOP TO BOTTOM): STONEHENGE AOTEAROA ASTRONOMY CENTER; CHRISTINE DREA; STEFANIE MÄRKLIN

PEOPLE

Edited by Yudhijit Bhattacharjee

JOBS

Sandia gold. Physicist Thomas Brennan worked at Sandia National Laboratories in Albuquerque, New Mexico, for 10 years before leaving to become an entrepreneur in 1996. Last month, he returned to help the lab turn more of its technologies into commercial ventures.

As Sandia's first entrepreneur in residence—similar positions exist at other institutions—Brennan hopes to get investors excited about what Sandia scientists are doing. The goal is to boost the local economy and "get some royalties back to the lab," he says.

Brennan, who has helped launch companies that manufacture diode lasers and water-purification systems, says his new job builds on his former life as a Sandia researcher. "I have a lot of respect for the work that scientists are doing at the lab," he says. "I am not just here to harvest their minds."

Changes at LBNL. Lawrence Berkeley National Lab has picked three new leaders to beef up its senior management and strengthen the University of California's (UC's) bid to retain management of the Department of Energy (DOE) facility. Last month, director Steven Chu announced that spectroscopist Graham Fleming (right) would take over as the lab's second in command, replacing Pier Oddone, who left in December to become director of Fermi National Accelerator Laboratory in Illinois (*Science*, 3 December 2004, p. 1679). Nanoscientist Paul Alivisatos will be the new physical sciences director, and David McGraw takes over as head of operations.

Berkeley insiders speculate that no other bids have been submitted to run the lab. (DOE officials are mum on the topic.) If UC is awarded the contract, a decision expected this spring, Fleming says the lab will launch initiatives on using solar power to generate carbon-neutral sources of chemical energy and unraveling the mystery of dark energy, the enigmatic force speeding up the expansion of the universe.

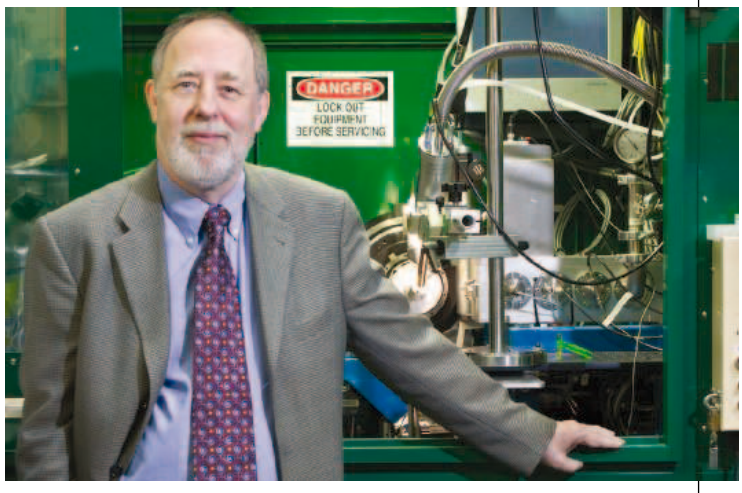

Going local. The new director of an international tropical research consortium headquartered at Duke University in Durham, North Carolina, wants to train more biologists in Latin American countries to boost conservation efforts there.

Forest ecologist Elizabeth Losos, who this week took the helm of the $6 million Organization for Tropical Studies, says expanding the organization's educational initiatives will help "place the fate of tropical forests in the hands of those who live there." Losos, 41, comes to the job after 11 years as head of the Smithsonian Institution's Center for Tropical Forestry Science.

Losos also hopes to bring greater financial stability to the consortium, which in recent years has laid off workers at two of its its three field stations in Costa Rica (*Science*, 17 October 2003, p. 389). But the worst is definitely over, says interim (and former) director Donald Stone of Duke University.

FOLLOW-UP

Look what they found. A German archaeologist who allegedly attempted to sell chimpanzee skulls owned by his institution (*Science*, 27 August 2004, p. 1237) has been found to have falsified scientific data and papers for decades. In January a panel from Goethe University in Frankfurt am Main investigating Reiner Protsch von Zeiten concluded, among other things, that Protsch couldn't operate his own carbon-dating equipment and had committed falsifications and plagiarism throughout his 30-year career. The report, part of which was made public on 17 February, also cited the university's failure to uncover the falsifications. Protsch retired in January, and a disciplinary panel is considering whether his pension should be withheld. He is also likely to face criminal charges for the improper sale of university artifacts.

Got any tips for this page? E-mail people@aaas.org

AWARDS

No longer a secret. In the fall of 1959, electronics engineer James Plummer told his colleagues at Lockheed Aircraft that he would be incommunicado for a while because of his work on a secret nuclear project. The real secret was Plummer's new job: helping the CIA build a spy satellite. Sixteen months later, Plummer and four other engineers had designed the Corona—which peered into Soviet missile sites and nuclear submarines from 130 kilometers above Earth.

Last week, that effort earned Plummer and his Corona colleagues—Minoru S. Araki, Francis J. Madden, Edward A. Miller, and Don H. Schoessler—the $500,000 Charles Stark Draper Prize from the National Academy of Engineering. Chemist Leland Clark Jr. was awarded the biennial $500,000 Fritz J. and Dolores H. Russ Prize for developing self-monitoring diabetes kits and devices that measure dissolved oxygen in industrial and environmental settings. And Purdue University engineers Edward Coyle, Leah Jamieson, and William Oakes shared the $500,000 Bernard M. Gordon Prize for innovation in engineering education.

CREDITS (TOP TO BOTTOM): ROY KALTSCHMIDT/LAWRENCE BERKELEY NATIONAL LABORATORY; SOURCE: TOM BRENNAN; MARCOS GUERRA/SMITHSONIAN TROPICAL RESEARCH INSTITUTE

Letters to the Editor

Letters (~300 words) discuss material published in *Science* in the previous 6 months or issues of general interest. They can be submitted through the Web (www.submit2science.org) or by regular mail (1200 New York Ave., NW, Washington, DC 20005, USA). Letters are not acknowledged upon receipt, nor are authors generally consulted before publication. Whether published in full or in part, letters are subject to editing for clarity and space.

Retraction

WE WISH TO RETRACT OUR RESEARCH ARTICLE "The bacterial condensin MukBEF compacts DNA into a repetitive, stable structure" (*1*). The conclusions of our paper, which used a single-molecule assay with an optical-trap microscope, were based on the interpretation of a flat sawtooth pattern in the force-extension curves as a progressive unraveling of compact MukBEF/DNA filaments. However, subsequent experiments done after the paper appeared suggested that the sawtooth pattern corresponds to the unzipping of the two strands of DNA (*2*). We now believe that nicks that arose indiscriminately along the DNA molecules from normal pipetting allowed interior biotin and Digoxigenin derivitization of the DNA tether. The combination of interior and terminal labels most likely generated a pulling geometry between the beads that led to the denaturation of the DNA. To test these ideas, we have now performed an extensive set of experiments.

First, the double-strand DNA was cross-linked with one psoralen cross-link per 100 base pairs to prevent the opposite strands from separating. The cross-linked DNA alone produced the expected force-extension curves for naked DNA (102 out of 103 cases). When the cross-linked DNA was incubated with purified MukBEF protein under our published conditions, in no case ($n = 180$) did we observe the previously observed sawtooth pattern.

Second, we designed a DNA tether that had both a nick and an adjacent biotin label 2-kb interior from its Digoxigenin-labeled end. The labels and nick were placed so that if the streptavidin bead attaches to both the interior and end-labeled biotin and the anti-Digoxigenin bead attaches to the Digoxigenin labeled DNA end, then pulling the beads apart would unzip the DNA between the interior- and the end-biotin label. With this DNA alone, the flat sawtooth pattern in the force-extension curves was readily observed, displaying little or no hysteresis between the pulling and relaxation paths. When these tethers were incubated with MukBEF protein, hysteresis then appeared between the pulling and relaxing pathways and the pattern was indistinguishable from the published sawtooth pattern.

Thus, we now believe that two DNA attachments were made to one of the beads in our published experiments. MukBEF interacted with the unzipped tether to slow reannealing, giving rise to the observed hysteresis. We deeply regret the misinterpretation and the confusion the original publication has caused.

RYAN B. CASE,[1,2] YUN-PEI CHANG,[3] STEVEN B. SMITH,[2,4] JEFF GORE,[2] NICHOLAS R. COZZARELLI,[1,3] CARLOS BUSTAMANTE[1,2,3,4]

[1]Department of Molecular and Cell Biology, [2]Department of Physics, [3]Biophysics Graduate Group, [4]Howard Hughes Medical Institute, University of California, Berkeley, Berkeley, CA 94720, USA.

References

1. R. B. Case *et al.*, *Science* **305**, 222 (2004).
2. U. Bockelmann, P. Thomen, B. Essevaz-Roulet, V. Viasnoff, F. Heslot, *Biophys. J.* **82**, 1537 (2002).

An Open Letter to Elias Zerhouni

THE NIH PEER-REVIEW PROCESS AND NIH investments in research on microbial physiology, genetics, and pathogenesis have made possible remarkable advances in science and public health and have underpinned the development of recombinant DNA technology and the biotechnology industry.

> "The diversion of research funds from projects of high public-health importance to projects of high biodefense but low public-health importance represents... a crisis for NIH-supported microbiological research."
>
> –*ALTMAN* ET AL.

However, the NIH peer-review process, and the research sector responsible for these achievements, are threatened by unintended consequences of the 2001–02 decision by the NIH National Institute for Allergy and Infectious Diseases (NIAID) to prioritize research of high biodefense, but low public-health significance (see Appendix 1) (*1*).

This prioritization, which was implemented by creation of funding set-asides, special funding review panels, and special funding review procedures, has transformed NIH-supported research in microbial physiology, genetics, and pathogenesis.

The result has been a massive influx of funding, institutions, and investigators into work on prioritized bioweapons agents: i.e., the agents that cause tularemia, anthrax, plague, glanders, melioidosis, and brucellosis. The number of grants awarded by NIAID that reference these agents has increased by 1500% (from 33 in 1996–2000 to 497 in 2001 to January 2005; see Appendix 2) (*1*).

Over the same period, there has been a massive efflux of funding, institutions, and investigators from work on non–biodefense-related microbial physiology, genetics, and pathogenesis. The number of grants awarded to study non–biodefense-related model microorganisms has decreased by 41% (from 490 in 1996–2000 to 289 in 2001 to January 2005; NIH Microbial Physiology and Genetics Initial Review Group; see Appendix 3) (*1*), and the number of grants to study non–biodefense-related pathogenic microorganisms has decreased by 27% (from 627 in 1996–2000 to 457 in 2001 to January 2005; NIH Bacteriology and Mycology Initial Review Group; Appendix 3) (*1*).

The diversion of research funds from projects of high public-health importance to projects of high biodefense but low public-health importance represents a misdirection of NIH priorities and a crisis for NIH-supported microbiological research.

The diversion of research funds comes at a time when research on non–biodefense-related microbial physiology, genetics, and pathogenesis is poised for significant breakthroughs, made possible by the application of genomics, proteomics, and systems-biology methods (see Appendix 4) (*1*). These breakthroughs, and the accompanying dividends for public health and economic development, now either may not occur, or may occur only outside the United States, to the detriment of the U.S. national interest.

As researchers who have served on the NIH Microbial Physiology and Genetics and NIH Bacteriology and Mycology Initial Review Groups, or who have received grants reviewed by those Initial Review Groups, we urge you to take corrective action (see policy recommendations in Appendix 4) (*1*).

SIDNEY ALTMAN, BONNIE L. BASSLER, JON BECKWITH, MARLENE BELFORT, HOWARD C. BERG, BARRY BLOOM, JEAN E. BRENCHLEY, ALLAN CAMPBELL, R. JOHN COLLIER, NANCY CONNELL, NICHOLAS R. COZZARELLI, NANCY L. CRAIG, SETH DARST, RICHARD H. EBRIGHT, STEPHEN J. ELLEDGE, STANLEY FALKOW, JORGE E. GALAN, MAX GOTTESMAN, RICHARD GOURSE, NIGEL D. F. GRINDLEY, CAROL A. GROSS, ALAN GROSSMAN, ANN HOCHSCHILD, MARTHA HOWE, JERARD HURWITZ, RALPH R. ISBERG, SAMUEL KAPLAN, ARTHUR KORNBERG, SYDNEY G. KUSTU, ROBERT C. LANDICK, ARTHUR LANDY, STUART B. LEVY, RICHARD LOSICK, SHARON R. LONG, STANLEY R. MALOY, JOHN J. MEKALANOS, FREDERICK C. NEIDHARDT,

NORMAN R. PACE, MARK PTASHNE, JEFFREY W. ROBERTS, JOHN R. ROTH, LUCIA B. ROTHMAN-DENES, ABIGAIL SALYERS, MOSELIO SCHAECHTER, LUCY SHAPIRO, THOMAS J. SILHAVY, MELVIN I. SIMON, GRAHAM WALKER, CHARLES YANOFSKY, NORTON ZINDER

Affiliations for these signatories and the names and affiliations of over 700 additional signatories are available in the Supporting Online Material (*1*).

Reference

1. Appendices and a complete list of signatories are available in the Supporting Online Material at www.sciencemag.org/cgi/content/full/307/5714/1409c/DC1.

A Small-Scale Foreign Aid Strategy

DONOR NATIONS SEND BILLIONS OF DOLLARS of aid to developing countries with little evidence for lasting positive effects (*1*). It is clear that more effective aid programs must be conceived that will have an enduring impact in spite of the difficult conditions prevailing in recipient nations (*2*, *3*). Small-scale efforts can make contributions to the global aid effort. I wish to share my experiences with one small organization that has achieved remarkable success with limited financial resources and a structure that demands only a modest commitment from the individual participants. "Coopération Genève-Yaoundé" (CGY) is an alliance between the medical faculties of the Universities of Geneva, Switzerland, and Yaoundé, Cameroon, whose primary goal is to improve the training of Cameroonian medical doctors. Two guiding principles of the CGY are that raising the standards of medical practice will have an immediate impact on the health of a population and that aid provided in the form of educational training is relatively immune to misappropriation and corruption.

Volunteers from Swiss medical faculties actively collaborate in the teaching and evaluation of medical students at the University of Yaoundé. Although each Swiss participant devotes only a period of 2 to 3 weeks of teaching per year, the students and local staff members also benefit greatly from the opportunities to interact informally with the foreign medical professionals.

The CGY organizes residency training in Swiss hospitals for young Cameroonian doctors committed to returning into active practice in their native regions. A major challenge facing programs that train healthcare workers in developing countries is the drain of graduates to countries offering higher salaries and a vastly superior work environment (*4*). The CGY has been fortunate in that all but one of the over 60 Cameroonian doctors selected for residency training in Geneva subsequently returned to work in their native country. This success rate reflects the requirement that candidates must have already completed an internship in Cameroon, as doctors trained entirely in our medical system will find it extremely difficult to adapt to working in African hospitals.

The medical faculty in Cameroon hosts 10 medical students from Geneva every year for a 2-month rotation in tropical medicine and community health. Apart from providing a unique opportunity to experience a different culture and its distinctive attitudes to health and disease, firsthand exposure to the daily frustrations encountered in African hospitals sensitizes these future Western doctors to our humanitarian obligations in the developing world.

I believe that this conceptually straightforward program can serve as a useful model for universities with an interest in contributing to education in poorer nations.

URS GERBER

Brain Research Institute, University of Zurich, Winterthurerstrasse 190, Zurich CH-8057, Switzerland.

References

1. "How to make Africa smile. A survey of sub-Saharan Africa," *Economist,* 17 Jan. 2004, pp. 1–16.
2. E. M. Einterz, *Lancet* **357**, 1524 (2001).
3. R. Klitgaard, *Tropical Gangsters* (Basic Books, New York, 1990).
4. C. Schubert, *Nature Med.* **9**, 979 (2003).

What Kind of Farming Works Best?

IN HIS REVIEW OF *MENDEL IN THE KITCHEN: A Scientist's View of Genetically Modified Foods* by N. Fedoroff and N. M. Brown ("Changing genes to feed the world," Books *et al.*, 29 Oct. 2004, p. 815), D. Pimentel misrepresents the impacts of genetically modified herbicide-tolerant (HT) crops and the consequences of organic farming, which he offers as a more sustainable way to meet the food challenges of the 21st century.

Pimentel derides HT crops because they result in increased herbicide use and potential pollution, yet are not significantly more effective against weeds than herbicides and tillage combined. This completely overlooks the drastically reduced soil erosion, increased soil organic matter, and reduced fossil fuel consumption made possible by herbicides and HT biotech crops. The Soil and Water Conservation Society says that herbicide-based, low- and no-tillage cropping systems are the most sustainable ever (*1*), points made in the book.

Pimentel further denies the benefits of HT crops when he claims that "the soil has to be tilled" with current annual grain crops, causing "serious soil erosion." Perversely, Pimentel uses this misrepresentation to promote organic farming, which relies heavily on erosion-causing tillage for its weed control.

Pimentel selectively cites Rodale Institute research to claim that organic crop yields are equivalent to nonorganic. Yet, many long-term studies have shown a 10 to 40% organic yield deficit (*2*–*4*).

Pimentel may be correct in claiming "organic approaches would reduce the use of fossil energy in corn production by about 30 percent" due to not using synthetic fertilizer, but as Fedoroff and Brown note, only by using far more land per ton of food produced. Replacing synthetic nitrogen fertilizer would require at least a fourfold increase in manure applications or equivalent green manure crops (*5*).

Humanity already farms more than one-third of Earth's total land area, and additional land cleared for organic fertility and yield deficits would be of lower productivity, greater erosion potential, and higher ecological sensitivity. As Fedoroff and Brown make clear, genetic engineering offers us powerful and important tools to sustainably feed the larger and more affluent global population without using more land and wasting resources.

ALEX A. AVERY,[1]* C. S. PRAKASH,[2] ALAN MCHUGHEN,[3] ANTHONY R. TREWAVAS,[4] THOMAS R. DEGREGORI[5]

[1]Hudson Institute, Center for Global Food Issues, Post Office Box 202, Churchville, VA 24421, USA. [2]Center for Plant Biotechnology Research, Tuskegee University, Tuskegee, AL 36088, USA. [3]Botany and Plant Sciences, University of California, Riverside, Riverside, CA 92521, USA. [4]Institute of Cell and Molecular Biology, University of Edinburgh, Darwin Building, Edinburgh EH9 3JR, Scotland, UK. [5]Department of Economics, University of Houston, Houston, TX 77204–5019, USA.

*To whom correspondence should be addressed. E-mail: aavery@cgfi.org

References

1. Soil and Water Conservation Society, *Farming for a Better Environment* (Soil and Water Conservation Society, Ankeny, IA, 1995).
2. J. Smolik, T. Dobbs, *J. Sust. Agric.* **9**, 63 (1996).
3. M. Shepard *et al.*, *An Assessment of the Environmental Impacts of Organic Farming: A review for Defra-funded Project OF0405* (U.K. Department for Environment, Food, and Rural Affairs, London, UK, 2003) (available at www.defra.gov.uk/science/project_data/DocumentLibrary/OF0405/OF0405_909_TRP.doc)
4. P. Mader *et al.*, *Science* **296**, 1695 (2002).
5. V. Smil, personal communication.

Response

AVERY *ET AL.* INCORRECTLY EQUATE HERBICIDE tolerance (HT) in crops with the no-till cultivation system. No-till may or may not be used with HT. For example, 75% of U.S. soybean plantings include HT, but only 30% of them are planted with no-till (*1*). No-till conserves soil and water resources, but HT itself does not conserve soil or increase soil organic matter. In fact, HT with clean culture (using an herbicide or other treatments to eliminate all weeds and leave only the crop growing cleanly without competition from weeds) significantly increases soil erosion. HT in crops increases the application of herbicides, and herbicides are the most serious pesticide pollutants in streams and groundwater in the United States (*2*). Ninety-five percent of corn production

acreage in Iowa receives herbicides, and 70% of this land is also cultivated for weed control (*3*). Soil erosion is a serious problem in the United States. Agricultural soil is being lost about 10 times faster than soil reformation and sustainability (*4*).

In reviewing the book, I was surprised that Federoff and Brown devoted such a large portion of it to attacking organic agriculture, when organic agriculture has little or nothing to do with plant breeding and genetic engineering. Because of this intense and misleading attack, I felt that I should present the results of the 22-year corn-soybean example of the Rodale Institute in which corn and soybean yields equaled those of conventional corn and soybean production. I agree that not all organic culture of crops produces yields the same as those of conventional crop cultivation (*5*).

Avery *et al.* imply that I reported that all U.S. and world agriculture could be grown organically without commercial nitrogen fertilizer. They are incorrect—I never said this in my review, nor have I ever said this in any of the more than 500 scientific papers that I have published.

Worldwide crops are cultivated on 11% of the world's land area, not 33% as Avery *et al.* report. Yes, the world has a severe food shortage problem; the World Health Organization recently reported that 3.7 billion people are malnourished. This is the largest number of malnourished people in history. Certainly, we need sound genetic engineering, as well as soil and water conservation, to increase the yields of our food crops and make agriculture ecologically and economically sustainable.

DAVID PIMENTEL

College of Agriculture and Life Sciences, Cornell University, Ithaca, NY 14853–0901, USA.

References

1. Economic Research Service, U.S. Department of Agriculture, Agricultural Chemicals and Production Technology: Questions and Answers, available at www.ers.usda.gov/Briefing/AgChemicals/.
2. U.S. Geological Survey, Fact Sheet 181-97, June 1998.
3. "Cultivation: An Effective Weed Management Tool," available at www.extension.iastate.edu/Publications/PM1623.pdf.
4. National Academies of Science, *Frontiers in Agricultural Research: Food, Health, Environment, and Communities* (National Academies Press, Washington, DC, 2003).
5. D. Pimentel, G. Berardi, S. Fast, *J. Agric. Ecosyst. Environ.* **9**, 359 (1983).

An Explanation for the Placebo Effect?

THE ELEGANT COMPUTATIONAL MODEL OF addiction described by A. D. Redish in his Report "Addiction as a computational process gone awry" (10 Dec. 2004, p. 1944) has the potential to provide an explanation for the placebo effect. In the temporal-difference reinforcement learning model (TDRL), actions by an individual are selected to maximize future reward. The greater the difference between expected and experienced rewards, the stronger the learning associating the sequence of states leading up to the reward.

A state in this context might describe the amount of satisfaction (or dissatisfaction) the individual derived from the outcome achieved by the most recent action. Dependencies between the states exist because the most recent action is, in part, shaped by the events of the previous state(s), through constant reevaluation of the initial expectation in each state and subsequent selection of action(s) for the next state. Consequently, by selectively minimizing the number of dissatisfying states in the association, an individual learns a specific behavioral path toward the reward.

Dopamine neurotransmission is involved in reward-mediated signaling, and dopaminergic neurons firing in response to behaviorally relevant stimuli exhibit a rapid burst of transmitter release (*1*). Because such phasing of dopamine has been hypothesized to signal the magnitude of the dis-

crepancy between expected and observed reward in addiction (*2*), and release of dopamine has been postulated to underlie the response to placebo in Parkinson's disease (*3*), it seems worthwhile to explore the implications of Redish's model on the placebo effect.

The value function at the core of the model provides a measure of expected future reward based upon a specific state and the elapsed time until the reward is obtained, such that the value function discounts rewards that take longer to achieve. Addiction is not the only condition where such a value function applies; the promise of improvement associated with a placebo justifies the use of Redish's model. Therefore, the value function for an individual suffering from an ailment for which a placebo has been given should demonstrate the discounting factor of delayed rewards. That is, the longer the placebo is supposed to take to elicit efficacy, the less likely the individual is to experience the placebo effect. Furthermore, under this model, one might expect that the greater the expectation of efficacy, the greater will be the resulting phasing in endogenous dopamine released in expectation of reward, in a manner similar to the cuing effects in the addiction model. The release of dopamine may well mediate the analgesic effects of some placebos by decreasing activity in pain-sensitive regions, as described by Wager *et al.* (*4*).

The fact that Redish's model can be extended to the placebo effect suggests that the use of computational models may provide a means of integrating and unifying seemingly disparate brain phenomena that may share, at least in part, common underlying biological factors.

KRISTOPHER J. L. IRIZARRY* AND JULIO LICINIO
NPI, University of California, Los Angeles, 695 Charles Young Drive, Los Angeles, CA 90095, USA.
*To whom correspondence should be addressd.
E-mail: kris@informatics.ucla.edu

References
1. R. M. Bilder *et al.*, *Neuropsychopharmacology* **29**, 1943 (2004).
2. W. Schultz, *J. Neurophysiol.* **80**, 1 (1998).
3. R. de la Fuente-Fernández *et al.*, *Science* **293**, 1164 (2001).
4. T. D. Wager *et al.*, *Science* **303**, 1162 (2004).

TECHNICAL COMMENT ABSTRACTS

COMMENT ON "Avian Extinction and Mammalian Introductions on Oceanic Islands"

Raphael K. Didham, Robert M. Ewers, Neil J. Gemmell

Blackburn *et al.* (Reports, 24 Sept. 2004, p. 1955) showed a positive correlation between avian extinctions and numbers of predatory mammal introductions on oceanic islands. We show that habitat conversion rates also correlate with observed extinctions, demonstrating that single-factor approaches cannot address the synergies among multiple agents of extinction.
Full text at www.sciencemag.org/cgi/content/full/307/5714/1412a

RESPONSE TO COMMENT ON "Avian Extinction and Mammalian Introductions on Oceanic Islands"

Tim M. Blackburn, Phillip Cassey, Richard P. Duncan, Karl L. Evans, Kevin J. Gaston

Didham *et al.* argue that the extent of habitat modification is confounded with the numbers of introduced mammal species on islands, such that the observed positive correlation between mammal introductions and avian extinctions may be spurious. We show that their analyses do not support this conclusion.
Full text at www.sciencemag.org/cgi/content/full/307/5714/1412b

HISTORY

A Saga of Wormholes and Anatase

William W. Fitzhugh

Some of the most intractable disputes in anthropology and history arise over the authenticity of unique archaeological artifacts or documents. Objects that have lost their contexts are particularly problematic when they appear without traceable provenance and may be nearly indistinguishable from clever fakes. Such is the case of Yale University's Vínland Map, the detailed forensic analysis of which is the subject of Kirsten Seaver's finely honed detective story, *Maps, Myths, and Men*. Like the Shroud of Turin, the map has inspired controversies that have proven difficult to resolve even with the most sophisticated scientific techniques.

Maps, Myths, and Men
The Story of the Vínland Map
by Kirsten A. Seaver

Stanford University Press, Palo Alto, CA, 2004. 504 pp. $65, £44.50. ISBN 0-8047-4962-0. Paper, $24.95, £17.50. ISBN: 0-8047-4963-9.

The topic of Vikings in North America is no stranger to controversy. Since Scandinavians began immigrating to North America in large numbers (some 200 years ago), a steady stream of claims has been made for Viking origins of the Newport Tower in Rhode Island, the Kensington Rune Stone in Minnesota, the Heavener Stone in Oklahoma, the Beardmore Relics in Ontario, and many other finds in equally improbable locations where Scandinavian descendants settled. All have been debunked, but they continue to enjoy popular support (*1*). The 1961 discovery of a Norse site in Newfoundland (*2*) and the numbers of Norse artifacts found in Native American archaeological sites (*3*, *4*) have helped move the debate from saga reconstructions (*5*) into the arena of science. Increasingly, scientific tools are aiding the evaluation of artifacts, monuments, and historical documents.

One of the most notorious points of contention is the Vínland Map. Drawn on parchment, the map purportedly shows lands described as "*Vinilanda Insula*" and "*Gronelãda*." If authentic, it provides the first cartographic location of Norse discoveries in America, and its caption referring to "companions Bjarni and Leif Eiriksson" confers authenticity to the Vínland sagas. Further, it locates Vínland and Greenland geographically and shows Greenland as an island rather than an arctic peninsula, as medieval cartographers had imagined. Bound together with an authentic 1440s copy of *Hystoria Tartarorum* (the "Tartar Relation"), the Vínland Map was presumed to have a similar date, making it the earliest cartographic representation of parts of North America.

In conjunction with the 1965 announcement of Yale's acquisition of the map, Yale University Press released a lavish, 300-page volume explaining its significance (*6*). Cartographers and historians soon began to question almost every aspect of the map: parchment, ink, watermarks, handwriting, binding, and wormholes. Skepticism was also fueled by Yale's evasiveness over provenance and acquisition history, its failure to engage independent experts, its compromised fiduciary arrangements, and the release of a second edition that did not address issues raised by the first. All in all, the Vínland Map has become one of the most high-profile, problematic, and—many might argue—unnecessary scholarly debates in recent history.

In 438 pages of densely argued and highly annotated text, Seaver effectively dismantles Yale's Vínland Map claim and in the process implicates many of the original proponents in a major scholarly debacle. She begins by summarizing Norse contacts in North America and their settlements in Greenland, which disappeared around 1450. Several chapters then describe how the map was discovered and introduced to Thomas Marston, Yale's rare-manuscript curator, by Laurence Witten, the private dealer in New Haven who had acquired it in 1957 from European sources. Seaver relates the fabulous story of how Witten discovered that the wormholes in the map and its accompanying *Hystoria Tartarorum* matched those in a second manuscript volume, *Speculum Historiale*, that just happened to be in Witten's possession. Not only did this suggest that all three had once been bound together circa 1440, it implied that the map's new cartographic information might have been supplied by Norse refugees from Greenland. To Witten and Marston, the wormholes were all the evidence they needed for "authentication." But to Seaver, missing physical evidence, shoddy scholarship, secret collaboration, and unprecedented promotion by Chester Kerr, then director of Yale University Press—all of which she documents in detail—make this part of the Vínland Map travesty a textbook example of a public relations nightmare.

With similar thoroughness, Seaver follows the events after the press launch, cannily planned for 11 October 1965, the day before Columbus Day. The first open scholarly scrutiny began with a symposium organized by Wilcomb Washburn at the Smithsonian (*7*). Shortly thereafter, Yale agreed to have the map inspected by A. D. Baynes-Cope at the British Museum Research Laboratory. His observations about the faded, two-tone, crumbling ink—which is unlike ink used in the Tartar Relation and *Speculum Historiale* manuscripts or any other medieval documents—reinforced skeptics who had made similar comments about the handwriting, watermarks, and binding.

By agreement with Yale, the British Museum reports were never made public. But they did convince Yale to commission a technical study of the ink by Walter and Lucy McCrone, who in 1974 reported the presence of commercial-grade titanium-based anatase unknown before the 1920s. Subsequently, Thomas Cahill affirmed the aberrant nature of the map ink but pointed out inconsistencies in the McCrone report. In contrast, Jacqueline Olin argued that the composition of the ink was still not defined and that similar forms of anatase might be present in medieval ink. Her view has been rebutted by Kenneth Towe, who has confirmed the McCrones' conclusion that the Vínland Map anatase was not natural but industrial. Each of these reports received coverage in the popular media, but the nature of the debate had become so complicated and technical that the general public and most reporters could no longer follow the argument, only the spin. Although the most definitive study—an accelerator radiocarbon analysis of the map parchment—produced a clean 15th-century date, that finding is beside the point because a modern fabricator would

Vínland Map (detail).

CREDIT: BEINECKE RARE BOOK AND MANUSCRIPT LIBRARY, YALE UNIVERSITY

The reviewer is at Arctic Studies Center, Department of Anthropology, National Museum of Natural History, Smithsonian Institution, Washington, DC 20560–0112, USA. E-mail: fitzhugh.william@nmnh.si.edu

certainly have used medieval-age parchment.

Most of these technical studies conclude that the map is almost certainly a 20th-century hoax. But if so: why? where? when? and by whom? Seaver presents a strong case that answers all these questions: Father Joseph Fischer (1858–1944), a German-Austrian Jesuit priest, had a life-long passion for Norse exploration, medieval manuscripts, and cartography. He knew the academic experts and had access to all of the archives and materials needed to create the Vínland Map. Seaver also identifies a likely motive in Fischer's reaction to the rise of the Nazis and the rampant nationalism of the 1930s. She suggests he created the map to gain favor with the Nazis, who idolized Norse heroics and disputed the authority of the Catholic Church. Her deduction is interesting and augments previous suspicions of Fischer. But like most other chapters of this story, absolute proof is still missing, and other scenarios have been suggested (*8*). Although *Maps, Myths, and Men* will not be the last nail in the coffin of the Vínland Map, it's difficult to imagine a more comprehensive analysis of this piece of parchment. Seaver has created the definitive portolan of the Vínland Map controversy and has shown us a route home.

References and Notes

1. B. Wallace, in *Vikings: The North Atlantic Saga*, W. Fitzhugh, E. Ward, Eds. (Smithsonian Institution Press, Washington, DC, 2000), chap. 29.
2. A. S. Ingstad, *The Discovery of a Norse Settlement in America: Excavations at L'Anse aux Meadows, Newfoundland, 1961–1968* (Norwegian Univ. Press, Oslo, 1977).
3. R. McGhee, *Am. Antiq.* **49**, 4 (1984).
4. See chapters by P. Sutherland and P. Schledermann in *Vikings: The North Atlantic Saga*, W. Fitzhugh, E. Ward, Eds. (Smithsonian Institution Press, Washington, DC, 2000).
5. For a contemporary version, see G. Sigurdsson, *The Medieval Icelandic Saga and Oral Tradition: A Discourse on Method* (Millman Collection, Cambridge, MA, 2004).
6. R. A. Skelton, T. E. Marston, G. D. Painter, *The Vinland Map and the Tartar Relation* (Yale Univ. Press, New Haven, CT, 1965).
7. W. E. Washburn, Ed., *Proceedings of the Vínland Map Conference* (Univ. Chicago Press, Chicago, 1971).
8. D. J. Bradbury, *The Vinland Map: A Short Summary* (Past Presented, Whitehaven, UK, 2004). (See: www.pastpresented.info/vinland)

10.1126/science.1103089

BIOTECHNOLOGY

Anthropologists in the Lab

William A. Haseltine

A Machine to Make a Future by Paul Rabinow and Talia Dan-Cohen is another chapter in Rabinow's anthropological study of the biotechnology community. His first work on the topic, *Making PCR*, a book of high drama and colorful personalities, describes the creation of the polymerase chain reaction technique at Cetus in the 1980s (*1*). The second installment—the informative, interesting, and inadvertently humorous *French DNA*—examines events in the early 1990s surrounding the creation of Genethon in France (*2*). The new work spotlights recent happenings at Celera Diagnostics. The book might well be subtitled "after the storm" as it begins after the announced completion of the human genome sequence and the departure of J. Craig Venter. An almost audible sigh of relief whispers from the page.

A Machine to Make a Future
Biotech Chronicles
by Paul Rabinow and Talia Dan-Cohen
Princeton University Press, Princeton, NJ, 2004. 204 pp. $24.95, £15.95. ISBN 0-691-12050-1.

Rabinow's methods are consistent throughout the trilogy. Key participants are interviewed over an extended period or during and after significant events. Several of those interviewed for this book appear in *Making PCR*, and the chief scientist of Celera Diagnostics, Tom White, is a key figure in both. The interviewer himself is very much present, asking penetrating questions and offering an occasional opinion. The authors provide supporting information helpful to the general reader. Less helpful to those interested in the science and business are dollops of anthropological theory, inspired by the French philosopher Michel Foucault, sprinkled throughout.

The reviewer is at Haseltine Associates, 3053 P Street NW, Washington, DC 20007, USA. E-mail: wahaseltine@verizon.net

In *A Machine to Make a Future*, we are introduced to Celera Diagnostics at the beginning of 2003. The company has separated from its more famous parent, Celera Genomics. It is charting a new course to discover and market predictive diagnostic genetic tests. The book clearly describes the origins of the scientific concepts and business rationale. The scientists tell us in their own words why they decide to pursue an approach different from that of the Human Genome Project. They focus on variations in DNA sequence that occur only in or very close to the segments of DNA that encode functional genes. They embark on an ambitious program to determine the genome sequence of 39 humans and one chimpanzee. The planning and execution of this strategy is the core of the story. Sadly, it is a tale without an end. Rabinow's intensive study ran only through September 2003, and we never learn if the approach is successful. The voices fall frustratingly silent.

The strength of Rabinow's approach is that we hear the voices of scientists at work. Not only do they describe the science itself, but they also provide their perception of its importance. Rabinow is a skillful interviewer who elicits motivation from his subjects. We are given a rare glimpse into the professional lives of the participants and the energy that drives their scientific and personal decisions. Collectively, the three books should help young scientists as they plan their future in academia or industry.

Rabinow's methods allow the reader to draw larger conclusions. In each story, we see both the depth and limitations of the participants' knowledge. We learn of their own social construction of their work. In this respect only, *A Machine to Make a Future* is the most interesting of the three works, because the participants are minor players in the greater scientific and biotechnology community. Their world, claustrophobic and self-referent, appears to exclude (to a significant extent) participation in the broader currents of scientific dialogue. This may well be a study of a community headed toward extinction.

The reader may or may not enjoy instruction regarding deconstructionist anthropology. The co-author's sole role is to observe the observer observing. "The interviews contained in this book," we are informed,

> are interventions elicited, transcribed, and framed during a specific period of time.… They are partial descriptions, chosen from a point of view, framed to manifest some aspects of a certain actuality. Our hypothesis is that by giving to our inquiry and to our narrative a form different from traditional anthropological monographs, we will produce a different kind of result, one that is not intrinsically more valuable but one that will frame a different experience for readers and writers alike. Evaluating the results is a task for the future, again one for readers and authors alike.

David Lodge, the inspired satirist of deconstructionist literature, could not have written a better parody.

For those interested in contemporary biotechnology and genomics, it is a pity that the canvass selected is so narrow—a young, small, isolated company. Absent are the bold concepts of *Making PCR* or the intricate internecine battles of *French DNA*. In *A Machine to Make a Future*, the trilogy ends not with a bang but with a whimper.

References

1. D. Rabinow, *Making PCR: A Story of Biotechnology* (Univ. Chicago Press, Chicago, 1996).
2. D. Rabinow, *French DNA: Trouble in Purgatory* (Univ. Chicago Press, Chicago, 1999).

10.1126/science.1110000

India's R&D: Reaching for the Top

Raghunath A. Mashelkar

Five years ago, during my presidential address to the Indian Science Congress, I made a prediction: "The next century will belong to India, which will become a unique intellectual and economic power to reckon with, recapturing all its glory, which it had in the millennia gone by," I told the gathering of 5000, among them the country's prime minister.

It must have sounded crazy. How could a country with so many impoverished people, and so many illiterates, rise to have such a central global role? What possibly could have given me the confidence to make such a prediction?

The confidence came from a little boy. In the late 1950s, this boy struggled to have two meals a day while he studied under the streetlights and went barefoot to school. This same boy almost left school in 1960, because his poor widowed mother could not support his education. That this boy, who is myself, could become the president of the Indian Science Congress is what gave me the confidence to say that India could again achieve intellectual and economic greatness. If this miracle could happen to any Indian, then given an opportunity, it can happen to every Indian.

My own turn toward science began at a poor school in Mumbai (the local name for Bombay). I remember Principal Bhave, who taught us physics. One day, he took us outside the classroom to demonstrate how to find the focal length of a convex lens. He focused the sun's rays onto a piece of paper and told us that the distance between the paper and the lens was the focal length. Then he held the lens in place until the paper burned. That's when he turned to me and said, "Mashelkar, if you can focus your energies like this and not diffuse them, you can burn anything in the world!" I decided at that moment to become a scientist.

I indeed focused on my goal, invariably placing first in my classes. After earning a bachelor's degree in chemical engineering from Bombay University in 1966, I received fellowship offers for graduate study in the United States and Canada. But I decided to remain in India to pursue my studies toward a Ph.D. I did postdoctoral research in the United Kingdom, held a faculty position there, and then had a brief stint in the United States as a visiting professor. But in the mid-1970s, when attractive offers came my way for faculty positions in top schools in the United States and United Kingdom, I decided to return to India.

In this essay, I focus on the importance of returnees to poor countries such as India. I will examine how demographic shifts are creating shortages of skilled scientists and engineers in developed economies and leading to a new dynamic in human capital that is enabling some developing countries to emerge as "global R&D hubs." I also address ways in which global funding sources can be leveraged in such countries to create new knowledge devoted to the global good.

This yearlong essay series celebrates 125 years of *Science* by inviting researchers from around the world to provide a regional view of the scientific enterprise. Series editor, Ivan Amato

Intellectual Capital

Let me first address the issue of migration of talented students from the developing world to the developed world. In 1926, the distribution of scientific productivity was analyzed by Alfred J. Lotka of the Metropolitan Life Insurance Company in New York. The result of his investigation, which remains largely valid, was an inverse square law of productivity, by which the number of people producing n papers is

CREDIT: COURTESY OF R.A. MASHELKAR

Raghunath A. Mashelkar
India

Raghunath A. Mashelkar began life in poverty, sometimes hungry and shoeless. Now he is the director general of the Council of Scientific & Industrial Research (CSIR), a chain of 38 publicly funded industrial R&D institutions in India, and president of the Indian National Science Academy. That personal experience of ascendance from dire circumstances, improvements in his country's infrastructure, and changing patterns of scientific emigration and immigration have convinced him that India is fated to become one of the world's greatest intellectual and economic engines. Before becoming a leading architect of his country's science and technology policies, Dr. Mashelkar did pioneering work in polymer science and engineering, which earned him many international laurels. He is a Fellow of the Royal Society (London), a Fellow of the Academy of Sciences for the Developing World (TWAS), and a Foreign Fellow of the U.S. National Academy of Engineering. Dubbed a "dangerous optimist" in India, he is deeply committed to championing the cause of the developing world. He is also known in India for several high-powered "Mashelkar Committees," which have influenced such societal sectors as higher education, drug regulatory systems, and national automobile fuel policy.

All essays appearing in this series can be found online at www.sciencemag.org/sciext/globalvoices/

inversely proportional to n^2. This means that for every 100 authors who produce, say, one paper in a given period of time, there are approximately $100/2^2$, or 25 authors, who produce two papers and one author, who will produce 10 papers. Thirty years later, the same law was found to be applicable to patents.

This means that the bulk of scientific and technological creativity and productivity lies in the minds and abilities of a small number of highly talented individuals. Since India gained independence in 1947, the country has consistently lost such individuals to the developed world. The country's leaders comforted themselves by assuming that the number of scientific émigrés was too small for a country of 1 billion people to worry about. But they were not considering Lotka's law and so did not realize that by losing the top tier of talent, we also lost most of our intellectual energy.

A recent report by the United Nations Development Programme* estimates that 100,000 Indian professionals leave the country every year to take up jobs in the United States. If one considers the potential economic gains, which these exceptionally talented people could have brought to India, one realizes that the economic losses due to this mass migration are enormous.

Indica-tions of things to come. The Indica car, first designed and built in India for Indians in the 1990s, now is selling in European markets.

Invariably it is assumed that the main driving force for the brain drain is economic. People go to the developed world in search of a higher income, so the theory goes. But I do not think material gain is the only reason. After all, according to a recent study by the U.S. National Science Foundation,† the number of scientists and engineers who left Japan to work in the United States and who did not return jumped by 100% between 1995 and 1999. Yet Japan, unlike India, already is a developed country with many high-paying jobs. The Italian scientist Riardo Giacconi, a Nobel Laureate in Physics, summed up what might be the most important factor behind such a brain drain when he said: "A scientist is like a painter. Michelangelo became a great artist, because he had been given a wall to paint. My wall was given to me by the United States."

Only now are such walls becoming available in developing countries, but for reasons that could not have been anticipated 10 years ago.

This past December, I visited the John F. Welch Technology Centre in Bangalore. With 2300 employees, it is General Electric's (GE's) largest single location for R&D in the world. I found that 700 of the employees were young Indians, who had chosen to come back to India from the United States during the preceding 3 to 4 years. GE is not alone in setting up shop in India. More than 100 global companies including IBM, Motorola, and Intel have established R&D centers in India during the past 5 years, and more are coming. Many Indians who received their training and early work experiences abroad are now returning to India to work in these research centers. There is a silent scientific repatriation taking place in India.

There is a silent scientific repatriation taking place in India.

Why are the foreign companies, some of whom have budgets larger than India's entire $6 billion R&D budget, moving a sizable portion of their R&D infrastructures to India? I was present in Bangalore, 5 years ago, when the John. F. Welch Technology Centre was set up. When Welch, who then was still GE's chief operating officer, was asked why he was taking this step, he replied: "India is a developing country, but it is a developed country as far as its intellectual infrastructure is concerned. We get the highest intellectual capital per dollar here."

One way to understand what Welch meant is to calculate the number of scientific research publications the country produces per dollar that is spent on R&D in India. Using the data provided by Sir David King‡ (chief scientific adviser to the UK government) for scientific publications in major, peer-reviewed journals (SCI publications), I calculated the number of journal publications per gross domestic product (GDP) per capita per year. The top three nations were India (31.7), China (23.32), and the United States (7.0). John Welch's intuition was right!

My calculation has to be viewed carefully, of course. After all, the percentage of all global SCI publications produced by India and China is less than 2% each. But this also means that if India and China were to increase their science and technology ranks by several fold (which they are perfectly capable of doing) and invest more per scientist (which already is happening), then it is possible for both countries to enhance their competitiveness several fold. Indeed, if we apply Lotka's law of scientific productivity, India's and China's competitive advantage ought to increase by several orders of magnitude as more and more of the most talented scientists return. In this way, by shifting much of their R&D activity to countries such as India and China, the world's industries can greatly bolster the domestic intellectual capital of these countries.

Scientific Repatriation

As the direction of the brain drain shifts away from developed countries, rather than toward them, shortages in R&D personnel in developed economies are likely to arise. And as that happens, there will be a greater drive toward multiple geographical and organizational sources of technology. The impact of such shortages can be seen by citing an example from the European Union (EU). For the EU to meet the goal set at the 2002 Barcelona Summit of increasing R&D spending as a share of GDP to 3% by 2010, the EU will have to add 700,000 new researchers to the workforce. As one EU representative put it recently, there will be a greater draw on "Third World researchers." As the professional opportunities and personal comforts in their own countries increase, however, will these researchers prefer migrating to Europe or working in their own countries?

The incentive to stay put is greater than ever. When I returned to India in 1976, the personal comforts and professional opportunities there were unbelievably limited. I

CREDIT: TATA MOTORS

remember having to endure a 3-year waiting list to get my first telephone, a 2-year wait to buy a scooter, and a 6-month wait to buy a black-and-white TV. Today you can walk into a showroom and choose from among 20 TV models. And millions of mobile phones now are sold in India every month.

Now consider the professional side. In my earlier career as a scientist, it took me 2 years to buy a special type of flow meter that I needed for my work on polymers. It was a struggle to gain access to even a rudimentary computer. And scientific journals used to arrive by sea mail, which made it hard for us to remain up-to-date on current research. Now we have our own supercomputers and, thanks to the cyber world, our scientists read *Science* at the same time as their American counterparts!

Most importantly, today's returnees to India are finding that the opportunity to do cutting-edge research has increased many fold compared to what it was when I returned in the 1970s. The latest Intel chip and the latest GE aeroengine are being designed in Bangalore, for example. True, these are multinational companies with headquarters outside of India, but India-based companies are changing too. For one thing, on 1 January 2005, India enacted a new patent regime that is compliant with the World Trade Organization's TRIPS (Trade Related Intellectual Property Rights) agreement, which establishes a set of rules to ensure that intellectual property rights are respected in international trade contexts.

In anticipation of the new challenges that will follow in the wake of this action, Indian drug and pharmaceutical industries have increased their R&D spending by 400% in the past 4 years, and they are now looking to hire hundreds of Ph.D.'s. They also are shifting toward more in-house innovative research. Rather than just copying drug molecules made by others, the R&D programs of these industries now are trying to create new therapeutic molecules. In a similar fashion, the Indian automobile industry now is exporting indigenously designed and manufactured cars such as the Indica to European markets.

Global Goods

Multinational companies are locating their R&D resources in India to create proprietary knowledge for private good—that is, for the stockholders—through private funding. However, my dream is to create a global knowledge pool for global good through global funding. Here, India can become an agent for change. This global-good perspective could become the case in diverse sectors ranging from biotechnology to information technology to space research.

This dream already has some momentum. First, consider a pedagogical tool, the computer-based functional literacy (CBFL) program, developed by Indian software pioneer Faqir Chand Kohli. Within a mere 8 to 10 weeks and at a cost of a mere U.S. $2 (provided a discarded computer is supplied for free), an illiterate adult using this tool can read his or her first newspaper. In the past 2 years alone, 40,000 adults from five states in India have been made literate. If CBFL is launched as the technical engine of a national literacy movement, in less than 5 years, 200 million adult illiterates can learn to read. The same Indian innovation could be of great service to the rest of the world's estimated 854 million illiterates too! To this end, the Indian Institute of Technology in Madras has created a low-cost wireless Internet access system that needs no modem and eliminates expensive copper lines. It is just what is needed to offer CBFL to low-income communities throughout India and beyond. The technology already is in use in many countries, among them Fiji, Yemen, Nigeria, and Tunisia, to name a few, and it has been licensed to manufacturers in India, Brazil, China, South Africa, and France.

India can similarly become an innovation hub for global health. Its reputation as a low-cost manufacturer of high-quality generic drugs already is high. Now discovery, development, and delivery of new drugs to the poor is another area in which India is becoming stronger. By following alternative paths rather than beaten ones, India is aiming to develop drugs at prices that are more affordable to more of the world's people. For instance, India is trying to build a golden triangle between traditional medicine, modern medicine, and modern science. By culling clues from traditional medical practices, researchers here are doing a sort of "reverse pharmacology," which is showing great promise. Our recent program on developing a treatment for psoriasis through a reverse pharmacology path (presently in phase II human clinical trials) is expected to take 5 years and cost $5 million. If successful, the resulting treatment will be priced at $50, quite a step down from a new $20,000 antibody injection treatment developed by a western biopharmaceutical company! The opportunities that are unfolding are breathtaking.

If India plays its cards right it can become by 2020 the world's number-one knowledge production center.

As I see it from my perch in India's science and technology leadership, if India plays its cards right, it can become by 2020 the world's number-one knowledge production center, creating not only valuable private goods but also much needed public goods that will help the growing global population suffer less and live better.

CREDIT: REUTERS

Tradition's future. Researchers in India are scouring traditional remedies, like this miraculous fish treatment for asthma, for clues to new medicines.

References

*United Nations Development Programme, *Human Development Report 2001: Making New Technologies Work for Human Development* (Oxford Univ. Press, New York, 2001).

†National Science Board, Science and Engineering Indicators 2002; available at www.nsf.gov/sbe/srs/seind02/start.htm.

‡D. King, *Nature* **430**, 311 (2004).

The author is director general of the Council of Scientific and Industrial Research (CSIR), New Delhi, India. E-mail: dgcsir@hq.csir.res.in

10.1126/science.1110729

MATERIALS SCIENCE

A Window on Biomineralization

Arthur Veis

Almost all living organisms can deposit minerals: Magnetotactic bacteria deposit iron oxide enclosed in organic sheaths, mollusks form calcite crystals in their shells, and vertebrates generate the apatite crystals found in bones and teeth (*1*, *2*). On page 1450 of this issue, Du *et al.* (*3*) shed light on one of these processes, namely the formation of enamel in vertebrate teeth. The results have wider implications for the mechanisms by which organisms control mineral deposition.

Enhanced online at www.sciencemag.org/cgi/content/full/307/5714/1419

As diverse as the minerals and the organisms giving rise to them may be, it has been hypothesized that there are just two pathways governing deposition. In "biologically induced" mineralization—for example, in corals—the minerals adopt crystal shapes similar to those formed by inorganic processes and have essentially random crystal orientations. In contrast, in "matrix-mediated" mineralization, the organism controls the nature, orientation, size, and shape of the mineral phase by creating closed compartments or defined channels in which the mineral crystals form. A specific set of macromolecules—including proteins, polysaccharides, proteolipids, and proteoglycans—regulates nucleation, growth, size, and orientation of the crystals.

There is general agreement that matrix macromolecules and tissue architecture are important in nucleating and localizing mineral formation, but major questions remain. Chief among these is how the organism can determine the crystal orientation. Du *et al.* (*3*) provide key insights into this problem by reporting the formation of highly ordered apatite crystals in an initially unstructured matrix during tooth enamel formation.

The author is in the Department of Cell and Molecular Biology, Northwestern University, Chicago, IL 60611, USA. E-mail: aveis@northwestern.edu

The vertebrate tooth is an excellent model for exploring how crystal orientation is controlled. More than 95% by weight of the mature enamel (which covers the outer surface of the tooth) is composed of millimeter-scale, well-organized rod-like aggregates comprising ribbons of carbonated apatite crystallites; organic matrix components make up less than 2% of the enamel. On the other hand, only 60% of the underlying dentin consists of mineral. Considering the high density of apatite, this means that less than 40% of the dentin volume consists of mineral.

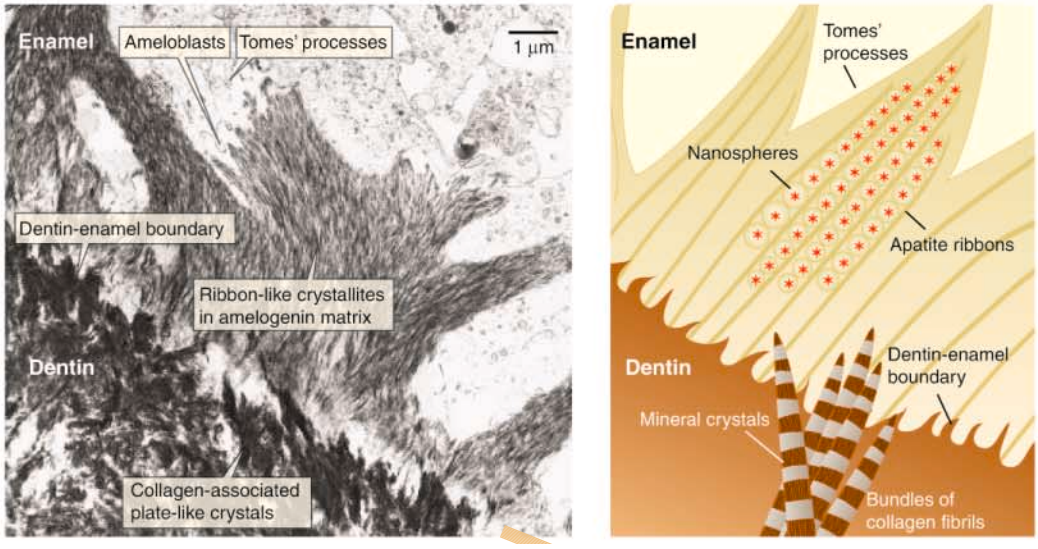

Crystallization at the dentin-enamel boundary. (**Left**) Micrograph of the dentin-enamel boundary in a developing tooth. The apatite of dentin (lower left) forms nanometer-scale plates that initially grow individually and independently in the gap spaces along the collagen fibrils. The ribbon-like apatite crystallites of the enamel (top right) form within the amelogenin-rich enamel matrix. (**Right**) A close-up view (not to scale) of the hypothesized (*3*) mineral deposition processes in dentin and enamel near the dentin-enamel boundary. In the dentin, plate-like apatite crystals grow in the periodic gap spaces along the collagen fibrils and fibril bundles. The apatite crystal *c* axis is mostly aligned with the long axis of the collagen fibril. In the enamel, Du *et al.* (*3*) propose that linear aggregates of polarized, self-assembled amelogenin nanospheres form a negatively charged template that induces apatite formation.

To understand how tooth dentin and enamel form, consider the dentin-enamel boundary in a developing tooth (see the figure, left panel). The dentin is largely comprised of collagen fibrils with a 67-nm periodicity. Because of this periodicity, the ~300-nm-long, rod-like collagen molecules cannot not be joined end-to-end in the fibrils, but are staggered and overlapped along their long axes, leaving gaps between the molecular ends. In the packed fibril, the gaps are in register, producing channels that run transverse to the fibril axis; their reduced density produces cross-striations in the fibrils. In the mineralized collagen fibrils in the left panel, the dark bands are caused by mineral crystals that have begun to grow in the gap spaces. The plate-like crystals fill the gap space, and their *c* axes align approximately with the long axis of the collagen fibrils.

It is easy to see how dentin mineralization may fit into the matrix-mediated scheme, with the collagen fibrils determining the crystal orientation. However, the collagen does not nucleate the crystals (*4*, *5*). It is secreted from cells called odontoblasts and organized into fibrils before mineralization begins (*6*). As the odontoblasts lay down the matrix, they move away from the dentin-enamel boundary, and the dentin layer thickens. In contrast, the mineral-related noncollagenous proteins are present only near the region where mineral deposition begins (*7*). They localize on the collagen fibril surfaces at the gap zones, nucleating crystal formation and guiding crystal growth. Thus, in the matrix-mediated scheme, the collagen fibril matrix provides the scaffold and space for the mineral. The noncollagenous matrix proteins nucleate the crystals and determine their growth and orientation in the gaps.

Mineral deposition in enamel (see the figure, left panel) is very different. Here, ameloblast cells elongate along the dentin-enamel boundary to form a palisade with tight

cell junctions. Each ameloblast develops an asymmetric structure called the Tomes' process. Like the ends of a picket fence, the Tomes' processes protrude without contacting each other. The spaces between them become filled with an amelogenin-rich matrix, a hydrated protein gel without apparent structure. In this matrix, oriented ribbon-like crystallites of enamel mineral assemble and elongate from the dentin-enamel junction to the outer enamel surface. The ribbons thicken and aggregate to form enamel rods, while the amelogenin matrix is degraded and removed. The spaces between the Tomes' processes are thus the closed compartments required in matrix-mediated mineralization. However, it has never been clear how the gel-like matrix provided by the amelogenin might nucleate and direct the oriented crystal growth. This is the aspect addressed by Du *et al.* (*3*).

Amelogenin molecules are mostly hydrophobic but contain a short carboxyl-terminal sequence of hydrophilic amino acids. In the extracellular space (the space surrounding the Tomes' processes) they assemble into nanospheres, each of which contains tens of molecules. Du *et al.* demonstrate (*3*) that in each molecule, the hydrophilic sequence resides on the surface. They also show that during nanosphere assembly, each nanosphere develops an asymmetric charge distribution. The nanospheres further assemble into ordered linear arrays, giving a defined, direction-dependent structure to the gel-like matrix.

The hypothesized colinear arrangement of the hydrophilic sequences of the nanospheres (*3*) could template crystal nucleation and growth in the enamel. This is conceptually similar to the binding of matrix proteins in the gaps between collagen fibrils to nucleate and orient the dentin mineral. The dentin and enamel mineralization systems—mechanistically very different but operating at the same time across the dentin-enamel boundary (see the figure, right panel)—show how the supramolecular organization and properties of the extracellular matrix regulate the nature and organization of the mineral phases.

The study by Du *et al.* further shows that the nanosphere self-assembly process can take place in vitro, without requiring ameloblasts. In vivo, two processes may play a role. First, the Tomes' processes may help to orient and elongate the enamel crystallite aggregates by controlling the orientation of the nanosphere chains. Second, the mineralized dentin, which protrudes into the amelogenin matrix at the dentin-enamel boundary, may orient the first nanospheres.

Others have shown that minerals can develop within protein and synthetic polypeptide gels (*8*, *9*), but a scaffold was necessary to provide long-range order. In contrast, Du *et al.* (*3*) show that the self-assembly of the amelogenin nanospheres, and their further assembly into nanosphere arrays, forms its own scaffold that can direct the alignment of the mineral crystallites. The in vitro self-assembly system of Du *et al.* will be a useful guide to the development of biomimetic structures.

References and Notes

1. H. A. Lowenstam, *Science* **171**, 487 (1971).
2. H. A. Lowenstam, S. Weiner, *On Biomineralization* (Oxford Univ. Press, Oxford, 1989).
3. C. Du *et al.*, *Science* **307**, 1450 (2005).
4. A. George *et al.*, *J. Biol. Chem.* **271**, 32869 (1996).
5. W. J. Landis, *Bone* **16**, 533 (1995).
6. E. Beniash, W. Traub, A. Veis, S. Weiner, *J. Struct. Biol.* **132**, 212 (2000).
7. A. M. Rabie, A. Veis, *Connect. Tissue Res.* **31**, 197 (1995).
8. J. D. Hartgerink, E. Beniash, S. I. Stupp, *Science* **294**, 1684 (2001).
9. L. A. Estroff, L. Addadi, S. Weiner, A. D. Hamilton, *Org. Biomol. Chem.* **2**, 137 (2004).
10. I thank T. G. H. Diekwisch for supplying the electron micrograph shown in the left panel of the figure.

10.1126/science.1109440

OCEAN SCIENCE

Lost City Life

Antje Boetius

One of the first underwater scenes in James Cameron's spectacular new IMAX adventure *Aliens of the Deep* stars a truly alien panorama. It is a stunning view of the giant white carbonate chimneys of a submarine hydrothermal vent field called Lost City, which looms like a conglomeration of colossal beehives from outer space. The discovery of the Lost City hydrothermal field in December 2000 was a real fluke (*1*). A team of scientists working with Deborah Kelley came across this new ecosystem during an off-axis camera survey near the Mid-Atlantic Ridge at 30°N. As Kelley *et al.* (*2*) report on page 1428 of this issue, they returned in 2003 for a detailed study of Lost City and discovered a remarkable array of micro- and macro-organisms that reside in this hydrothermal ecosystem, which is fueled by abiotic methane and hydrogen. Their results provide fascinating insights into the nature of life at Lost City. Although Lost City represents a unique vent system, the underlying processes responsible for its formation and geochemical setting are likely to drive many other vent ecosystems. This has important implications for biogeochemical cycles, for ocean exploration, and for understanding microbial habitats on Earth and beyond.

The Lost City vent field is characterized by carbonate towers up to 60 m in height. It is located on 1.5-million-year-old rock that is 15 km away from the spreading center. This implies that hydrothermal venting must be more widespread than previously assumed. In the case of Lost City, venting is the consequence of serpentinization reactions between seawater and fresh peridotite, which lead to formation of heat, hydrogen, and methane (*3*, *4*). Typical for exothermic subsurface reactions with iron-bearing olivine, the hydrothermal fluids of Lost City are characterized by temperatures of 40° to 90°C, high pH (9 to 11), a low concentration of magnesium, and elevated concentrations of hydrogen and methane (*1*). Früh-Green *et al.* (*5*) found that this type of hydrothermal venting may have been present for more than 30,000 years at the Lost City field. This lifetime exceeds that of most of the known black smoker–type hydrothermal vents by at least two orders of magnitude. Considering Lost City's longevity and the active proliferation of methane and hydrogen, it seems odd that not much life was observed at this type of vent system, except for some cryptic microbial mats hidden inside the carbonate towers (*1*, *7*).

Kelley and her collaborators went back to Lost City in 2003 for a month-long field expedition (*2*). With the research vessel Atlantis, the submersible Alvin, and the Autonomous Benthic Explorer (ABE) at their disposal, they were able to conduct detailed mapping of the vent field. This multidisciplinary research adventure is beautifully illustrated at www.lostcity.washington.edu. A principal goal of the expedition was to discern how vent fluids, mineral precipitation, and microbial metabolisms interact to produce this extraordinary hydrothermal ecosystem and its underlying flow of energy and carbon.

The vent fluids of the Lost City system are very different from those of black smokers, white smokers, and other Mid-Atlantic Ridge systems fueled by serpentinization reactions. Seawater-basalt reactions driving volcanically hosted vents produce substantial amounts of CO_2, sulfide in the millimolar range, and low pH (3 to 5), as well as extremely high temperatures (200° to 400°C). In contrast, the Lost City vents lack CO_2 but provide high fluxes of hydrogen and methane at warm temperatures and high pH (see the figure, A). The fluids of other very iron- and magnesium-rich (ultra-

The author is at the Max Planck Institute for Marine Microbiology, Bremen 28359, Germany. E-mail: aboetius@mpi-bremen.de

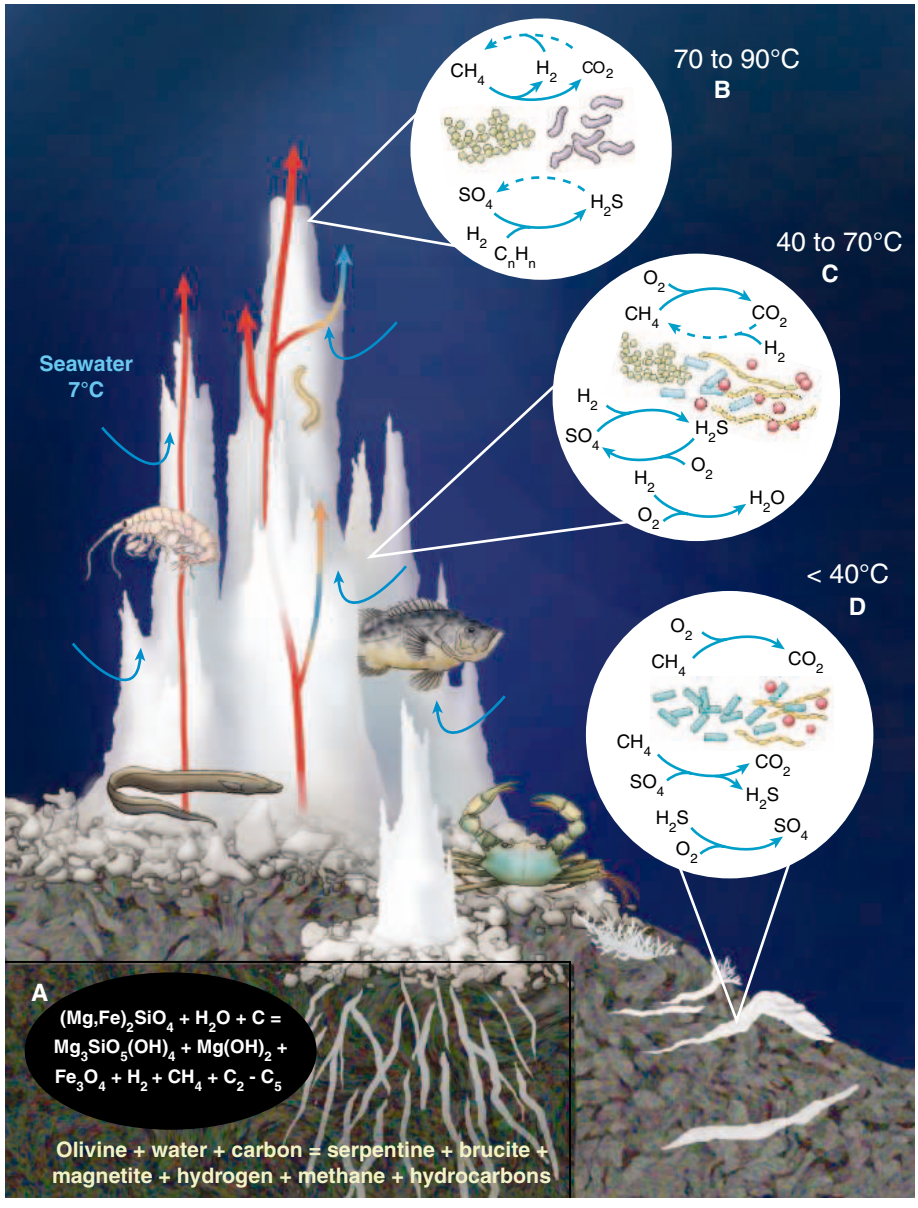

A beehive of activity. Microbial niches in serpentinization-influenced environments at the Lost City hydrothermal field. (**A**) Exothermic serpentinization reactions within the subsurface produce fluids of high pH enriched in methane and hydrogen, as well as some hydrocarbons. (**B**) Environments within the warm interior of carbonate chimneys in contact with end-member hydrothermal fluids host biofilms of *Methanosarcina*-like archaea (green circles). These organisms may play a dominant role in methane production and methane oxidation within the diverse environments present in the chimneys. Bacterial communities within these biotopes are related to the Firmicutes (purple rodlike cells). These organisms may be important for sulfate reduction at high temperature and high pH. (**C**) Moderate-temperature (40° to 70°C) endolithic environments with areas of sustained mixing of hydrothermal fluids and seawater support a diverse microbial community containing *Methanosarcina*-like archaea, ANME-1 (a methane-oxidizing phylotype; blue rectangular cells), and bacteria that include ε- and γ-proteobacteria (yellow filaments and red circles). The oxidation and reduction of sulfur compounds, the consumption and production of methane, and the oxidation of hydrogen most likely dictate the biogeochemistry of these environments. (**D**) In cooler environments (<40°C) associated with carbonate-filled fractures in serpentinized basement rocks, ANME-1 is the predominant archaeal phylotype. The bacterial populations contain aerobic methanotrophs and sulfur-oxidizing phylotypes.

mafic) vent systems at the Mid-Atlantic Ridge, such as at Logatchev and Rainbow, also show substantial methane and hydrogen anomalies but are distinguished by their much higher temperatures, low sulfide flux, and acidic pH (*6*). This difference between Lost City and other vent sites explains the lack of chemoautotrophic symbiotic organisms in Lost City fauna. Most of the reduced energy at the Lost City field is provided by hydrogen. Today, no animals are known to harbor hydrogen oxidizers as symbionts. Kelley *et al.* (*2*) found a high diversity of small invertebrates associated with the active carbonate structures, with a relatively high endemicity of nearly 60%. These invertebrates—snails, bivalves, polychaetes, amphipods, and ostracods—most likely derive some fraction of their energy requirement and carbon source by grazing on vent-associated carbonates and microbial biofilms (*1*).

The carbonate vents hold the key for understanding what is new about the metabolism, diversity, and distribution of microbial life at Lost City. An astonishingly high cell biomass is found inside the cavities and channel systems of the actively venting chimneys. The first analysis of such fluid-filled carbonate channels revealed the presence of archaeal biofilms (*7*). With their systematic study of diverse carbonate samples, Kelley *et al.* (*2*) now show that an almost pure culture of a new type of archaea develops in a specific setting within the chimneys characterized by direct contact with the hot end-member fluids (see the figure, B). The dominant archaea are phylogenetically related to the methanogenic archaea of the order Methanosarcinales. Interestingly, their closest relatives belong to ANME-3, a group of uncultivated anaerobic methanotrophs from cold-seep environments (*8*, *9*). However, lipid biomarker analyses of the Lost City archaeal biofilms show an isotopic enrichment in ^{13}C relative to source methane, indicative of a dominance of methanogenic growth. But the cooler parts of the vented carbonates appear to represent a crossroads between methanogenic and methanotrophic microniches (see the figure, C). This is indicated by the presence of both Methanosarcinales and ANME-1, as well as of functional genes indicative of anaerobic oxidation of methane (*10*, *11*). The anaerobic oxidation of methane is assumed to function as a reversal of methanogenesis. However, no microorganism capable of switching between the two types of metabolism has yet been identified. Perhaps such an organism lives in Lost City. Indeed, physiological experiments with the new group of archaea dominating the Lost City vents may shed light on this question. Within carbonates hosted by basement rocks at ambient temperature (see the figure, D), gene and biomarker lipid analyses point to the coexistence of ANME-1 and sulfate-reducing bacteria, as in other methanotrophic ANME-1/carbonate habitats (*12*). Hence, abiotic and microbial methane production based on serpentinization reactions may be globally very high, but this methane appears to be directly con-

CREDIT: TAINA LITWAK

sumed within neighboring microniches.

Ultramafic rocks favoring serpentinization reactions may have been some of the oldest habitats for microbial life on Earth. With their detailed study of the Lost City vent field, Kelley *et al*. present the first systematic portrayal of this type of subsurface ecosystem, which may still be widespread today. As proposed for early life on Earth and for potential life in outer space, this is an ecosystem in which abiotic methane and hydrogen production is exploited for anaerobic microbial methane and CO_2 fixation as the primary processes for generating biomass. Intriguingly, the resulting biomass of the modern day analog at Lost City has an average isotopic carbon signature that we would not interpret as a signature of life, because it is not different from abiotic carbon sources. Hence, the submarine Lost City hydrothermal field discovered by Kelley and her team is one of the most interesting natural laboratories available to geologists, chemists and biologists, for studying the biogeochemical signatures of ecosystems driven by abiotic methane and hydrogen.

References

1. D. S. Kelley *et al.*, *Nature* **412**, 145 (2001).
2. D. S. Kelley *et al.*, *Science* **307**, 1428 (2005).
3. J. L. Charlou, J. P. Donval, *J. Geophys. Res.* **98**, 9625 (1993).
4. J. Horita, M. E. Berndt, *Science* **285**, 1055 (1999).
5. G. L. Früh-Green *et al.*, *Science* **301**, 495 (2003).
6. J. L. Charlou *et al.*, *Chem. Geol.* **191**, 345 (2002).
7. M. O. Schrenk *et al.*, *Environ. Microbiol.* **6**, 1086 (2004).
8. V. Orphan *et al.*, *Appl. Environ. Microbiol.* **67**, 1922 (2001).
9. K. Knittel *et al.*, *Appl. Environ. Microbiol.* **71**, 467 (2005).
10. M. Krüger *et al.*, *Nature* **426**, 878 (2003).
11. S. J. Hallam *et al*, *Science* **305**, 1457 (2004).
12. W. Michaelis *et al.*, *Science* **297**, 1013 (2002).

10.1126/science.1109849

HIV/AIDS

HIV: Experiencing the Pressures of Modern Life

David Nolan, Ian James, Simon Mallal

No doubt many readers are familiar with the dilemmas posed by multiple competing pressures: each demanding attention that must be allotted from a finite store; each with a more or less strict deadline that must be met; and each extracting some cost to our resources, in terms of both the effort involved in achieving success and the pain derived from failing a given task. For all of us who need to deal with these dynamic and constantly varying pressures, we can now spare a thought for the human immunodeficiency virus (HIV) as it attempts to deal with what is becoming increasingly apparent as a complex and formidably variable immune environment provided by the human host. New findings presented on page 1434 of this issue by Gonzalez and colleagues (*1*) add to our appreciation of host genetic diversity, along with a grudging respect for HIV and its ability to successfully negotiate the challenges it faces on many fronts. This study also provides evidence that the boundary between immunology and virology, in which interactions between host and pathogen are explored at a population and even global level, is a fertile research area.

Many of the barrier and immune surveillance systems that humans use against invading pathogens can be overcome by successful viruses such as HIV, using reasonably stereotypic responses. Indeed, the ability of a virus to establish pandemic levels of infection presupposes that it arrives at its human host with an array of tools designed to foil the immune response. A recent case study is provided by a family of host cytidine deaminases (termed APOBEC proteins) that are capable of introducing lethal editing errors in HIV DNA transcripts (*2*, *3*). This antiviral mechanism, despite its biological elegance, is readily countered by the presence of an accessory HIV protein (Vif) that binds to APOBEC proteins and targets the resulting complex for proteasomal degradation and destruction. Through strategies that are similarly uniform, in which the virus often harnesses itself to indispensable host cellular functions, HIV is able to access the very core of the human immune machinery and establish infection.

There is another layer of complexity, however, to the host response to HIV-1 infection. Highly polymorphic genetic systems of the host can determine an immunological "landscape" that is highly individual-specific, thereby creating challenges that HIV-1 must negotiate in each and every new host (see the figure). In their new work, Gonzalez *et al*. show that chemokine receptor 5 (CCR5), a HIV coreceptor, and its ligand partners (including CCL3L1) form a genetic barrier to HIV infection in certain individuals. The authors demonstrate that the copy number of a segmental duplication encompassing the gene encoding CCL3L1 varies markedly between individuals and between different populations. Those with a high *CCL3L1* gene copy number are more resistant to HIV infection than those with a low copy number, presumably because there is more ligand to compete with HIV during binding to CCR5. In addition, those individuals with a low *CCL3L1* gene copy number combined with a disease-accelerating CCR5 genotype are even more susceptible to HIV infection.

The complexity of the CCR5-CCL3L1 genetic system can be attributed to genetic traits that are both qualitative (dictated by variant alleles that influence protein expression and function) and quantitative (dictated by the number of *CCL3L1* gene copies inherited). CCR5 and CCL3L1 (as well as other CCR5 ligands) thus create a variable barrier to HIV binding to its coreceptor, ultimately modulating disease susceptibility and clinical endpoints such as pretreatment viral load and rate of $CD4^+$ T cell decline. The phenotypic effects of genetic variation within this system suggest that the CCR5 receptor-ligand network serves an important role in HIV pathogenesis that cannot readily be subserved by alternative chemokine receptors (that is, redundancy in this system is low). Accordingly, adaptive responses by HIV-1 such as alternative tropisms (the use of other coreceptors) appear unable to reproduce the disease-accelerating effects of permissive CCR5 variants and low *CCL3L1* gene copy number.

A similar conceptual framework may be applied to the dynamic interaction between HIV-1 and polymorphic host human leukocyte antigen (HLA) molecules (see the figure). Here, the extreme genetic diversity of the HLA system and the importance of these cell surface molecules to the generation of antiviral cytotoxic T lymphocyte (CTL) responses provide a powerful individual-specific host environment for HIV infection. This has been highlighted recently in studies by Goulder and colleagues (*4*, *5*). These investigators demonstrated the importance of the HLA-B gene locus and its numerous allelic variants in shaping the HIV-specific immune response. They also have elegantly mapped the dynamic interplay between host HLA-restricted selection pressure and adaptive HIV escape mutations that subvert this immune recognition system by altering viral epitopes (see the figure). Again, this polymorphic genetic system provides a highly variable barrier to HIV replication

The authors are at the Centre for Clinical Immunology and Biomedical Statistics, Royal Perth Hospital and Murdoch University, Perth, Western Australia 6000, Australia. E-mail: S.Mallal@murdoch.edu.au

that must be negotiated by the virus in each host. In each instance, this requires a reequilibration of benefit (escape from CTL-mediated destruction) versus cost (effects of mutation on viral replicative capacity and pathogenicity).

So where is this research endeavor heading, in both a conceptual and a practical sense? We offer three observations, each taken from a different perspective. First, these studies allow a glimpse of the consequences of uncontrolled, pandemic infection in human populations. HIV is a highly successful pathogen in the sense that its extreme adaptive capacity allows it to cope with the vast majority of immune selection pressures that it encounters. Moreover, it is able to maintain sufficient pathogenicity in the face of these challenges, which prove lethal in most cases if left untreated. Although history suggests that many viruses are driven toward a more symbiotic relationship with their human hosts over time, evidence from the chimpanzee genome indicates that viruses such as SIV (the simian precursor to HIV-1) are likely to have been responsible for a selective sweep of both HLA and CCR5 genetic diversity (*6*, *7*). Thus, the virus is eventually limited to a relatively small reservoir of naturally protected hosts with limited genetic diversity as the result of a "bottleneck" effect in which nonprotective alleles do not survive.

Second, these findings have immense importance for vaccine design and assessment (*8*). Through an appreciation of dynamic host-viral interactions, with their own temporal patterns and finely tuned balance of cost versus benefit, we can begin to envisage the development of vaccines capable of providing broad coverage against incoming (often highly adapted) viral strains in a genetically diverse vaccinee population. The nonrandom frequency distribution of both HLA and chemokine receptor haplotype diversity in different demographic/ethnic populations (*1*, *9*, *10*) also indicates that genetic variation needs to be considered on a global scale but that vaccine design needs to be population-specific.

Finally, these data offer a conceptual challenge to both virologists and immunologists to explore the intersections between these two disciplines. To take an overly simplistic view, it may be said that the virologist will tend to acknowledge the inherent variation in viral populations while considering the host immune response to be relatively fixed. In contrast, the immunologist is more likely to appreciate the nuances of host immunology but underestimate the variability and adaptability of the pathogens to which it is exposed. Each viewpoint has its benefits and weaknesses. But the willingness to negotiate complexity—and ultimately to recognize that order and constraint may operate in interacting systems that at first appear almost infinitely and chaotically variable—is likely to produce considerable dividends, particularly in relation to the development of HIV vaccines. So far, we have developed effective vaccines against relatively

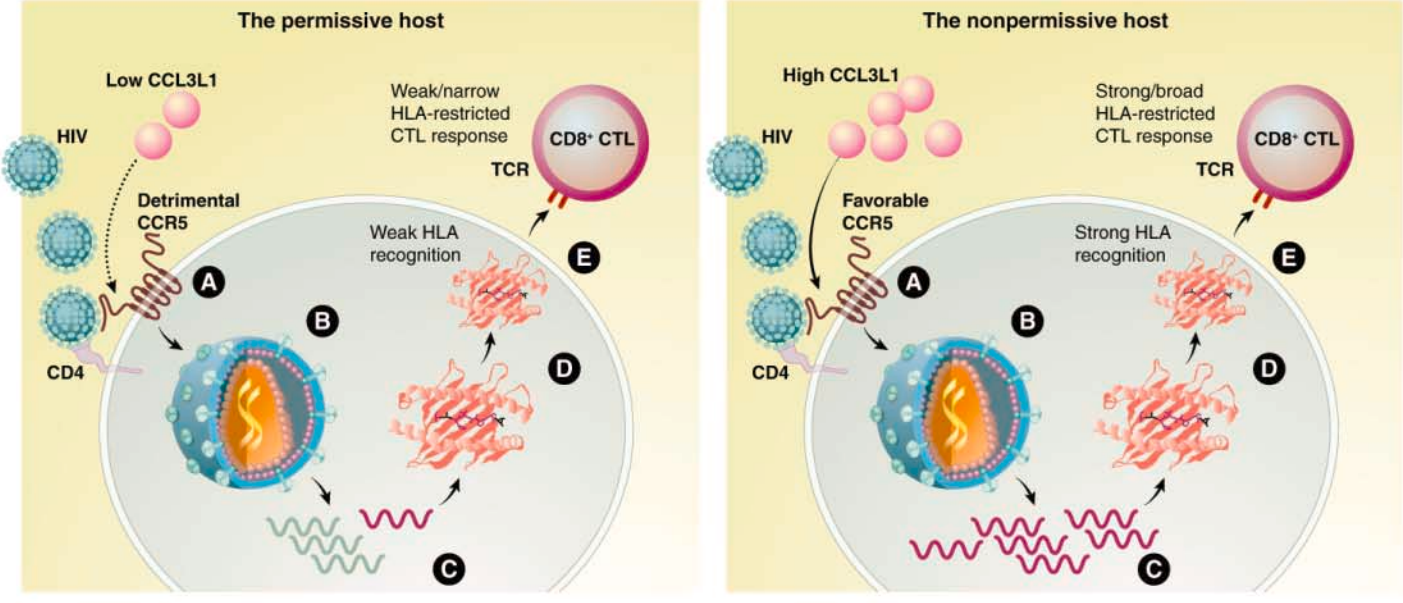

CREDIT: PRESTON HUEY, KATHARINE SUTLIFF/*SCIENCE*

Permissive and nonpermissive human hosts for HIV. The exploration of host genetic factors that influence HIV acquisition and disease progression tends to focus on "nonpermissive" hosts, who are protected from acquiring HIV or who experience a slow disease progression, and "permissive" hosts, who have a rapid progression to AIDS. This approach offers many critical insights into HIV pathogenesis but, at a population level, it is necessary to consider these cases as extreme ends of a spectrum in which each individual provides a unique host environment to which HIV must attempt to adapt. (Left) In the permissive host, viral invasion of $CD4^+$ T cells (**A**) may be facilitated by a lack of competition from endogenous CCR5 ligands, such as CCL3L1, and by CCR5 genetic variants that favor efficient HIV coreceptor binding. In this idealized individual, viral uncoating (**B**) and proteasomal processing of viral proteins to create short (8 to 10 amino acid) peptide epitopes (**C**) may produce a limited number of epitopes (due to HIV mutation/adaptation at proteasomal cleavage sites). These epitopes may be poorly recognized by host HLA molecules (**D**). Subsequent presentation of HLA-bound peptides may elicit only weak and narrowly focused $CD8^+$-cytotoxic T cell responses after binding of viral epitopes to the T cell receptor (**E**). This scenario demonstrates the many possibilities for HIV adaptation and "escape" from host immune responses, such that host-viral interactions represent a dynamic system. (Right) In the nonpermissive host, a combination of host genetic factors—in this case, "high" *CCL3L1* gene copy number and a favorable repertoire of CCR5 alleles (for example, *CCR5Δ32*) and HLA alleles (for example, *HLA-B57*)—direct efficient and powerful host cytotoxic T cell (CTL) responses against HIV. If HIV adaptation is limited by low replicative capacity and costs to viral fitness associated with CTL escape mutations, then "long-term nonprogressor status" may be conferred on the host. In both examples, the selection of adaptive mutations in HIV viral populations would be minimal. However, HIV diversity and adaptation would be favored in the more common situation in which the host provides some degree of barrier to productive HIV infection, but where the benefits of adaptation (such as escaping HLA recognition) outweigh the potential costs (for example, loss of viral fitness associated with mutation). Hence, population-based therapeutic strategies, such as HIV vaccine development, demand an improved understanding of how host-viral interactions shape HIV diversity. Gonzalez *et al.* (*1*) provide more evidence that the CCR5-ligand network is one of a number of highly polymorphic genetic systems that need to be considered in these comprehensive models.

nonadaptable organisms, such as poliovirus and the smallpox (vaccinia) virus, using empirical approaches. However, the many remaining global health challenges caused by adaptable organisms such as HIV require more reductionist approaches that take this inherent complexity into account.

As we celebrate the centenary of Albert Einstein's theory of special relativity, the thoughts of someone whose genius was based on organizing complexity have a particular resonance: "Everything should be made as simple as possible, but not more simple."

References

1. E. Gonzalez *et al.*, *Science* **307**, 1434 (2005); published online 6 January 2005 (10.1126/science.1101160).
2. A. M. Sheehy *et al.*, *Nature* **418**, 646 (2002).
3. V. N. KewalRamani, J. M. Coffin, *Science* **301**, 923 (2003).
4. P. Kiepiela *et al.*, *Nature* **432**, 769 (2004).
5. A. J. Leslie *et al.*, *Nature Med.* **10**, 282 (2004).
6. S. Wooding *et al.*, *Am. J. Hum. Genet.* **76**, 291 (2005).
7. N. G. de Groot *et al.*, *Proc. Natl. Acad. Sci. U.S.A.* **99**, 11748 (2002).
8. P. J. Goulder, D. I. Watkins, *Nature Rev. Immunol.* **4**, 630 (2004).
9. E. Gonzalez *et al.*, *Proc. Natl. Acad. Sci. U.S.A.* **98**, 5199 (2001).
10. S. B. Gabriel *et al.*, *Science* **296**, 2225 (2002); published online 23 May 2002 (10.1126/science.1069424)

10.1126/science.1110009

ASTRONOMY

Our Interstellar Neighborhood

J. R. Jokipii

On page 1447 of this issue, Lallement *et al.* report exciting new observations of the local interstellar medium, just beyond the boundary of the heliosphere (the region influenced by our Sun and its magnetic field) (*1*). The results provide insights into how the supersonic solar wind that flows outward from the Sun interacts with the interstellar medium.

The solar wind expands radially outward from the Sun, sweeping out the interstellar plasma and magnetic field to create a vast spheroidal cavity called the heliosphere. Well beyond the orbit of Pluto, at about 100 astronomical units (AU; 1 AU is the distance from Earth to the Sun) from the Sun, the wind becomes too dispersed to further push out the interstellar medium, and the supersonic flow slows down abruptly at a termination shock. The interaction between the outward-moving solar plasma and the interstellar plasma is complicated and has been the topic of much study and speculation.

The motion of the local interstellar plasma past the Sun compresses the heliopause on one side, producing a droplike shape with an extended tail (see the figure). The surface separating the interstellar plasma from the solar plasma is termed the heliopause. Because the motion of the interstellar plasma may be mildly supersonic, a weaker "bow shock" may be present upstream of the heliopause.

The interstellar plasma carries a magnetic field, the intensity and direction of which were poorly known before the work of Lallement *et al.* (*1*). In addition, the plasma contains neutral gases, mainly hydrogen and helium, that also flow past the heliosphere. The neutral hydrogen and helium and the charged plasma particles collide with each other, but on very large scales compared to the size of the heliosphere. The neutral atoms do, however, interact with the heliosphere through various ionization and charge exchange processes.

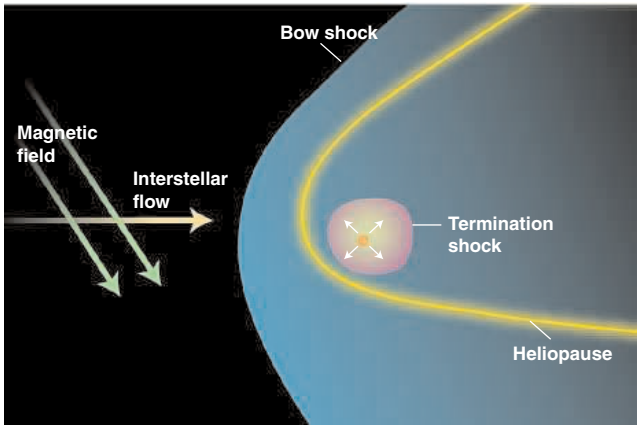

How the heliosphere interacts with the interstellar medium. The figure shows the plane containing the magnetic field and the interstellar medium velocity vector. The interstellar plasma and neutral hydrogen and helium flow in from the left. The plasma produces the shapes of the termination and bow shocks and carries with it a magnetic field. The asymmetric magnetic field forces cause the shock surfaces to be closer to the Sun at the bottom and flared out at the top. In the absence of the magnetic forces, the system would be laterally symmetric about a horizontal line through the Sun (*12*).

The size and shape of the heliosphere and the nature of its interaction with the interstellar medium depend on the properties of both the solar wind and the local interstellar medium. Data on the solar wind inside of the termination shock have been collected for several decades, mostly from spacecraft. Its nature is thus reasonably well known. Observations of the local interstellar medium are more sketchy.

Neutral hydrogen and helium atoms in the local interstellar medium can be detected through their back-scattering of solar photons. Absorption of starlight by nearby hydrogen in the upstream direction can also be observed. "Pickup ions," which are created when an electron is removed from neutral atoms by ionization or charge exchange, can be observed in the solar wind from spacecraft. Observations of integrated line-of-sight effects on the radiation from nearby stars provide further information about the interstellar medium on scales of several hundred thousand AU (*2*).

Energetic particle observations from Voyager 1 since mid-2002 suggest that it is approaching the termination shock. The spacecraft is now at a distance of about 90 AU from the Sun; Voyager 2 is still closer to the Sun at about 70 AU. Two groups have reported (*3, 4*) a dramatic enhancement in the anomalous cosmic ray intensity from mid-2000 to early 2003 at Voyager 1, but not at Voyager 2. However, they interpreted the data very differently.

Krimigis *et al.* (*3*) concluded that the observed increase occurred when the termination shock moved inward and crossed the path of Voyager 1, and that the event ended when the shock recrossed the spacecraft's path. In contrast, McDonald *et al.* (*4*) concluded that the spacecraft had not yet crossed the shock. This issue is still a matter of controversy, although magnetic field and radio (*5*, *6*) data provide no evidence of a shock crossing. A similar second event has since been observed (*7*).

Theoretical studies have attempted to interpret the observed enhanced cosmic ray intensities (*8*–*10*). The overall shape of the heliosphere is important in understanding the data. However, because the spacecraft data are essentially single point observations, they do not directly constrain the shape. This is where the new observations of Lallement *et al.* (*1*) are important. The interstellar magnetic field carried with the interstellar plasma exerts forces on the plasma that change the nature of its interaction with the heliosphere. In particular, if the magnetic field is not oriented parallel or perpendicular to the direction of the interstellar plasma flow past the heliosphere, it can produce a lateral asymmetry in the heliospheric shape (see the figure).

Using observations of solar radiation

The author is in the Department of Planetary Sciences, University of Arizona, Tucson, AZ 85721, USA. E-mail: jokipii@lpl.arizona.edu

back-scattered from interstellar hydrogen atoms, Lallement *et al.* (*1*) have detected a small (about 4°) difference between the flow directions of neutral hydrogen and helium in the region where the interstellar medium and the heliosphere interact. Well away from the heliosphere, the helium and hydrogen in the interstellar medium should move in the same direction at the same speed. But nearer to the heliosphere, the two gases are expected to behave differently. Helium is not affected much by the interaction with the outer parts of the heliosphere, whereas hydrogen is slowed and can also be deflected sideways by any lateral asymmetry in the shape of the heliosphere, such as that produced by the interstellar magnetic field.

Lallement *et al*. point out that the most plausible cause of the observed deflection is a lateral asymmetry caused by the interstellar magnetic field. The physical picture is complex, but based on their observations and results from numerical simulations, the authors present a convincing picture. They determine the angular direction (but not the sense) of the projection of the magnetic field on the sky. The fact that the magnetic field is sufficiently strong to change the shape of the heliosphere also places constraints on its magnitude, although the authors do not discuss this point.

Radio emissions observed by the Voyagers over the past 12 years have recently been interpreted as constraining the direction of the local magnetic field (*11*). This approach yields a different direction from that found in (*1*), but it is less direct.

The observations reported by Lallement *et al.* (*1*) substantially improve our understanding of both the nature of the interaction of the Sun with its local interstellar environment and the structure of the local interstellar medium. Future in situ measurements of the magnetic field, perhaps from Voyager 1, may allow its magnitude and the full three-dimensional vector to be determined.

References

1. R. Lallement *et al.*, *Science* **307**, 1447 (2005).
2. P. Frisch, *Space Sci. Rev.* **72**, 499 (1995).
3. S. M. Krimigis *et al.*, *Nature* **426**, 45 (2003).
4. F. B. McDonald *et al.*, *Nature* **426**, 48 (2003).
5. L. F. Burlaga *et al.*, *Geophys. Res. Lett.* **30**, 2072 (2003).
6. D. Gurnett *et al.*, *Geophys. Res. Lett.* **30,** 2209 (2003).
7. F. B. McDonald, in *Physics of the Outer Heliosphere*, V. Florinski, N. V. Pogorolov, G. P. Zank, Eds. (American Institute of Physics, Melville, NY, 2004), pp. 139–149.
8. J. R. Jokipii, J. Giacalone, *Astrophys. J.* **605**, L145 (2004).
9. L. A. Fisk, in *Physics of the Outer Heliosphere*, V. Florinski, N. V. Pogorolov, G. P. Zank, Eds. (American Institute of Physics, Melville, NY, 2004), pp. 365–372.
10. J. R. Jokipii, J. Giacalone, J. Kota, *Astrophys. J.* **611**, L141 (2004).
11. W. S. Kurth, D. A. Gurnett, *J. Geophys. Res.* **108**, 10.1029/2003JA009860 (2003).
12. R. Ratkiewicz, J. Grygorczuk, L. Ben-Jaffel, in *Physics of the Outer Heliosphere*, V. Florinski, N. V. Pogorolov, G. P. Zank, Eds. (American Institute of Physics, Melville, NY, 2004), pp. 93–98.

10.1126/science.1109701

STRUCTURAL BIOLOGY

Membrane Protein Insertion and Stability

Roderick MacKinnon

Whether a protein is targeted for insertion into a cell membrane or for transport across the cell membrane, it is directed to the same molecular structure in the endoplasmic reticulum known as the translocon. The translocon is a membrane protein with the dual capacity to insert or secrete a newly synthesized polypeptide chain. How does the translocon decide which task to perform? The instructions must reside within the amino acid composition of the substrate protein, but exactly what is this information and how does the translocon read it? Given that transmembrane helices are mostly composed of hydrophobic amino acids (such as isoleucine, leucine, phenylalanine, and valine), the degree of hydrophobicity clearly is important. However, given the structural complexity of biological membranes, the information "code" might be more complicated than the degree of hydrophobicity alone.

New studies by Hessa, von Heijne, White and their colleagues in a recent issue of *Nature* (*1*) and on page 1427 of this issue (*2*) reach an astonishingly simple explanation for how the decision is made by the translocon to insert or secrete its substrate protein. The new findings place constraints on physical models for how the translocon might work, but more importantly, they allow the prediction of energetic stability in transmembrane helices. The predictions are not always intuitive and suggest altogether new possibilities for membrane protein structure and mechanism of action.

The authors begin by asking a simple question: How does the translocon respond when it is challenged with a polypeptide whose hydrophobicity is intermediate between that of a protein that is normally inserted and one that is normally secreted? Their assay makes use of a carrier membrane protein that they have modified by inserting a test polypeptide segment into a carboxyl-terminal region that is normally exposed to the extracellular milieu. This test segment is flanked on both sides by glycosylation acceptor sites, which permit detection of its position within the cell membrane. If the segment is secreted (that is, delivered to the luminal space of the endoplasmic reticulum in pancreatic microsomes), then both glycosylation acceptor sites become glycosylated. However, if it is inserted into the membrane, then only a single site becomes glycosylated.

So, what is the destiny of a 19–amino acid test segment with an intermediate degree of hydrophobicity? The answer is that the test segment partitions between two possible outcomes—a fraction of it is secreted and a fraction is inserted into the membrane. The fraction that is inserted increases as hydrophobicity increases, for example, when alanine amino acid residues are systematically replaced with leucine. Quantification of this effect leads to a fundamental observation: The probability of insertion is related to the number of leucine residues (that is, to the degree of hydrophobicity) according to a Boltzmann distribution. This distribution implies that partitioning between inserted versus secreted states is determined by the energy difference between possible outcomes in an equilibrium process. The energy difference is given by the sum of individual contributions from each amino acid in the test segment.

How much energy does it cost to insert a leucine, an arginine, or any other amino acid into a cell membrane? This question is answered by changing the central amino acid in the test segment and measuring its effect on the ratio of inserted to secreted fractions. To make accurate measurements, the authors counterbalance highly polar and charged amino acids that are energetically unfavorable inside the membrane by increasing hydrophobicity at other positions within the test segment. This forces the energetically unfavorable amino acids to enter the membrane (see the figure). From these measurements, the investigators construct a quantitative amino acid energy scale for the propensity of translocon-mediated membrane insertion. The authors call it the "biological" hydrophobicity scale, and remarkably, it correlates very well with the Wimley-White scale, which is based on equilibrium free energies determined from the partitioning of peptides between water and octanol (*3*). The close correlation between the true equilibrium chemical scale of Wimley-White and the new biological scale further reinforces the idea that translocon-mediated membrane insertion reflects an equilibrium process. It

The author is at the Howard Hughes Medical Institute, Rockefeller University, New York, NY 11021, USA. E-mail: mackinn@rockefeller.edu

also nicely illustrates how an apparently complex cellular process can be reduced to the simple rules of chemical thermodynamics.

The hydrophobic core of a cell membrane is sandwiched between the polar head group layers of its constituent phospholipids (see the figure). Given this structural complexity, one might expect that the energetic contribution of an amino acid would depend on its position along the test segment—and it does, at least for some amino acids. A larger energetic penalty is incurred when polar and charged amino acids are placed near the center of the membrane. This makes perfect sense, because close to the polar head group layers electrostatic forces help to stabilize the positive charge of arginine or lysine side chains. And if there is a gradient of water molecules tending to penetrate the membrane surface, then polar side chains closer to the edge will gain an energetic advantage through partial hydration by even one or two water molecules. Tryptophan and tyrosine are especially interesting because they are energetically unfavorable at the membrane center, but energetically favorable near the head group layers. In other words, there are energy wells near the edge of the membrane for these particular amino acids. This finding offers a simple explanation for why tryptophan and tyrosine are usually found near the membrane-water interface of membrane proteins (*4*). In their energy wells, these amino acids confer stability to a protein's transmembrane helix.

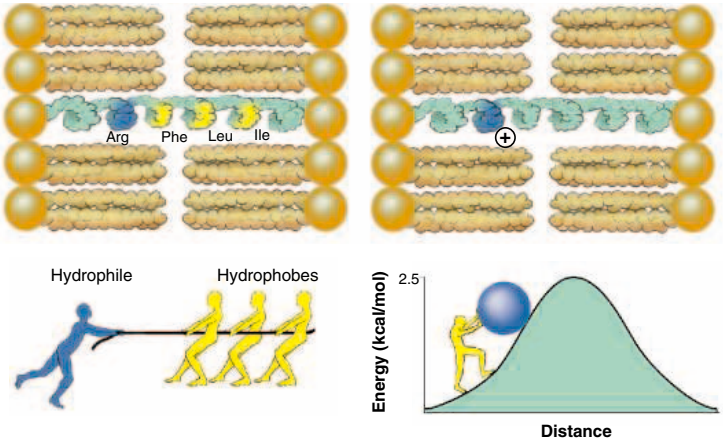

Two important aspects of transmembrane-helix stability. (Left) Hydrophobic amino acids of membrane proteins are favored inside the lipid membrane interior, whereas hydrophilic amino acids are favored in the aqueous exterior. Whether a transmembrane α helix is stable inside the membrane depends on a net energy balance. Hydrophilic and even charged amino acids become inserted into the membrane if they are forced to do so by a sufficient number of hydrophobic amino acids. This idea of energetic counterbalance is illustrated by a tug-of-war between hydrophobic amino acids (phenylalanine, leucine, and isoleucine) and a hydrophilic amino acid (arginine). **(Right)** The energy cost for transferring a positively charged amino acid such as arginine from water to the membrane depends on its depth in the membrane. The "energy hill" is sharply peaked and is mostly concentrated within a distance of ~8 Å on either side of the middle of a 30 Å–wide hydrophobic core.

Let's return to the question of how the translocon knows what to do with the polypeptide segment that sits inside of it. The authors offer a simple explanation based on the apparent equilibrium behavior of the system. If the translocon allows the peptide segment to sample the lipid environment while it is being transported across the membrane, then the peptide is presented with a choice: It can either dissociate from the translocon and insert itself into the membrane or it can remain adherent to the translocon and continue across the membrane. The final outcome is dictated by the amino acid composition and sequence of the peptide. The basic idea—that the peptide segment samples its environment and is essentially at equilibrium with the membrane and the translocon channel—is elegant in its simplicity. The idea also seems compatible with the crystal structure of a prokaryotic homolog of the endoplasmic reticulum translocon, which is closed, but is proposed to open from the side into the membrane (*5*).

What do these results tell us about transmembrane helix stability and membrane protein structures? They suggest that far more powerful membrane helix prediction algorithms can be developed, because the biological hydrophobicity scale, together with position-dependent energy terms for each amino acid, provides a rich data set with which to analyze protein sequences. Such predictions might seem to be of limited use because most helical membrane proteins simply contain the most hydrophobic amino acids (isoleucine, leucine, phenylalanine, and valine) in the center of their membrane-spanning helices, with tyrosine and tryptophan near the water interface (*4*). The biological hydrophobicity scale predicts that these amino acids will give rise to the most stable membrane-spanning helices. But the scale also predicts that less stable helices are thermodynamically possible. Recall, for example, that the authors used the principle of energetic counterbalance to force polar and charged amino acids into the hydrophobic center of the membrane. Is it possible that nature could have done the same thing to endow proteins with specific functions? From extensive studies of soluble proteins, we know that function is very often achieved at the expense of structural stability. Shouldn't the same sort of balancing act between the requirements of protein stability and function apply to membrane proteins?

In this issue, Hessa *et al.* (*2*) demonstrate such a balancing act with their study of the voltage sensor of the KvAP voltage-dependent K^+ channel of an archaebacterium (*6*, *7*). KvAP and other voltage-dependent ion channels contain a transmembrane "S4" helix with positively charged arginine residues. S4 moves its charges relative to the membrane electric field when the channel opens, conferring voltage dependence. Because of its positive charges, S4 was considered too unstable near the low-dielectric lipid membrane, and so it was thought to be located in an aqueous environment surrounded by protein (*8*). But structural and functional studies of KvAP suggest that S4 is located at the protein-lipid interface (*6*, *7*). Is such a location thermodynamically possible? The membrane-insertion assay shows that S4 is inserted as a transmembrane helix with ~50% probability. As the authors point out, this is an ideal situation for a voltage-dependent switch that changes its position in response to voltage changes. What is most impressive is that the authors decompose S4 into individual amino acid energy terms and demonstrate that the probability of insertion is essentially predictable. The key to prediction is to understand energetic counterbalance (hydrophobic amino acids work against polar amino acids through additivity of energy terms) as well as positional dependence (the energy penalty for arginine peaks sharply near the center of a transmembrane helix).

Analysis of the protein structure database has led us to expect that helical membrane proteins should always have maximally stable transmembrane helices. The new studies (*1*, *2*) show that this does not have to be the case. If specific functions are required, less stable transmembrane helices are possible. It is intriguing to ponder what nature might have in store for us in our quest to understand the structures and mechanisms of membrane proteins. Oddities like voltage-dependent ion channels might be just the tip of the iceberg.

References

1. T. Hessa *et al.*, *Nature* **433**, 377 (2005).
2. T. Hessa, S. H. White, G. von Heijne, *Science* **307**, 1427 (2005); published online 27 January 2005 (10.1126/science.1109176).
3. W. C. Wimley, T. P. Creamer, S. H. White, *Biochemistry* **35**, 5109 (1996).
4. M. B. Ulmschneider, M. S. Sansom, *Biochim. Biophys. Acta* **1512**, 1 (2001).
5. B. Van den Berg *et al.*, *Nature* **427**, 36 (2004).
6. Y. Jiang *et al.*, *Nature* **423**, 33 (2003).
7. Y. Jiang, V. Ruta, J. Chen, A. Lee, R. MacKinnon, *Nature* **423**, 42 (2003).
8. F. Bezanilla, *Physiol. Rev.* **80**, 555 (2000).

10.1126/science.1110525

CREDIT: TAINA LITWAK

Membrane Insertion of a Potassium-Channel Voltage Sensor

Tara Hessa,[1] Stephen H. White,[2] Gunnar von Heijne[1]*

The structure of the KvAP voltage-dependent K^+ channel shows two distinct features: the voltage-sensor domains and the central pore domain (*1*). The critical element in the sensor domains in virtually all voltage-gated ion channels is the S4 helix, which contains four or more regularly spaced Arg residues interspersed with hydrophobic residues. Voltage activation has been suggested to involve paddles, each composed of a mildly hydrophobic S3 helix packed against a highly charged S4 helix, that move through the lipid bilayer in response to membrane depolarization (*2*). This controversial mechanism of gating is at odds with models that envisage the S4 segment as isolated from the lipid bilayer in canaliculi within the channel protein. At the heart of the controversy is the idea that the paddle model is implausible, because of the energetic cost of burying charges in a lipid bilayer (*3*).

We investigated the membrane insertion of the KvAP S4 helix using an experimental system (*4*, *5*) that permits accurate measurements of the apparent free energy (ΔG_{app}) of translocon-mediated integration of transmembrane (TM) helices into the endoplasmic reticulum (ER) membrane (Fig. 1A). Using this system, we previously derived a base biological hydrophobicity scale and demonstrated that the contribution to ΔG_{app} can depend strongly on a residue's position within the helix (*4*).

The isolated S4 helix inserts to a measurable extent as a TM helix (ΔG_{app} = 0.5 kcal/mol) (Fig. 1B). An S4-related segment with two of the Arg residues moved one step toward the C terminus (S4mut) inserts even better (ΔG_{app} = 0.0 kcal/mol). Membrane integration in this system likely reflects a peptide's ability to partition across a lipid bilayer (*4*); thus, we conclude that the S4 helix is poised near the threshold of efficient bilayer insertion, which makes sense for a voltage-dependent switch. Earlier studies have shown that the S4 helix can associate to some extent with the ER membrane as assayed by resistance to alkaline extraction (*6*).

To resolve how a segment containing four Arg residues can show this kind of behavior, we scanned single Arg and Gly residues across a hydrophobic, 19-residue-long segment and measured ΔG_{app} for each construct. The contribution of the Arg residue to ΔG_{app} depended strongly on its position within the segment (Fig. 1C). Using the base biological hydrophobicity scale (*4*) without taking the positional variation for the Arg and Gly contributions into account yields an estimated ΔG^{calc}_{app} of 3.9 kcal/mol for the S4 segment (*5*). However, including the position-dependent corrections derived from Fig. 1C reduces ΔG^{calc}_{app} to 0.9 kcal/mol (0.4 kcal/mol for S4mut), close to the experimental value. If one or two of the Arg residues in S4 are partially shielded from direct lipid contact in the intact K^+ channel structure, as has been proposed (*7*), ΔG_{app} might be further reduced.

Our results suggest that the paddle model is not inconsistent with the high Arg content of S4. They also highlight the importance of residue position within TM helices as a determinant of insertion efficiency, an aspect that current TM helix prediction schemes do not address adequately. The physical basis for the TM stability of S4 is not entirely clear, but molecular dynamics simulations suggest that the membrane-buried Arg may be accompanied by a few water molecules (*8*).

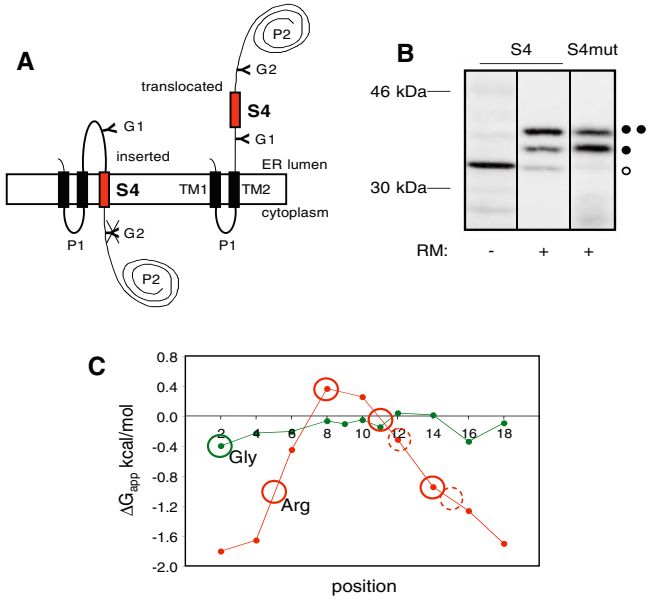

Fig. 1. (**A**) Our test protein (*Escherichia coli* Lep) has two N-terminal TM segments (TM1 and TM2), a cytoplasmic loop (P1), and a large luminal domain (P2). The KvAP S4 segment was inserted into the P2 domain, where it is flanked by two glycosylation acceptor sites (G1 and G2). If S4 integrates across the membrane, only G1 will be glycosylated (left); otherwise both G1 and G2 will be glycosylated (right). The apparent free energy of insertion of S4 is defined as $\Delta G_{app} = -RT \ln(f_{1g}/f_{2g})$, where R is the gas constant, T is the absolute temperature, and f_{1g} and f_{2g} are the fractions of singly and doubly glycosylated molecules, respectively. (**B**) Membrane integration of S4 and S4mut. Plasmids encoding the constructs were transcribed and translated in vitro in the absence (–) and presence (+) of dog pancreas rough microsomes (RM) (*5*). White dot, unglycosylated protein; one black dot, single glycosylation; two black dots, double glycosylation. (**C**) Scans with a single Arg (red) or Gly (green) in the test segments 1R/6L/12A and 1G/4L/14A (*5*). The positions of Arg and Gly are indicated on the *x* axis. Circles indicate the positions in S4; the repositioned Arg residues in S4mut are dashed.

References and Notes

1. Y. Jiang *et al.*, *Nature* **423**, 33 (2003).
2. Y. Jiang, V. Ruta, J. Chen, A. Lee, R. MacKinnon, *Nature* **423**, 42 (2003).
3. M. Grabe, H. Lecar, Y. N. Jan, L. Y. Jan, *Proc. Natl. Acad. Sci. U.S.A.* **101**, 17640 (2004).
4. T. Hessa *et al.*, *Nature* **433**, 377 (2005).
5. Materials and methods are available as supporting material on *Science* Online.
6. L. Tu, J. Wang, A. Helm, W. R. Skach, C. Deutsch, *Biochemistry* **39**, 824 (2000).
7. R. MacKinnon, *Science* **306**, 1304 (2004).
8. J. A. Freites, S. H. White, unpublished data.

9. We thank E. Missioux. Supported by the Swedish Cancer Foundation, the Marianne and Marcus Wallenberg Foundation, the Swedish Research Council (G.v.H.), and the National Institute of General Medical Sciences (grant nos. GM46823 and GM68002, S.H.W.).

Supporting Online Material
www.sciencemag.org/cgi/content/full/307/5714/1427/DC1
Materials and Methods

27 December 2004; accepted 19 January 2005
Published online 27 January 2005;
10.1126/science.1109176
Include this information when citing this paper.

[1]Department of Biochemistry and Biophysics, Stockholm University, SE-106 91 Stockholm, Sweden. [2]Department of Physiology and Biophysics and the Program in Macromolecular Structure, University of California at Irvine, Irvine, CA 92697–4560, USA.

*To whom correspondence should be addressed. E-mail: gunnar@dbb.su.se

A Serpentinite-Hosted Ecosystem: The Lost City Hydrothermal Field

Deborah S. Kelley,[1]* Jeffrey A. Karson,[2] Gretchen L. Früh-Green,[3] Dana R. Yoerger,[4] Timothy M. Shank,[4] David A. Butterfield,[5] John M. Hayes,[4] Matthew O. Schrenk,[1] Eric J. Olson,[1] Giora Proskurowski,[1] Mike Jakuba,[6] Al Bradley,[4] Ben Larson,[1] Kristin Ludwig,[1] Deborah Glickson,[1] Kate Buckman,[4] Alexander S. Bradley,[7] William J. Brazelton,[1] Kevin Roe,[5] Mitch J. Elend,[1] Adélie Delacour,[3] Stefano M. Bernasconi,[3] Marvin D. Lilley,[1] John A. Baross,[1] Roger E. Summons,[7] Sean P. Sylva[4]

The serpentinite-hosted Lost City hydrothermal field is a remarkable submarine ecosystem in which geological, chemical, and biological processes are intimately interlinked. Reactions between seawater and upper mantle peridotite produce methane- and hydrogen-rich fluids, with temperatures ranging from <40° to 90°C at pH 9 to 11, and carbonate chimneys 30 to 60 meters tall. A low diversity of microorganisms related to methane-cycling Archaea thrive in the warm porous interiors of the edifices. Macrofaunal communities show a degree of species diversity at least as high as that of black smoker vent sites along the Mid-Atlantic Ridge, but they lack the high biomasses of chemosynthetic organisms that are typical of volcanically driven systems.

In 1979, the world was astounded by the discovery of hydrothermal chimneys and black smoker vents driven by the cooling of magma beneath mid-ocean ridges and hosting oases rich in chemosynthetically based biological communities (*1*). Since that pivotal find, more than 200 vent fields have been documented in the ocean basins (*2*). The associated metal deposits and diverse biota of clams, tubeworms, and swarming shrimp have become the familiar hallmarks of submarine hydrothermal vent systems. Many of these high-temperature systems are restricted to the axis of the global mid-ocean ridge spreading network, where more than 85% of Earth's magmatic output is localized (*3*). This localization has led researchers to focus on an extremely narrow corridor (<1 to 5 km wide) along the axis of the ridge.

In 2000, a hydrothermal field called Lost City was serendipitously discovered more than 15 km away from the spreading axis of the Mid-Atlantic Ridge (MAR) at a water depth of 750 to 900 m (Fig. 1). Initial studies based on a single dive by the deep submergence vehicle *Alvin* showed that it was unlike any hydrothermal system found to date, hosting diffusely venting carbonate monoliths towering tens of meters above the seafloor (*4*). The composition of its fluids derives from reactions between seawater and uplifted mantle peridotite rather than from interactions between seawater and cooling basalts (*4*). Subsurface, exothermic, mineral-fluid reactions associated with the oxidation of iron in cooling mantle peridotite produce alkaline fluids rich in hydrogen and methane at venting temperatures up to 90°C (*4*, *5*). These high-pH volatile-rich fluids trigger carbonate precipitation upon mixing with seawater and serve as important energy sources for microorganisms that thrive in the porous chimney walls.

These peridotite-hosted biotopes differ substantially from axial, magmatically driven vent systems in which carbon dioxide and hydrogen sulfide are the dominant volatile species (*5*, *6*). Exposed serpentinized peridotites are widespread (*7*–*10*), and reactions similar to those producing the Lost City hydrothermal field (LCHF) are probably common in these areas, implying that there may be extensive unexplored regions of the ocean basins harboring life forms that are not solely supported by magmatically driven hydrothermal flow. In addition, peridotite-hosted systems can be long-lived: ^{14}C dating shows that hydrothermal activity at Lost City has been ongoing for at least 30,000 years (*11*). Modeling of this system suggests that hydrothermal activity sustained by serpen-

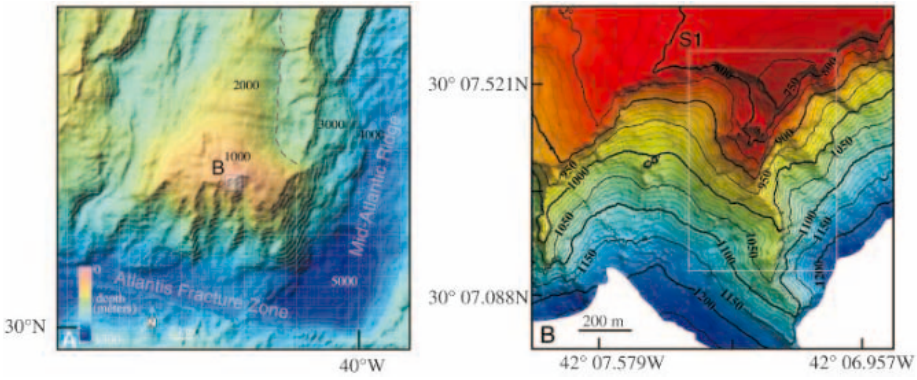

Fig. 1. (**A**) The Atlantis massif is located ~15 km to the west of the MAR axial valley. The intersection of the Atlantis Fracture Zone and the MAR is marked by a ~6000-m-deep nodal basin. Within a horizontal distance of ~20 km, the seafloor rises to within 700 m of the surface. On the basis of magnetic data, the massif has been uplifted at rates comparable to those of the Himalayan mountains (*15*). Well-developed corrugations on the surface of the massif are believed to be traces of a long-lived detachment fault that dips gently beneath the axis of the MAR (*15*). The flat elongate bench on the eastern side of the massif is interpreted as the hanging wall of the fault and is composed of volcanic material. Lost City is located within the small box near the central summit of the massif. (**B**) Shaded bathymetric map based on *ABE* data for the LCHF and adjacent terrain. Most of the small mound-shaped structures are individual chimneys or clusters of carbonate chimneys that delineate an east-west trend that marks a major lineament. A zone of continuous carbonate composed of multiple edifices forms the core of the field. It extends nearly 200 m in length and several tens of meters down the cliff face to the south. Hydrothermal fluids are weeping actively from many of these steep cliffs. S1, fig. S1.

[1]School of Oceanography, University of Washington, Seattle, WA 98195, USA. [2]Division of Earth and Ocean Sciences, Duke University, Durham, NC 27708, USA. [3]Department of Earth Sciences, ETH-Zentrum, Zurich, Switzerland. [4]Woods Hole Oceanographic Institution (WHOI), Woods Hole, MA 02543, USA. [5]Joint Institute for the Study of the Atmosphere and Ocean, University of Washington, and National Oceanic and Atmospheric Administration Pacific Marine Environmental Laboratory, Seattle WA 98115, USA. [6]MIT/WHOI Joint Program, WHOI, Woods Hole MA 02543, USA. [7]Department of Earth, Atmospheric, and Planetary Sciences, Massachusetts Institute of Technology, Cambridge MA 02139, USA.

*To whom correspondence should be addressed. E-mail: kelley@ocean.washington.edu

tinization reactions may last for hundreds of thousands of years (*11*, *12*). Alkaline systems such as the LCHF may have been characteristic of early Earth hydrothermal environments, where the eruption of Mg-rich komatiitic lavas was common (*13*).

In 2003, a second expedition returned to the LCHF to study the linkages between hydrothermal alteration of mantle peridotite, fluid geochemistry, and biological activity. The field program included 19 dives with the submersible *Alvin* and an unconventional mapping effort with the *Autonomous Benthic Explorer* (*ABE*) in this area of extreme topography (*14*). Ten discrete active vent sites were sampled for the first time for co-registered fluids, rocks, and biota (Figs. 1 and 2 and fig. S1). Here we present an integrated summary of our field studies and laboratory findings. Our results provide a comprehensive overview of the geological and structural controls on fluid flow at Lost City and elucidate the consequences of fluid/rock interaction in the basement for fluid chemistry and chimney growth and for the life that can be supported in these environments.

Geologic setting. The *Alvin* and *ABE* surveys delineate the southern scarp of the massif and the major fault lineaments that intersect it (Figs. 1B and 2 and fig. S1). Variably foliated serpentinite, talc-amphibole schist, and metagabbroic rocks make up the nearly continuous cliffs at the top of the scarps to the northwest and northeast of the LCHF. Near the summit of the massif, we identified a ~50-m-thick mylonitic-to-cataclastic shear zone that includes lenses of less deformed material (Fig. 3 and fig. S1). This shear zone is probably the long-lived detachment fault that exposed the mantle and lower crustal rock sequences that make up the massif (*15*). This zone grades downward into massive jointed rocks that lack a strong deformation fabric. The basement rocks in the vicinity of the field are cut by veins of calcite and aragonite, which derive from some of the oldest hydrothermal activity at this site (*11*).

The summit of the massif is capped by 1 to 3 m of flat-lying sedimentary breccias overlain by variably lithified, fossiliferous pelagic limestone with sparse bedrock clasts. The breccias probably represent debris slide deposits shed onto the sloping detachment fault surface when it defined the median valley wall. As that surface moved off axis and flattened into its present subhorizontal orientation, the sedimentary regime changed from clastic to pelagic. Exiting high-pH hydrothermal fluids generated by serpentinization probably enhanced carbonate precipitation and cementation of these sediments (*16*). The resulting cap rock was important in the formation of the LCHF, acting as an impervious lid trapping both fluids and heat.

The LCHF. The LCHF lies atop the sedimentary cap rock, on a triangular down-dropped block that forms a terrace on the edge of the south wall (Figs. 1B and 3). Our mapping indicates that the largest and most active vents are along an east-west trending lineament more than 300 m long (Fig. 1B and fig. S1). The lineament is intersected by a fault trending approximately north-south, which exposes massive jointed outcrops of relatively undeformed serpentinized harzburgites that form the major north-south ridge just south of the field. Toward the top of the scarp, these rocks are strongly foliated and are overlain by the sedimentary cap rocks. This distinctive surface is seen in the higher scarps to the northeast and northwest. The difference in depth between equivalent outcrops indicates that there has been at least 150 m of vertical displacement on a fault that trends west-northwest. This fault and faults with similar trends are essentially parallel to the nearby Atlantis Transform fault. Transform-parallel faults with extensive vertical offsets are typical of many other oceanic massifs (*7*, *17*).

The fracture and fault network in the basement provides permeable pathways that control outflow at the main vent sites. In addition to the subvertical faults that channel flow to the largest structures, much of the subsurface flow emanates from surfaces that are parallel to basement foliation and subparallel to gently west-dipping faults (Fig. 3). The steep faults expose relatively old inactive stockworks

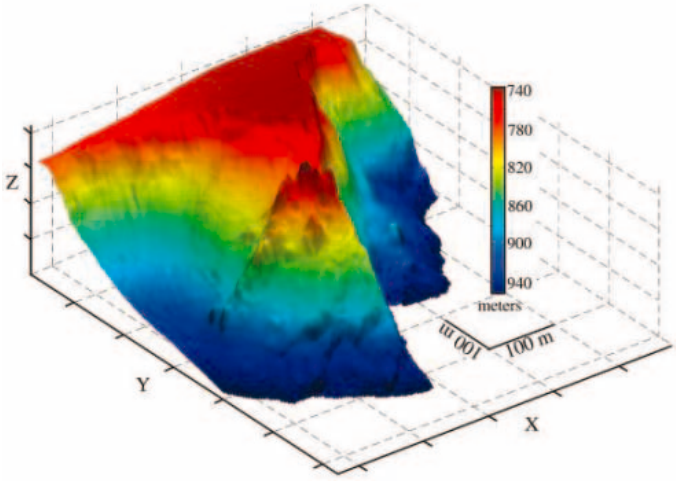

Fig. 2. Three-dimensional view, looking toward the northeast, of the LCHF. This image is based on 17 *ABE* missions using the SM2000 sonar system in a down-looking and side-looking mode. The LCHF is in the foreground; at depths less than ~900 m, the area is characterized by nearly continuous carbonate chimneys, spires, and debris. The massive pinnacles at the summit of this platform are the composite, actively venting edifices that make up the massive 60-m-tall structure called Poseidon. The area is characterized by extreme topographic relief, with vertical-to-subvertical cliffs and overhanging ledges in the serpentinite bedrock. The smooth surface in the background is the summit of the Atlantis massif.

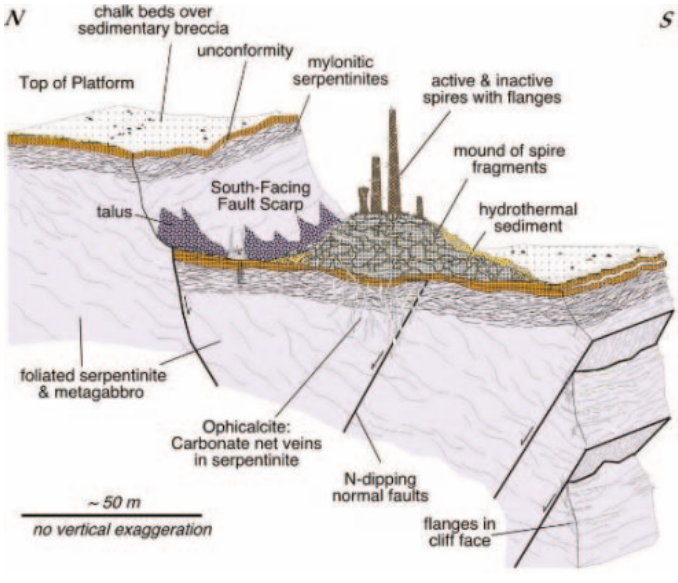

Fig. 3. Diagrammatic sketch showing geologic and tectonic relationships at Lost City. Hydrothermal structures are located on a faulted down-dropped block of variably altered and deformed crust composed predominantly of serpentinite. It is likely that hydrothermal flow is focused by intersecting fractures associated with transform fault development and uplift of the massif. In addition, an up to 40% increase in rock volume resulting from serpentinization may enhance fracturing, significant mass wasting (in a manner analogous to subaerial frost action), and hydrothermal flow. The networks of carbonate veins and carbonate cemented breccias associated with this field are very similar to ophicalcite deposits found in Alpine ophiolites and in other more ancient ophiolites.

of carbonate veins and subhorizontal-to-subvertical open fractures in the basement rock. These are actively leaking hydrothermal fluid and feeding young white hydrothermal precipitates (Fig. 4).

The white hydrothermal deposits range from arrays of delicate fingerlike crystals to beehivelike masses that are a few tens of centimeters across, growing directly out of cracks (Fig. 4E). Individual conduits are sealed by growths of calcium carbonate. Overgrowths and swaths of younger carbonate cutting across older material suggest reactivation and multiple stages of fracturing. Control of the hydrothermal outflow by fractures is particularly obvious where walls of massive shingled carbonate have been deposited on the steep scarps, highlighting the fact that much of the LCHF plumbing system is in marked contrast to the vertical conduits that typify black smoker environments and continental sulfide deposits.

The core of the field is dominated by the actively venting carbonate monolith called Poseidon (fig. S1), an edifice that rises >60 m above the seafloor (~800 m of water depth). This composite structure is composed of four large columns that are several meters in diameter (Figs. 2 and 4B). These pinnacles coalesce at their base to form a massive east-west trending structure extending at least 50 m. Parasitic chimneys, resembling inverted stalactites, are particularly abundant on the northwest face, as are actively venting flanges, or ledges that protrude several meters from the main trunk (Fig. 4C).

The most visually striking region is just northeast of Poseidon, in an area about 70 m in length at a water depth of 800 to 900 m (markers 7 and H, fig. S1). In this area, the vertical serpentinite cliffs are draped with deposits that have astoundingly diverse morphologies. Fluids weeping from the scarp face have produced clusters of delicate multipronged carbonate growths that extend outward like the fingers of upturned hands. Multipinnacled chimneys, some reaching 10 m in height, grow vertically out of the cliff faces (Fig. 4A), and single chimneys that sprout from more gently dipping bedrock reach 30 m in height (Fig. 4D and movie S1). These structures form a nearly continuous carbonate deposit that can be traced for over 200 m in length along the 850- to 900-m contour (fig. S1).

The northern portion of the field is bounded by a shallow depression (Fig. 1B) that is closed to the east and gradually deepens to the west. Nicknamed ''Chaff Beach'' (fig. S1), this gently sloping area is covered by variably cemented foraminifera, pteropod shells, coral debris, urchin spines, and hydrothermally derived carbonate crust. Concentrations of CH_4 in the water column here are 30 times (55 nM) those in background ocean water at depths ~50 m above the seafloor [supporting online material (SOM) text and fig. S1]. Hydrogen concentrations are over 100 times (349 nM) those of background seawater values. This ground fog of volatile-enriched fluids may represent the leaking of diffuse alkaline fluids through the underlying serpentinites, leading to rapid lithification of the pelagic sediments. Hydrocasts conducted ~75 to 100 m east of the main field also detected volatile enrichment up to 150 m above the seafloor; the highest concentrations of CH_4 were measured here, reaching values of 180 nM.

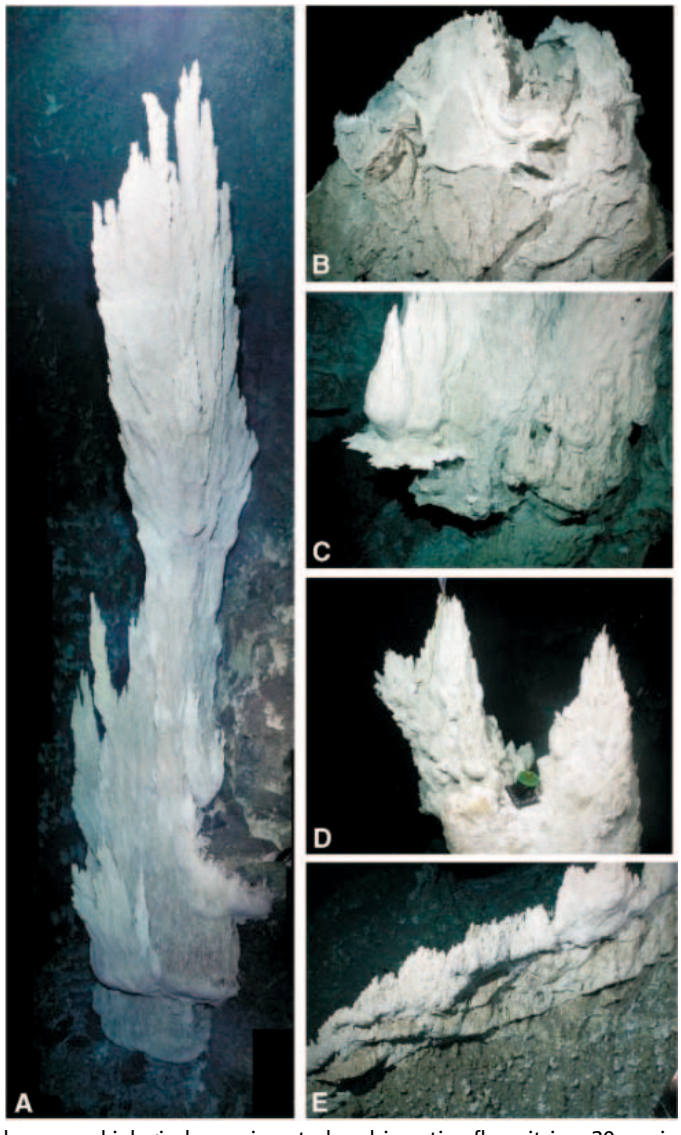

Fig. 4. Hydrothermal deposits at Lost City. (**A**) Graceful, 10-m-tall, actively venting carbonate chimney growing directly out of a serpentinite cliff on the eastern side of the field. The small carbonate deposits in the background mark sites of active and inactive seeps along the steep walls. (**B**) One of four actively venting peaks that make up the massive hydrothermal structure called Poseidon. Young and/or actively venting material is white in color; inactive areas are brown to cream-colored. This pinnacle is ~4 m across. (**C**) The base of the "IMAX" flange, which is a three-story-tall spirelike growth on the side of Poseidon. This area is actively venting 55°C fluids that support dense microbial communities. (**D**) Actively venting 50°C pinnacle on the east side of the field, showing young feathery growths of carbonate. This edifice is growing in a large vertical crevice within the wall. Actively venting carbonate flanges, which are several meters across, form overhanging ledges above and to the sides of the chimney. The green-capped black cylinder at the notch between the two pinnacles was a biological experiment placed in active flow; it is ~20 cm in diameter. (**E**) Feathery carbonate growth rising from a vein within the serpentinite bedrock. Many of these veins are several centimeters across. Near the summit of the massif they form dense cross-cutting networks that mark fossilized stockwork systems, which fed past sites of venting.

Carbonate fluid chemistry. Geochemical and petrologic analyses of the carbonate rocks reveal distinct differences between the active and extinct structures. Actively venting chimneys and flanges are highly porous, friable formations composed predominantly of aragonite and brucite (Fig. 5). Brucite commonly encloses dendritic feathery growths of aragonite, showing that it is a later phase probably formed through mixing of magnesium-rich seawater and hydrothermal fluid. Distinct annular orifices, which are common in black smoker systems, are rare at Lost City. Instead, fluids emerge from complex networks of centimeter-sized channels. Petrographic analyses of the carbonate chimneys show fine anastomosing networks of carbonate lined with brucite, indicating mixing of seawater and hydrothermal fluids within the interior walls.

In contrast to the active structures, extinct chimneys are less porous, well lithified, and have a higher abundance of calcite. Prolonged lower-temperature interactions with seawater

and hydrothermal fluids within the chimneys result in the conversion of aragonite to calcite, the enrichment of some trace metals (such as Mn, Sr, and Ti), and the dissolution of brucite (SOM text). They also promote the incorporation of foraminifera within the outer cemented walls of the carbonate structures. Mineralogical transformations are reflected in the bulk rock chemistry of the structures. The most active structures contain up to 27 weight % (wt %) Mg and down to 5 wt % Ca, whereas the extinct structures contain as little as <1 wt % Mg and up to 36 wt % Ca. Changes in strontium isotopic compositions accompany these transformations, with the youngest active samples yielding mantle-influenced $^{87}Sr/^{86}Sr$ values of 0.7076 to 0.7079. Inactive samples yield ratios of up to 0.7090, which is near that of seawater (*11*).

Analyses of stable isotopes in >50 vent and fissure-filling carbonates sampled in 2000 and 2003 yielded highly variable carbon and oxygen isotope compositions (SOM text). Although >70% of the samples have $\delta^{13}C$ values close to marine values within 2 per mil (‰) of 0 versus Vienna Pee Dee belemnite (VPDB) values, the range extends from –7 to +13‰. The oxygen isotope compositions vary from –7 to +5‰ (VPDB). A large number of samples have $\delta^{18}O$ values >2‰ and probably reflect enrichment in ^{18}O during fluid/rock interaction, either within the vent structures or in the basement. Discrete carbonate veins and bulk carbonate in the basement have $\delta^{13}C$ values of –6 to +3.5‰ and $\delta^{18}O$ values down to –19‰. Large differences occur within single samples and at different locations, but the greatest variations are in vent samples with abundant brucite. This variability suggests that fluid compositions, temperatures, and microbial activity fluctuate geographically as well as through time.

The LCHF provides a rare example of seawater interacting directly with peridotite exposed on the seafloor. The chemistry of the fluids (and vent structures) is controlled by relatively low-temperature (<~150°C) reactions between seawater and peridotite beneath the Atlantis massif. The hottest samples collected from Poseidon (91°C) have Mg concentrations of <1 mmol/kg, verifying that a zero-Mg end member is produced in the serpentinization reaction zone (SOM text). Oxygen isotopic compositions of vent waters ($0.2 \leq \delta^{18}O \leq 0.7$‰ Vienna standard mean ocean water) increase linearly with temperature and depletion of Mg. Concentrations of sulfate in the hydrothermal end members are 1 to 4 mmol/kg. Significantly lower values would be expected if anhydrite were being precipitated. Accordingly, fluid temperatures within the massif under Lost City currently must be less than 150°C. The measured venting temperatures overlap with temperatures calculated from $\delta^{18}O$ analyses of the chimneys but are lower than those recorded in some basement samples, which locally indicate paleotemperatures up to ~185°C (*11*).

In the high-pH (10 to 11) end-member fluids, carbonate ion (CO_3^{2-}) is the dominant form of dissolved inorganic carbon (DIC), and carbonate alkalinity is less than one-third of seawater values, whereas calcium concentrations are elevated (up to 30 mmol/kg). Carbon dioxide normally contributed by magmatic sources at mid-ocean ridges is absent in the LCHF fluids (*5*, *18*). Thus, autotrophic organisms living in vents must be adapted to a low-DIC, CO_2-poor, and H_2-rich environment.

Isotopic compositions ($\delta^{13}C$) of DIC in the fluids range from –8 to –2‰ in low-sulfate end-member fluids and –1 to +3‰ in samples with sulfate concentrations closer to those of seawater (SOM text). S-isotope compositions of sulfate ($\delta^{34}S$) range from +30‰ (Vienna Canyon Diablo troilite) in the end-member fluids to +21‰ in those fluids with higher sulfate concentrations (SOM text). Although we consider the $\delta^{13}C$ (DIC) values to be minimum estimates (SOM text), the observed compositions are consistent with those of the vent carbonates and reflect the ^{13}C-enriched nature of carbon components in the LCHF system. This covariance suggests local sulfate reduction in the vent structures and/or in the shallow subsurface.

Methane concentrations are elevated relative to seawater, but fall within a narrow range between 1 and 2 mmol/kg. In contrast, hydrogen concentrations vary from <1 to 15 mmol/kg, spanning the range for nearly all vents measured along the global mid-ocean ridge system (*5*, *18*, *19*). The extreme enrichment of hydrogen with lesser methane is characteristic of fluids formed through serpentinization reactions (*20*–*24*). Methane of the LCHF fluids has high $\delta^{13}C$ values of –13.6‰ to –8.8‰ VPDB. These compositions are 5 to 10‰ enriched relative to CH_4 from East Pacific Rise and southern Juan de Fuca fluids (*25*–*27*), but are similar to CH_4 sampled near ultramafic sequences of the Oman ophiolite (*28*). They are slightly depleted (2 to 6‰) relative to CH_4 at the Zambales ophiolite (*29*). As discussed in detail below, a determination of the CH_4 source cannot be made from the stable isotope data alone.

Life in high-pH systems. The metabolic menu for autotrophic microbes at hydrothermal vents is defined by the fluid chemistry. In this respect, the LCHF offers markedly different fare from that at magmatically hosted sites on ridge axes. Hydrogen is the dominant reduced product of serpentinization reactions beneath the massif, and it is also the most abundant energy source for microbes. Methane is also found in these vent fluids. Together, H_2 and CH_4 account for more reducing power at the LCHF than sulfide, which is the most abundant reduced product in solution at hydrothermal sites associated with basaltic volcanism (*18*). Concentrations of dissolved metals are much lower at the LCHF, and the suite of hydrothermal precipitates is completely different from that at typical sulfide-hosted mid-ocean ridge vent sites. These differences are reflected by the distinct microbial communities found within

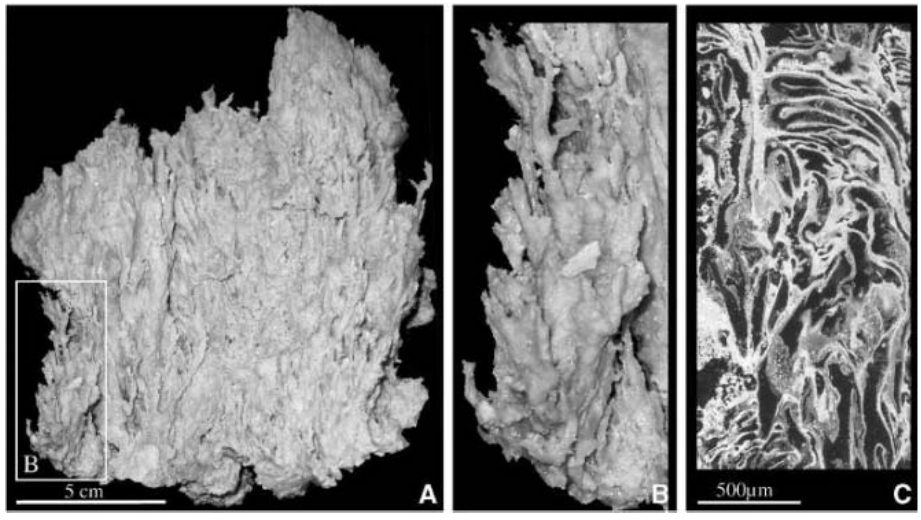

Fig. 5. Active vent deposits from Lost City. (**A**) Aragonite-rich sample recovered from near the summit of Poseidon. The sample was bathed in 59°C hydrothermal fluids. (**B**) Closeup of sample shown in (A), highlighting characteristic fragile intergrowths of aragonite and brucite. Carbonate chimneys and vein material in areas of active venting are snow white in color, extremely friable, and very porous. (**C**) Photomicrograph showing anastomosing aragonite intergrowths that are reminiscent of filamentous bacteria present in areas of diffuse flow (movie S2). This sample was recovered from a several-centimeter-wide "artery" of carbonate cutting the massif flanks of Poseidon. Feathery growths of carbonate several centimeters long protrude from the vein in a similar fashion to the deposit shown in Fig. 4E.

carbonate samples in contact with the warm high-pH hydrothermal fluids (*30*) (movie S2).

A suite of >60 active and inactive carbonate structures and venting hydrothermal fluids collected during the 2000 and 2003 cruises to the LCHF were investigated to quantify the numbers of microorganisms and their phylogenetic diversity (Table 1, Fig. 6, fig. S2, and SOM text). A range of biotopes harboring distinct microbial communities appear to be present at the LCHF. Carbonate samples in contact with active venting of warm volatile-rich hydrothermal fluids consistently harbored large numbers of microbes, nearly 10^7 to 10^8 cells per gram of wet weight (gww) (Table 1). In contrast, there were lower densities (<10^7 gww) in extinct samples (Table 1).

Overall, 29 to 57% of the cell population associated within active hydrothermal venting was counted by fluorescence in situ hybridization (FISH), and all of the higher-temperature (>50°C) samples yielded a higher proportion of archaea than bacteria. These results confirm our initial findings on a limited number of carbonate samples from the 2000 cruise, which showed the predominance of a single phylotype related to the archaeal order Methanosarcinales in spatially distinct sites on the Poseidon edifice (SOM text) (*30*). Between 70 and >90% of the archaeal cells in all of the higher-temperature samples hybridized with an oligonucleotide probe targeting this phylotype (Table 1) (*30*). The more recent samples support this conclusion and further suggest that both methane-producing and methane-consuming Archaea are present, on the basis of analyses of the *mcrA* (Fig. 6) and 16*S* ribosomal RNA (rRNA) genes (fig. S2). Our analyses indicate that the methanosarcinal phylotype found at the LCHF appears to be associated with carbonate-hosted environments in contact with higher-temperature end-member fluids. In contrast, both 16*S* rRNA and *mcrA* genes related to the anaerobic methane-oxidizing phylotype ANME-1 were found in cooler environments associated with hydrothermal flanges on the carbonate chimney and carbonate-lined fractures along the walls of the peridotite massif (Table 1).

Based on phylogenetic analyses, the eubacterial diversity associated with active carbonate samples from the LCHF was similarly high; sequences related to the Firmicutes were present at higher-temperature sites, and representatives of the Chloroflexi, epsilon, and gamma proteobacteria occurred within cooler environments (Table 1). The distribution of Firmicutes at the LCHF is especially intriguing given the physiological adaptations of this group to high temperature and high pH (*31*). Additionally, some species within the Firmicutes have been isolated from extreme environments and are capable of oxidizing hydrogen and reduced sulfur species. Therefore, they may play a critical role in the ecology of high-temperature environments at the LCHF. The bacterial sequences found at the LCHF included relatives of sulfur- and

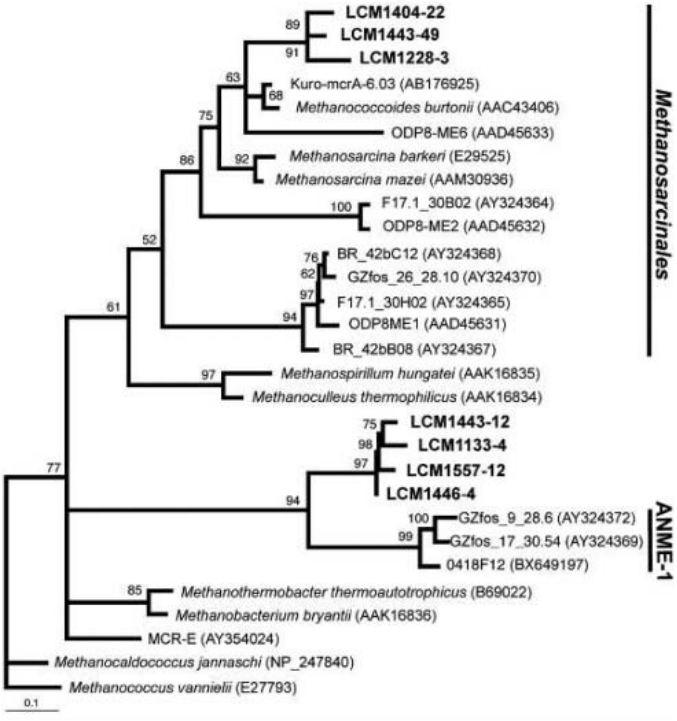

Fig. 6. Phylogenetic tree of partially sequenced *mcrA* clones isolated from carbonate samples relative to published sequences constructed with TREE-PUZZLE version 5.0 (*46*). Quartet-puzzling support values are shown at branch points; *Methanocaldococcus jannaschii* was used as the outgroup. LCM1404-22, LCM1443-49, LCM1443-12, and LCM1446-4 were isolated from marker C and LCM1228-3 from marker H, both of which are actively venting structures (see fig. S1 for locations). LCM1133-4 and LCM1557-12 were isolated from carbonate veins in serpentinite. GenBank Accession numbers for LCHF *mcrA* clones are AY760633 through AY760639. The scale bar represents 0.1 changes per nucleotide base.

Table 1. Biological Communities at Lost City.

Sample	*T* (°C)*	Microscopy				Phylogenetic analyses§									
		Cells (gww)†	FISH‡			Archaea			Eubacteria					*mcrA*	
			A	B	MS	MS	AN-1	MG1	γ	δ	ε	Fm	Cx	MS	AN-1
Poseidon															
Marker 2 (IMAX)flange	53–60	0.6 × 10^8 to 5.2 × 10^8	33	18	29	+			+		+	+	+		
Marker 3: top	59–75	0.02 × 10^8 to 1.3 × 10^8	41	12	33	+			+						
Marker C: flange and spire[e]	54–70	0.1 × 10^8 to 8.4 × 10^8	28	23	19	+	+		+	+	+		+	+	+
Beehive	91.4	5.8 × 10^6	21	8	18										
Other chimneys															
Marker 7: spire	24	<LOD = 4.7 × 10^8	22	24	17										
Marker H: spire and flange	17–67	0.03 × 10^8 to 3.1 × 10^8	19	38	10	+	+		+					+	
Peripheral (diffuse) regions	>7	0.1 × 10^8 to 4.8 × 10^8	8	29	5	+			+		+				
Near wall															
Spire on wall	>7	2.3 × 10^8 to 7.4 × 10^8	25	13	14										
Carbonate veins	>7	<LOD = 2.2 × 10^8	19	15	9		+		+		+				+
Extinct samples	Ambient	<LOD = 1.4 × 10^7	5	17	<1			+	+						

*Temperature (*T*) measured in situ either with *Alvin*'s temperature probe or with a sensor mounted on the hydrothermal fluid particulate sampler. †Number of organisms in gww; limit of detection (LOD) = ~ 10^4 cells gww. ‡Fluorescence in situ hybridization (FISH). FISH data are in % of total cell numbers. Abbreviations are as follows: A, Archaea; B, Eubacteria; MS, Lost City methanosarcinal phylotype. §Phylogenetic abbreviations are as follows: MS, Lost City methanosarcinal phylotype; AN-1, ANME-1; MGI, marine group 1 Crenarchaeota; γ, gamma proteobacteria; δ, delta proteobacteria; ε, epsilon proteobacteria; Fm, Firmicutes; Cx, Chloroflexi.

methane-oxidizing phylotypes and sulfate-reducing delta proteobacteria. The presence of distinct methane- and sulfur-cycling microbial communities at multiple temperature and environmental settings indicates a complex interaction between subseafloor geochemical processes at this site and chemolithotrophic microbial activity.

Structural and isotopic studies of lipid biomarkers in the LCHF samples document the presence of particular microbial lineages and the importance of specific metabolic processes. The carbonate vent structures contain up to 0.6 wt % total organic carbon (TOC), indicating a relatively high content of living and dead biomass within the vent structures. Abundances of $^{13}C_{TOC}$ varied widely from –3.1 to –18.1‰ (SOM text and table S1). Lipid extracts yielded abundant archaeal biomarkers consistent with results of the DNA analyses. The ether lipids archaeol, *sn*-2 and *sn*-3 hydroxyarchaeol, a putative dihydroxyarchaeol, and the hydrocarbon 2,6,10,15,19-pentamethylicosane (PMI), all found in the LCHF samples, have been linked to archaeal methanogens and methanotrophs (*32*, *33*). Less prevalent at the LCHF were biomarkers indicating the presence of eukaryotes (sterols) and bacteria (hopanoids). However, the presence at several vents of glycerol mono- and diethers with saturated and unsaturated C_{15} to C_{20} *n*-alkyl chains indicates that bacterial sulfate reduction may also be an active metabolic pathway. These data are also consistent with the observed strong negative correlation between concentrations of total sulfide and sulfate in LCHF vent fluids.

The archaeal populations are unusually enriched in ^{13}C. Values of $\delta^{13}C$ for TOC are positively correlated with the abundance of archaeal lipids. TOC from chimneys on the far eastern side of the field and from near the base of Poseidon is enriched in ^{13}C (δ = –4.6, -3.1‰ VPDB) and relatively rich in archaeal lipids, whereas a sample from a 91°C beehive structure on Poseidon has low concentrations of archaeal lipids and TOC with δ = –18.5‰. The causes of this trend can be examined by means of compound-specific isotopic analyses. The archaeal lipids discussed above have δ values ranging from –8.5 to +4.8‰ VPDB and they average –0.3‰. Glycerol mono- and diethers are similarly enriched in ^{13}C, whereas bacterial fatty acids are significantly depleted at –25‰. The isotopic composition of TOC must therefore represent a mass balance of isotopically distinct components.

The close association of archaea with sulfate-reducing bacteria that produce glycerol-ether lipids invites comparisons with microbial consortia operative at methane seeps (*33*, *34*). In seep environments, the two families of ether-linked lipids (archaeal and bacterial) have similar isotopic compositions. At the LCHF, the archaeal lipids are highly enriched in ^{13}C and are associated with relatively heavy $\delta^{13}C$ values of CH_4 in the vent fluids. The high H_2 concentrations, the occurrence of ^{13}C-enriched carbonate minerals (up to +13‰), and the abundance of ^{13}C-enriched archaeal lipids are all consistent with a role for H_2-consuming methanogens that use seawater DIC as a substrate and thus produce both CH_4 and biomass that is unusually enriched in ^{13}C. Therefore, in addition to an abiogenic origin of methane, produced by Fischer-Tropsch–type reactions involving H_2 and either mantle CO_2 or seawater bicarbonate, microbial activity is a viable source of CH_4 at Lost City. Given the wide variations in temperature and redox state, it is likely that further investigations will reveal a mosaic of processes, both abiotic and microbially catalyzed.

The highly sculpted large surface area of the Lost City structures provides ample space for faunal habitats, and many invertebrates were located within the porous channels and crevices of the carbonate. Actively venting carbonate habitats (~10° to 40°C) were dominated by several species of gastropods and amphipods, including *Bouvierella* affn. *curtirama*. The most abundant nonvent fauna were deep-sea euphausids and the amphipod *Primno evansi* (SOM text), which were probably attracted to the submersible lights during their diurnal vertical migrations. The hydrothermally active portions of friable flanges and spires were inhabited by numerous species of endemic polychaetes, nematodes, ostracods, stomatopods, and bivalves. Nonventing habitats less than a few meters away (such as the sides of inactive solidified carbonate structures, sedimented areas, and breccia cap rock) were dominated by nonendemic *Lophelia*, gorgonian, and *Desmophyllum* corals; galatheid crabs; turrid gastropods; foraminifera; pteropods; urchins; asteroids; ophiuroids; and typical deep-sea barnacles (such as *Poecilasma aurantia* and *Metaverruca inermis*). Thus, the boundary between vent and nonvent habitats is strongly demarcated at Lost City.

Initial in situ visual observations of the Lost City edifices suggested a notable absence of fauna (*4*), and even a cursory biomass comparison between the dominant Lost City fauna and Mid-Atlantic Ridge, East Pacific Rise, and Juan de Fuca vent fauna revealed significantly lower macrofaunal biomass at Lost City. The largest contributor to biomass at Lost City is the large mobile megafauna, including the wreckfish (*Polyprion americanus*), cut-throat eels (*Synaphobranchus kaupi*), and large geryonid crabs, which were all readily visible around active vents. The high-pH CH_4- and H_2-rich fluids are poor in the sulfide species that are typically relied on by vent faunal assemblages, and these factors may contribute to the relatively lower biomass observed at Lost City.

Despite the absence of readily observable fauna, the LCHF supports a species diversity that appears to be as high as that of any other known Mid-Atlantic Ridge vent site. Vent sites on the Mid-Atlantic Ridge typically host 30 to 50 macrofaunal species, with a total ~100 species residing within the eight major Mid-Atlantic Ridge sites (*35*, *36*). Initial analyses of >40 faunal samples recovered revealed that over 65 morpho-species representing 13 phyla are present. The majority (>90%) of these fauna were on the order of hundreds of micrometers or less in size. These were sampled via suction sampler from >10 active vent edifices and showed qualitative differences in species abundance and composition with substrate type.

Four morphospecies of gastropods were the most abundant fauna sampled from the carbonate. The most diverse group of invertebrates dominating the flange areas was polychaetes, including the families Dorvelleidae (including new species of *Ophiotrocha*), Ceratulidae, Glyceridae, Amphinomidae, and Polynoidae. A minimum of nine species were found, one-third of which are new. Current assessments of vent-dependent fauna within the Lost City field reveal that 58% of these fauna are endemic.

Implications. The range and complexity of environments hosting peridotites and other ultramafic rocks is vast. Under appropriate conditions, any of these might support hydrothermal systems similar to the LCHF. From ancient komatiitic rocks of the Early Archaean (*37*) to ophicalcite deposits within the Apennine ophiolites (*38*) comes evidence that hydrothermal systems have indeed been operative within ultramafic environments for much of Earth's history. Within the contemporary oceanic crust, there is a diverse array of submarine environments affected by ongoing serpentinization reactions, which include systems such as the Mariana forearc (*39*, *40*), the Arctic (*9*), the Antarctic (*10*), the Southwest Indian and Mid-Atlantic Ridge spreading networks (*41*, *42*), major transform faults (*17*, *43*), and highly extended rifted margins (*44*). Any of these tectonic settings could host LCHF-type ecosystems. Such systems may also have played a role in the origin and evolution of life on this planet and perhaps elsewhere (*45*).

References and Notes

1. F. N. Spiess *et al.*, *Science* **207**, 1421 (1980).
2. *The Subseafloor Biosphere at Mid-Ocean Ridges*, W. W. Wilcock, E. DeLong, D. S. Kelley, J. A. Baross, S. C. Cary, Eds. (Geophysical Monograph 144, American Geophysical Union, Washington, DC, 2004).
3. P. Michael, *Nature* **419**, 445 (2002).
4. D. S. Kelley *et al.*, *Nature* **412**, 145 (2001).
5. D. S. Kelley, G. L. Früh-Green, M. D. Lilley, in (*2*), pp. 167–189.
6. M. D. Lilley, D. A. Butterfield, J. A. Lupton, E. J. Olson, *Nature* **422**, 878 (2003).
7. Y. Lagabrielle, D. Bideau, M. Cannat, J. A. Karson, C. Mevel, in *Faulting and Magmatism at Mid-Ocean Ridges*, W. R. Buck, P. T. Delaney, J. A. Karson, Y. Lagabrielle, Eds. (Geophysical Monograph 106, Amer-

ican Geophysical Union, Washington, DC, 1998), pp. 153–176.
8. W. Bach, N. R. Banerjee, H. J. B. Dick, E. T. Baker, *Geochem. Geophys. Geosyst.* **3**, GC000279 (2001).
9. H. N. Edmonds *et al.*, *Nature* **421**, 252 (2003).
10. H. J. B. Dick, J. Lin, H. Schouten, *Nature* **426**, 405 (2003).
11. G. L. Früh-Green *et al.*, *Science* **302**, 495 (2003).
12. R. P. Lowell, P. A. Rona, *Geophys. Res. Lett.* **29**, 10.1029/2001GL01411 (2002).
13. T. L. Grove, S. W. Parman, *Earth Planet. Sci. Lett.* **219**, 173 (2004).
14. Materials and methods are available as supporting material on *Science* Online.
15. D. K. Blackman *et al.*, *Marine Geophsy. Res.* **23**, 443 (2004).
16. T. Schroeder, B. John, B. R. Frost, *Geology* **30**, 367 (2002).
17. J. A. Karson, in *Faulting and Magmatism at Mid-Ocean Ridges*, W. R. Buck, P. T. Delaney, J. A. Karson, Y. Lagabrielle, Eds. (Geophysical Monograph 106, American Geophysical Union, Washington, DC, 1998), pp. 177–218.
18. D. S. Kelley, J. A. Baross, J. R. Delaney, *Annu. Rev. Earth Planet. Sci.* **30**, 385 (2002).
19. J. L. Charlou, J. P. Donval, Y. Fouquet, P. Jean-Baptiste, N. Holm, *Chem. Geol.* **191**, 345 (2002).
20. D. R. Janecky, W. E. Seyfried Jr., *Geochim. Cosmochim. Acta* **50**, 1357 (1986).
21. C. Neal, G. Stanger, *Earth Planet. Sci. Lett.* **66**, 315 (1983).
22. M. E. Berndt, D. Allen, W. E. Seyfried Jr., *Geology* **24**, 351 (1996).
23. L. R. Wetzel, E. L. Shock, *J. Geophys. Res.* **105**, 8319 (2000).
24. T. M. McCollom, J. S. Seewald, *Geochim. Cosmochim. Acta* **65**, 3769 (2001).
25. M. D. Lilley *et al.*, *Nature* **364**, 45 (1993).
26. J. A. Welhan, H. Craig, *Eos* **60**, 863 (1979).
27. J. A. Welhan, H. Craig, in *Hydrothermal Processes at Seafloor Spreading Centers*, A. Rona Peter, K. Bostrom, L. Laubier, L. Smith Kenneth Jr., Eds. (Plenum, New York, 1983), pp. 391–409.
28. P. Fritz, I. D. Clark, J. C. Fontes, M. J. Whiticar, E. Faber, in *Proceedings of the 7th International Symposium on Water-Rock Interaction; Volume 1, Low Temperature Environments*, K. Kharaka Yousif, S. Maest Ann, Eds. (International Association of Geochemistry and Cosmochemistry and Alberta Research Council, Sub-Group on Water-Rock Interaction, Edmonton, Alberta, Canada, 1992), pp. 793–796.
29. T. A. Abrajano *et al.*, *Chem. Geol.* **71**, 211 (1988).
30. M. O. Schrenk, D. S. Kelley, S. A. Bolton, J. A. Baross, *Environ. Microbiol.* **6**, 1086 (2004).
31. A.-L. Reysenbach, D. Götz, D. Yernool, in *Biodiversity of Microbial Life*, J. T. Staley, A.-L. Reysenbach, Eds. (Wiley-Liss, New York, 2002), pp. 345–422.
32. J. M. Hayes, J. W. Valley, D. R. Cole, Eds., *Stable Isotope Geochemistry, Reviews in Mineralogy and Geochemistry* (Mineralogical Society of America, Washington, DC, 2001), vol. 43, chap. 3.
33. K. U. Hinrichs, R. E. Summons, V. Orphan, S. P. Sylva, J. M. Hayes, *Org. Geochem.* **31**, 1685 (2000).
34. V. Orphan *et al.*, *Proc. Natl. Acad. Sci. U.S.A.* **99**, 7663 (2002).
35. V. Tunnicliffe, C. M. R. Fowler, *Nature* **379**, 531 (1996).
36. A. V. Gebruk, S. V. Galkin, A. L. Vereshchaka, L. I. Moskalev, A. J. Southward, *Adv. Mar. Biol.* **32**, 93 (1997).
37. A. A. Suror, E. H. Arfa, *J. Afr. Earth Sci.* **24**, 315 (1997).
38. B. E. Treves, G. D. Harper, *Ofioliti* **19b**, 435 (1994).
39. M. M. Mottl, S. C. Komor, P. Fryer, C. L. Moyer, *Geochem. Geophys. Geosyst.* **4**, 11 (2003).
40. P. Fryer, C. G. Wheat, M. J. Mottl, *Geology* **27**, 103 (1997).
41. E. Gracia, J. L. Charlou, J. Radford-Knoery, L. Parson, *Earth Planet. Sci. Lett.* **177**, 89 (2000).
42. J. L. Charlou, J. P. Donval, Y. Fouquet, P. Jean-Baptiste, N. Holm, *Chem. Geol.* **191**, 345 (2002).
43. E. Bonatti, P. J. Michael, *Earth Planet. Sci. Lett.* **91**, 297 (1989).
44. T. J. Reston *et al.*, *Geology* **29**, 587 (2001).
45. E. L. Shock, M. D. Schulte, *J. Geophys. Res.* **103**, 28,513 (1998).
46. H. A. Schmidt, K. Strimmer, M. Vingron, A. von Haeseler, *Bioinformatics* **18**, 502 (2002).
47. We express our deep appreciation to the crews of the R/V *Atlantis* and *Alvin* for their support and help with the 2003 Lost City expedition. Their humor, friendship, and professionalism were instrumental to the success of the field program. We also very much appreciate the helpful comments of four anonymous reviewers. We thank B. Nelson for his time and help with the Sr analyses and for making his laboratory available to us, S. R. Emerson for guidance in chemical analyses of the carbonate samples and use of his laboratory facilities, and M. Lin for technical assistance with phylogenetic analyses. We acknowledge funding from NSF grants OCE0137206 (D.S.K.), OCE0136816 (J.A.K.), and OCE0136871 (D.R.Y. and T.M.S.). Work by J.A.B. was also supported by the NASA Astrobiology Institute through the Carnegie Geophysical Institute. Support to G.L.F.-G. was through Swiss National Science Foundation grant 2100-068055. J.M.H. was supported in part by the NASA Astrobiology Institute through the University of Rhode Island.

Supporting Online Material
www.sciencemag.org/cgi/content/full/307/5714/1428/DC1
Materials and Methods
SOM Text
Figs. S1 and S2
Table S1
References
Movies S1 and S2

9 July 2004; accepted 21 January 2005
10.1126/science.1102556

The Influence of *CCL3L1* Gene–Containing Segmental Duplications on HIV-1/AIDS Susceptibility

Enrique Gonzalez,[1]* Hemant Kulkarni,[1]* Hector Bolivar,[1]*† Andrea Mangano,[2]* Racquel Sanchez,[1]‡ Gabriel Catano,[1]‡ Robert J. Nibbs,[3]‡ Barry I. Freedman,[4]‡ Marlon P. Quinones,[1]‡ Michael J. Bamshad,[5] Krishna K. Murthy,[6] Brad H. Rovin,[7] William Bradley,[8,9] Robert A. Clark,[1] Stephanie A. Anderson,[8,9] Robert J. O'Connell,[9,10] Brian K. Agan,[9,10] Seema S. Ahuja,[1] Rosa Bologna,[11] Luisa Sen,[2] Matthew J. Dolan,[9,10,12]§ Sunil K. Ahuja[1]§

Segmental duplications in the human genome are selectively enriched for genes involved in immunity, although the phenotypic consequences for host defense are unknown. We show that there are significant interindividual and interpopulation differences in the copy number of a segmental duplication encompassing the gene encoding CCL3L1 (MIP-1αP), a potent human immunodeficiency virus–1 (HIV-1)–suppressive chemokine and ligand for the HIV coreceptor CCR5. Possession of a *CCL3L1* copy number lower than the population average is associated with markedly enhanced HIV/acquired immunodeficiency syndrome (AIDS) susceptibility. This susceptibility is even greater in individuals who also possess disease-accelerating *CCR5* genotypes. This relationship between *CCL3L1* dose and altered HIV/AIDS susceptibility points to a central role for CCL3L1 in HIV/AIDS pathogenesis and indicates that differences in the dose of immune response genes may constitute a genetic basis for variable responses to infectious diseases.

Duplicated host defense genes that are known to have dosage effects are thought to contribute to the genetic basis of some complex diseases, although direct evidence for this is lacking. We surmised that a hotspot for segmental duplications on human chromosome 17q might be relevant to immunity against infectious diseases such as HIV-1 because it encompasses two CC chemokine genes, CC chemokine ligand 3-like 1 (*CCL3L1*; other names, *MIP-1αP* and *LD78*β) and *CCL4L1* (*MIP-1*β*-like*), which represent the duplicated isoforms of the genes encoding CCL3 and CCL4, respectively (*1*–*3*). As a consequence of these duplications, the copy number of *CCL3L1* and *CCL4L1* varies among individuals (*2*, *3*) (fig. S1A). This is important because CCL3L1 is the most potent known ligand for CC chemokine receptor 5 (CCR5), the major coreceptor for HIV, and it is a dominant HIV-suppressive chemokine (*3*).

In light of this relationship between CCL3L1 and its in vitro effect on HIV infection, we selected HIV infection as a model system in which to test our hypothesis that segmental duplications causing dosage effects of host defense genes are associated with phenotypic effects in vivo. To test this hypothesis, we determined the distribution of chemokine gene–containing segmental duplications in 1064 humans from 57 populations and 83 chimpanzees (*4*). We next analyzed 4308 HIV-1–positive (HIV^+) and HIV-1–negative (HIV^-) individuals from groups with different geographical ancestries (e.g., Africans and Europeans) to determine if the risk of acquiring HIV and the rate at which HIV disease progressed were sensitive to differences in the dose of *CCL3L1*

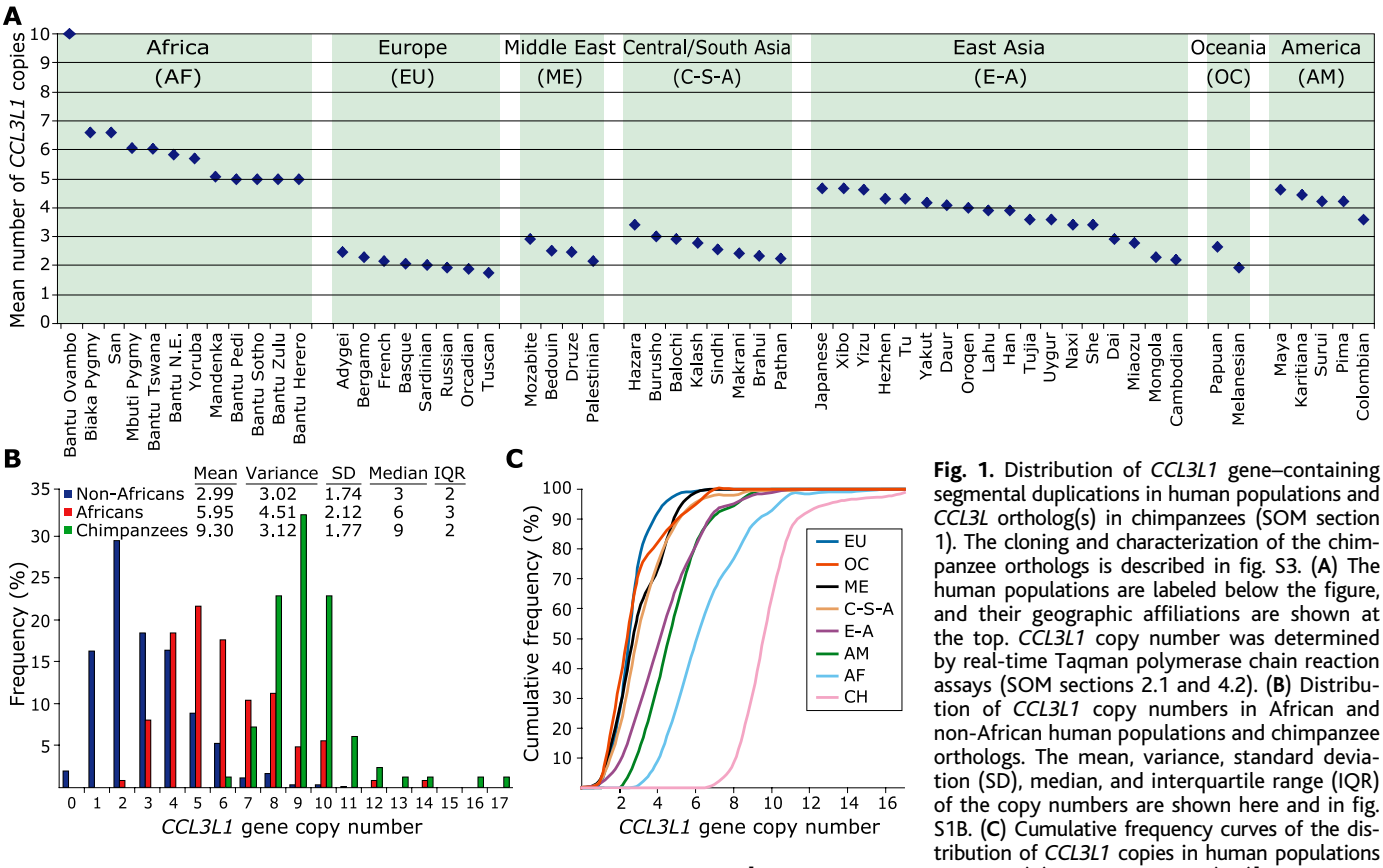

Fig. 1. Distribution of *CCL3L1* gene–containing segmental duplications in human populations and *CCL3L* ortholog(s) in chimpanzees (SOM section 1). The cloning and characterization of the chimpanzee orthologs is described in fig. S3. (**A**) The human populations are labeled below the figure, and their geographic affiliations are shown at the top. *CCL3L1* copy number was determined by real-time Taqman polymerase chain reaction assays (SOM sections 2.1 and 4.2). (**B**) Distribution of *CCL3L1* copy numbers in African and non-African human populations and chimpanzee orthologs. The mean, variance, standard deviation (SD), median, and interquartile range (IQR) of the copy numbers are shown here and in fig. S1B. (**C**) Cumulative frequency curves of the distribution of *CCL3L1* copies in human populations from different geographic regions and chimpanzee. The order of the abbreviations [geographic regions shown in (A) and chimpanzee (CH)] matches the order of the cumulative frequency curves from left to right.

gene–containing segmental duplications (*4*) [supporting online material (SOM) section 4.1].

Nonrandom distribution of *CCL3L1*-containing segmental duplications. African populations possessed a significantly greater number of *CCL3L1* gene copies than non-Africans (Fig. 1 and fig. S1B). The geographic region of origin explained nearly 35% of the total variation in the distribution of *CCL3L1* gene copies (analysis of variance: $F = 94.41$, df = 6, 1037; $P = 1.23 \times 10^{-94}$). Corroborating this, in separate cohorts of HIV$^-$ subjects, there were significant interindividual and interpopulation differences in *CCL3L1* copy numbers. The median copy number in HIV$^-$ Argentinean children was two, and in HIV$^-$ African-American (AA), European-American (EA), and Hispanic-American (HA) adults, it was four, two, and three, respectively (Fig. 2, A to D, open bars, and fig. S2).

The duplicated region encoding human CCL3L1 had an ancestral correlate in chimpanzee (Fig. 1 and fig. S3). Together, these results demonstrated that there were significant differences between species and among human populations in the frequency of chemokine gene–containing segmental duplications (Fig. 1, B and C). Despite these differences, the dispersion around the average copy number was similar in both human populations and chimpanzees (Fig. 1B and fig. S1B). On the basis of these observations, we hypothesized that it is not the absolute copy number per se, but rather the gene dose relative to the average copy number in each population that confers HIV/AIDS susceptibility.

***CCL3L1* gene dose and HIV/AIDS susceptibility.** Several lines of evidence, from four different human populations and in the setting of two different modes of acquiring HIV (i.e., mother-to-child and adult-to-adult), indicated that possession of a low *CCL3L1* copy number was a major determinant of enhanced HIV susceptibility among individuals. Individuals with a low *CCL3L1* copy number were overrepresented among the HIV$^+$ compared with HIV$^-$ subjects (shift to the left in Fig. 2, A to D, and figs. S2 and S4). On the basis of the consistency, strength, and significance of the differences in the distribution of *CCL3L1* copy numbers in the HIV$^+$ and HIV$^-$ individuals in each of the cohorts studied, we rejected the null hypothesis of no association between risk of acquiring HIV and *CCL3L1* copy number (Fig. 2, A to D, and fig. S2).

We next determined the strength of the association between *CCL3L1* copy number and risk of acquiring HIV (Fig. 2, E to H). In our initial analyses, we chose the population-specific median copy number in the uninfected group as a reference point to compute the risk of acquiring HIV (SOM section 5.1). Compared with possession of two copies of *CCL3L1*, children possessing less than two or more than two copies had significantly higher or lower risks, respectively, of acquiring HIV (Fig. 2E). This association was

[1]Veterans Administration Research Center for AIDS and HIV-1 Infection, South Texas Veterans Health Care System, and Department of Medicine, University of Texas Health Science Center, San Antonio, TX 78229, USA. [2]Laboratorio de Biología Celular y Retrovirus–Consejo Nacional de Investigaciones Científicus y Tecnicas, and [11]Servicio de Infectología, Hospital de Pediatría "J. P. Garrahan," 1245 Buenos Aires, Argentina. [3]Cancer Research UK Beatson Laboratories, Glasgow G61 1BD, Scotland, UK. [4]Department of Internal Medicine, Wake Forest University School of Medicine, Winston-Salem, NC 27157, USA. [5]Departments of Human Genetics and Pediatrics, University of Utah, Salt Lake City, UT 84112, USA. [6]Southwest Foundation for Biomedical Research, San Antonio, TX 78227, USA. [7]Division of Nephrology, Ohio State University, Columbus, OH 43210, USA. [8]Henry M. Jackson Foundation, [9]Tri-Service AIDS Clinical Consortium, and [10]Infectious Diseases Service, Wilford Hall Medical Center, Lackland Air Force Base, TX 78236, USA. [12]Defense Institute for Medical Operations, Brooks City-Base, TX 78235, USA.

*These authors contributed equally to this work.
†Present address: AIDS Clinical Research Unit, University of Miami, Miller School of Medicine, Miami, FL 33136, USA.
‡These authors contributed equally to this work.
§To whom correspondence should be addressed. E-mail: ahujas@uthscsa.edu (S.K.A.); matthew.dolan@brooks.af.mil (M.J.D.)

evident in the analysis of the entire cohort of children with (table S1A) or without (Fig. 2E) adjustments for receipt of zidovudine prophylaxis given to reduce the risk of transmission and for individuals who received no prophylaxis (table S1A). Notably, with each increase in *CCL3L1* copy number above the median, there was a dose-dependent, stepwise decrease in the risk for acquiring HIV (Fig. 2E). The findings depicted in Fig. 2, F to H, and those derived from a separate analysis in another cohort of 1133 HIV$^-$ individuals matched for ethnicity/race (fig. S2), indicated that adults who possessed a *CCL3L1* copy number lower than the population-specific median were at a higher risk of acquiring HIV. Thus, in each population, the median number of *CCL3L1* copies served as the transition point at which the balance tilted in favor of protection against acquiring HIV.

We also estimated the risk of acquiring HIV across the cline of population-specific high to low *CCL3L1* copy numbers (fig. S4). Depending on the study population, each *CCL3L1* copy lowered the risk of acquiring HIV by 4.5 to 10.5%, indicating that the population-specific high and low *CCL3L1* copy numbers are at different ends of a distribution of HIV susceptibility (SOM section 5.2). Substantiating this, relative to possession of the population-specific high *CCL3L1* copy numbers shown in fig. S4, individuals who had a low copy number had between 69 and 97% higher risk of acquiring HIV (fig. S4).

The aforementioned analyses were conducted with logistic regression. Although membership in either the HIV$^+$ or HIV$^-$ group is not a random outcome, to the extent that these two groups can be thought of as random samples from their respective subsets of a well-defined population, logistic regression on group membership allows estimation of the relative odds of being HIV$^+$ or HIV$^-$ for two different copy numbers. In this sense, logistic regression permits the determination of the association between *CCL3L1* copy number and risk of acquiring HIV. Because the number of *CCL3L1* copies followed a Poisson distribution, we also used Poisson regression analysis to determine the association between *CCL3L1* copy number and risk of acquiring HIV infection. These analyses assume that copy numbers are conditional on HIV status and show that HIV$^+$ subjects have significantly lower *CCL3L1* copy numbers than do HIV$^-$ subjects (Fig. 2I). Although the true risk of HIV acquisition associated with possession of different *CCL3L1* gene copy numbers can theoretically only be estimated from a longitudinal study, in the cohorts we studied, the results of two different statistical approaches demonstrate a strong association between possession of low *CCL3L1* copy number and risk of acquiring HIV infection (Fig. 2, E and J, and table S1B).

In addition to influencing HIV acquisition, the number of *CCL3L1* copies was associated with variable rates of disease progression (figs. S5 and S6). For example, in the adult HIV$^+$ cohort, a gene dose lower than the overall cohort median or population-specific median was associated with a dose-dependent increased risk of progressing rapidly to AIDS or death (Fig. 3, A and B, and figs. S5). A disease-influencing effect of *CCL3L1* dose was not detected in the HIV$^+$ children, suggesting either that the roles of CCL3L1 in HIV$^+$ adults and children differ or that the

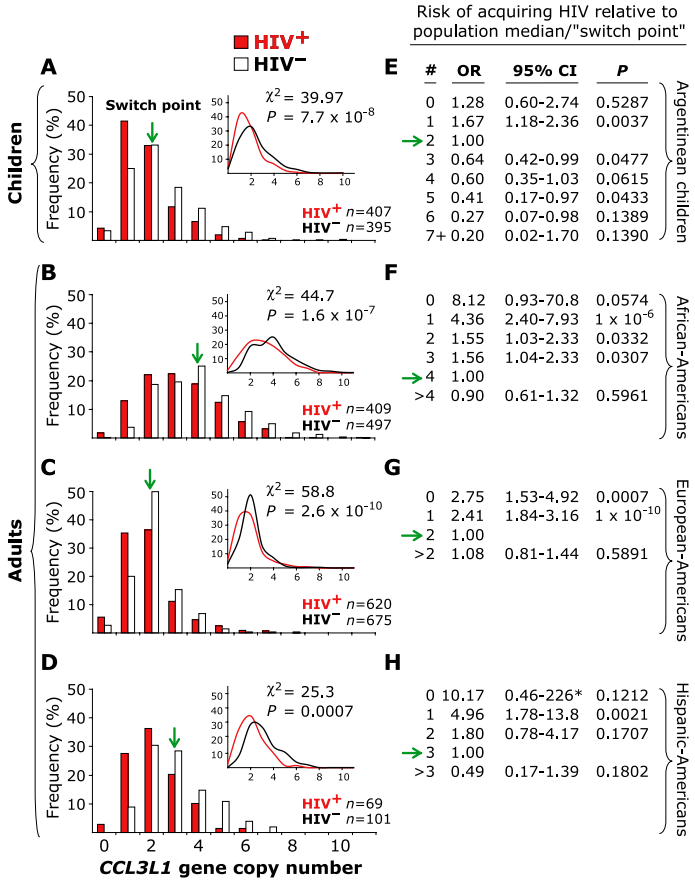

Risk of acquiring HIV relative to population median/"switch point"

E

#	OR	95% CI	P	
0	1.28	0.60-2.74	0.5287	Argentinean children
1	1.67	1.18-2.36	0.0037	
→2	1.00			
3	0.64	0.42-0.99	0.0477	
4	0.60	0.35-1.03	0.0615	
5	0.41	0.17-0.97	0.0433	
6	0.27	0.07-0.98	0.1389	
7+	0.20	0.02-1.70	0.1390	

F

#	OR	95% CI	P	
0	8.12	0.93-70.8	0.0574	African-Americans
1	4.36	2.40-7.93	1 x 10⁻⁶	
2	1.55	1.03-2.33	0.0332	
3	1.56	1.04-2.33	0.0307	
→4	1.00			
>4	0.90	0.61-1.32	0.5961	

G

#	OR	95% CI	P	
0	2.75	1.53-4.92	0.0007	European-Americans
1	2.41	1.84-3.16	1 x 10⁻¹⁰	
→2	1.00			
>2	1.08	0.81-1.44	0.5891	

H

#	OR	95% CI	P	
0	10.17	0.46-226*	0.1212	Hispanic-Americans
1	4.96	1.78-13.8	0.0021	
2	1.80	0.78-4.17	0.1707	
→3	1.00			
>3	0.49	0.17-1.39	0.1802	

I

#	HIV$^+$ subjects		HIV$^-$ subjects	
	Subjects	*CCL3L1* gene copies Mean (95% CI)	Subjects	*CCL3L1* gene copies Mean (95% CI)
1.	Arg. children	1.85 (1.72–1.99)	Arg. children	2.41 (2.26–2.57)
2.	WHMC EA+HA	1.88 (1.74–1.99)	WHMC EA+HA	2.10 (1.99–2.22)
3.	WHMC AA	3.26 (3.08–3.44)	WHMC AA	3.79 (3.60–3.98)
4.	WHMC EA	1.86 (1.75–1.97)	Non-WHMC EA	2.13 (2.02–2.24)
5.	WHMC AA	3.26 (3.08–3.44)	Non-WHMC AA	3.90 (3.73–4.08)
6.	WHMC HA	2.06 (1.73–2.43)	Non-WHMC HA	3.08 (2.75–3.44)

J

#	Poisson regression			Logistic regression		
	RR	95% CI	P	OR	95% CI	P
1.	0.77	0.70-0.85	6.7 x 10⁻⁷	0.71	0.63–0.80	6.7 x 10⁻⁹
2.	0.90	0.83-0.97	0.0059	0.83	0.75–0.92	0.0005
3.	0.86	0.80-0.93	6.6 x 10⁻⁵	0.81	0.74–0.88	3.3 x 10⁻⁶
4.	0.87	0.81-0.95	0.0007	0.80	0.72–0.89	2.2 x 10⁻⁵
5.	0.84	0.78-0.90	4.7 x 10⁻⁷	0.78	0.72–0.85	8.4 x 10⁻⁹
6.	0.67	0.55-0.82	8.5 x 10⁻⁵	0.49	0.36–0.67	9.0 x 10⁻⁶

Fig. 2. *CCL3L1* dose and risk of acquiring HIV-1. (**A** to **D**) Histograms and the cubic-spline smoothed frequency curves (insets) show that the distribution of the *CCL3L1* copy numbers (*x* axis) in HIV$^+$ (red bars or red lines in inset) versus HIV$^-$ (open bars or black line in inset) individuals is markedly different (χ^2 and *P* values above insets; *n* = number of individuals in each group). Vertical green arrow indicates the switch point (copy number at which the HIV$^+$/HIV$^-$ ratio switched from >1 to ≤1) (SOM section 5.1). The cohort of Argentinean children is composed of children exposed perinatally to HIV (*4*). The HIV$^+$ adults from the indicated ethnic/racial groups (noted on the right) are from the Wilford Hall Medical Center (WHMC) cohort (*14*) and are compared with a control group from the general population that is matched for ethnicity/race (*4*). (**E** to **H**) Risk of acquiring HIV relative to the population-specific median [horizontal arrow; odds ratio (OR) = 1] was determined by multivariate logistic regression analyses. *, Jewell correction (*4*); #, *CCL3L1* gene copy number; CI, confidence interval; *P*, significance value. (**I**) Distribution of *CCL3L1* copies in the indicated subject groups (Poisson means and exact 95% CI). #, group number. Arg., Argentinean. SOM section 1.1 provides details of these study groups. In the HIV$^-$ WHMC cohort, as HAs were categorized with EAs, they were placed within a single group (WHMC EA + HA) and compared with subjects from the HIV$^+$ WHMC cohort that are matched for ethnicity/race. (**J**) Results of Poisson and logistic regression models in the study groups indicated in (I) (#1 to 6) for the association between *CCL3L1* copies and risk of acquiring HIV infection were comparable (table S1B). RR, relative risk.

short follow-up time in the pediatric cohort was insufficient to detect an effect.

Mechanistic links between *CCL3L1* dose and HIV/AIDS susceptibility. Increasing *CCL3L1* copy number was positively associated with CCL3/CCL3L1 secretion and negatively associated with the proportion of CD4$^+$ T cells that express CCR5 (Fig. 3, C and D) (*2*). Additionally, there was a dose-dependent association between *CCL3L1* copy number and the viral set point and rate of change in CD4$^+$ T cell counts, two well-established predictors of clinical outcome (*5*); low *CCL3L1* doses were associated with a higher viral set point and greater subsequent T cell loss (Fig. 3, E and F). These relationships might explain the association between *CCL3L1* gene dose and risk of acquiring HIV and disease progression given that (i) chemokines are thought to mediate their HIV-suppressive activity by steric blocking of the interaction between glycoprotein (gp) 120 and CCR5 or ligand-mediated internalization of CCR5, reducing its availability for use by gp 120 (*3*), and (ii) high CCR5 ligand and/or low CCR5 receptor expression represents a correlate of HIV/AIDS protection (*6*–*12*).

Phenotypic equivalency of population-specific *CCL3L1* gene doses. Human populations differ in their *CCL3L1* gene content (Fig. 1). Accordingly, it was important to determine whether an absolute *CCL3L1* copy number (e.g., two copies) was associated with similar transmission- and/or disease-influencing phenotypic effects in different populations. To do so, we compared the associated phenotypic effects of similar and dissimilar *CCL3L1* copy numbers in HIV$^+$ EAs and AAs (Fig. 3, G to N), and the change in the frequency distribution of copy number in these two populations over time (Fig. 3, O and P). The findings indicated that in HIV$^+$ EAs and AAs, the *CCL3L1* copy numbers that corresponded to the population-specific median, half-median, and low doses (i) were associated with comparable rates of disease progression or changes in CD3$^+$, CD4$^+$, or CD8$^+$ T cell counts (Fig. 3, G to N, and table S2), and (ii) had similar trajectories with respect to the changes in their distribution profiles over time (Fig. 3, O and P, and figs. S7 and S8). By contrast, possession of two *CCL3L1* copies (i.e., the median and half-median gene dose in EAs and AAs, respectively) was associated with differing rates of disease progression (Fig. 3K). Consistent with this finding, the trajectories of the change in the frequency distribution of individuals possessing two *CCL3L1* copies differed over time: increasing in HIV$^+$ EAs, but declining in HIV$^+$ AAs (Fig. 3, O and P). These findings, together with those shown in Fig. 2 and SOM section 5.1, collectively support the concept that different *CCL3L1* gene doses among populations are associated with phenotypically similar effects (Fig. 3Q).

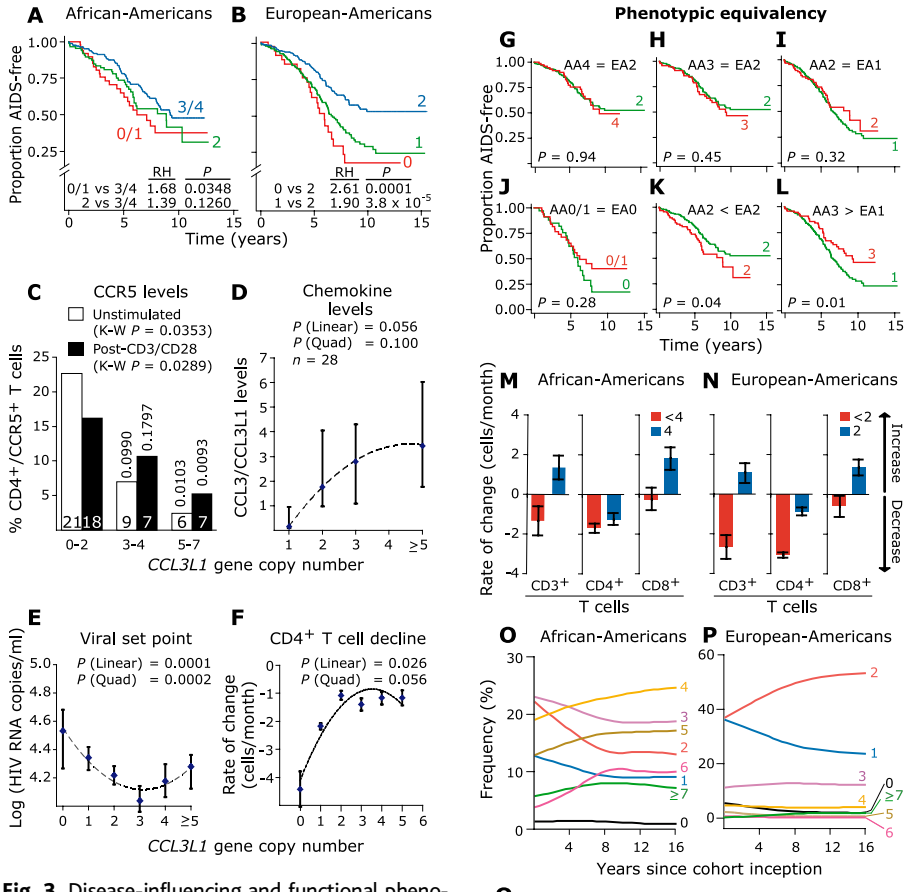

Fig. 3. Disease-influencing and functional phenotypic effects associated with number of *CCL3L1* copies. (**A** and **B**) Kaplan-Meier (KM) survival curves of the development of AIDS in (A) AAs and (B) EAs from the adult WHMC HIV$^+$ cohort who possess a *CCL3L1* copy number equal to or lower than the population-specific median (copy numbers noted adjacent to KM curves). As the population-specific median number of *CCL3L1* copies was three and four in HIV$^+$ and HIV$^-$ AAs, respectively, these two copy numbers were used as the reference genetic strata in (A); the reference group in EAs is two copies. *P* and relative hazard (RH) below the KM curves were determined by Cox proportional hazard models. Overall log-rank significance values and 95% CI for the RHs are shown in fig. S5. (**C**) Relationship between number of *CCL3L1* copies and percentage of CD4$^+$/CCR5$^+$ cells in unstimulated (open bars) or anti-CD3/CD28–stimulated peripheral blood mononuclear cells (black bars). Numbers inside the bars denote the number of individual blood samples studied with the indicated copy numbers. K-W *P*, overall Kruskal-Wallis test *P* value. Vertically oriented numbers indicate *P* values by the Mann-Whitney test for comparison of possession of zero to two versus three to four or five to seven *CCL3L1* copies within each experimental condition. (**D** to **F**) Second-order polynomial regression curves show that (D) CCL3/CCL3L1 concentrations in supernatants of freshly isolated peripheral blood mononuclear cells [for units, see (*4*); *n* = number of individuals], (E) baseline log viral RNA (viral set point), and (F) monthly CD4$^+$ T cell loss have a threshold-type association with *CCL3L1* copies (SOM sections 4.5 to 4.7). (D) and (E) depict medians (±1.7 SD of medians), and (F) depicts 95% CI around the point estimates of the regression coefficients obtained by the General Estimating Equations (GEE) method (*4*). *P* linear and quadratic (quad) indicate significance values for the linear and quadratic terms in the polynomial regression equation, respectively. (**G** to **L**) KM curves of the development of AIDS in HIV$^+$ AAs (red) and EAs (green) who possess a similar or dissimilar *CCL3L1* copy number. The disease-influencing effects associated with possession of [(G) and (H)] median, (I) half-median, and (J) low/null *CCL3L1* doses were similar in EAs and AAs. However, the disease-influencing effects of possession of (K) two copies in AAs (half-median dose in HIV$^-$ AAs) and EAs (median dose) or (L) three copies in AAs (median in HIV$^+$ AAs) and one copy in EAs (half-median in EAs) were not equivalent [see (A) regarding differences in median copy numbers in HIV$^-$ and HIV$^+$ AAs]. Numbers adjacent to the population designators AA and EA indicate the number of copies (e.g., AA4 indicates four copies in AAs). *P* values indicate significance value by log-rank test. =, >, or < indicates the direction of the associated effects. (**M** and **N**) Direction and magnitude of the rate of change in CD3$^+$, CD4$^+$, and CD8$^+$ T cell counts are similar in HIV$^+$ EAs and AAs who possess a *CCL3L1* copy number equal to or lower than the population-specific median (error bars indicate 95% CI; table S2). (**O** and **P**) Results of discrete-time Markov modeling of the evolution of changes in the frequency distribution of *CCL3L1* copy numbers in infinite-sized AA and EA cohorts over 15 years (SOM section 4.8). Numbers adjacent to the curves indicate *CCL3L1* copy numbers. (**Q**) Schema of phenotypic equivalency of the risk of acquiring HIV and disease-influencing effects of population-specific *CCL3L1* doses in EAs and AAs.

They also imply that the phenotypic effects associated with *CCL3L1* gene dosage cannot be estimated by knowing only the absolute *CCL3L1* copy number. This value, in any given individual, is meaningful only if compared with the distribution of *CCL3L1* copies in the geographic ancestral population of the given individual (SOM section 5.1).

Distribution of *CCL3L1* gene copies under HIV selective pressure. The association between *CCL3L1* gene dose and HIV/AIDS susceptibility in adults (Figs. 2 and 3, A and B) predicts that the following pattern should be discernable in a prospective longitudinal cohort in which subjects are recruited at an early stage of infection. Initially, the HIV^+ cohort will be enriched for individuals with *CCL3L1* copy numbers lower than the population-specific median. Over time, the prevalence of these individuals will decrease because of their rapid progression to AIDS/death. As a result, the prevalence of HIV^+ subjects with *CCL3L1* copy numbers equal to or greater than the population-specific median will increase. Thus, with increasing follow-up times, the distribution of *CCL3L1* copies will begin to resemble that found in HIV^- subjects. The value of testing this prediction is that it combines into a single analytical model the analyses of (i) the susceptibility to infection in individuals with different numbers of *CCL3L1* copies, and (ii) the time to equilibrium between the virus and *CCL3L1* genotype–dependent events in the infected host. Our results are consistent with these predictions (Fig. 3, O and P, and figs. S7 to S9). These observations suggest that infection with HIV-1 can exert a negative selective pressure on individuals with low copy numbers that, depending on the strength of this effect in the general population, could change the population-specific distribution of *CCL3L1* copy number.

***CCL3L1* dose and *CCR5* genotypes in HIV/AIDS susceptibility.** We and others have shown that *CCR5* haplotypes that include *CCR5* promoter polymorphisms as well as coding polymorphisms in *CCR2* (CCR2-V64I) and *CCR5* (Δ*32*) influence the risk of acquiring HIV and the rate of disease progression (*12*–*15*). However, CCR5 is part of a complex system in which virus interacts with CCR5 and CCR5 interacts with various ligands. Thus, if gene-gene interactions are not considered, these interactions might complicate analysis of the in vivo contributions of *CCR5* genotypes. This concern is made all the more apparent by the observation that CCR5 protein expression levels are influenced not only by variants in *CCR5* (*16*, *17*), but also by *CCL3L1* (Fig. 3C). Thus, virus × CCR5 × CCL3L1 interactions in vivo and the phenotypic effects associated with *CCR5* genotypes could depend, in part, on the genetic background conferred by *CCL3L1* dose. To test this hypothesis, we determined the phenotypic effects attributable to *CCL3L1* gene dose alone, *CCR5* haplotype pairs (genotypes) alone, and their combined effects.

The HIV^+ adult cohort was stratified into four mutually exclusive genetic risk groups (GRGs) based on possession of a population-specific low or high number of *CCL3L1* copies ($CCL3L1^{low}$ or $CCL3L1^{high}$) and disease-accelerating, i.e., detrimental (det) or non-detrimental (non-det) *CCR5* genotypes ($CCR5^{det}$ or $CCR5^{non\text{-}det}$) (Fig. 4A). Of the four GRGs, $CCL3L1^{high}CCR5^{non\text{-}det}$ and $CCL3L1^{low}CCR5^{det}$ were at the two extremes of HIV/AIDS susceptibility (Fig. 4, B to I). Relative to possession of $CCL3L1^{high}CCR5^{non\text{-}det}$, $CCL3L1^{low}CCR5^{det}$ was associated with a ≥ threefold greater risk of progressing rapidly to 8 of 12 AIDS-defining illnesses (Table 1). By contrast, the $CCL3L1^{high}CCR5^{det}$ and $CCL3L1^{low}CCR5^{non\text{-}det}$ genotypes were associated with a ≤ threefold higher risk of progressing to 3 or 4 of these 12 illnesses, respectively (Table 1).

The trajectory of the frequency distribution profiles of the four *CCL3L1/CCR5* GRGs in individuals with varying follow-up times were also revealing in that they closely paralleled those described previously for a variable number of *CCL3L1* copies alone (compare Fig. 4J with Fig. 3, O and P, and fig. S7 to fig. S9). Thus, significant changes occurred only in the frequencies of the two GRGs that contained $CCL3L1^{low}$ and $CCL3L1^{high}CCR5^{non\text{-}det}$, such that over time the distribution of the GRGs in surviving HIV^+ subjects approached ever closer to the values observed in the HIV^- population (Fig. 4, J to L).

Taken together, in the context of a well-characterized prospective cohort composed of HIV^+ EAs and AAs, the *CCL3L1/CCR5*-based genomic signature for HIV/AIDS susceptibility was $CCL3L1^{low}CCR5^{det} > CCL3L1^{low}CCR5^{non\text{-}det} \geq CCL3L1^{high}CCR5^{det} > CCL3L1^{high}CCR5^{non\text{-}det}$. This observation implied that $CCL3L1^{low}$ may have a stronger effect than disease-accelerating, detrimental *CCR5* genotypes in influencing HIV/AIDS pathogenesis in these two populations. Additionally, these findings suggest that a population-specific low *CCL3L1* dose provides a permissive genetic background for the full expression of the phenotypic effects associated with detrimental *CCR5* genotypes. This was apparent because (i) relative to genotypes that contained only $CCR5^{det}$, those that contained $CCL3L1^{low}$ with or without $CCR5^{det}$ were associated with a higher risk of acquiring HIV (compare green with orange or red color-coded GRGs in Fig. 4, H and I); and (ii) the maximal disease-accelerating effects associated with detrimental *CCR5* genotypes occurred mainly in individuals who also possessed a low number of *CCL3L1* copies relative to the population-specific average (compare Kaplan-Meier plots for $CCL3L1^{high}CCR5^{det}$ and $CCL3L1^{low}CCR5^{det}$ in Fig. 4, E and F).

Public health impact of variations in *CCL3L1* and *CCR5*. In the populations examined, up to 42% of the burden of infection and ~30% of the accelerated rate of progression to AIDS were attributable to variations in

Table 1. Risk of AIDS-defining illness with *CCL3L1/CCR5* GRGs. The reference GRG for statistical analysis is $CCL3L1^{high}CCR5^{non\text{-}det}$ (RH = 1). The AIDS-defining illnesses with sufficient events for statistical analyses recorded in the adult HIV^+ cohort are shown. CMV, cytomegalovirus; HAD, HIV-associated dementia; MAC, *Mycobacterium avium* complex; PCP, *Pneumocystis carinii* pneumonia; PML, progressive multifocal leukoencephalopathy; *n*, number of individuals with the indicated AIDS-defining illness; values in bold and italic indicate significant association.

AIDS-defining illness	*n*	$CCL3L1^{high}CCR5^{det}$			$CCL3L1^{low}CCR5^{non\text{-}det}$			$CCL3L1^{low}CCR5^{det}$		
		RH	95% CI	*P*	RH	95% CI	*P*	RH	95% CI	*P*
CMV infection	100	1.53	0.71–3.30	0.278	1.60	1.00–2.58	0.051	***6.21***	***3.63–10.63***	***2.7×10^{-11}***
Cryptococcosis	33	3.27	0.98–10.87	0.053	***2.46***	***1.00–6.02***	***0.048***	***8.11***	***2.93–22.46***	***5.6×10^{-5}***
Cryptosporidiosis	24	1.21	0.27–5.47	0.802	1.21	0.49–3.00	0.686	1.63	0.36–7.37	0.526
HAD	54	2.05	0.82–5.13	0.126	1.65	0.87–3.11	0.124	***3.18***	***1.33–7.60***	***0.009***
Herpes simplex	26	1.78	0.50–6.41	0.375	1.22	0.49–3.04	0.668	1.66	0.36–7.53	0.513
Histoplasmosis	20	3.32	0.83–13.30	0.090	***2.81***	***1.02–7.74***	***0.045***	1.56	0.19–13.01	0.682
Kaposi sarcoma	74	1.76	0.76–4.05	0.186	1.66	0.96–2.86	0.069	***3.86***	***1.90–7.83***	***2.0×10^{-4}***
Lymphoma	37	***2.87***	***1.10–7.48***	***0.031***	1.42	0.66–3.08	0.369	***3.38***	***1.21–9.43***	***0.020***
MAC	92	***2.22***	***1.09–4.55***	***0.029***	***1.73***	***1.05–2.87***	***0.032***	***5.13***	***2.79–9.45***	***1.5×10^{-7}***
PCP	196	***2.13***	***1.33–3.42***	***0.002***	***1.71***	***1.22–2.39***	***0.002***	***2.95***	***1.84–4.75***	***7.8×10^{-6}***
PML	18	1.72	0.36–8.10	0.494	1.27	0.44–3.67	0.657	2.41	0.51–11.43	0.268
Toxoplasmosis	27	1.49	0.32–6.91	0.610	1.69	0.67–4.25	0.268	***5.34***	***1.77–16.07***	***0.003***

CCL3L1/CCR5 (black bars in Fig. 5 and fig. S11). The largest contributor to the burden of HIV/AIDS was possession of a population-specific low *CCL3L1* copy number (Fig. 5, compare combination of red and orange to green bars, and fig. S11). These findings suggest that the contribution of *CCL3L1* copy number is comparable to or more than that of the *CCR5* genotype in influencing the epidemiology of HIV in the populations examined. These results also substantiate the observation that the disease-accelerating effects associated with variation in *CCR5* depend, in part, on the genetic background of *CCL3L1* copy number.

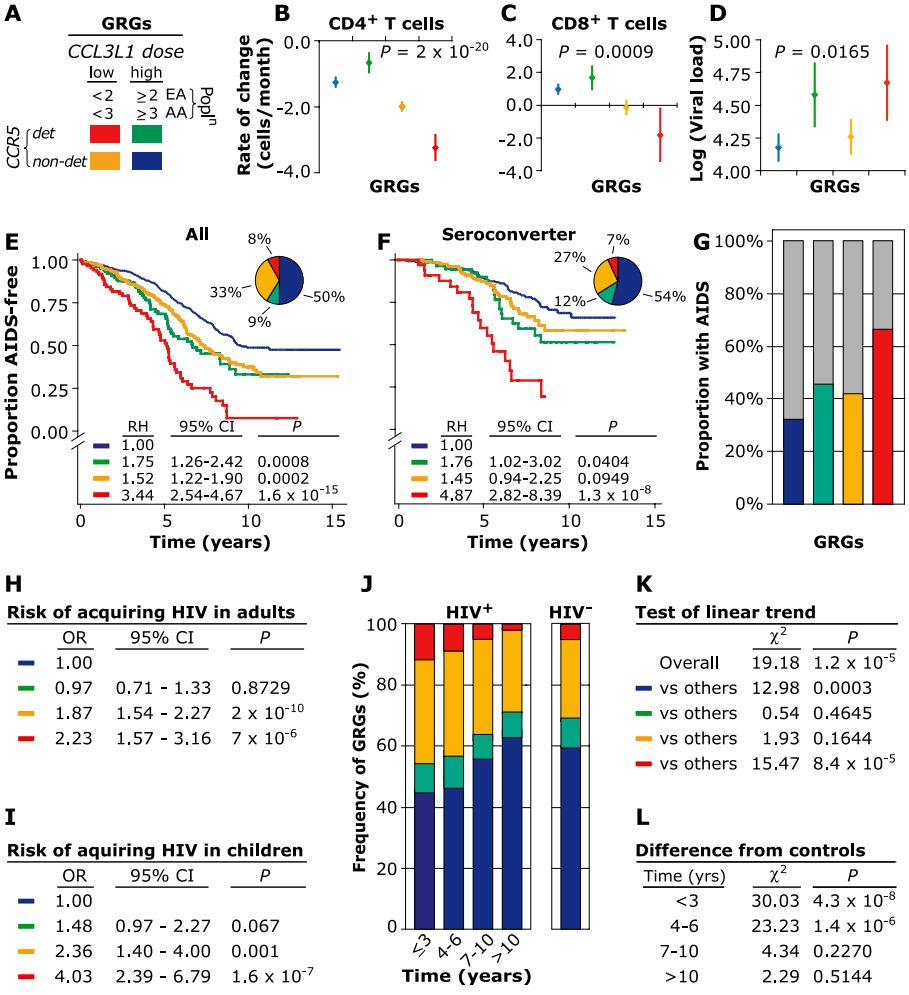

Fig. 4. Risk of acquiring HIV and disease-influencing effects associated with variations in *CCL3L1* and/or *CCR5*. (**A**) Genetic stratification system (SOM section 3). In each population (popl^n), *CCL3L1* dose and *CCR5* genotypes were dichotomized on the basis of whether they were associated with an accelerated disease course (tables S3 to S5). *CCL3L1^{low}* and *CCL3L1^{high}* denote copy numbers < or ≥ population-specific median, respectively (table S3). *CCR5^{det}* and *CCR5$^{non\text{-}det}$* denote population-specific, disease-accelerating, i.e., detrimental (*det*), or nondetrimental *CCR5* genotypes, respectively (table S4). Compared with possession of *CCL3L1^{high}* or *CCR5$^{non\text{-}det}$*, *CCL3L1^{low}* or *CCR5^{det}* was associated with an accelerated disease course (fig. S10). These dichotomized compound genotypes were used to stratify the cohort further into four mutually exclusive GRGs, which reflected (i) the independent disease-accelerating effects associated with population-specific low *CCL3L1* gene doses (*CCL3L1^{low}CCR5$^{non\text{-}det}$*, orange) or detrimental *CCR5* genotypes (*CCL3L1^{high}CCR5^{det}*, green); or (ii) their combined effects (*CCL3L1^{low}CCR5^{det}*, red), all relative to *CCL3L1^{high}CCR5$^{non\text{-}det}$* (blue). This color code is used in the rest of the panels to indicate the four *CCL3L1/CCR5* GRGs. (**B**) CD4$^+$ and (**C**) CD8$^+$ T cell changes associated with the GRGs are depicted as 95% CI around the point estimates of the regression coefficients obtained by the GEE method (*4*). (**D**) Baseline log viral RNA [viral set point; median (±1.7 SD of the median)] associated with the GRGs. *P* values reflect significance values for differences between *CCL3L1^{high}CCR5$^{non\text{-}det}$* and *CCL3L1^{low}CCR5^{det}* by Student's *t* test in (B) and (C) and the Mann-Whitney test in (D). (**E** and **F**) KM curves of the development of AIDS in EAs and AAs from the entire (E) or seroconverting portion (F) of the HIV$^+$ adult cohort after stratifying for the GRGs. (Inset) Pie charts depicting frequency distribution of the GRGs. (**G**) Proportions of individuals within each GRG that developed AIDS. (**H** and **I**) Association of indicated GRGs and risk of acquiring HIV infection in (H) adults or (I) children exposed perinatally to HIV. ORs are lowest in GRGs that lack *CCL3L1^{low}* (green). (**J** and **K**) Changes in the frequency distributions of the GRGs and test of linear trend for individuals with varying follow-up times. (**L**) Differences in the frequency distribution of GRGs between HIV$^+$ and HIV$^-$ adults. In (H) and (J), to ensure appropriate ethnic/racial matching for the comparisons of the frequency distributions between HIV$^+$ and HIV$^-$ individuals, these analyses are for the EA, AA, and HA portions of the infected adult cohort (tables S3 and S4; tables also show the genotypes used for the pediatric cohort in (I) (*4*).

Discussion. These findings have five major implications. First, they provide a precedent for a link between segmental duplication events leading to changes in the dose of an immune response gene and variability in the phenotypic response to an infectious disease. Recent human-nonhuman primate comparative genomic analyses have led to the prediction that genes embedded within segmental duplications might have enhanced the ability of humans to adapt to their environments (*1*, *18*). Our findings support this prediction.

Second, *CCL3L1* gene dose is a previously unrecognized means of buffering against the risk of HIV infection and/or disease progression in the populations examined. *CCL3L1* gene doses lower than the population-specific average provide a genetically "unbuffered" state with respect to the risk of HIV/AIDS susceptibility. However, it is important to emphasize that it is not the absolute gene copy number per se, but the copy number within the overall genetic context that confers phenotypic expression. This genetic context varies among populations as a result of their different demographic and evolutionary histories. Thus, an individual's specific *CCL3L1* gene dose and *CCR5* genotype are associated with susceptibility to HIV/AIDS, but only when viewed in the context of that person's geographical ancestry (Fig. 3Q) (*14*).

Third, within the populations examined, the Bradford-Hill criteria (*19*) for causality between *CCL3L1* dose and risk of acquiring HIV were met (SOM section 5.3). Thus, by analogy to the genetic studies that established the paradigm of "no CCR5–no HIV-1 infection," the current

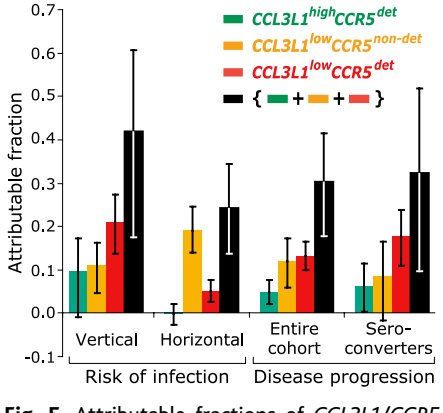

Fig. 5. Attributable fractions of *CCL3L1/CCR5* GRGs for risk of acquiring HIV (vertical, mother-to-child; horizontal, adult-to-adult) and rate of disease progression relative to *CCL3L1^{high}CCR5$^{non\text{-}det}$* in the indicated clinical settings. Vertical bars indicate the point estimate, whereas error bars represent the 95% CI around the point estimate of the attributable fraction.

findings establish that of "*CCL3L1*^{low}–enhanced HIV/AIDS susceptibility." These findings provide strong genetic underpinnings for the substantial body of evidence that CCR5 ligands play an important anti–HIV-1 role in vivo (*20*). Paradoxically, they also indicate that a network of HIV-suppressive CCR5 ligands (e.g., CCL5) cannot fully compensate for the functional state conferred by *CCL3L1*^{low}. Therefore, CCL3L1-mediated immune responses may be required to thwart HIV infection and the complications that occur during HIV-induced immune suppression.

Fourth, *CCL3L1* gene dose may be an important genetic correlate of vaccine responsiveness. A comparative analysis of the immunological phenotype linked to the GRGs associated with the extremes of susceptibility (i.e., *CCL3L1*^{low}*CCR5*^{det} and *CCL3L1*^{high}*CCR5*$^{non\text{-}det}$) could provide key insights into the immune correlates of an effective vaccine. This stems from several vaccine studies in simian models showing that CCR5 ligand production is a true predictor of protection and animals that produce higher levels of chemokines prevaccination exhibit greater protection (*20*–*22*).

Finally, and of broader import, 5% of the human genome contains duplicated sequences enriched for genes involved in immunity (*1*), and some of these genes have dosage effects. Thus, the present findings provide both a precedent and a framework for elucidating their relationship to human diseases.

References and Notes

1. J. A. Bailey *et al.*, *Science* **297**, 1003 (2002).
2. J. R. Townson, L. F. Barcellos, R. J. Nibbs, *Eur. J. Immunol.* **32**, 3016 (2002).
3. P. Menten, A. Wuyts, J. Van Damme, *Cytokine Growth Factor Rev.* **13**, 455 (2002).
4. Materials and methods are available as supporting material on *Science* Online.
5. J. W. Mellors *et al.*, *Ann. Intern. Med.* **126**, 946 (1997).
6. L. Wu *et al.*, *J. Exp. Med.* **185**, 1681 (1997).
7. D. Zagury *et al.*, *Proc. Natl. Acad. Sci. U.S.A.* **95**, 3857 (1998).
8. A. Garzino-Demo *et al.*, *Proc. Natl. Acad. Sci. U.S.A.* **96**, 11986 (1999).
9. J. Reynes, V. Baillat, P. Portales, J. Clot, P. Corbeau, *J. Acquir. Immune Defic. Syndr.* **34**, 114 (2003).
10. H. Ullum *et al.*, *J. Infect. Dis.* **177**, 331 (1998).
11. W. A. Paxton *et al.*, *J. Infect. Dis.* **183**, 1678 (2001).
12. J. Tang, R. A. Kaslow, *AIDS* **17** (suppl. 4), S51 (2003).
13. M. P. Martin *et al.*, *Science* **282**, 1907 (1998).
14. E. Gonzalez *et al.*, *Proc. Natl. Acad. Sci. U.S.A.* **96**, 12004 (1999).
15. A. Mangano *et al.*, *J. Infect. Dis.* **183**, 1574 (2001).
16. S. Mummidi *et al.*, *J. Biol. Chem.* **275**, 18946 (2000).
17. J. R. Salkowitz *et al.*, *Clin. Immunol.* **108**, 234 (2003).
18. R. V. Samonte, E. E. Eichler, *Nature Rev. Genet.* **3**, 65 (2002).
19. D. L. Weed, *Hematol. Oncol. Clin. North Am.* **14**, 797 (2000).
20. A. L. DeVico, R. C. Gallo, *Nature Rev. Microbiol.* **2**, 401 (2004).
21. J. L. Heeney *et al.*, *Proc. Natl. Acad. Sci. U.S.A.* **95**, 10803 (1998).
22. R. K. Ahmed *et al.*, *Clin. Exp. Immunol.* **129**, 11 (2002).

23. We thank the Board members and reviewers, including the statistical referee, for critically reviewing various aspects of this work and for very valuable suggestions; G. Crawford, B. Kasinath, G. Nabel, J. Burns, B. Cherniak, members of the Infectious Diseases division for helpful discussions and critical reading of the manuscript; E. Fattig and M. Hildebrand for technical assistance; N. Chopra and J. Sharron for graphic work; and A. S. Ahuja for forbearance. The Henry M. Jackson Foundation and the Military HIV Program, Walter Reed Army Institute of Research contributed support for the WHMC patient cohort as part of the Tri-Service HIV Program. Supported by the Veterans Administration Center on AIDS and HIV-1 infection, and grants from NIH (AI046326, AI043279, and MH069270) (S.K.A.). S.K.A. is a recipient of the Elizabeth Glaser Scientist Award and the Burroughs Wellcome Clinical Scientist Award in Translational Research. Because of space constraints, we regret our inability to cite additional excellent work. The views expressed herein are those of the authors and do not reflect the official policy of the Department of Defense or other departments of the U.S. government.

Supporting Online Material
www.sciencemag.org/cgi/content/full/1101160/DC1
Materials and Methods
SOM Text
Figs. S1 to S16
Tables S1 to S7
References and Notes

7 June 2004; accepted 22 December 2004
Published online 6 January 2005;
10.1126/science.1101160
Include this information when citing this paper.

REPORTS

The Geometric Distance and Proper Motion of the Triangulum Galaxy (M33)

Andreas Brunthaler,[1,2]* Mark J. Reid,[3] Heino Falcke,[4,5] Lincoln J. Greenhill,[3] Christian Henkel[1]

We measured the angular rotation and proper motion of the Triangulum Galaxy (M33) with the Very Long Baseline Array by observing two H_2O masers on opposite sides of the galaxy. By comparing the angular rotation rate with the inclination and rotation speed, we obtained a distance of 730 ± 168 kiloparsecs. This distance is consistent with the most recent Cepheid distance measurement. M33 is moving with a velocity of 190 ± 59 kilometers per second relative to the Milky Way. These measurements promise a method to determine dynamical models for the Local Group and the mass and dark-matter halos of M31, M33, and the Milky Way.

Measuring the proper motion and geometric distances of nearby galaxies has been a long-standing problem. As part of a famous debate about the nature of galaxies, van Maanen—an experienced observer—claimed in 1923 to have measured a large proper motion and angular rotation rate for the Triangulum Galaxy (M33) on photographic plates separated by 12 years (*1*). These results were proven incorrect by Hubble through the discovery of Cepheids in M33 that showed a large distance (*2*). Measuring proper motions at this large distance was beyond the capabilities of their time. This pushed the detection of galaxy proper motions beyond the capabilities of past experiments. Yet galaxy proper motions are important for many astrophysical issues, of which two are addressed in this report.

First, measuring accurate distances is of great importance to all fields of astrophysics, from stellar astronomy to cosmology. The calibration of most standard candles used for measuring extragalactic distances is tied directly or indirectly to the distance to one galaxy, the Large Magellanic Cloud (LMC), which remains controversial (*3*, *4*). Hence, it is important to obtain geometric distances to nearby galaxies in which well-understood standard candles can be studied. This allows independent calibration and verification of the extragalactic distance scale.

Another important issue is the distribution of luminous and dark matter in the local universe. The problem when trying to derive the gravitational potential of the Local Group of galaxies (*5*) is that usually only radial velocities are known from the Doppler effect and statistical approaches have to be used (*6*, *7*). The proper motions of some nearby galaxies in the Milky Way subgroup have been obtained from comparing historic photographic plates (*8*, *9*), but a confirmation

[1]Max-Planck-Institut für Radioastronomie, Auf dem Hügel 69, 53121 Bonn, Germany. [2]Joint Institute for Very Long Baseline Interferometry in Europe, Postbus 2, 7990 AA Dwingeloo, Netherlands. [3]Harvard-Smithsonian Center for Astrophysics, 60 Garden Street, Cambridge, MA 02138, USA. [4]ASTRON, Postbus 2, 7990 AA Dwingeloo, Netherlands. [5]Department of Astrophysics, Radboud Universiteit Nijmegen, Postbus 9010, 6500 GL Nijmegen, Netherlands.

*To whom correspondence should be addressed. E-mail: brunthaler@jive.nl

of these measurements will require decades. With very long baseline interferometry (VLBI) and phase-referencing techniques, the proper motions for galaxies within the Local Group, on scales of tens of microarcseconds per year, can now be measured. The most suitable strong and compact radio sources in the Local Group for such a VLBI experiment are the strong H_2O masers in M33 and in the galaxy IC 10 (*10*, *11*).

We observed two H II (ionized atomic hydrogen) regions in M33 (*12*) with known H_2O maser activity, M33/19 and IC 133, with the National Radio Astronomy Observatory (NRAO) Very Long Baseline Array (VLBA), eight times between March 2001 and January 2004. M33/19 is located in the southeastern part of M33, whereas IC 133 is located in the northeast of M33 (Fig. 1). Our observations are grouped into four epochs, each comprising two closely spaced observations, to enable assessment of overall accuracy and systematic errors (Table 1). The separations of the two observations within each epoch were large enough that the weather conditions were uncorrelated but small enough that changes in the positions were negligible during this time.

We observed four 8-MHz bands in dual circular polarization. The 128 spectral channels in each band yielded a channel spacing of 62.5 kHz, equivalent to 0.84 km s^{-1}, and covered a velocity range of 107 km s^{-1}. The observations involved rapid switching between the phase-calibrator J0137+3122, which is a compact background source with continuum emission, and the target sources IC 133 and M33/19 in the sequence J0137+3122, IC 133, J0137+3122, M33/19, J0137+3122. With source changes every 30 s, an integration time of 22 s was achieved. The background source was unresolved in all epochs and was assumed to be stationary on the sky. Because J0137+3122 was separated by only 1° on the sky from the masers, we obtained a precise angular separation measurement for all sources.

The data were edited and calibrated with standard techniques in the Astronomical Image Processing System (AIPS) as well as zenith delay corrections (*13*). The masers in IC 133 and M33/19 were imaged with standard techniques in AIPS. In IC 133, we detected 29 distinct emission features in position, and the spatial distribution was very similar to earlier observations (*10*, *14*, *15*). All components were unresolved. In M33/19, we detected eight maser features. Two features were separated by less than a beam size and blended together. These two features were fit by two elliptical Gaussian components simultaneously. All other features were fit by a single elliptical Gaussian component.

The maser emissions in M33/19 and IC 133 are variable on time scales less than 1 year. Between the epochs, new maser features appeared and others disappeared. However, we were able to detect and follow the motions of four features in M33/19 and six features in IC 133 over all four epochs. The feature identification was based on the positions and radial velocities of the maser emissions. Each feature was usually detected in several frequency channels. A rectilinear motion was fit to each maser feature in each velocity channel separately. We discarded fits with reduced χ^2 larger than 3, as they are likely affected by blending or component misidentification. All features showed consistent motions within their errors (2σ). The accuracy and number of measured motions was not adequate to model the internal dynamics of the IC 133 and M33/19 regions (such as outflow) as was done in earlier observations (*15*, *10*).

We then calculated the variance weighted average of all motions. This yielded an average motion of the maser features in M33/19 of 35.5 ± 2.7 microarc sec (μas) $year^{-1}$ in right ascension and −12.5 ± 6.3 μas $year^{-1}$ in declination relative to the background source. For IC 133, we obtained an average motion of 4.7 ± 3.2 μas $year^{-1}$ in right ascension and −14.1 ± 6.4 μas $year^{-1}$ in declination.

We also calculated the average position of all maser features for each observation (Figs. 2 and 3). We used the individual fits for each maser feature to remove a constant position offset for each maser feature. We used the position offsets at day 229 of 2002, which is in the middle of our observations. We then calculated the variance weighted average of the positions of all detected features. A fit of a rectilinear motion to these average positions yielded motions of 37 ± 5 μas $year^{-1}$ in right ascension and −13 ± 6 μas $year^{-1}$ in declination for M33/19. For IC 133, we obtained

Table 1. Observation date, observation length t_{obs}, beam size θ, and position angle *PA*.

Epoch	Date	t_{obs} (hours)	θ (mas)	PA (°)
I	03/27/2001	10	0.88 × 0.41	164
I	04/05/2001	10	0.86 × 0.39	169
II	01/28/2002	10	0.62 × 0.33	176
II	02/03/2002	10	0.71 × 0.33	175
III	10/30/2002	10	0.87 × 0.38	171
III	11/12/2002	10	0.84 × 0.36	165
IV	12/14/2003	12	0.85 × 0.36	159
IV	01/08/2004	12	1.15 × 0.47	164

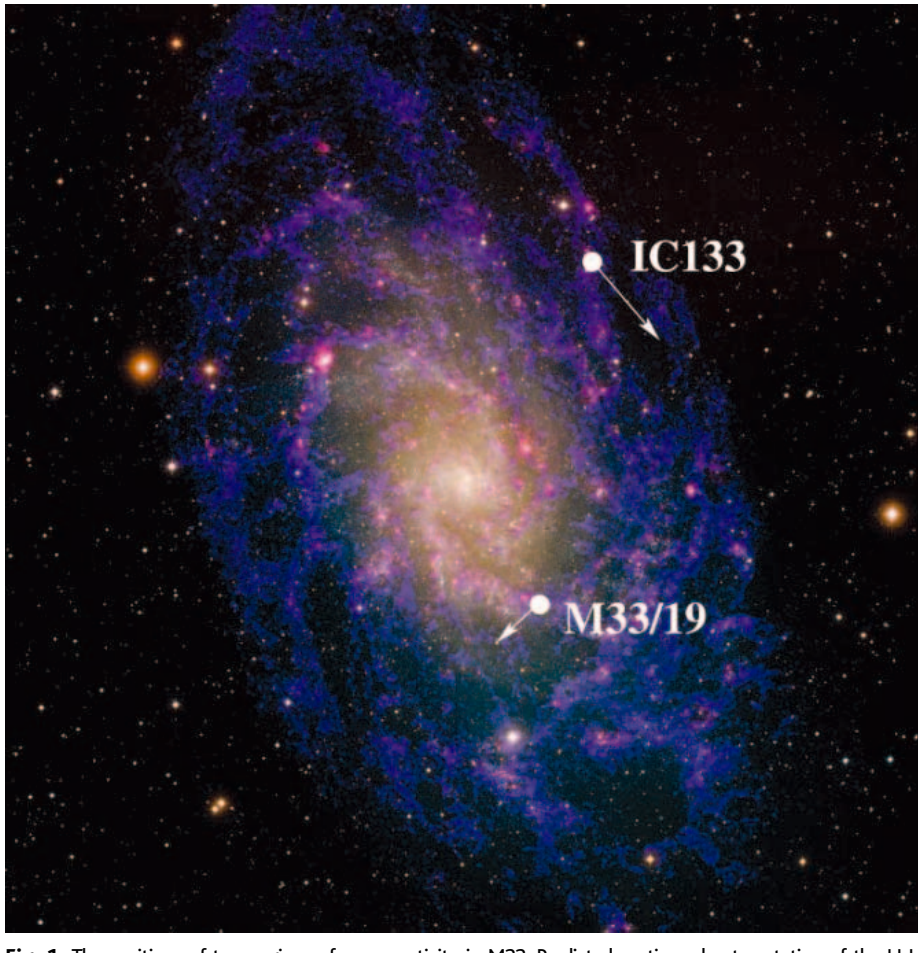

Fig. 1. The positions of two regions of maser activity in M33. Predicted motions due to rotation of the H I disk are also shown. [Image courtesy of T. A. Rector [National Radio Astronomy Observatory (NRAO)/Associated Universities, Inc. (AUI)/NSF and National Optical Astronomy Observatory (NOAO)/Association of Universities for Research in Astronomy (AURA)/NSF], D. Thilker (NRAO/AUI/NSF), and R. Brown (ASTRON)].

a motion of 3 ± 3 μas year^{-1} in right ascension and −13 ± 10 μas year^{-1} in declination. This is consistent with the variance weighted average of all maser feature motions and suggests that the systematic internal motions within the two regions (such as outflow) are probably not a substantial source of bias. The difference in the maser position of the two closely spaced observations within each epoch was used to estimate the accuracy of the position measurements. The average position error over the four epochs was 7.7 μas in right ascension and 9.8 μas in declination.

The relative motions between M33/19 and IC 133 are independent of the proper motion of M33 and any contribution from the rotation of the Milky Way. Knowing the rotation curve and inclination of the galactic disk, we can predict the relative angular motion of the two masing regions as a function of distance. The rotation of the H I gas in M33 has been measured, and the measured velocities were fit with a tilted-ring model (*16*). We used this model of the rotation of M33 to calculate the expected transverse velocities of M33/19 and IC 133. For M33/19, we expect a motion of 42.4 km s^{-1} in right ascension and −39.6 km s^{-1} in declination. For IC 133, we expect −64.0 km s^{-1} in right ascension and −74.6 km s^{-1} in declination. This gives a relative motion of 106.4 km s^{-1} in right ascension and 35 km s^{-1} in declination between the two regions of maser activity.

The radial velocities of the H_2O masers in M33/19 and IC 133 and the H I gas at the same positions agree (<10 km s^{-1} difference). This suggests that the maser sources are moving with the H I gas in the galaxy. However, although the rotation model and the radial velocity of the H I gas at the position of IC 133 is also consistent (<5 km s^{-1}), there is a difference of ~15 km s^{-1} at the position of M33/19. This indicates the presence of a tilt in the disk that is not covered by the model of (*16*). Because of this uncertainty in the rotation model, we conservatively assume a systematic error of 20 km s^{-1} in each velocity component for the relative velocity of the two maser components.

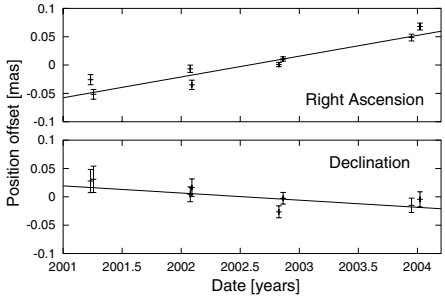

Fig. 2. Average position of the maser M33/19 in (**top**) right ascension and (**bottom**) declination relative to a background source. mas, milliarcseconds.

Comparing the measured angular motion of 30.8 ± 4 μas year^{-1} in right ascension with the expected linear motion of 106 ± 20 km s^{-1}, one gets a geometric distance of D = 730 ± 100 ± 135 kpc, where the first error indicates the statistical error from the proper motion measurements and the second error is the systematic error from the rotation model. After less than 3 years of observations, the uncertainty in the distance estimate is dominated by the uncertainty of the rotation model of M33. Within the errors, the geometric distance of 730 ± 100 ± 135 kpc is consistent with recent Cepheid and tip of the red giant branch (TRGB) distances of 802 ± 51 kpc and 794 ± 23 kpc, respectively (*17*, *18*). It also agrees with a geometric distance estimate of 800 ± 180 kpc (*10*).

The observed proper motion $\vec{v}_{prop}$ of a maser (e.g., M33/19 or IC 133) in M33 can be decomposed into three components: $\vec{v}_{prop} = \vec{v}_{rot} + \vec{v}_{\odot} + \vec{v}_{M33}$. Here $\vec{v}_{rot}$ is the motion of the maser due to the internal galactic rotation in M33, and $\vec{v}_{\odot}$ is the apparent motion of M33 caused by the rotation of the Sun around the Galactic center. The last contribution, $\vec{v}_{M33}$, is the proper motion of M33 relative to the Milky Way.

The motion of the Sun can be decomposed into a circular motion of the local standard of rest (LSR) and the peculiar motion of the Sun. The peculiar motion of the Sun has been determined from Hipparcos data (*19*) to be 10.00 ± 0.36 km s^{-1} radially inwards, 5.25 ± 0.62 km s^{-1} in the direction of Galactic rotation, and 7.17 ± 0.38 km s^{-1} vertically upwards. The International Astronomical Union adopted LSR moves with a velocity of 220 km s^{-1} toward a Galactic longitude of l = 90° and latitude of b = 0° (*20*). New VLBI measurements of the proper motion of Sgr A*, the compact radio source at the Galactic center, indicate a slightly higher circular velocity of the LSR, 236 ± 15 km s^{-1}, for a distance of 8 ± 0.5 kpc between the Sun and the Galactic center, where the uncertainty is dominated by the uncertainty in the distance to the Galactic center (*13*). Using a LSR velocity of 236 ± 15 km s^{-1} plus the peculiar velocity of the Sun from (*19*), the motion of the Sun causes an apparent proper motion of $\dot{\alpha}_{\odot}$ = 52.5 ± 3.3 μas year^{-1} in right ascension and $\dot{\delta}_{\odot}$ = −37.7 ± 2.4 μas year^{-1} in declination, assuming a distance of 730 kpc and the Galactic coordinates of M33 (l = 133.6°, b = −31.3°).

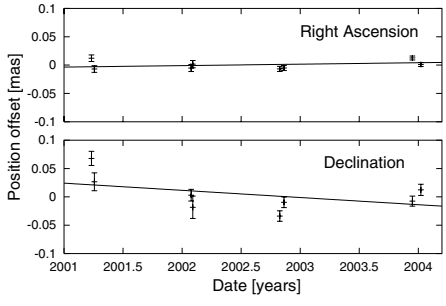

Fig. 3. Average position of the maser IC 133 in (**top**) right ascension and (**bottom**) declination relative to a background source.

Using the rotation model of (*16*), the contribution from the rotation of M33 (for IC 133) is $\dot{\alpha}_{rot}$ = −18.5 ± 6 μas year^{-1} in right ascension and $\dot{\delta}_{rot}$ = −21.6 ± 6 μas year^{-1} in declination. Here, we assumed again an uncertainty of 20 km s^{-1} for the rotation velocity and a distance of 730 kpc. Combining these velocity vectors, we get the proper motion of M33:

$$\dot{\alpha}_{M33} = \dot{\alpha}_{prop} - \dot{\alpha}_{rot} - \dot{\alpha}_{\odot}$$
$$= (4.7 \pm 3.2 + 18.5 \pm 6 - 52.5 \pm 3.3)\frac{\mu as}{year}$$
$$= -29.3 \pm 7.6\frac{\mu as}{year}$$
$$= -101 \pm 35\frac{km}{s}$$

and

$$\dot{\delta}_{M33} = \dot{\delta}_{prop} - \dot{\delta}_{rot} - \dot{\delta}_{\odot}$$
$$= (-14.1 \pm 6.4 + 21.6 \pm 6 + 37.7 \pm 2.4)\frac{\mu as}{year}$$
$$= 45.2 \pm 9.1\frac{\mu as}{year}$$
$$= 156 \pm 47\frac{km}{s}$$

The transverse velocity changes by less than 5 km s^{-1} if we use the TRGB distance of 794 ± 23 kpc (*18*) for this analysis. Finally, the systemic radial velocity of M33 is −179 km s^{-1} (*16*). The radial component of the rotation of the Milky Way toward M33 is −140 ± 9 km s^{-1}. Hence, M33 is moving at −39 ± 9 km s^{-1} toward the Milky Way. This gives us the three-dimensional velocity vector of M33 (Fig. 4). The total velocity of M33 relative to the Milky Way is 190 ± 59 km s^{-1}.

For Andromeda (galaxy M31), only one component of the three-dimensional velocity vector is known: the radial velocity of

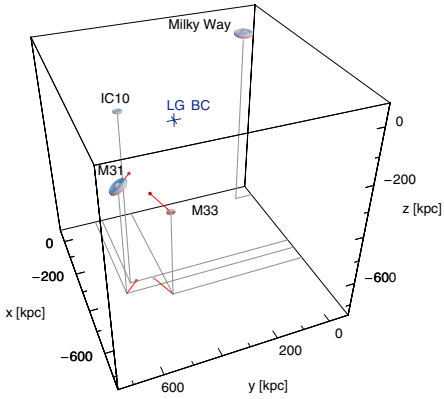

Fig. 4. Schematic view of the Local Group with the space velocity of M33 and the radial velocity of M31. The blue cross marks the position of the Local Group Barycenter (LG BC) (*25*).

116 km s^{-1} (301 km s^{-1} systemic velocity minus 185 km s^{-1} contribution from solar motion) toward the Milky Way. However, the Milky Way is possibly falling toward M31, because there are no other large galaxies in the Local Group to generate angular momentum through tidal torques (*21*). Following this argument, we assume a proper motion of 0 for M31. The geometry of the Andromeda subgroup depends on the relative distance between M31 and M33. Thus, it is crucial to use distances for the two galaxies that have similar systematic errors, and we used the TRGB distances to M33 and M31 (*18*, *22*). The angle between the velocity vector of M33 relative to M31 and the vector pointing from M33 toward M31 was 30° ± 15°. For an angle of 30°, only elliptical orbits with eccentricities of $e > 0.88$ are possible. For the largest allowed angle of 45°, the eccentricities are restricted to $e > 0.7$. This eccentricity limit weakens if the proper motion of M31 is non-negligible, and for a motion of >150 km s^{-1}, any eccentricity is possible.

If M33 is bound to M31, then the relative velocity of the two galaxies must be smaller than the escape velocity. This gives—for a zero proper motion of M31—a lower limit for the mass of M31 of 1.2×10^{12} solar mass ($M_\odot$). A substantial proper motion of M31 could reduce or increase the relative velocity and the lower mass limit of M31. On the other hand, the dynamical friction of M31 on M33 indicates that M31 cannot have a very massive halo of more than $\sim 10^{12}$ $M_\odot$ unless the orbit of M33 has a low eccentricity. Otherwise, the dynamical friction would have led to a decay of the orbit of M33 (*23*). This agrees with a recent estimate of $12.3^{+18}_{-6} \times 10^{11}$ $M_\odot$ derived from the three-dimensional positions and radial velocities of its satellite galaxies (*24*).

More than 80 years after van Maanen's observation, we have measured the rotation and proper motion of M33. These measurements provide a method to determine dynamical models for the Local Group and the mass and dark matter halo of Andromeda and the Milky Way.

References and Notes

1. A. van Maanen, *Astrophys. J.* **57**, 264 (1923).
2. E. P. Hubble, *Astrophys. J.* **63**, 236 (1926).
3. W. L. Freedman *et al.*, *Astrophys. J.* **553**, 47 (2001).
4. A. Udalski *et al.*, *Astrophys. J.* **L509**, L25 (1998).
5. The Local Group is a small galaxy group in the local universe that includes the Milky Way, M31, M33, and 30 to 40 other small galaxies within a radius of ~1 Mpc.
6. F. D. A. Hartwick, W. L. W. Sargent, *Astrophys. J.* **221**, 512 (1978).
7. A. S. Kulessa, D. Lynden-Bell, *Mon. Not. R. Astron. Soc.* **255**, 105 (1992).
8. B. F. Jones, A. R. Klemola, D. N. C. Lin, *Astron. J.* **107**, 1333 (1994).
9. A. E. Schweitzer, K. M. Cudworth, S. R. Majewski, N. B. Suntzeff, *Astrophys. J.* **110**, 2747 (1995).
10. A. L. Argon *et al.*, *Astrophys. J.* **615**, 702 (2004).
11. A. L. Argon *et al.*, *Astrophys. J.* **422**, 586 (1994).
12. F. P. Israel, P. C. van der Kruit, *Astron. Astrophys.* **32**, 363 (1974).
13. M. J. Reid, A. Brunthaler, *Astrophys. J.* **616**, 872 (2004).
14. L. J. Greenhill *et al.*, *Astrophys. J.* **364**, 513 (1990).
15. L. J. Greenhill, J. M. Moran, M. J. Reid, K. M. Menten, H. Hirabayashi, *Astrophys. J.* **406**, 482 (1993).
16. E. Corbelli, S. E. Schneider, *Astrophys. J.* **479**, 244 (1997).
17. M. G. Lee, M. Kim, A. Sarajedini, D. Geisler, W. Gieren, *Astrophys. J.* **565**, 959 (2002).
18. A. W. McConnachie *et al.*, *Mon. Not. R. Astron. Soc.* **350**, 243 (2004).
19. W. Dehnen, J. J. Binney, *Mon. Not. R. Astron. Soc.* **298**, 387 (1998).
20. F. J. Kerr, D. Lynden-Bell, *Mon. Not. R. Astron. Soc.* **221**, 1023 (1986).
21. F. D. Kahn, L. Woltjer, *Astrophys. J.* **130**, 705 (1959).
22. A. W. McConnachie *et al.*, *Mon. Not. R. Astron. Soc.* **356**, 979 (2005).
23. S. T. Gottesman, J. H. Hunter, V. Boonyasait, *Mon. Not. R. Astron. Soc.* **337**, 34 (2002).
24. N. W. Evans, M. I. Wilkinson, *Mon. Not. R. Astron. Soc.* **316**, 929 (2000).
25. S. van den Bergh, *Astron. Astrophys. Rev.* **9**, 273 (1999).

26. The VLBA is operated by the NRAO, a facility of the NSF operated under cooperative agreement by Associated Universities, Inc.

6 December 2004; accepted 14 January 2005
10.1126/science.1108342

Laser-Initiated Shuttling of a Water Molecule Between H-Bonding Sites

Jasper R. Clarkson,[1] Esteban Baquero,[1] V. Alvin Shubert,[1] Evgeniy M. Myshakin,[2] Kenneth D. Jordan,[2] Timothy S. Zwier[1]*

The two-step laser excitation scheme of stimulated emission pumping (SEP) induces shifts of a single water molecule between two remote hydrogen bonding sites on *trans*-formanilide. This reaction can be initiated by selective excitation of either isomer (C=O-bound or NH-bound) with different SEP excitation wavelengths. Energy (*E*) thresholds for isomerization in both directions have been measured [796 wave numbers ≤ *E*(C=O→NH) ≤ 988 wave numbers and 750 wave numbers ≤ *E*(NH→C=O) ≤ 988 wave numbers], and the energy difference Δ*E* between the C=O-bound and NH-bound isomers was extracted (–238 wave numbers ≤ Δ*E* ≤ +192 wave numbers).

The strong solvating capacity of water is due in large part to formation of hydrogen bonds with solutes. If a solute has both donor (XH—OH_2) and acceptor (X′–HOH) H-bonding sites, an individual water molecule can bind to either one. The full solvation shell is a complex network of many H-bonded water molecules, and the interplay between solvent and solute that affects the physical and reactive properties of the embedded solute is difficult to sort out (*1*–*6*).

In a gas-phase supersonic expansion, it is possible to form isolated, specific solute-$(H_2O)_n$ clusters and to probe them spectroscopically (*7*–*11*). During the cooling that accompanies the expansion, the water molecules preferentially bind to the solute at one of the H-bonding sites on the molecule. Spectroscopic studies of these complexes have determined structures and measured binding energies of the water molecule to the solute (*7*, *8*, *11*–*14*). Such data can be used to refine the semi-empirical potentials (*15*–*19*) that are widely used in molecular dynamics and Monte Carlo simulations of chemical and biological processes in aqueous solution. However, studies of solute-$(H_2O)_n$ clusters typically probe the region of the intermolecular potential energy surface only near the most stable minima. As a result, semi-empirical and ab initio–based intermolecular potentials often lack molecular-scale checks on their accuracy far away from the potential minima, particularly regarding the energy barriers that separate the minima.

We recently introduced an experimental method that can directly measure the energetic barriers to conformational isomerization in flexible molecules (*20*). Here, we apply this method to the isomerization of a 1:1 water-solute complex, in which the water molecule moves between H-bonding sites on the same solute. This isomerization reaction requires the water molecule to break one H bond with the solute and then, after translation, to form a second H bond. The barrier probed is caused by a transition state configuration in which the water molecule lies between the two sites, still interacting with the solute in a configuration far from either minimum.

The solute chosen for these studies, *trans*-formanilide (TFA), has a *trans*-amide group attached to an aromatic ring, with its N–H donor and C=O acceptor sites pointing in opposite directions (Fig. 1A). The TFA-H_2O complex is among the most thoroughly studied water-containing complexes, partly because it is prototypical of water's interactions with the

[1]Department of Chemistry, 560 Oval Drive, Purdue University, West Lafayette, IN 47907–2084, USA. [2]Department of Chemistry, University of Pittsburgh, Pittsburgh, PA 15260, USA.

*To whom correspondence should be addressed. E-mail: zwier@purdue.edu

biologically important amide group and partly because it is formed in a supersonic expansion with roughly equal populations in the NH-bound and C=O-bound isomeric forms (*21*–*25*).

These two isomers are readily distinguished from one another spectroscopically. A laser-induced fluorescence spectrum (Fig. 1B) identifies the $S_1 \leftarrow S_0$ origin transitions of the two isomeric complexes, which connect the zero-point vibrational level (ZPL) of the ground electronic state to the zero-point level of the first singlet excited electronic state (*21*, *22*). Fluorescence-dip infrared spectroscopy has been used to record infrared spectra of each complex in the OH and NH stretch region (2800 to 3800 cm^{-1}) (fig. S1) (*26*), confirming the assignments of earlier work. (*23*) On this basis, the labeled transitions (Fig. 1B) could be assigned unambiguously to the NH-bound and C=O-bound TFA-H_2O complexes, respectively (Fig. 1A) (*23*).

To determine the energy needed to isomerize between these two structures, we used a cool-excite-recool-probe temporal protocol (Fig. 1C) introduced recently (*20*, *27*–*29*). In the first step, the NH-bound and carbonyl-bound TFA-water complexes are formed and cooled to their ZPLs early in the supersonic expansion. The complexes are then vibrationally excited via a two-laser pump-dump sequence called stimulated emission pumping (SEP) (*20*).

The SEP pump laser (0.1 mJ per pulse) is fixed to the $S_1 \leftarrow S_0$ origin transition of one of the TFA-H_2O isomers (36,118 cm^{-1} for the C=O-bound isomer and 35,787 cm^{-1} for the NH-bound isomer). A second ultraviolet (UV) laser beam (the dump laser, 1mJ per pulse), spatially overlapped with the first and delayed by 2 ns, was tuned through the transitions from the S_1 ZPL to specific vibrational levels in the ground electronic state [$S_1(ZPL) \rightarrow S_0(v)$]. This time delay is short compared with the S_1 excited state lifetime of the complex (~10 ns). Stimulated emission from $S_1(ZPL)$ to $S_0(v)$ was possible because of the population inversion between the S_1 0^0 level (populated by the pump pulse) and the $S_0(v)$ lower level, which has all of its population removed by the cooling in the expansion.

The wavelength λ_2 is tuned to different $S_1(0^0) \rightarrow S_0(v)$ transitions to place a well-defined amount of internal energy into one isomer of the complex. A second stage of collisional cooling dissipates the excess vibrational energy, and then in the collision-free region of the expansion a UV probe pulse (of fixed wavelength λ_3) interrogates the resulting population of reactant or product by using laser-induced fluorescence (LIF).

If the dump laser populates a vibrational level below the lowest barrier to isomerization, no reaction can occur in the absence of tunneling. However, when the vibrational energy E_{vib} exceeds the barrier to isomerization, some of the molecules isomerize and can be cooled subsequently to the zero-point level of the product. The population transfer (PT) spectrum therefore highlights the population changes induced by the dump laser as it is tuned (*20*). Alternatively, the reactant channel can be monitored to observe the population not transferred but recooled to its original form. To highlight the population changes induced by the dump laser, we operated the pump and probe lasers at twice the repetition rate (20 Hz) of the dump laser (10 Hz) while recording the difference in probe LIF signal between successive pulses with use of active baseline subtraction in a gated integrator.

To observe the population changes induced by the SEP process, the majority of the TFA-H_2O complexes must be formed before SEP excitation. A series of LIF scans taken as a function of distance from the 1.2-mm-diameter expansion orifice (fig. S2) confirmed this criterion. The transition intensities of the TFA-H_2O complex transitions have reached their final fractional abundance relative to the monomer transitions by 3.0 mm downstream, which is the distance where SEP excitation occurs.

For comparison with the population transfer spectra, the SEP spectra of both isomers were also recorded. Instead of LIF, we used two-color, resonant two-photon ionization (2C-R2PI) detection in a molecular beam time-of-flight mass spectrometer (*7*). This technique avoids the interference from scattered laser light in LIF. When the SEP dump pulse is nonresonant with a transition to the ground state, it can ionize the complex from the $S_1(0^0)$ level. Thus, when a dump transition to a vibrational level in the ground state occurs, the decrease in $S_1(0^0)$ population creates a dip in the $(TFA\text{-}H_2O)^+$ ion current otherwise produced. The abscissa on these traces (Figs. 2A and 3A) is the energy (in wave numbers) above the reactant ZPL, that is, the amount of internal energy placed in the complex by the SEP process.

The PT spectrum (Fig. 2B) recorded by exciting the TFA-H_2O(C=O) complex and monitoring the population of the TFA-H_2O(N–H) complex shows a clear onset at 988 wave numbers (equivalent to 11.8 kJ mol^{-1}), indicating that the energy threshold for the TFA-H_2O(C=O) → TFA-H_2O(N–H) isomerization

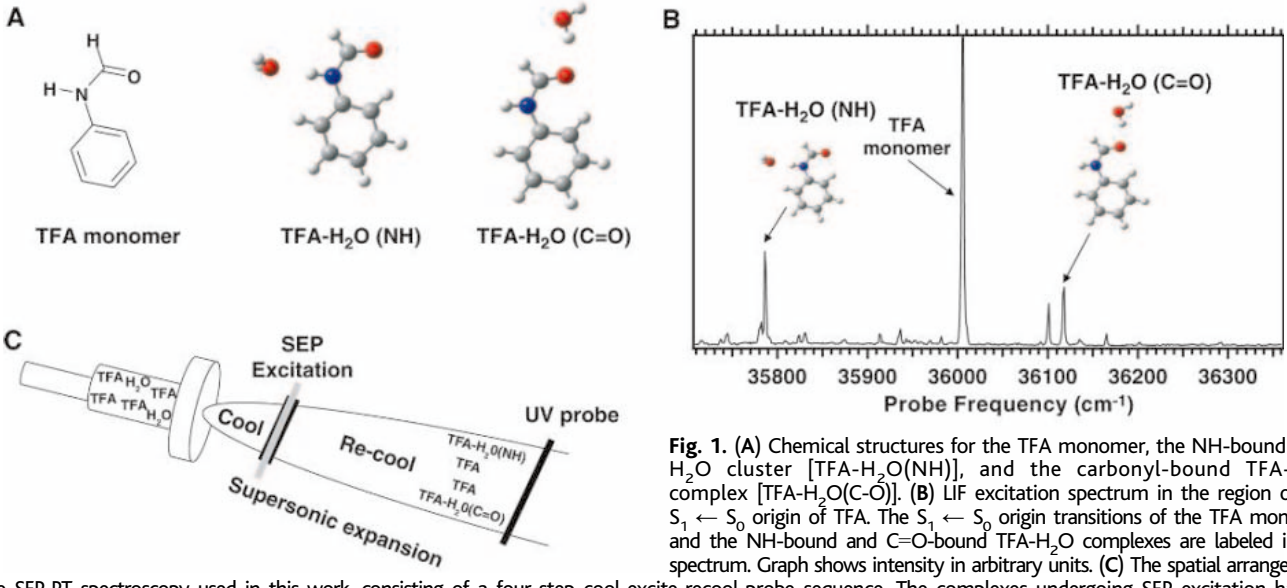

Fig. 1. (**A**) Chemical structures for the TFA monomer, the NH-bound TFA-H_2O cluster [TFA-H_2O(NH)], and the carbonyl-bound TFA-H_2O complex [TFA-H_2O(C-O)]. (**B**) LIF excitation spectrum in the region of the $S_1 \leftarrow S_0$ origin of TFA. The $S_1 \leftarrow S_0$ origin transitions of the TFA monomer and the NH-bound and C=O-bound TFA-H_2O complexes are labeled in the spectrum. Graph shows intensity in arbitrary units. (**C**) The spatial arrangement of the SEP-PT spectroscopy used in this work, consisting of a four-step cool-excite-recool-probe sequence. The complexes undergoing SEP excitation have a definite initial internal vibrational energy determined by the wavelength difference between pump (λ_1) and dump (λ_2) lasers. The probe laser (λ_3) interrogates the population of reactant or product downstream via LIF.

must be less than 988 cm^{-1}. All transitions above this threshold are observed with relative intensities consistent with the SEP spectrum above it (Fig. 2A). This threshold represents a firm upper bound to the energy barrier to the TFA-H_2O(C=O) → TFA-H_2O(N–H) isomerization. In the same way, the lack of a transition in the population transfer spectrum at 796 cm^{-1}, a resonance clearly observed in the SEP spectrum, places a lower bound on the isomerization barrier if the isomerization rate at threshold is fast compared to the collisional cooling rate. The magnitude of this kinetic shift is estimated to be small (<50 cm^{-1}) (*30*). Thus, $E_{barrier}$(C=O → NH) is bounded by ~796 cm^{-1} and 988 cm^{-1}.

The analogous SEP and PT spectra (Fig. 3, A and B) for the reverse process, namely TFA-H_2O(NH) → TFA-H_2O(C=O) isomerization, give bounds on the energy barrier for this process of ~750 $cm^{-1} \leq E_{barrier}$(NH→C=O) ≤ 988 cm^{-1}. Therefore, within the bounds of the measurement, the barrier is the same in both directions. Because these experiments probe the same barrier from different starting points, the combined NH → C=O and C=O → NH measurements can be used to determine the relative energies of the TFA-H_2O(NH) and TFA-H_2O(C=O) minima. The bounds so determined [–238 $cm^{-1} \leq E_{min}$(C=O) – E_{min}(NH) ≤ +192 cm^{-1}] place the minima close to one another in energy, as anticipated on the basis of the similar relative intensities of the $S_1 \leftarrow S_0$ origin transitions of the two isomers (Fig. 1B).

Probing the unreactive TFA-H_2O(NH) population after excitation of this isomer (Fig. 3C) offers a complementary threshold measurement. Below the threshold for isomerization, the SEP process drives the TFA-H_2O(NH) population back down into the TFA-H_2O(NH) reactive well, increasing the ground state population and therefore the LIF signal, when the dump laser is resonant with a transition. However, the LIF intensities in this spectrum decrease substantially for all transitions at or above 988 cm^{-1}. This result is consistent with isomerization siphoning off a fraction of the population to TFA-H_2O(C=O) product. Above the 988 cm^{-1} threshold, the relative transition intensities in the NH → C=O and NH → NH PT spectra (Fig. 3, B and C) match those in the SEP spectrum (Fig. 3A), indicating that the isomerization quantum yield stays roughly constant with increasing energy. This lack of energy dependence on the quantum yield is consistent with fast isomerization that equilibrates the populations of the two isomers before the reaction is quenched by collisional cooling.

Lastly, the same methods can be used to determine the binding energy of the complex. When the SEP excitation energy exceeds the binding energy, water dissociation occurs to produce TFA monomers, which are cooled to their zero-point level before detection downstream with the probe laser. When the TFA monomer $S_1 \leftarrow S_0$ origin is monitored after SEP excitation of the TFA-H_2O(C=O) complex, the first monomer product signal is observed at an internal energy of 1990 cm^{-1}, equivalent to a binding energy of 23.8 kJ mol^{-1} (fig. S3). This value is consistent with the binding energy determined by other means for the C=O-bound water molecule (22.6 ± 1.2 kJ mol^{-1}) (*24*).

The experimental results for the barrier heights and relative energy minima were compared with density functional theory calculations (*31*) with use of the Becke3LYP functional (*32*, *33*) and the 6-31+G* basis set (*34*) (Fig. 4). The lowest calculated transition state energy (1110 cm^{-1}) is somewhat above the experimental bounds (799 to 988 cm^{-1}). A second calculated transition state that places the water molecule above the TFA ring is about 200 cm^{-1} higher in energy (1330 cm^{-1}). The close correspondence of the experimentally determined barrier height with that calculated for the first transition state supports the assignment of this transition state to that probed experimentally. In the lowest energy transition state, the water molecule stays in the plane of the TFA molecule and acts as an acceptor to a weak C–H…OH_2 hydrogen bond with the aldehyde C–H group.

The minimum-energy pathway associated with the lowest-energy transition state involves in-plane motion of the water molecule as it moves around the amide group from reactant to product well (Fig. 4A). This pathway, computed with the nudged elastic band algorithm (*35*, *36*), can be broken up into three sections: (i) an initial steep ascent out of the H-bonded reactant well as the H bond breaks, (ii) a broad, flat section, covering much of the pathway, in which water skirts around the amide group in an acceptor orientation, and (iii) a steep descent and fast reorientation of water as it slides into the H-bonding well on the other side.

With increasing energy, more pathways are available, such as that which passes through an out-of-plane transition state over the phenyl ring with an energy of 1330 cm^{-1} (Fig. 4B). A second out-of-plane pathway (not shown) with a very similar energy traverses over the top of the amide group. Thus, as the energy available to the complex is increased from the isomerization threshold (988 cm^{-1}) to the dissociation threshold (1990 cm^{-1}), the water molecule can move over larger and larger regions of the surface of TFA while it passes from one well to the other, reducing the

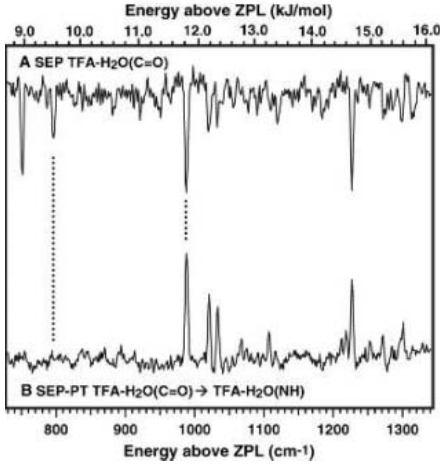

Fig. 2. (**A**) SEP spectrum of the carbonyl-bound TFA-H_2O complex recorded under collision-free conditions in a molecular beam time-of-flight mass spectrometer. The ion-dip detection scheme is described in the text. (**B**) SEP-population transfer spectrum for the TFA-H_2O(C=O) → TFA-H_2O(NH) isomerization process. The SEP excitation of the TFA-H_2O(C=O) complex is carried out in the collision-dominated region of the expansion (Fig. 1C). The isomerization to TFA-H_2O(NH) is probed via LIF. The sharp onset for the population gain signal due to the TFA-H_2O(NH) product at 988 cm^{-1} constitutes an upper bound on the energy barrier for TFA-H_2O(C=O) → TFA-H_2O(NH) isomerization.

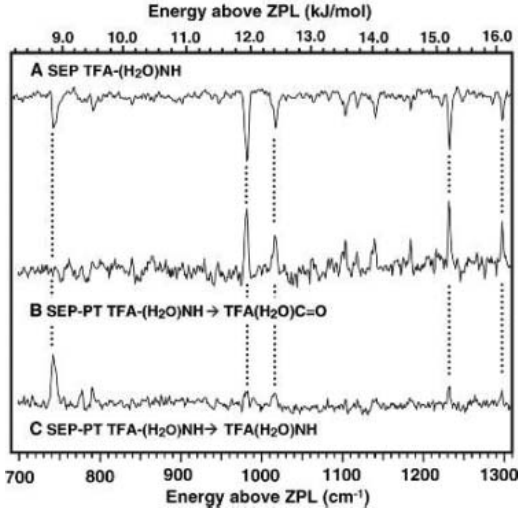

Fig. 3. (**A**) SEP spectrum of the TFA-H_2O(NH) complex over the 700-to-1300 cm^{-1} region. All conditions are the same as those used for the spectra in Fig. 2. (**B**) SEP-PT spectrum for the TFA-H_2O(NH) → TFA-H_2O(C=O) isomerization, the reverse process of that in Fig. 2. The sharp onset at 988 cm^{-1} constitutes an upper bound to the energy barrier for the process. (**C**) Analogous SEP-PT spectrum for the TFA-H_2O(NH) → TFA-H_2O(NH) unreactive channel, showing the effect of the isomerization threshold on the reactant population.

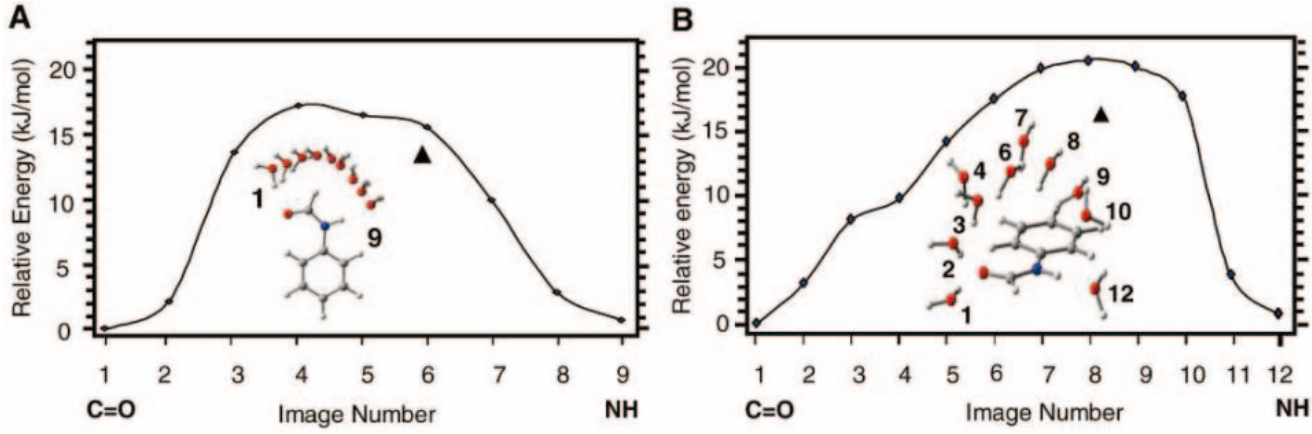

Fig. 4. Nudged elastic band (NEB) calculations of two minimum-energy pathways for the isomerization of water between the C=O-bound and NH-bound sites on TFA. The calculations were carried out by using density functional theory (*31*) with the Becke3LYP functional (*32*, *33*) and a 6-31+G* basis set (*34*). The NEB method uses a discrete representation of the reaction path (*41*), with the points (images) along the path being relaxed by using first derivatives only. The initial geometries for the images were constructed by linear interpolation between the C=O- and N–H-bound minima. The images were relaxed by using a modified Broyden optimization scheme (*42*) until the root mean square was below 0.5 kJ·mol^{-1} nm^{-1}. The highest energy images for each pathway were taken as guessed transition state geometries in a transition state search by the QST3 method used in Gaussian 03. (**A**) In-plane pathway with the lowest energy barrier to isomerization. The fully optimized energy of the transition state for this pathway is 1320 cm^{-1} (15.8 kJ mol^{-1}) without correction for zero-point energy effects. The barrier drops to 1110 cm^{-1} (13.3 kJ mol^{-1}) when zero-point energy corrections are included (marked by a triangle). (**B**) The analogous over-the-ring pathway for the water molecule. The fully optimized energy of the transition state for this pathway is 1610 cm^{-1} (19.4 kJ mol^{-1}) without correction for zero-point energy effects. The zero-point energy-corrected transition state for this pathway is 220 cm^{-1} higher than the in-plane transition state (1330 cm^{-1} = 15.9 kJ mol^{-1}, also marked with a triangle). The fact that some of the points along the NEB pathway are slightly higher in energy than the transition state (which is optimized with use of Hessian-based methods) arises because of the tighter convergence criterion used in the transition state optimization (10^{-5} kJ mol^{-1}).

importance of any particular transition state (*37*). As a result, it seems likely that modifications to transition state theory (*38*) will be needed in order to describe the rate of this reaction and its dependence on internal energy (*39*).

Because the isomerization process is initiated by SEP, the vibrational modes carrying the oscillator strength in the $S_1(0^0) \rightarrow S_0(v)$ dump transition are largely localized on the TFA molecule (*40*). In order for isomerization to occur, the laser-excited intramolecular vibrations of TFA must couple to the intermolecular vibrations of the complex. Collisions can contribute to this energy scrambling, but they also could selectively remove energy from the low-frequency intermolecular modes, thereby inhibiting isomerization. For these reasons, it seemed possible that near threshold the isomerization efficiency would show mode-specific dependence on the vibrational level excited by the SEP process. The matched intensities in the SEP and PT spectra (Figs. 2 and 3) argue against the importance of such mode-specific effects in TFA-H_2O. However, in a different system, excitation of localized solute vibrations near the water-binding site might selectively enhance the solvent rearrangement, motivating further work on these solvent-switching reactions.

References and Notes

1. J. Bertran, *Theor. Chem. Acc.* **99**, 143 (1998).
2. Y. Q. Deng, R. M. Stratt, *J. Chem. Phys.* **117**, 1735 (2002).
3. J. L. Gao, M. Garcia-Viloca, T. D. Poulsen, Y. R. Mo, *Adv. Phys. Org. Chem.* **38**, 161 (2003).
4. P. M. Kiefer, J. T. Hynes, *J. Phys. Chem. A* **106**, 1834 (2002).
5. R. M. Levy, L. Y. Zhang, E. Gallicchio, A. K. Felts, *J. Am. Chem. Soc.* **125**, 9523 (2003).
6. R. Rey, K. B. Moller, J. T. Hynes, *Chem. Rev.* **104**, 1915 (2004).
7. T. S. Zwier, *Annu. Rev. Phys. Chem.* **47**, 205 (1996).
8. T. Watanabe, T. Ebata, S. Tanabe, N. Mikami, *J. Chem. Phys.* **105**, 408 (1996).
9. Y. Matsumoto, T. Ebata, N. Mikami, *J. Chem. Phys.* **109**, 6303 (1998).
10. J. Crooks, A. J. Stace, B. J. Whitaker, *J. Phys. Chem.* **92**, 3554 (1988).
11. A. Bach, S. Coussan, A. Muller, S. Leutwyler, *J. Chem. Phys.* **113**, 9032 (2000).
12. T. M. Korter, D. W. Pratt, J. Kupper, *J. Phys. Chem. A* **102**, 7211 (1998).
13. M. J. Tubergen, C. R. Torok, R. J. Lavrich, *J. Chem. Phys.* **119**, 8397 (2003).
14. W. Roth *et al.*, *Chem. Phys.* **239**, 1 (1998).
15. F. N. Keutsch, R. J. Saykally, *Proc. Natl. Acad. Sci. U.S.A.* **98**, 10533 (2001).
16. J. Wang, R. M. Wolf, J. W. Caldwell, P. A. Kollman, D. A. Case, *J. Comput. Chem.* **25**, 1157 (2004).
17. A. D. MacKerell, N. Banavali, N. Foloppe, *Biopolymers* **56**, 257 (2000).
18. M. W. Mahoney, W. L. Jorgensen, *J. Chem. Phys.* **112**, 8910 (2000).
19. J. W. Ponder, D. A. Case, *Adv. Protein Chem.* **66**, 27 (2003).
20. B. C. Dian, J. R. Clarkson, T. S. Zwier, *Science* **303**, 1169 (2004).
21. J. A. Dickinson, M. R. Hockridge, E. G. Robertson, J. P. Simons, *J. Phys. Chem. A* **103**, 6938 (1999).
22. A. V. Fedorov, J. R. Cable, *J. Phys. Chem. A* **104**, 4943 (2000).
23. E. G. Robertson, *Chem. Phys. Lett.* **325**, 299 (2000).
24. M. Mons *et al.*, *J. Phys. Chem. A* **105**, 969 (2001).
25. S. Ullrich, X. Tong, G. Tarczay, C. E. H. Dessent, K. Muller-Dethlefs, *Phys. Chem. Chem. Phys.* **4**, 2897 (2002).
26. Details of the methods and materials are available at *Science* Online.
27. B. C. Dian, A. Longarte, T. S. Zwier, *Science* **296**, 2369 (2002); published online 23 May 2002 (10.1126/science.1071563).
28. B. C. Dian, A. Longarte, P. R. Winter, T. S. Zwier, *J. Chem. Phys.* **120**, 133 (2004).
29. B. C. Dian, G. M. Florio, J. R. Clarkson, A. Longarte, T. S. Zwier, *J. Chem. Phys.* **120**, 9033 (2004).
30. Assuming a 750 cm^{-1} barrier, the isomerization rate at E = 796 cm^{-1} is $k(E) = 3 \times 10^8$ s^{-1} on the basis of an Rice-Ramsperger-Kassel-Marcus (RRKM) estimate using a harmonic density of states calculation. At the position of SEP excitation (x/D = 2.5), the collision rate of the TFA-H_2O complex with helium is 2 × 10^9 s^{-1}. On the basis of previous studies of vibrational cooling in the supersonic expansion (*28*, *29*), the average energy lost per collision with helium is about 2 cm^{-1} at 750 cm^{-1} internal energy, resulting in a kinetic shift of less than 50 cm^{-1}.
31. M. J. Frisch *et al.*, *Gaussian 03* Software Suite (Gaussian, Pittsburgh, PA, 2003).
32. A. D. Becke, *J. Chem. Phys.* **98**, 5648 (1993).
33. C. Lee, W. Yang, R. G. Parr, *Phys. Rev. B* **37**, 785 (1988).
34. M. J. Frisch, J. A. Pople, J. S. Binkley, *J. Chem. Phys.* **80**, 3265 (1984).
35. G. Mills, H. Jonsson, *Phys. Rev. Lett.* **72**, 1124 (1994).
36. G. Henkelman, H. Jonsson, *J. Chem. Phys.* **113**, 9978 (2000).
37. D. Townsend *et al.*, *Science* **306**, 1158 (2004); published online 21 October 2004 (10.1126/science.1104386).
38. D. G. Truhlar, B. C. Garrett, S. J. Klippenstein, *J. Phys. Chem.* **100**, 12771 (1996).
39. D. M. Leitner, B. Levine, J. Quenneville, T. J. Martinez, P. G. Wolynes, *J. Phys. Chem. A* **107**, 10706 (2003).
40. The S_0-S_1 Franck-Condon factors are small to levels involving intermolecular vibrational excitation.
41. D. R. Alfonso, K. D. Jordan, *J. Chem. Phys.* **116**, 3612 (2002).
42. D. D. Johnson, *Phys. Rev. B* **38**, 12807 (1988).

43. T.S.Z. and K.D.J. thank NSF for support of this work under grants CHE-0242818 and CHE-0078528.

Supporting Online Material

www.sciencemag.org/cgi/content/full/1106977/DC1
Materials and Methods
Figs. S1 to S3

1 November 2004; accepted 18 January 2005
Published online 3 February 2005;
10.1126/science.1106977
Include this information when citing this paper.

Deflection of the Interstellar Neutral Hydrogen Flow Across the Heliospheric Interface

R. Lallement,[1]* E. Quémerais,[1] J. L. Bertaux,[1] S. Ferron,[1] D. Koutroumpa,[1] R. Pellinen[2]

Using an absorption cell, we measured the Doppler shifts of the interstellar hydrogen resonance glow to show the direction of the neutral hydrogen flow as it enters the inner heliosphere. The neutral hydrogen flow is found to be deflected relative to the helium flow by about 4°. The most likely explanation of this deflection is a distortion of the heliosphere under the action of an ambient interstellar magnetic field. In this case, the helium flow vector and the hydrogen flow vector constrain the direction of the magnetic field and act as an interstellar magnetic compass.

The Sun is moving at a velocity of 25.5 km s^{-1} through a tenuous, 20 to 30% ionized interstellar cloud (*1*–*3*). The inflowing interstellar plasma forces the solar wind to turn back and confines it within the heliosphere, whereas the interstellar plasma is diverted around the heliopause (*4*). Interstellar neutral species separate from the plasma, cross the heliospheric interface, and reach the inner solar system, forming the so-called interstellar wind (*5*). However, this separation is not complete because of charge-transfer reactions between ions and atoms, which, beyond the heliopause, have a characteristic length scale on the order of the size of the heliosphere [≈100 astronomical units (AU)]. This process replaces a fraction of the initial interstellar H atoms with a new population of atoms that are instantaneously moving in the same direction and at the same speed as the decelerated and heated interstellar protons (*6*–*8*). Unlike H, neutral He experiences much less charge transfer and, when entering the heliosphere, keeps the characteristics of the ambient circumsolar interstellar medium (*2*). The differences between the neutral H flow and that of neutral He (i.e., the deceleration, heating, and filtering of neutral H), because they measure the imprints of the plasma, constrain the plasma flow properties and the heliospheric interface structure and size (*9*–*13*).

The direction and strength of the interstellar magnetic field B_{IS} in the solar neighborhood are unknown. Measurements over large distances show that galactic magnetic field intensities are on the order of a few microgauss. Therefore, the ambient interstellar magnetic pressure may be large compared with the gas pressure and thus may influence the size and shape of the heliosphere. There is no physical reason for any particular angle between the heliocentric-wind vector (which depends on the random motion of the Sun) and the magnetic field vector (which depends on the history of the local interstellar medium and the interaction of the local cloud with other clouds). As a consequence, an additional magnetic confinement of the heliosphere is likely to produce departures from axial symmetry of the heliospheric plasma interface, and, in turn, the detection of a difference between the H and He flow directions would be a sign for such an asymmetry of the plasma distribution.

The solar wind anisotropies (SWAN) experiment (*14*) on board the Solar and Heliospheric Observatory (SOHO) satellite is mapping the solar Lyman-α (Ly-α) radiation (with a wavelength of 121.6 nm) that is resonantly backscattered by interstellar H atoms, called the H glow. Most of the glow is generated within ≈10 AU from the Sun. When activated, an absorption cell blocks out a fraction of the emission line [supporting online material (SOM) text 1]. The absorption line's Doppler shift depends on the relative motion between the emitter (the interstellar H flow) and the absorber (the cell or the spacecraft). To first order, the transmitted fraction is a minimum for a line of sight that is perpendicular to the relative-velocity vector. The locations on the sky of the maximum absorption directions form a pattern that is close to a circle, called the zero–Doppler shift circle (ZDSC) (SOM text 2). During the year, the gas velocity in the SOHO frame changes in modulus and direction, and the ZDSC changes accordingly (Fig. 1). A cell thus acts as a negative scanning spectrometer, providing information on the emission line and thus the velocity distribution of the interstellar atoms.

We extracted several series of data points forming secants of the ZDSC (Fig. 1). Within each series, the direction of sight moves from one side to the other of the ZDSC. Along each of these secants, we derived the coordinates of the minimum transmission

[1]Service d'Aéronomie du Centre National de la Recherche Scientifique, Institut Pierre Simon Laplace, Boite Postale 3, 91371 Verrières-le-Buisson, France. [2]Finnish Meteorological Institute, Post Office Box 503, 00101 Helsinki, Finland.

*To whom correspondence should be addressed. E-mail: rosine.lallement@aerov.jussieu.fr

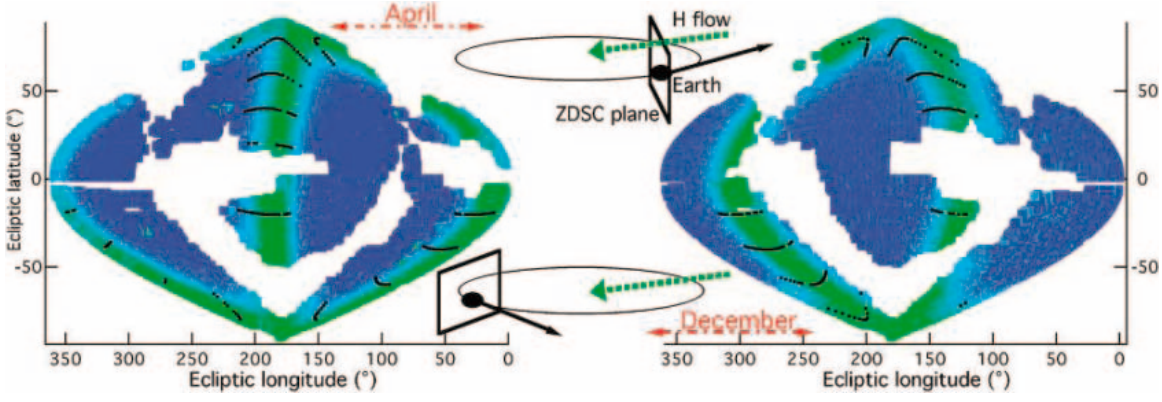

Fig. 1. Two examples of absorption cell transmission maps recorded by SOHO/SWAN (on 25 April 1996 and 29 December 1996). Maps are in ecliptic coordinates. Blank areas correspond to the absence of measurements or to contaminated data. Maximum absorption directions (green areas) form a pattern close to a great circle. This ZDSC is in a plane that is perpendicular to the interstellar gas velocity in the observer frame, i.e., the difference between the H flow motion (green dashed vector) and the Earth velocity (black vector). The data used for the present analysis (black dots) are series of secants of the ZDSC.

direction (SOM text 3). In parallel, we calculated the transmission predicted by a forward model of a homogeneous, single-fluid, neutral H flow (SOM text 4) and derived the coordinates of the predicted minimum-transmission direction. Finally, for each secant, we calculated the angle between the measured and modeled directions. The model has been adjusted to the data by minimizing these angles using a least squares method.

Our method uses the line Doppler shifts only, which allows us to neglect the cell characteristics and their temporal variations (aging), as well as line broadening caused by radiative transfer of photons (SOM text 5) (*15*). We performed a parametric study within the optically thin assumption (photons are scattered once), and we varied, in addition to the wind's direction, its bulk velocity and its temperature. The ratio of radiation pressure to solar gravity was also varied between 0.8 and 1.0 (*11*, *16*). We used the self-reversed solar line measured as in (*17*). The rate of ionization under the influence of the solar wind and solar extreme-ultraviolet photons was varied between 1.0×10^{-6} and 1.5×10^{-6} s^{-1} at 1 AU, and a 40% decrease of the ionization between the Sun's equator and the pole was assumed. The derived bulk speed (22 ± 1.0 km s^{-1}) and the derived temperature of the incoming H flow (11,500 ± 1000 K) (SOM text 6) are similar to previous measurements (*10*, *11*). These derived measurements, when compared with He measurements (bulk speed of 26.3 ± 0.4 km s^{-1} and temperature of 6300 ± 340K) from (*18*, *19*), confirm the deceleration and heating of the H flow. The minimum reduced χ^2 is found for (λ, β) = (252.5°, 8.8°, where λ is the ecliptic longitude and β is the ecliptic latitude).

A different, model-independent method of line profile reconstruction (*12*) was also applied to the same data. By combining measurements taken toward the same given direction in the sky and recorded from all the SOHO vantage points during a year (i.e., with varying Doppler shifts of the cell absorption line), it is possible to fully or partially reconstruct the line profile corresponding to this given direction. By using the resulting map of projected velocities, we found the wind axis (*12*) to vary in a systematic way from the upwind to the downwind side [from (λ, β) ≈ (249°, 8°) to (λ, β) ≈ (253°, 9.5°)], as if the flow were rotating by about 3° to 4° around the Sun. This trend has raised some doubts about the possibility of comparing the direction of H flow with the direction of He flow. We used our model to perform a test of this method and found that this shift is mainly caused by the assumption that the line profile from a given direction is independent of the location of the observer along Earth's orbit (SOM text 7) (*12*). We used this analysis to calculate corrections to the earlier results of (*12*). After correction, the wind directions are less scattered and are centered on (λ, β) = (252.2°, 9.0°) (Fig. 2). The two independent methods, a data-model adjustment of the ZDSC location and the model-independent line profile reconstruction, are consistent (SOM text 8). We have considered the difference between the two results as representative of the uncertainties on the wind axis direction; that is, our error bars are on the order of 0.5° and take into account the existence of residual systematic effects caused by our monofluid approximation, departures from stationariness, or solar wind anisotropies (SOM text 8).

Interstellar neutral He has been found to flow from (λ, β) = (254.7° ± 0.4°, 5.2° ± 0.2°) (*18–20*), which is different from the H flow direction by 4° ± 1°. The reason for such a deviation of the H flow is most likely linked to a distortion of the heliosphere, probably under the action of an ambient B_{IS}. Other explanations are less likely, but the most serious other candidate is a combination of strong solar wind latitudinal anisotropies and a strong north-south solar wind asymmetry (SOM text 9). A number of magneto-hydrodynamic (MHD) models of the heliosphere in the case of an inclined interstellar magnetic field that include a simplified treatment of charge exchange have been calculated (*21–23*), but no fully self-consistent model has been built yet.

A common feature of the models, including pure MHD models (*24*), is a large distortion of the bow shock and the heliopause (Fig. 3) for 30° < α < 60°, where α is the angle between B_{IS} and the bulk-flow velocity vector V (both the field-aligned flow and the perpendicular case lead to axisymmetry). A fraction of the H atoms that reach the Sun come directly from the interstellar medium. This is the so-called primary component (flow 1 in Fig. 3), which keeps its initial direction (the He flow direction). A second flow of neutral atoms reaching the inner solar system is made of the trans-charged (neutralized by charge transfer) interstellar protons, the so-called secondary atoms (flow 2). Most of those secondaries are born in the outer heliosheath between the bow shock and the heliopause (*8*). The major difference between the secondaries in the

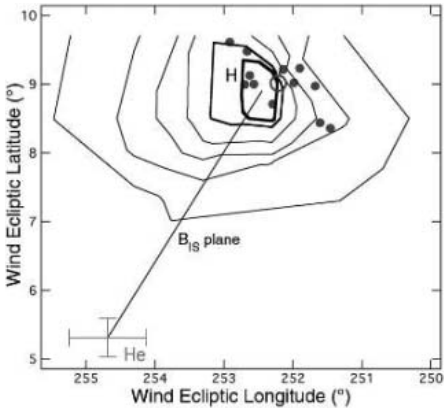

Fig. 2. H flow direction determination. Directions with χ^2 = 1.14 (bold line), 1.16, 1.21, 1.5, and 2.0 from the maximum-absorption location method are shown with solid lines. Dots indicate the series of corrected directions derived from the line profile reconstruction method. The He flow direction and its error bars are shown for comparison. If the deflection is associated with a magnetically distorted heliosphere, the H and He flow directions define the interstellar magnetic field plane.

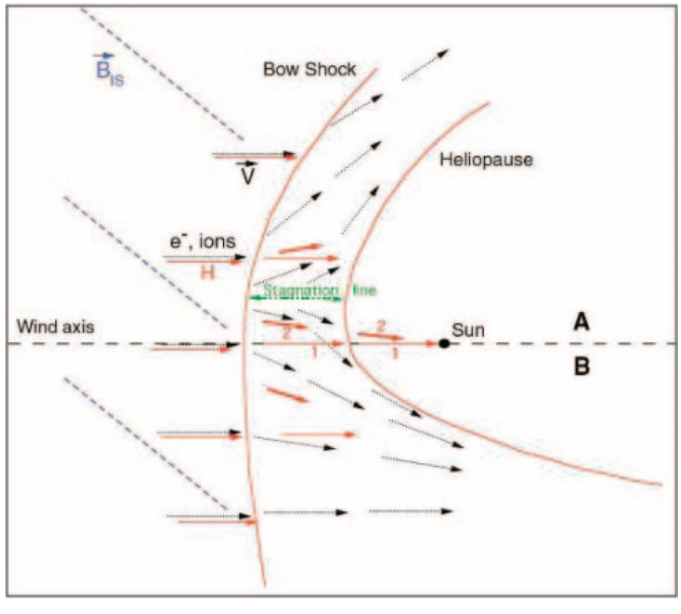

Fig. 3. A schematic view of the heliosphere in the case of a B_{IS} inclined with respect to the flow direction [adapted from (*24*) and (*25*)]. Neutral (red arrows) and plasma (electrons and ions, black arrows) flows are sketched in the plane containing B_{IS} (dashed lines) and the wind flow vector. The secondary flow of H atoms (marked 2) is generated between the bow shock and the heliopause in a region between the Sun-wind axis and the displaced stagnation line (green dashed line). According to such a scheme, the plane containing the primary flow (nondeviated, marked 1) and the secondary flow also contains the magnetic field, and the secondary flow arrival direction lies between the wind axis and the field direction.

axisymmetric case (no magnetic field or parallel or perpendicular magnetic field) and the general case ($0° \ll \alpha \ll 90°$) is that the stagnation line (which separates the ions deflected on both sides of the heliopause) is no longer aligned with the Sun-wind axis but is offset. As a consequence, a larger number of secondary atoms able to reach the Sun (with the ion velocity vector directed toward the Sun before charge transfer) are formed on one side of the Sun-wind axis and form a deflected flow. The gas that is observed in the inner heliosphere is the sum of population 1 (nondeviated) and population 2 (deviated), and thus is itself deviated, although to a lesser extent, which depends on the relative contributions of the two fluxes. The departure of this average flow from the He flow is an imprint of the charge-exchange processes in the nonaxisymmetric outer heliosphere.

Three constraints on the direction of B_{IS} can be derived. First, B_{IS} is contained in the plane defined by the H and He flow vectors; that is, B_{IS} is perpendicular to (λ, β) = (167°, –30°). Second, according to models, draping of magnetic field lines around the asymmetric heliopause is such that the high-pressure side of the heliosheath is opposite to the displaced stagnation line (Fig. 3). The other side, which contains the stagnation line, is filled with a less compressed flow of plasma and secondary neutrals and is the low-pressure region. The magnetic field from the interstellar side toward the inner heliosphere is thus oriented like the secondary flow of neutral H with respect to the wind axis but further away. The third constraint comes from the conditions on the angle α between B_{IS} and the bulk velocity V. Assuming that α is between 30° and 60°, an estimate range for the ecliptic coordinates of B_{IS} is λ = 30° to 60°, β = –30° to –60° (or the opposite direction). In galactic coordinates, this translates to (l, b) = (205° to 240°, –38° to –60°), which can be compared with the spatial distribution of the local interstellar cloudlets derived from interstellar absorption lines recorded in the spectra of nearby stars (*25*, *26*). The projection of B_{IS} onto the galactic plane is more or less tangent to the boundary of the local interstellar cloud, in the region that is facing the neighboring cooler and faster G cloud (so-called because it is located on the galactic center side), as would be the case if the magnetic field lines were compressed between the two cloudlets (Fig. 4).

The most compressed part of the heliosheath on the upwind side is opposite to the direction of deflection and thus is toward lower ecliptic latitudes (less than 5°) and higher longitudes (more than 254°) as compared with the wind axis. This should influence the direction of energetic neutral atoms originating from charge transfer with the subsonic solar wind and with accelerated particles. On the other hand, an additional magnetic compression is expected to increase the density of secondary neutral species piling up at the interface, reinforcing the so-called hydrogen wall (*8*), and possibly explaining ultraviolet spectrometer Ly-α data recorded over the past 10 years, which suggest an H wall–related emission increase stronger than what self-consistent models without a magnetic field predict (*27*).

If the heliosphere is distorted as in Fig. 3 under the action of a magnetic field, then the heliosphere is more elongated toward increasing ecliptic latitude. Voyager 1, which is at about 90 AU and is heading toward the northern ecliptic hemisphere, would be moving toward an elongated part of the termination shock. Indeed, such a configuration has been invoked recently (*28*, *29*) to reconcile all kinds of data recently collected (*30*–*32*) and to explain how Voyager 1 can detect energetic particles accelerated at the shock barrier without having crossed it yet.

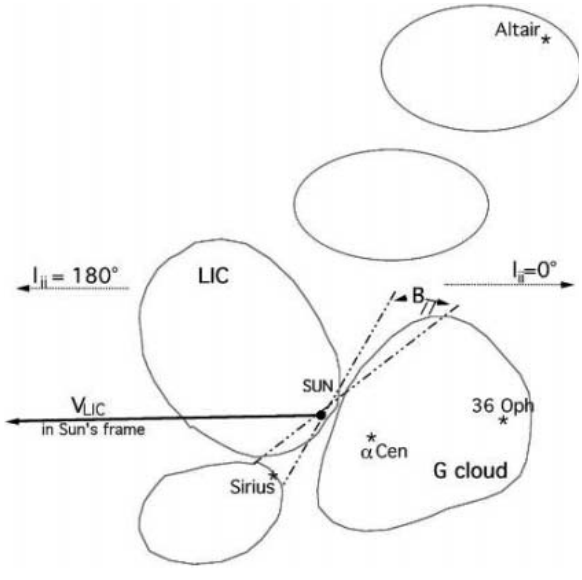

Fig. 4. Interstellar cloudlets around the Sun in the galactic plane [sketch adapted from (*26*) and (*27*)]. The galactic center direction [galactic longitude (l_{ii} = 0°)] and the anticenter (l_{ii} = 180°) are indicated. The local interstellar cloud (LIC) is surrounded by masses of gas with different velocities, temperatures, and abundances. Dot-dashed lines are the projections onto the galactic plane of the inferred B_{IS} in the two cases α = 30° and α = 60°, which are considered as limits. αCen, alpha Centauri; 36 Oph, 36 Ophiuchi.

References and Notes

1. R. Lallement, P. Bertin, *Astron. Astrophys.* **266**, 479 (1992).
2. P. Bertin, R. Lallement, R. Ferlet, A. Vidal-Madjar, *J. Geophys. Res.* **98**, 15193 (1993).
3. R. Lallement, R. Ferlet, *Astron. Astrophys.* **324**, 1105 (1997).
4. G. P. Zank, *Space Sci. Rev.* **89**, 413 (1999).
5. J. L. Bertaux, J. E. Blamont, *Astron. Astrophys.* **11**, 200 (1971).
6. M. K. Wallis, *Nature* **254**, 202 (1975).
7. T. E. Holzer, *Rev. Geophys. Space Phys.* **15**, 467 (1977).
8. V. B. Baranov, Y. Malama, *J. Geophys. Res.* **98**, 157 (1993).
9. R. Lallement, J. L. Bertaux, J. T. Clarke, *Science* **260**, 1095 (1993).
10. R. Lallement *et al.*, *Solar Wind 9 Am. Inst. Phys. Conf. Proc.* **471**, 205 (1999).
11. J. Costa *et al.*, *Astron. Astrophys.* **349**, 660 (1999).
12. E. Quémerais *et al.*, *J. Geophys. Res.* **104**, 12585 (1999).
13. V. V. Izmodenov *et al.*, *J. Geophys. Res.* **104**, 4731 (1999).
14. J. L. Bertaux *et al.*, *Sol. Phys.* **162**, 403 (1995).
15. E. Quémerais, V. Izmodenov, *Astron. Astrophys.* **396**, 269 (2002).
16. T. E. Woods, W. Kent Tobiska, G. J. Rottman, J. R. Worden, *J. Geophys. Res.* **105**, 27195 (2000).
17. P. Lemaire *et al.*, in *Proceedings of the SOHO 11th Workshop* (European Space Agency Special Publication 508, European Space Agency Publications Division, Noordwijk, Netherlands, 2002), p. 219.
18. M. Witte, *Astron. Astrophys.* **426**, 835 (2004).
19. J. Vallerga *et al.*, *Astron. Astrophys.* **426**, 855 (2004).
20. G. Gloeckler *et al.*, *Astron. Astrophys.* **426**, 845 (2004).
21. R. L. McNutt, J. Lyon, C. C. Goodrich, M. Wiltberger, *Solar Wind 9 Am. Inst. Phys. Conf. Proc.* **471**, 823 (1999).
22. T. J. Linde, T. I. Gombosi, P. L. Roe, K. G. Powell, D. L. DeZeeuw, *J. Geophys. Res.* **103**, 1889 (1998).
23. R. Ratkiewicz, A. Barnes, H.-R. Müller, G. P. Zank, G. M. Webb, *Adv. Space Res.* **29**, 433 (2002).
24. N. Pogorelov, G. P. Zank, T. Ogino, *Astrophys. J.* **614**, 1007 (2004).
25. R. Lallement, R. Ferlet, A. M. Lagrange, M. Lemoine, A. Vidal-Madjar, *Astron. Astrophys.* **304**, 461 (1995).
26. S. Redfield, J. L. Linsky, *Astrophys. J.* **534**, 825 (2000).
27. E. Quémerais, J.-L. Bertaux, R. Lallement, B. R. Sandel, V. Izmodenov, *J. Geophys. Res.* **108**, 8029 (2003).
28. J. R. Jokipii, J. Giacalone, J. Kóta, *Astrophys. J.* **611**, L141 (2004).
29. E. C. Stone, COSPAR, *Adv. Space Res.*, in press.
30. S. M. Krimigis *et al.*, *Nature* **426**, 45 (2003).
31. F. B. McDonald *et al.*, *Nature* **426**, 48 (2003).
32. L. F. Burlaga, N. F. Ness, F. B. McDonald, J. D. Richardson, C. Wang, *Astrophys. J.* **582**, 540 (2003).

33. The SOHO mission is a European Space Agency–NASA international cooperation. SWAN was financed in France by the Centre National d'Etudes Spatiales with support from the French National Center for Scientific Research (CNRS) and in Finland by Tekes and the Finnish Meteorological Institute. The data were obtained thanks to the help of the Experiment Operation and Flight Operation Teams at the Goddard Space Flight Center.

Supporting Online Material

www.sciencemag.org/cgi/content/full/307/5714/1447/DC1
SOM Text
Fig. S1
References

29 November 2004; accepted 13 January 2005
10.1126/science.1107953

Supramolecular Assembly of Amelogenin Nanospheres into Birefringent Microribbons

Chang Du,[1] Giuseppe Falini,[2] Simona Fermani,[2] Christopher Abbott,[1] Janet Moradian-Oldak[1]*

Although both tooth enamel and bone are composed of organized assemblies of carbonated apatite crystals, enamel is unusual in that it does not contain collagen nor does it remodel. Self-assembly of amelogenin protein into nanospheres has been recognized as a key factor in controlling the oriented and elongated growth of carbonated apatite crystals during dental enamel biomineralization. We report the in vitro formation of birefringent microribbon structures that were generated through the supramolecular assembly of amelogenin nanospheres. These microribbons have diffraction patterns that indicate a periodic structure of crystalline units along the long axis. The growth of apatite crystals orientated along the *c* axis and parallel to the long axes of the microribbons was observed in vitro. The linear arrays (chains) of nanospheres observed as intermediate states before the microribbon formation give an important indication as to the function of amelogenin in controlling the oriented growth of apatite crystals during enamel mineralization.

Protein self-assembly into ordered structures is a critical step toward the control of mineral deposition in biomineralizing systems such as bone, teeth, and mollusk shells. Mammalian tooth enamel, the hardest tissue in the vertebrate body, is a secretory product of cells of epithelial origin called ameloblasts (*1*, *2*). During enamel development, ameloblasts and the adjacent cells pass through several stages with well-characterized morphologies that are related to their functions (*3*, *4*). The cellular behavior has been linked to chemical changes in the enamel in terms of matrix processing and mineralization (*4*, *5*). The relation between gene expression and assembly of the organic matrix component controlling the structural hierarchy of enamel has also been reported (*6*). As characterized by Eastoe (*2*), developing enamel does not contain collagen, nor does it remodel. The partially mineralized extracellular matrix at the initial secretory stage contains, by weight, approximately 30% mineral, and the remainder is organic material and water (*7*). At this stage, amelogenin proteins comprise more than 90% (w/w) of the organic matrix. Other important protein components include enamelins, ameloblastins, and enamel proteinases (*1*). After their secretion, amelogenins are almost immediately processed in a stepwise and controlled manner, and eventually are removed from the extracellular space during the late maturation stage. Massive degradation of the enamel extracellular matrix components (mostly amelogenins) is concomitant with the rapid growth of enamel crystals, creating a highly organized structure that is almost completely inorganic (>90% mineral) (*5*, *7*). The highly elongated and oriented ribbonlike carbonated hydroxyapatite crystals in mature enamel are quite different in size and morphology from those of bone, cartilage, and dentin, which have a platelike morphology (*8*, *9*). Amelogenins have been postulated to fulfill major structural roles during the oriented growth of enamel crystals. They are hydrophobic in nature because they are enriched in proline, glutamine, histidine, and leucine. Sequence conservation is remarkably high among species, particularly in the N- and C-terminal regions of the protein (*10*).

The complete secondary and tertiary structures of amelogenin are obscure. The early x-ray diffraction (XRD) studies suggested a cross-β or β-sheet structure in the enamel matrix (*11*); circular dichroism (CD), Fourier transform infrared (FTIR), and Raman spectroscopy studies have suggested that amelogenin molecules contain β sheets and β turns (*12*, *13*). The difficulty in elucidating the structure and function of amelogenin has been partly due to its tendency to form aggregates, which are sensitive to and reversible by temperature changes (*14*, *15*). Eastoe has suggested that the amelogenin-rich enamel extracellular matrix was an "unstructured" gel with thixotropic properties that functioned to "nurture" the growth of the enamel crystallites (*2*). Others have reported the presence of some relatively ordered structures in developing enamel that might represent the ultrastructure of the organic matrix (*16*–*19*). With the use of a freeze-fracturing technique, collinear spherical structures of 30 to 50 nm in diameter arranged in linear arrays organized in the direction of the crystallites' long axis have been detected (*19*). It was not known whether these represented organic material or some kind of organic-mineral quasi-crystalline subunit structures. The structural studies of a recombinant murine amelogenin, together with a comparison to transmission electron microscope (TEM) preparations of developing enamel from different species, led to the conclusion that amelogenin proteins self-assemble into supramolecular structures, termed "nanospheres" (*20*). The nanospheres have been proposed to be the basic structural entities of the developing enamel extracellular matrix and to play a crucial function in enamel biomineralization (*20*).

We investigated the process of amelogenin self-assembly in vitro and explored the formation of higher levels of ordered structures from the nanospheres. We report the spontaneous assembly and hierarchical organization of birefringent "microribbons" of a full-length recombinant porcine amelogenin (rP172). We further observed the formation and *c*-axial orientation of hydroxyapatite on the self-assembled amelogenin microribbons during an in vitro mineralization study. We suggest that the substantial alignment of amelogenin nanospheres into long chains may be relevant to the mechanism of its function as a scaffold in facilitating the elongated and oriented growth of apatite crystals during enamel biomineralization.

The full-length recombinant porcine amelogenin rP172 formed microribbons under a wide variety of solution conditions (table S1 and fig. S1) (*21*). In contrast, a native porcine amelogenin lacking the hydrophilic 25–amino acid C terminus (P148 or the 20k amelogenin) failed to form microribbons under the same conditions (*22*). Figure 1, A to C, shows three notable stages of amelogenin assembly and highlights a specific trend in amelogenin precipitates during crystallization of the microribbons. When amelogenin molecules assemble into the form of a filamentous web structure (Fig. 1, B and C), this material evolves over time into more organized entities that show strong birefringence (Fig. 1D) and have defined edges, which we term microribbons (Fig. 1E). Interestingly, the thickness and the width of the mature ribbons are almost constant, regardless of the solution conditions for assembly, whereas their length varies widely even under a single set of experimental conditions (Fig. 1E). The mature microribbons were stable and their overall shape was conserved in the precipitation media for several months, and even after they were air

[1]Center for Craniofacial Molecular Biology, School of Dentistry, University of Southern California, 2250 Alcazar Street, CSA 103, Los Angeles, CA 90033, USA. [2]Dipartimento di Chimica G. Ciamician, Alma Mater Studiorum Università di Bologna, via Selmi 2, 40126 Bologna, Italy.

*To whom correspondence should be addressed. E-mail: joldak@usc.edu

dried. Only strong thermal treatment, such as an electron beam, or harsh dehydration conditions (e.g., in a desiccator in the presence of P_2O_5) provoked a collapse of the ribbon structure.

The highly birefringent microribbons had a weak but unique XRD pattern that indicates a preferential orientation of crystalline units along the long axis (Fig. 1F and table S2). We speculate that the lattice spacing along this direction (0.26, 0.34, and 0.52 nm) results from a unique conformation and secondary structure of folded amelogenins. The only structure that can possibly fit such periodicity is the β spiral (a repetitive β-turn structure). This structure was previously predicted by Renugopalakrishnan *et al.* (*23*) on the basis of a molecular mechanics-dynamics study of a bovine amelogenin. The proposed structure contained a repetitive sequence of $(Gln\text{-}Pro\text{-}X)_9$ forming repetitive β turns. FTIR and Raman spectroscopy have supported the presence of repetitive β-turn structures in a bovine amelogenin, which is a prerequisite for the stability of such β-spiral structures (*12*, *13*). The porcine amelogenin rP172 contains characteristic proline-rich sequences of $(Y\text{-}Pro\text{-}X)_n$ (more than 50% of the Y's are Gln). Computational analysis of the rP172 sequence has predicted a high probability for the formation of concatenated β turns in the proline-rich regions that provide a high probability for a β-spiral structure (fig. S2). It is noteworthy that such a type of sequence has been highly conserved among amelogenins from different species (*10*). Following the proposed β-spiral model with helical parameters of translation per residue h = 0.251 nm and number of residues per turn n = 3.95 (*23*), and assuming a periodicity of approximately 1 nm, we predict that the meridional reflections at 0.52 nm (medium), 0.34 nm (weak), and 0.26 nm (strong) (Fig. 1F and table S2) correspond to the second, third, and fourth order, respectively. The presence of diffractions along the equatorial axis at 0.39 and 0.53 nm suggests an ordered lateral assembly among the crystalline units. Overall, the diffraction pattern suggests that the molecules, or certain domains of the molecules, can evolve into a relatively ordered array during the formation and maturation of the microribbons.

Amelogenin molecules can spontaneously form nanosphere structures under a wide variety of conditions (*24*, *25*). To further investigate the formation, stability, and equilibrium states of the nanosphere structures and their subunits, we systematically analyzed the particle size distribution of rP172 in acetate buffer, water, and 60% aqueous acetonitrile by dynamic light scattering analysis (DLS) (figs. S3 and S4; tables S3 and S4) (*21*). Overall, typical nanospheres with hydrodynamic radii (R_H) of 13.2 to 27.5 nm were the most stable assembling form (over 75% of the mass) in either acetate buffer (pH 4.5) or distilled water (pH ~6.5). They had a narrow particle size distribution over a wide range of concentrations (figs. S3, A and B, and S4; table S3). The smaller assemblies (R_H < 10 nm) detected by DLS in a short interval suggested subunits within the nanosphere structures (figs. S3, D and E, and S4; table S4). Monomers and discrete oligomers such as dimers, trimers, and hexamers were detected in the diluted protein solutions with 60% aqueous acetonitrile as a solvent (figs. S3, C and F, and S4; tables S3 and S4). Larger aggregates (>100 nm in size) existed in small amounts. Direct visualization by TEM, scanning electron microscopy (SEM), and atomic force microscopy (AFM) revealed that these larger aggregates were the result of further association of nanospheres in a linear arrangement (Fig. 2 and figs. S1D and S5).

The substructures of the nanospheres were revealed by TEM (Fig. 2A, insets). Those subunits inside a nanosphere had a quasi-spherical appearance, 4 to ~8 nm in diameter, consistent with the DLS measurement of amelogenin oligomers. The "bridging" between nanospheres was observed by thin threads (white arrow in the inset), the width of which was in the same scale as that of the subunits. The "fusion" of adjacent nanospheres is manifested as a sharing of subunits (black arrow in the inset). The linear alignment of several subunits was evident inside some nanospheres (upper inset). The further association of nanospheres led to higher levels of hierarchical structures. Nanosphere chains were observed under TEM as an intermediate state before the formation of microribbons (Fig. 2A). The nanochain structures were also observed in the microribbons by AFM (Fig. 2, B and C). The size range of the nanospheres (10 to 20 nm in diameter) in the microribbon was consistent with the lower limit from DLS measurement in solution. Those nanochains more than 100 nm long were aligned roughly parallel to the long axis of the ribbons (Fig. 2C and fig. S5D).

The nanospheres may either align directly or reorganize into the nanochain structures. A finite number of identical spheres can achieve optimal packing that is defined by the minimization of any physically reasonable variable (*26*). Minimizing the volume of

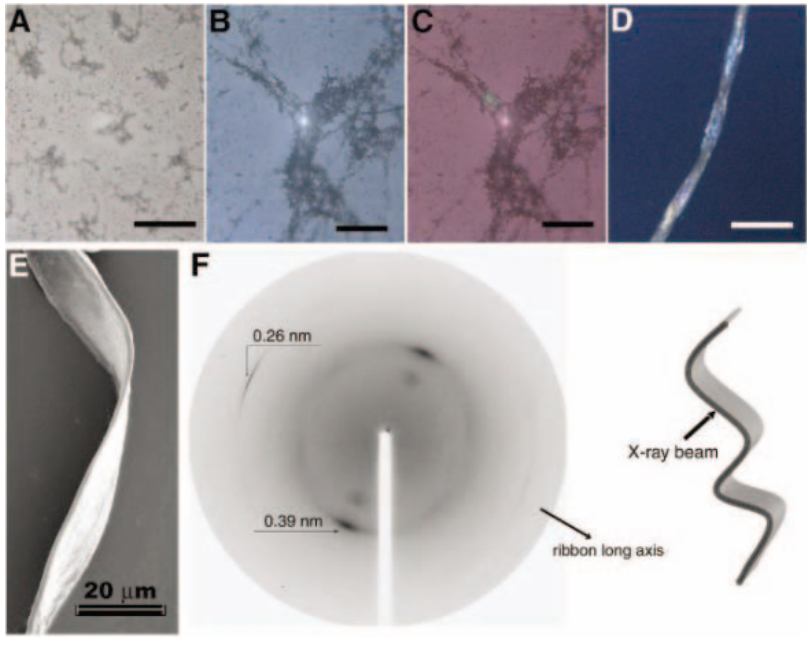

Fig. 1. Formation and characterization of amelogenin microribbons. (**A** to **D**) Optical micrographs of amelogenin precipitates formed under different solution conditions during hanging drop crystallization experiments. Scale bars, 0.1 mm. The protein was dissolved in 25 mM sodium acetate buffer (pH 4.5) at 10 mg/ml. (A) Precipitants: 30% polyethylene glycol, molecular weight 4000 (PEG 4000), and 0.2 M $MgCl_2$. The amelogenin precipitate shows almost no structure with a few filaments. (B) Precipitants: 30% PEG 4000 and 0.2 M Li_2SO_4. The precipitate forms a web structure in which many filaments are present. (C) The same sample in (B) under cross-Polaroid after crystallization. The starting stage of ribbon formation can be observed within the filamentous web structure. (D) Polarized light micrograph of a mature ribbon precipitated under the condition (B) in about 2 weeks. (**E**) SEM micrograph of a mature amelogenin ribbon demonstrating well-defined edges. Microribbons measured 200 to ~1200 μm in length, 29 ± 4 μm (n = 21) in width (±SD), and 2.7 ± 0.6 μm (n = 10) in thickness. (**F**) Synchrotron XRD of a ribbon in its edge-on orientation. The scheme at right shows the orientation of the ribbon toward the x-ray beam. The x-ray spacings of the most intense reflections are indicated. The x-ray spacings of all reflections are reported in table S2.

the packing leads to the form of linear chains made of 13 spheres (*27*). We therefore speculate that the short linear arrangements of the nanospheres are a favorable constraint for a highly hydrophobic protein, such as amelogenin, in aqueous solutions. Assuming that the microribbons are made of nanochains, these ribbons would have the optimal packing of the structural units in terms of their volume. The lateral packing of the nanochain structures may elicit a birefringence. This collinear organization also suggests that amelogenin nanospheres in the chain structures are not chemically isotropic. This property could be partly related to the hydrophobic/hydrophilic bipolar nature of the molecules (fig. S2) or to the presence of helical structures within the molecules (i.e., β spiral). In a highly aggregated amorphous precipitate of protein, the interchain repulsion resulting from the exposed C termini of the molecules tends to further force those molecules into an ordered register to evenly distribute their charges. This process can eventually lead to the formation of a ribbon structure with ordered domains that produce not only birefringence but also diffraction patterns originating from the specific molecular conformation. The current data are insufficient to determine whether there is a specific interaction between two molecules that would define a specific mutual orientation. The fact that those oligomers between trimer and hexamer are not detected by DLS may suggest an additional mechanism besides symmetry for the association of molecules and deserves further investigation. Our proposed hypothetical model for the step-by-step mechanism of this organized assembly and the architecture of amelogenin microribbons is schematically presented in Fig. 3.

Immersion of the microribbons into a metastable calcium phosphate solution (*21*) resulted in the formation of ordered and oriented crystals, aligned approximately along the long axis of the ribbons (Fig. 4). TEM and the corresponding electron diffraction patterns of crystals obtained from the tips of the mineralized microribbons confirmed the formation of oriented apatite crystals along their *c*-axial direction (Fig. 4, A and B). SEM micrographs of microribbons that have been pretreated with phosvitin followed by mineralization revealed the notable orientation of the crystals grown on the surface of these microribbons (Fig. 4, C and D, white arrows). The average length (±SD) of such crystals was 1.2 ± 0.2 μm. Phosvitin is a highly phosphorylated protein that was used in our experiments as a model for a potent nucleator. As suggested by our proposed model, the linear alignment of nanospheres in vitro creates an ideal framework that facilitates the oriented growth of apatite crystals regardless of the presence of an acidic protein such as phosvitin. The oriented nucleation of such crystals in vitro could be promoted through the interactions of the structured amelogenin framework with the highly phosphorylated protein, phosvitin. In the enamel extracellular matrix, this control can be achieved by the interaction of amelogenin and the nonamelogenin proteins such as the acidic enamelin or ameloblastin (*28*). Alternatively, the ordered hydrophobic/hydrophilic partitioning of amelogenin molecules could create an oriented array of acidic peptides on a hydrophobic substrate. A recent solid state nuclear magnetic resonance study provided experimental evidence to support the idea of direct amelogenin-apatite interaction through the hydrophilic C terminus (*29*). The control of crystallization events by ordered arrays of acidic functional groups has been widely implicated in the biomineralization world (*30*).

Whether similar microribbon structures exist in the enamel extracellular matrix in vivo is not known. Here, we demonstrate that amelogenin molecules have a strong tendency to assemble in vitro into organized microribbons under a wide variety of solvent conditions, without the presence of cells, crystals, or any other nonamelogenin proteins (i.e., enamelin or ameloblastin) (*1*). Some of these conditions included pH and ionic strength close to physiological conditions (table S1). This intrinsic property of the molecule and the remarkable alignment of the nanospheres into linear arrays, even in short intervals of a few hundred nanometers, gives us a valuable clue to amelogenin function during enamel biomineralization. This is particularly relevant in terms of the control over crystal orientation and growth in length at the early stage of enamel formation and adjacent to the dentino-enamel junction. Travis and Glimcher (*16*) originally reported the appearance of "short, swollen, fragmented filaments" in partially demineralized developing embryonic bovine enamel. The "intraprismatic" organic material or "tubular sheaths" appeared to be parallel to one another and to the long axes of the inorganic crystals. It was then proposed that the organization of the "tubular sheaths" played a major role in the ordered arrangement of the inorganic crystals within the prisms. The notion that apatite crystallite growth in the *c* axis might be directly controlled by the manner in which the spheres become oriented in the enamel tissue has also been proposed by Robinson *et al*. (*19*). Furthermore, fusion of enamel crystallites at the early stage of mineral formation has been proposed to explain the unusually long crystals formed in mature enamel (*16*). Careful SEM examination of our mineralized

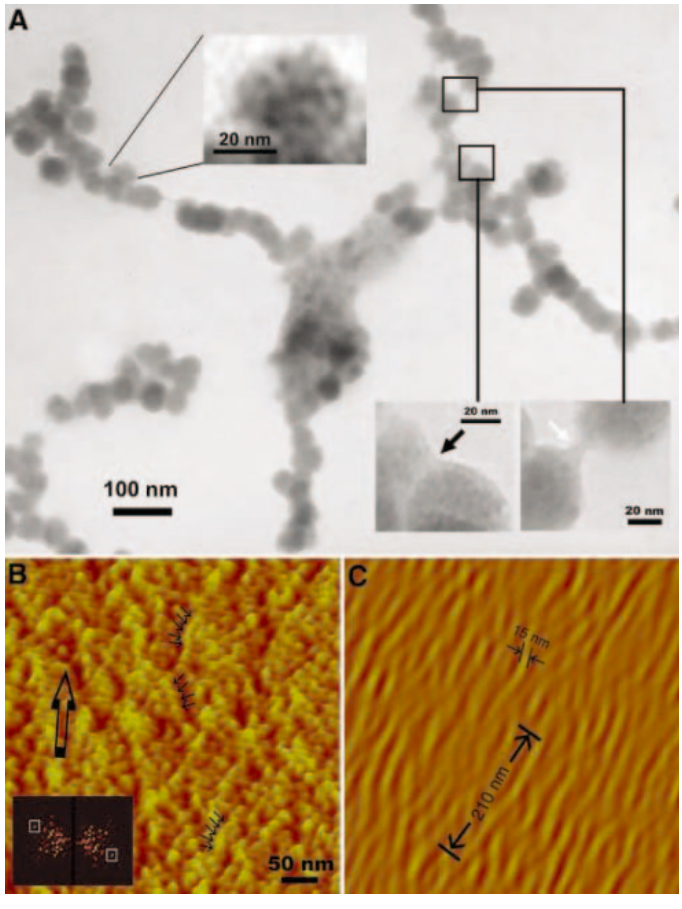

Fig. 2. Imaging of subunits and linear chains of nanospheres formed during amelogenin supramolecular assembly. (**A**) TEM micrographs of the linear arrays of amelogenin nanospheres collected from a protein crystallization solution at intermediate states during microribbon organization. (Insets) Subunits (4 to 8 nm in diameter) inside each nanosphere (~50 nm in diameter). The white and black arrows show the "bridging" and "fusion" of the adjacent nanospheres, respectively. (**B**) AFM phase image of the surface of an amelogenin ribbon showing linear arrays of nanospheres along the ribbon long axis (block arrow). (Inset) The anisotropic pattern of Fourier transform spectra. (**C**) Back-transform with the frequencies within the box in (B) confirming the length and thickness of linear arrays formed.

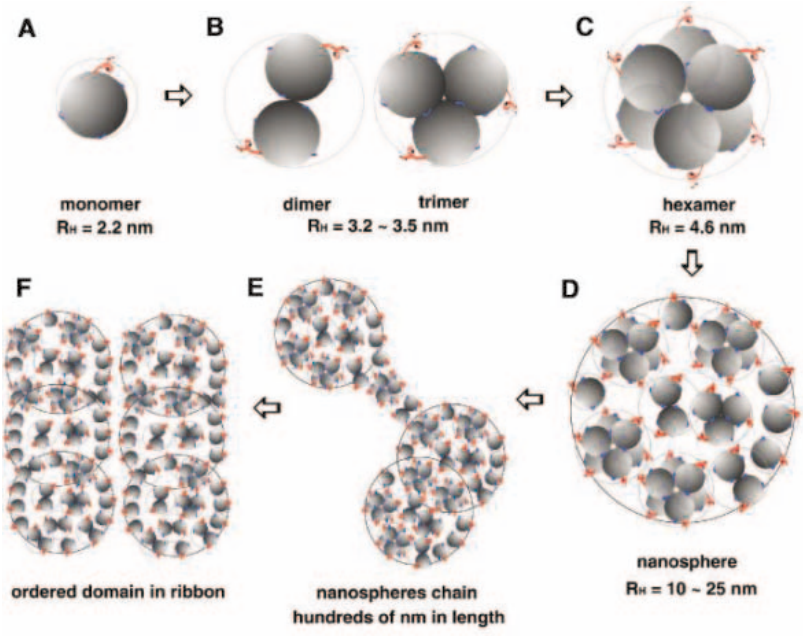

Fig. 3. A schematic model of amelogenin self-assembly based on DLS analysis, TEM, SEM, and AFM observations. (**A**) The amelogenin molecule can fold into a unique globular form that preserves a bipolar nature derived from its primary structure (fig. S2). The hydrophilic C-terminal (-Thr-Lys-Arg-Glu-Glu-Val-Asp) "tail" (red thread) is flexible and exposed on the surface of the molecule. (**B** and **C**) Oligomerization of amelogenin molecules occurs mainly by means of hydrophobic interactions. The calculated apparent radii for the ideal hard-sphere type of oligomers are 3.5 nm for a dimer and trimer, and 4.2 nm for a hexamer. (**D**) Nanosphere structures are formed through association of monomers and oligomers. (**E**) Further association of nanospheres results in larger assemblies among which linear chains of 10 to 15 nanospheres were mostly favorable. Association of the nanospheres was also observed in water. This process was facilitated by increasing amelogenin concentration or adding a hydrophilic ingredient such as PEG. (**F**) The bipolar nature of the molecule can facilitate the formation and/or the reorganization of the chain structures. This process can eventually lead to the formation of a ribbon structure.

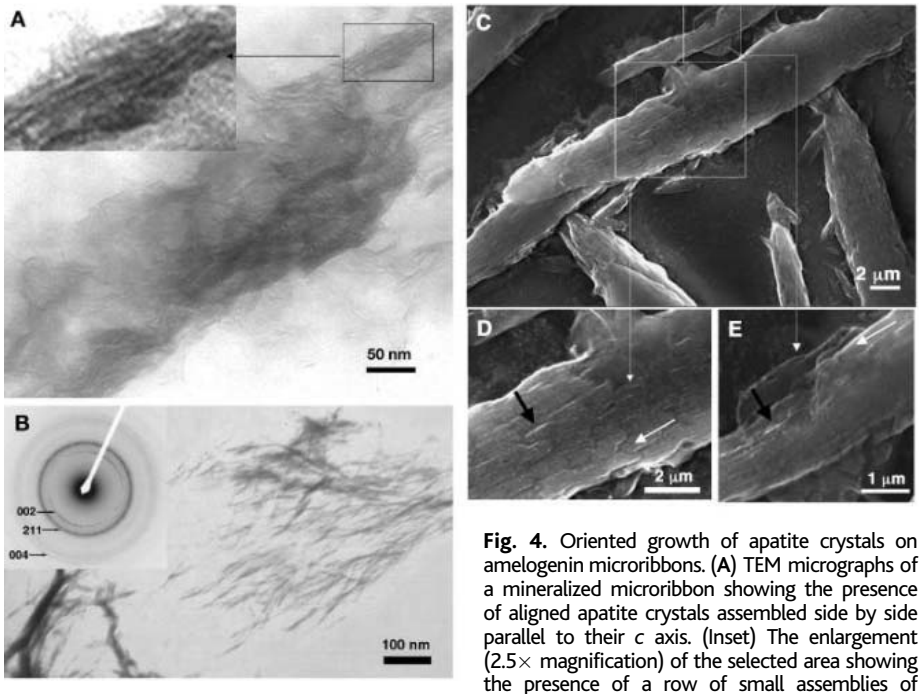

Fig. 4. Oriented growth of apatite crystals on amelogenin microribbons. (**A**) TEM micrographs of a mineralized microribbon showing the presence of aligned apatite crystals assembled side by side parallel to their *c* axis. (Inset) The enlargement (2.5× magnification) of the selected area showing the presence of a row of small assemblies of several nanometers in diameter. (**B**) TEM micrograph and the corresponding electron diffraction pattern of a region taken from the edge of a mineralized ribbon. Typical reflections of hydroxyapatite are marked. (**C** to **E**) Scanning electron micrographs of amelogenin microribbons, mineralized after pretreatment with phosvitin, showing the ordered platelike crystals along the ribbon axis. Black arrows show the edges of such crystals and white arrows show the direction of their orientation.

microribbons (Fig. 4, C to E) revealed fusion of some crystals at their tips that might eventually result in the formation of even more elongated crystals. Amelogenin nanospheres have been detected in vivo as "beaded rows" along the *c* axis of developing enamel crystallites, suggesting their close interaction with the crystal surface (*20*). We suggest that the organized assembly of amelogenin nanospheres into collinear arrays is critical at the initial stage of mineral deposition and adjacent to the dentino-enamel junction, both when oriented nucleation occurs (most likely as a result of other enamel proteins interacting with the structured amelogenin framework) and before amelogenin processing and degradation. After the orientation of the crystals is achieved, amelogenin protein starts to be processed at its C terminus. This results in the formation of the most abundant amelogenin proteolytic product ("20 KD" in the case of porcine), which has the potential to affect the morphology of calcium phosphate crystals in a very specific manner. Recent in vitro studies have demonstrated that amelogenins lacking the hydrophilic C terminus increase the ratios of length/width and thickness/width of octacalcium phosphate crystals by specifically interacting with the side (010) faces (*31*).

We demonstrate that amelogenin protein has a strong tendency to assemble in linear arrays of nanospheres, and we propose that this property is a key to its function as a scaffolding protein during the early stage of enamel mineralization. Our finding provides insight into the mechanisms of biomineralization, highlights the ability of an extracellular matrix component to control crystal orientation through supramolecular self-assembly, and contributes to the future fabrication of prototypes for biomimetic material design.

References and Notes

1. A. G. Fincham, J. Moradian-Oldak, J. P. Simmer, *J. Struct. Biol.* **126**, 270 (1999).
2. J. E. Eastoe, *Nature* **187**, 411 (1960).
3. E. J. Reith, *J. Biophys. Biochem. Cytol.* **9**, 825 (1961).
4. C. E. Smith, *Crit. Rev. Oral Biol. Med.* **9**, 128 (1998).
5. C. Robinson, H. D. Briggs, P. J. Atkinson, *Calcif. Tissue Int.* **33**, 513 (1981).
6. M. L. Paine *et al.*, *Matrix Biol.* **20**, 273 (2001).
7. C. Robinson, P. Fuchs, D. Deutsch, J. A. Weatherell, *Caries Res.* **12**, 1 (1978).
8. G. Daculsi, B. Kerebel, *J. Ultrastruct. Res.* **65**, 163 (1978).
9. S. Weiner, P. A. Price, *Calcif. Tissue Int.* **39**, 365 (1986).
10. S. Toyosawa, C. O'hUigin, F. Figueroa, H. Tichy, J. Klein, *Proc. Natl. Acad. Sci. U.S.A.* **95**, 13056 (1998).
11. L. C. Bonar, M. J. Glimcher, G. L. Mechanic, *J. Ultrastruct. Res.* **13**, 308 (1965).
12. V. Renugopalakrishnan, E. S. Strawich, P. M. Horowitz, M. J. Glimcher, *Biochemistry* **25**, 4879 (1986).
13. S. Zheng, A. T. Tu, V. Renugopalakrishnan, E. Strawich, M. J. Glimcher, *Biopolymers* **26**, 1809 (1987).
14. G. Nikiforuk, N. S. Simmons, *J. Dent. Res.* **44** (suppl.), 1119 (1965).
15. G. L. Mechanic, E. P. Katz, M. J. Glimcher, *Biochim. Biophys. Acta* **133**, 97 (1967).

16. D. F. Travis, M. J. Glimcher, *J. Cell Biol.* **23**, 447 (1964).
17. M. L. Watson, *J. Biophys. Biochem. Cytol.* **7**, 489 (1960).
18. F. C. Smales, *Nature* **258**, 772 (1975).
19. C. Robinson, P. Fuchs, J. A. Weatherell, *J. Cryst. Growth* **53**, 160 (1981).
20. A. G. Fincham *et al.*, *J. Struct. Biol.* **115**, 50 (1995).
21. Materials and methods are available as supporting material on *Science* Online.
22. C. Du, G. Falini, S. Fermani, C. Abbott, J. Moradian-Oldak, data not shown.
23. V. Renugopalakrishnan, N. Pattabiraman, M. Prabhakaran, E. Strawich, M. J. Glimcher, *Biopolymers* **28**, 297 (1989).
24. J. Moradian-Oldak *et al.*, *Biopolymers* **34**, 1339 (1994).
25. J. Moradian-Oldak, W. Leung, A. G. Fincham, *J. Struct. Biol.* **122**, 320 (1998).
26. V. N. Manoharan, M. T. Elsesser, D. J. Pine, *Science* **301**, 483 (2003).
27. U. Betke, M. Henk, J. M. Wills, *Discrete Comput. Geom.* **13**, 297 (1995).
28. N. Bouropoulos, J. Moradian-Oldak, *J. Dent. Res.* **83**, 278 (2004).
29. W. J. Shaw, A. A. Campbell, M. L. Paine, M. L. Snead, *J. Biol. Chem.* **279**, 40263 (2004).
30. S. Weiner, L. Addadi, *J. Mater. Chem.* **7**, 689 (1997).
31. M. Iijima, J. Moradian-Oldak, *J. Mater. Chem.* **14**, 2189 (2004).
32. Supported by the National Institute of Dental and Craniofacial Research–NIH grants to J.M.-O.: R01-DE-13414 and R21-DE-15332. We thank C. Shuler, M. Snead, and C. Wuenschell from the Center for Craniofacial Molecular Biology, University of Southern California for reading this manuscript before its submission. We thank J. Aizenberg from the Bell Labs, Lucent Technologies, New Jersey, for useful discussions.

Supporting Online Material
www.sciencemag.org/cgi/content/full/307/5714/1450/DC1
Materials and Methods
Figs. S1 to S5
Tables S1 to S4
References

27 September 2004; accepted 12 January 2005
10.1126/science.1105675

Residential Biofuels in South Asia: Carbonaceous Aerosol Emissions and Climate Impacts

C. Venkataraman,[1]* G. Habib,[1] A. Eiguren-Fernandez,[2] A. H. Miguel,[2] S. K. Friedlander[3]

High concentrations of pollution particles, including "soot" or black carbon, exist over the Indian Ocean, but their sources and geographical origins are not well understood. We measured emissions from the combustion of biofuels, used widely in south Asia for cooking, and found that large amounts of carbonaceous aerosols are emitted per kilogram of fuel burnt. We calculate that biofuel combustion is the largest source of black carbon emissions in India, and we suggest that its control is central to climate change mitigation in the south Asian region.

The effect of pollution particles measured over the Indian Ocean (*1*–*3*) on the regional atmospheric radiation balance is about 10 times the effect of greenhouse gases (*4*), leading to a large cooling at Earth's surface and a strong heating of the atmosphere. Large changes in atmospheric absorption and the radiation balance could affect rainfall patterns (*5*), which in turn could contribute to increased intensity of droughts and floods, for example, in China and potentially in neighboring India. Emissions control of light-absorbing soot, in addition to control of greenhouse gases, has been suggested as a measure to slow global warming (*6*, *7*). Soot or black carbon (BC) emissions in the south Asian region arise from fuel combustion for transportation, industrial, and residential uses. Here we find, from carbonaceous aerosol measurements and fuel use estimates, that the combustion of solid biofuels—such as wood, agricultural waste, and dried animal manure in cooking stoves—is the largest source of BC emissions in India. We therefore suggest that the control of these emissions through cleaner cooking technologies, in addition to reducing health risks to several hundred million users, could be of crucial importance to climate change mitigation in south Asia. Similar considerations may also apply to other regions of Asia, as well as Africa and South America, where residential biofuel combustion is prevalent.

Whereas greenhouse gases trap heat in Earth's atmosphere, aerosols (particles with diameters from 0.01 to 20 μm) can cool or heat the atmosphere, depending on their light-scattering or light-absorbing nature. Atmospheric aerosols contain acidic species (including sulfates and nitrates), carbonaceous constituents [BC and organic carbon (OC)], inorganic matter (fly ash), sea salt, and dust. Light-absorbing sp^2-bonded carbon, measured by change in light transmittance or reflection, is termed BC; refractory graphitic carbon, measured by thermal evolution under high-temperature oxidation (sometimes with simultaneous change in light transmittance or reflection), is termed elemental carbon (EC) (*8*, *9*). Most measurements of EC are treated as equal to BC.

High atmospheric concentrations of BC were recently measured in the south Asian region (*1*–*3*). These aerosols were attributed largely to fossil fuel emissions [according to the chemical mass balance principle (*10*)], but the particulate chemical signatures typical of fossil fuel and biomass burning sources (*1*, *2*) were not specific to south Asia. At the same time, estimates of energy use (*8*, *11*–*13*) showed a large amount of biofuel combustion for cooking, not believed so far to be a significant source of climate-forcing pollutants in terms of its negligible contribution to global CO_2 emissions (*14*). BC emission factors, not yet published for biofuel cooking stoves, are typically estimated from reported particle emission factors in inventory and review studies (*8*, *11*–*13*, *15*). The quantity and composition of particulate emissions (*16*) and their radiation absorption (*17*) depend on fuel species, moisture content and size, burn rate, and firing practice, making them highly source-specific. We report measurements of carbonaceous aerosol emission factors (in terms of grams of carbon per kilogram of fuel burnt) from combustion of a variety of biofuels widely used in the south Asian region, estimate their contribution to regional and global BC emissions, and discuss climate implications.

We conducted laboratory combustion experiments with four species of wood, six types of crop waste, and dried cattle manure (table S1), widely used as biofuels in India (*13*), in a traditional one-pot stove estimated to account for more than 80% of Indian stove use (*13*). A dilution sampler, developed and optimized in previous work (*18*, *19*), was used to achieve postcombustion quenching and gas/particle partitioning that would occur in actual indoor environments (fig. S1A). Emissions were entrained into a hood, and particles smaller than 2.5 μm aerodynamic diameter (PM-2.5), sampled through a probe, were collected on prebaked quartz-fiber filters by a cyclone-inlet particle sampler during combustion experiments (fig. S1B) and were analyzed for BC and OC to calculate emission factors (*18*).

[1]Department of Chemical Engineering, Indian Institute of Technology Bombay, Powai, Mumbai 400 076, India. [2]Southern California Particle Center and Supersite, Institute of the Environment, University of California, CHS 51-297, 650 Charles E. Young Drive, Los Angeles, CA 90095, USA. [3]Department of Chemical Engineering, University of California, Los Angeles, CA 90095, USA.

*To whom correspondence should be addressed. E-mail: chandra@che.iitb.ac.in

The burn cycle, designed to simulate local cooking practice (*13*, *19*, *20*), included low- and high-power phases and involved heating 0.5 kg of water from room temperature to its boiling point, then simmering for 5 min. To capture variation in rural cooking practice (*13*, *20*), we burned wood at average burn rates of 0.9 to 2.0 kg hour^{-1} (using two fuel charges), dried cattle manure at 1.3 kg hour^{-1} (using two charges), and crop waste at 1.1 to 1.9 kg hour^{-1} (using three charges) (table S1), with fuel charges suited to fit the stove combustion chamber and deliver the required power. We also burned two fossil fuels—liquefied petroleum gas (LPG) and kerosene—at 0.1 and 0.2 kg hour^{-1}, respectively, in stove burners used widely for residential cooking. Measured combustion temperatures, corrected for the heat lost by radiation [following (*19*)], varied from 300° to 670°C for different fuels and combustion conditions. Ambient air diluted the combustion gases at dilution mass ratios of 10 to 40 during combustion of different biofuels (table S2). The estimated equivalence ratios (table S1) were greater than 1, implying highly fuel-rich flame conditions—that is, the actual fuel-to-air ratios in the flame were higher than the corresponding stoichiometric ratios for complete oxidation of fuel constituents (table S2).

Measured BC emission factors ranged from 0.38 to 0.62 g kg^{-1} from wood combustion [for varying burn rates (0.9 to 2.0 kg hour^{-1}) and corresponding combustion temperatures (396° to 644°C)] and from 0.12 to 0.17 g kg^{-1} from straw and dried cattle manure; these values were at the lower end of the range 0.3 to 1.4 g kg^{-1} estimated in recent inventories (*8*, *12*, *13*, *15*). Measured OC emission factors were 0.17 to 4.69 g kg^{-1}, again lower than estimates of 1.7 to 7.8 g kg^{-1} in inventory studies (*8*, *12*, *13*, *15*), and varied with fuel type, increasing systematically with burn rate (table S1). On the basis of fuel burnt, BC and OC emission factors from kerosene and LPG stoves were lower than those from biofuel stoves by a factor of 3 to 50 (table S1)—or, in terms of megajoules of heat recovery, lower by a factor of 15 to 150—because of the higher thermal efficiencies of kerosene and LPG stoves.

In thermal-optical measurement methods (*18*), such as the one used in this study, the relative amount of evolved carbon allocated as BC and OC is sensitive to the temperature program chosen, particularly for wood smoke samples (*9*). The method adopted here uses a maximum temperature of 870°C (fig. S2), as opposed to 550° to 750°C, for pyrolysis under pure helium to correct for the error in BC from charring of OC, and results in lower BC values than the low-temperature methods would have yielded (*9*). Artifact OC enhancement was measured through OC adsorption on a quartz-fiber filter in a parallel stream, after particle filtering (*18*), and subtracted from the sample OC (fig. S3 and table S3). Artifact OC was specifically high for two wood species, jamun and neem (table S3). An uncertainty in this measurement would not change the BC but would increase the OC emission factors for these species. This would reduce the spread in the BC/OC ratio from different wood species but would not change the mean value significantly, nor would it alter our overall conclusions.

BC constituted 5 to 52% of PM-2.5 mass, consistent with the observation that large BC fractions are possible in emissions from small cooking fires (*8*). This range is also substantially larger than the 3 to 6% reported from large fires in different forest and grassland classes (*15*, *21*). OC fractions of 14 to 52% from biofuel were correspondingly lower than the 60 to 70% reported from open biomass burning (*15*). We found that BC and OC constituted 51 to 67% of biofuel PM-2.5; together with potassium and levoglucosan, they are reported to constitute 70 to 85% of PM-2.5 from open burning. Our data yielded BC/OC ratios of 0.11 to 3.53 in biofuel aerosols; these values are significantly higher than the ratios of 0.06 to 0.14 reported from open burning and are indistinguishable from the ratio of 1.0 reported from diesel transport and household coal emissions (*2*).

Although the formation of BC and OC in biomass and biofuel fires is not well understood and is beyond the scope of this work, it would depend on variables such as burn rate, air-fuel ratio, flame turbulence, and combustion temperature. We estimate biomass burn rates in forest fires to range from 100 to 3000 kg hour^{-1} on the basis of reported experimental burns (*22*). Typical burn rates in fireplaces and space-heating stoves (*23*, *24*) are 2 to 9 kg hour^{-1}, significantly higher than in the biofuel cooking fires studied here. The low burn rates in biofuel cooking fires result in very low air induction into the flame by thermal buoyancy, as evidenced by the large equivalence ratios (table S1) characteristic of fuel-rich flame conditions, which can result in high BC and low OC formation. We therefore emphasize that small biofuel fires are distinct in nature from large fires and that a more complete understanding of their aerosol emissions, especially chemical and optical characteristics relevant to climate, remains to be gained.

The large BC content in emissions from biofuel combustion has the potential for significant atmospheric impact given the extensive use of these fuels in India (*13*). In Table 1, BC emissions from biofuel combustion in India are estimated from the emission factors we measured, together with fuel usage data for India (*13*) and other world regions (*8*, *25*). Because biofuel combustion for cooking occurs most often in indoor environments, we consider in these estimates the fraction of emissions that penetrate to the ambient air, estimated at about 80% on the basis of typical ventilation and particle deposition rates in rural kitchens (*26*). BC emissions from biofuel combustion in India are 172 to 340 Gg year^{-1}, hence the relative contributions to total BC emissions from fossil fuel, open burning, and biofuel combustion are 25%, 33%, and 42%, respectively. The corresponding OC emissions are 582 to 1683 Gg year^{-1}, so that

Table 1. Black carbon (BC) emissions from biofuel combustion in India, Asia, and the world. Estimates of BC emissions from biofuel combustion made use of emission factors (g kg^{-1}) from table S1. In the rightmost column, the total includes BC emissions from forest, savanna, and crop waste open burning as well as fossil fuel combustion.

Region	Base year	Biofuel consumption (Tg year^{-1})			Black carbon emissions (Gg year^{-1})				BC source ratio (biofuel/total) (%)
		Fuelwood	Dried cattle manure	Crop waste	Fuelwood	Dried cattle manure	Crop waste	Total biofuel	
India	1995	281* (192–409)‡ (*13*)	62* (35–108)‡ (*13*)	36* (20–67)‡ (*13*)	143* (75–272)‡	8* (3–17)‡	21* (9–51)‡	172* (87–340)‡	44†
Asia		800–930§ (*8*, *25*)	130–200§ (*8*, *25*)	430–545§ (*8*, *25*)	400–470	15–25	220–280	635–775	30‡
Global		1324–1615§ (*8*, *25*)	150–410§ (*8*, *25*)	442–707§ (*8*, *25*)	670–820	20–50	230–360	920–1230	15‡
India	1985	220 (*25*)	93 (*25*)	86 (*25*)	110	10	40	160	54
Asia		753 (*25*)	133 (*25*)	545 (*25*)	385	15	280	680	23
Global		1324 (*25*)	136 (*25*)	597 (*25*)	675	15	300	990	7

*Central value of biofuel consumption for cooking and BC emissions. †Central value of percent contribution of BC from biofuel combustion. ‡Lower and upper bound estimates of biofuel consumption for cooking and BC emissions at 95% confidence interval. §Asia and global numbers include biofuel consumption for cooking and space heating, excluding the amount used in industry. The ranges are from two different studies (*8*, *25*).

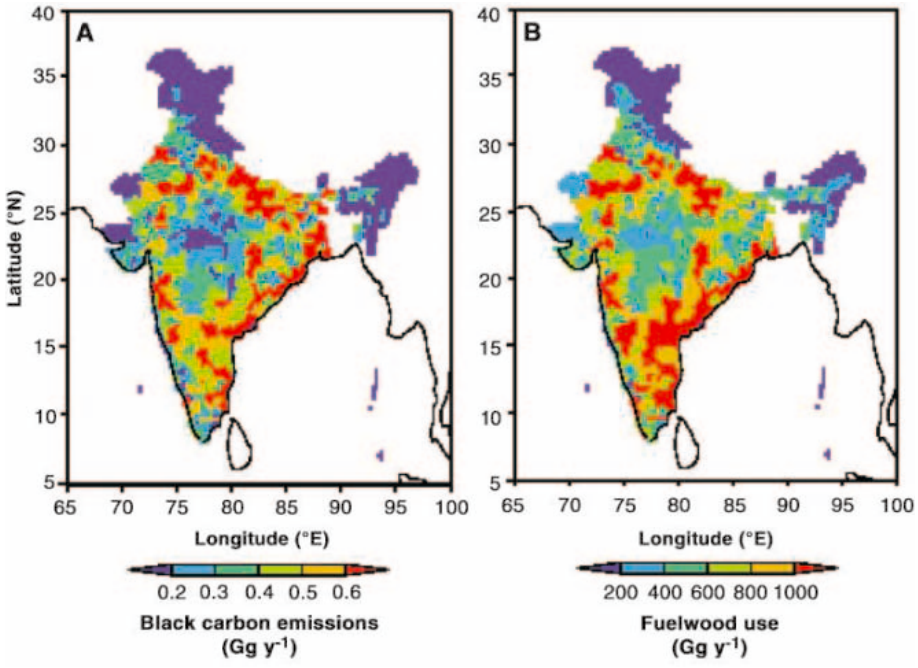

Fig. 1. Spatial distribution of (**A**) black carbon emissions (Gg year^{-1}) from biofuel combustion and (**B**) fuelwood use (Gg year^{-1}) in India.

the relative contributions to total OC emissions from fossil fuel, open burning, and biofuel combustion are 13%, 43%, and 44%, respectively.

Between 1985 and 1995, the reduction in the relative contribution of biofuels to Indian BC emissions (Table 1) resulted not from a reduction in this source, but from an increase in BC emissions from fossil fuel combustion during this period. Biofuel BC emissions from India have essentially remained unchanged during the 1985–1995 period (Table 1), implying that cleaner cooking technologies have been introduced very slowly. Other estimates of 207 to 425 Gg year^{-1} BC and 484 to 2105 Gg year^{-1} OC emissions from biofuel combustion in India (*8*, *11*, *12*) differ from our findings in that they use calculated emission factors, highly uncertain per capita biofuel usage in India, and an assumed 100% rural user population for all three biofuel types, thus making direct comparisons untenable.

High BC concentrations and atmospheric absorption measured during the Indian Ocean Experiment (INDOEX) have been related through trajectory analysis to source regions in the Indo-Gangetic plain, central/east coast, and south India (*1*, *27*). The potential contribution of biofuel emissions was examined by estimating spatial distributions of biofuel combustion and related BC emissions, using district-level biofuel user populations (*28*) and the emission factors reported here. The emission rates of BC from biofuels (Fig. 1A) and use of wood as biofuel (Fig. 1B) were both high in regions from which highly absorbing aerosols had originated during INDOEX. This suggests that the combustion of biofuels, especially wood, is a potentially significant source of atmospheric BC and related climate effects (*5*) in south Asia. The large radiation perturbations from aerosols (*4*) and the resulting potential changes in tropical rainfall (*5*) would have important implications for agricultural productivity and the economy of the region.

An analysis of the climate response of soot emissions from fossil fuel and biofuel combustion has suggested that control of soot, in addition to greenhouse gases, is an important measure to slow global warming, especially on short time scales (*6*, *7*). Our results suggest that biofuel combustion could significantly affect atmospheric BC concentrations in the south Asian region. The climate effects of biofuel combustion aerosols have been combined with the effects of open biomass burning in the scientific consensus reports of the Intergovernmental Panel on Climate Change (*29*). We suggest that biofuel combustion needs to be addressed as a distinct source, and that cleaner cooking technologies not only could yield significant local health and air quality benefits but also could have an important role in climate change mitigation in the south Asian region.

References and Notes

1. C. Neusüß, T. Gnauk, A. Plewka, H. Herrmann, *J. Geophys. Res.* **107**, 10.1029/2001JD000327 (2002).
2. O. L. Mayol-Bracero *et al.*, *J. Geophys. Res.* **107**, 10.1029/2000JD000039 (2002).
3. V. Ramanathan *et al.*, *J. Geophys. Res.* **106**, 28371 (2001).
4. S. K. Satheesh, V. Ramanathan, *Nature* **405**, 60 (2000).
5. S. Menon, J. Hansen, L. Nazarenko, Y. Luo, *Science* **297**, 2250 (2002).
6. M. Jacobson, *J. Geophys. Res.* **107**, 10.1029/2001JD001376 (2002).
7. M. Jacobson, *J. Geophys. Res.* **109**, 10.1029/2004JD004945 (2004).
8. T. C. Bond *et al.*, *J. Geophys. Res.* **109**, 10.1029/2003JD003697 (2004).
9. J. J. Schauer *et al.*, *Environ. Sci. Technol.* **37**, 993 (2003).
10. S. K. Friedlander, *Environ. Sci. Technol.* **7**, 235 (1973).
11. M. S. Reddy, C. Venkataraman, *Atmos. Environ.* **36**, 699 (2002).
12. D. G. Streets *et al.*, *J. Geophys. Res.* **108**, 10.1029/2002JD003093 (2003).
13. G. Habib *et al.*, *Global Biogeochem. Cycles* **18**, 10.1029/2003GB002157 (2004).
14. J. G. J. Olivier *et al.*, *Applications of EDGAR* (Emission Database for Global Atmospheric Research) *Including a Description of EDGAR 3.2: Reference Database with Trend Data for 1970–1995* [Report 773301001, National Institute for Public Health and the Environment (RIVM), Netherlands, 2002]; available at www.rivm.nl/bibliotheek/rapporten/773301001.pdf.
15. M. O. Andreae, P. Merlet, *Global Biogeochem. Cycles* **15**, 955 (2001).
16. J. R. Rau, *Aerosol Sci. Technol.* **10**, 181 (1989).
17. T. C. Bond, *Geophys. Res. Lett.* **28**, 4075 (2001).
18. See supporting data on *Science* Online.
19. C. Venkataraman, G. U. M. Rao, *Environ. Sci. Technol.* **35**, 2000 (2001).
20. K. R. Smith *et al.*, *Greenhouse Gases from Small-Scale Combustion Devices in Developing Countries: Phase IIA—Household Stoves in India* (Report EPA/600/R-00/052, U.S. Environmental Protection Agency, Washington, DC, 2000); available at www.epa.gov/ORD/NRMRL/Pubs/600R00052/600R00052.pdf.
21. P. V. Hobbs *et al.*, *J. Geophys. Res.* **108**, 10.1029/2002JD002352 (2003).
22. W. S. Trollope, L. A. Trollope, A. L. F. Potgieter, N. Zambatis, *J. Geophys. Res.* **101**, 23531 (1996).
23. P. M. Fine, G. R. Cass, B. R. T. Simoneit, *Environ. Sci. Technol.* **35**, 2665 (2001).
24. J. R. Sheesley, J. J. Schauer, Z. Chowdhury, G. R. Cass, B. R. T. Simoneit, *J. Geophys. Res.* **108**, 10.1029/2002JD002981 (2003).
25. R. Yevich, J. A. Logan, *Global Biogeochem. Cycles* **17**, 10.1029/2002GB001952 (2003).
26. W. Nazaroff, personal communication.
27. K. Franke *et al.*, *J. Geophys. Res.* **108**, 10.1029/2002JD002473 (2003).
28. *National Family Health Survey (NFHS-2)*, India 1998–99 (International Institute for Population Sciences, Mumbai, India, 2001); available at www.nfhsindia.org/india2.html.
29. J. E. Penner *et al.*, in *Climate Change 2001: The Scientific Basis, Contribution of Working Group I to the Third Assessment Report of the Intergovernmental Panel on Climate Change*, J. T. Houghton *et al.*, Eds. (Cambridge Univ. Press, Cambridge, 2001), pp. 289–348.

30. Supported by grants from the Indian Space Research Organization–Geosphere Biosphere Program (ISRO-GBP) and the Center for Clouds, Chemistry and Climate (C4), University of California, San Diego. Additional support (A.H.M. and A.E.-F.) was provided by National Institute of Environmental Health Sciences grant 5P30 ES07048 to the Southern California Environmental Health Sciences Center and by U.S. EPA grants R827352-01-0 and CR-82805901 to the Southern California Particle Center and Supersite. We thank M. Hakami for chemical analysis assistance. The late Prof. Glen R. Cass (California Institute of Technology and Georgia Institute of Technology) was instrumental in the initiation of this work.

Supporting Online Material

www.sciencemag.org/cgi/content/full/307/5714/1454/DC1
Materials and Methods
Figs. S1 to S3
Tables S1 to S3

23 August 2004; accepted 24 January 2005
10.1126/science.1104359

Nutritional Status and Diet Composition Affect the Value of Diatoms as Copepod Prey

Ruth H. Jones and Kevin J. Flynn*

The role of diatoms as key food for copepods at the base of pelagic food chains has been questioned recently on the grounds of toxicity. We show, using unialgal versus mixed algal diets of different nutritional status (i.e., nitrogen:carbon ratio) fed to *Acartia tonsa*, that diatoms per se are not toxic but that single-diatom diets are inadequate. Additionally, the nutritional state of the phytoplankton has a profound effect on copepod growth and growth efficiency. The ecological significance of laboratory demonstrations of diatom toxicity needs to be reconsidered.

Diatoms are important primary producers traditionally seen as keystone organisms, leading through copepods to marine fish production (*1*, *2*). However, the consumption of diatoms may be deleterious for copepod egg production (*3*, *4*), hatching success (*5*, *6*), and subsequent development (*7*) because of toxicity (*5*, *8*) or the absence of essential dietary components (*9*, *10*). A resolution of the debate about the value of diatoms as food for copepods (*5*, *8*, *11*) is important. If diatoms are toxic under all conditions, then their consumption will always negatively affect copepod production. This would overturn the traditional view of the importance of the diatom-copepod-fish food chain. If the inadequacy of diatoms (*3*, *4*) results from the absence of a dietary factor (e.g., a fatty acid), then the ecological consequence would be limited. Even in the densest monospecific diatom blooms, alternative prey are available. Copepods are also well known for their selective feeding behavior (*12*–*14*). If, on the other hand, phytoplankton nutrient status [for instance, the nitrogen:carbon ratio (N:C)] substantially affected copepod production, then—given that the entire phytoplankton population would likely be subjected simultaneously to a similar nutrient stress—there would be major consequences for the trophic web, from nutrient regeneration to fish production.

To investigate these alternatives, experiments need to consider the consequences of feeding copepods with different mixtures of phytoplankton of different nutrient status (*15*). We studied the effect of diatoms on copepod production using *Acartia tonsa*, a copepod representative of species common to many temperate and subtropical coastal marine environments (*16*). The experimental procedure was similar to that of previous studies (*8*), but we monitored the effect on the whole copepod life cycle of monodiets versus mixed diets of diatoms and dinoflagellates that had been grown under different nutrient conditions (*17*). We also monitored ingestion of the different prey items throughout the 15-day experiments, allowing us to calculate the population growth efficiency (PGE) (*17*).

In the first of two studies on the adequacy of different diets, copepods were fed the diatoms *Thalassiosira pseudonana* and *T. weissflogii*, with a range of different percentages of the dinoflagellate *Aureodinium pigmentosum* (Table 1). It has been suggested, in laboratory experiments where copepods are fed a monodiet of diatoms, that any deleterious effects may not appear for at least a week (*11*). In our study, the effects of a diatom monodiet were clear within 3 days; the juvenile stages (nauplii) fed on only diatoms were small, pale, and lethargic, and the adults laid fewer and smaller eggs in comparison with those fed a mixed algal diet or even a monodiet of dinoflagellate (fig. S1). By day 15, all copepods on a diatom monodiet had died (Fig. 1, treatments 1 and 2). A mixed-species diatom diet was more beneficial (Fig. 1, treatment 3), possibly because of the presence of different fatty acids in individual diatom species (*18*). Nevertheless, we observed the same rapid effect on nauplii growth that others have attributed to aldehyde toxins (*8*) when nauplii were fed a diatom monodiet (fig. S1). Prey consumption did not halt when only diatoms were consumed (Fig. 1A, treatments 1 to 3, and fig. S1), but copepod production was not realized (Fig. 1B), and egg production and survival rates were poor. Generally, egg production increases with increasing food concentration (*19*, *20*), but clearly the dietary composition can override this, because we supplied saturating concentrations of prey.

Even a small proportion of nondiatom (dinoflagellate) food in the suspension had a disproportionately beneficial effect on copepod production and growth efficiency (Fig. 1, B and C, treatments 4 to 6), with clear indications of preferential selective grazing on the dinoflagellate. In treatment 4, only 5% of the available diet was dinoflagellate (Table 1), but the contribution of dinoflagellates to ingested biomass was 40% (Fig. 1A). However, this treatment still failed to support copepod growth. In treatments 5 to 7, increasing proportions of dinoflagellate were available, and a threshold consumption of dinoflagellates was crossed, enabling net copepod growth. Treatment 6 (in which dinoflagellates were 25% of the available diet and >70% of ingested biomass) showed the maximum growth yield (Fig. 1B) and growth efficiency (Fig. 1C and fig. S1). Population growth with a mixed diet (treatment 6) was higher than that on a dinoflagellate monodiet (treatment 8). Selection of prey items is thus an important feature of the predator-prey process, enabling the success of the copepod.

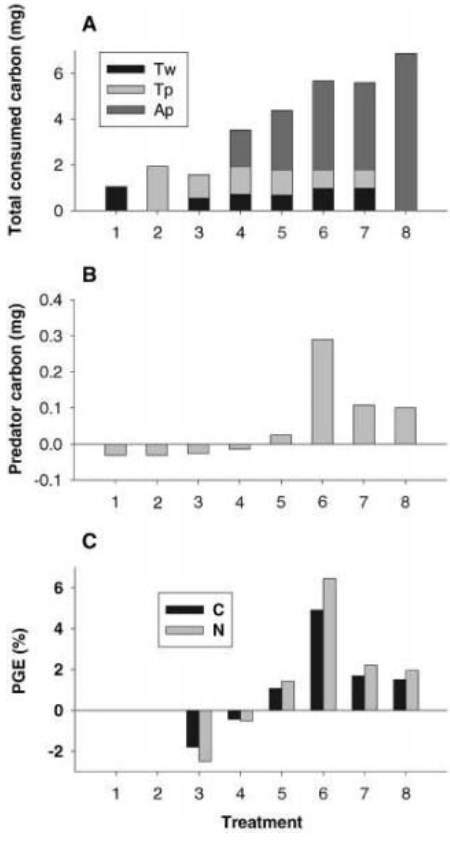

Fig. 1. Prey consumption, copepod production, and PGEs from study 1. (**A**) Total cumulative carbon consumed per treatment for each prey. Tw, *T. weissflogii*; Tp, *T. pseudonana*; Ap, *Au. pigmentosum*. (**B**) Average total change in *A. tonsa*. Negative results indicate copepod death. Starting biomass was 0.03 mg of C. (**C**) Total PGEs for *A. tonsa* (*17*, *25*) expressed in terms of carbon or nitrogen. Negative PGE reflects copepod death. Treatments 1 and 2 contained 0 mg of predator C at the end of the study, so PGE could not be calculated. The composition of algal prey in different treatments is given in Table 1.

Institute of Environmental Sustainability, University of Wales, Swansea, SA2 8PP, UK.

*To whom correspondence should be addressed. E-mail: k.j.flynn@swansea.ac.uk

The development of the copepod *Calanus helgolandicus* has been found to arrest when the copepod feeds exclusively on the diatom *Skeletonema costatum*, with low egg-hatching success and poor development of nauplii that do hatch (*8*). It was concluded that the decrease in recruitment was because the diatom was toxic to the copepod, because of its ability to produce aldehydes. Our results indicate that diatoms are not toxic but are of lower nutritional value than dinoflagellates. Importantly, the presence of a non-diatom did not adversely affect predation on the diatom but instead resulted in an elevation of overall efficiency in copepod growth and development (Fig. 1, A and C, and fig. S1); this is more in keeping with a dietary inadequacy than a toxic event. The PGE for nitrogen (PGE-N) was higher than that for carbon (PGE-C) in growing populations (treatments 5 to 7) and lower than PGE-C in dying or poorly growing populations (treatments 3 and 4) (Fig. 1C), which is consistent with stoichiometric demands in the former instance (prey N:C < predator N:C) and with copepod starvation in the dying populations.

In our second study, we considered the effect of prey nutrient (nitrogen) status and species supply timing on *Acartia* production. The Mix treatments (controls) had a diatom:dinoflagellate diet ratio close to that of the optimal in treatment 6 in our first study (Fig. 1). The Alt treatments had an alternating diet of just diatoms (both diatom species for 3 or 4 days) or just dinoflagellates (for 1 or 2 days). Prey in the Mix-s and Alt-s treatments were nitrogen sufficient, and those in the Mix-d and Alt-d conditions were nitrogen depleted (Table 1). Although consumption of prey in these four treatments was broadly similar (Fig. 2A), this did not translate in any way to copepod production (Fig. 2B). The value of mixed diets has been considered before (*21*), but we studied the longer term effects over the whole life cycle. A mixed diet also becomes all the more important when prey are nitrogen deprived (Fig. 2, treatments Mix-s and Mix-d). Even so, a dinoflagellate of low N:C still supported higher copepod production than diatoms of high N:C, possibly because of differences in essential fatty acid or amino acid composition. Although the stoichiometric (carbon:nitrogen:phosphorus) composition of prey is important (*22*), other stoichiometric-linked factors can have as great or greater effect on growth efficiency and should be considered over the whole life cycle (as here) rather than over just one part of the cycle (*23*, *24*).

Table 1. Composition of algal prey treatments in which the diatoms *T. pseudonana* (Tp) and *T. weissflogii* (Tw) and the dinoflagellate *Au. pigmentosum* (Ap) were supplied to the copepod *A. tonsa*. Treatments contained prey at a total of 3 mg of carbon per L, with contributions of individual species indicated as percentage of total carbon biomass. In study 2, prey were supplied either as a mixture of diatom and dinoflagellate (Mix) or with alternating periods of supply (Alt) either as mixed diatoms (Tp and Tw) or as dinoflagellate (Ap). Prey nutrient status (NStat) was either nitrogen sufficient (s) or nitrogen depleted (d). For the s and d diets, respectively, prey mass N:C was Tp, 0.13 and 0.09; Tw, 0.15 and 0.11; and Ap, 0.12 and 0.075.

Treatment	Algal prey (%)			NStat	Diet
	Tp	Tw	Ap		
		Study 1			
1		100		s	Mix
2	100			s	Mix
3	50	50		s	Mix
4	47.5	47.5	5	s	Mix
5	45	45	10	s	Mix
6	37.5	37.5	25	s	Mix
7	25	25	50	s	Mix
8			100	s	Mix
		Study 2			
Mix-s	33.3	33.3	33.3	s	Mix
Mix-d	33.3	33.3	33.3	d	Mix
Alt-s	50	50	100	s	Alt
Alt-d	50	50	100	d	Alt

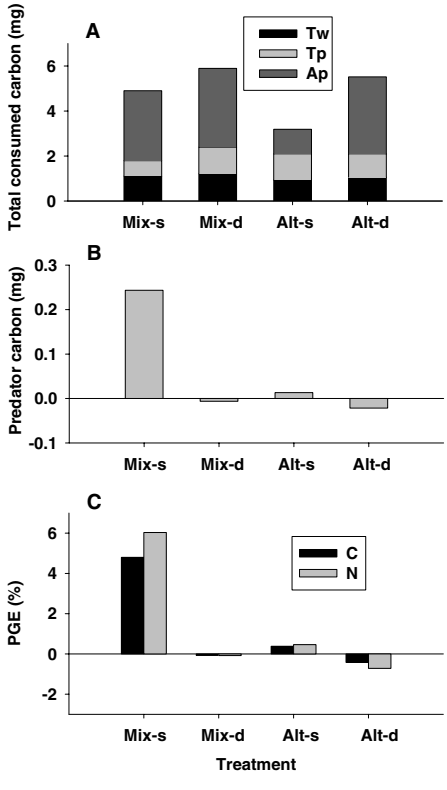

Fig. 2. Prey consumption, copepod production, and PGEs from study 2. (**A**) Total cumulative carbon consumed per treatment for each prey. (**B**) Average total change in *A. tonsa*. Negative results indicate copepod death. (**C**) Total PGEs for *A. tonsa*. Negative PGE reflects copepod death. The composition of algal prey in different treatments is given in Table 1.

When copepods were fed an alternating diet, growth efficiency was again very poor (Fig. 2C), although the consumption of prey was still high (Fig. 2A). Even with a repeated cycle of alternating prey, a short period on a monodiet of diatoms had an obvious deleterious effect on copepod growth and development, with copepods fed the Alt regime being smaller and slower to develop than those fed the Mix regime (fig. S2). Copepods fed the alternating diet did, however, fare better than those fed a continuous monodiet of diatoms (compare Fig. 2B, treatment Alt-s, with Fig. 1B, treatments 1 to 3). Although copepod production was able to recover to some extent when they were fed dinoflagellates for 1 to 2 days, recovery was insufficient to maintain parity with the copepods fed a mixed diet (Fig. 2B). These results indicate the potential consequences of encountering patches of different prey types of different nutritional status and the importance of selective feeding to ensure a mixed diet if copepods are to maximize their growth.

The effect of the nutritional status of the prey is clearly substantial, not only on predator growth but also on growth efficiency (*25*). In the attempt to resolve the controversy over the value of diatoms for copepod growth, it is essential that the nutritional status of the prey items be considered. Given the abilities of copepods to select their prey (*13*), the presence of a near-monospecific phytoplankton bloom need not mean that the dominant organism is the only or even the main food item. There is also a possibility that the consumption of microzooplankton, which have themselves fed on diatoms, will provide a route for enhanced diatom support of copepod growth. Protistan microzooplankton are now recognized as important food for copepods (*26*); their role may be all the more important if they alter the dietary value of the original phytoplankton prey (*27*).

In our experiments, the use of monodiets of two diatom species, *T. pseudonana* and *T. weissflogii*, produced the same recruitment failure reported with a monodiet of *S. costatum* (*8*). However, mixing the diatoms with the dinoflagellate *Au. pigmentosum* clearly indicated that the diatoms were not toxic but nutritionally deficient. We conclude that any evaluation of toxicity not only requires the use of a mixed diet, but also that an assessment of the nutritional status (e.g., N:C) of the prey is critically important.

References and Notes

1. S. M. Marshall, A. P. Orr, *The Biology of a Marine Copepod, Calanus finmarchicus* (*Gunnerus*) (Oliver & Boyd, London, 1955).
2. M. Starr, J. A. Runge, J.-C. Therriault, *Sarsia* **84**, 379 (1999).
3. S. A. Poulet, A. Ianora, A. Miralto, L. Meijer, *Mar. Ecol. Prog. Ser.* **111**, 79 (1994).
4. S. Ban *et al.*, *Mar. Ecol. Prog. Ser.* **157**, 287 (1997).
5. A. Miralto *et al.*, *Nature* **402**, 173 (1999).

6. A. Ianora, S. A. Poulet, A. Miralto, R. Grottoli, *Mar. Biol.* **125**, 279 (1996).
7. Y. Carotenuto, A. Ianora, I. Buttino, G. Romano, A. Miralto, *J. Exp. Mar. Biol. Ecol.* **276**, 49 (2002).
8. A. Ianora *et al.*, *Nature* **429**, 403 (2004).
9. S. H. Jónasdóttir, *Mar. Biol.* **121**, 67 (1994).
10. K. Shin *et al.*, *Prog. Oceanogr.* **57**, 265 (2003).
11. X. Irigoien *et al.*, *Nature* **419**, 387 (2002).
12. T. Kiørboe, E. Saiz, M. Viitasalo, *Mar. Ecol. Prog. Ser.* **143**, 65 (1996).
13. B. Meyer-Harms, X. Irigoien, R. Head, R. Harris, *Limnol. Oceanogr.* **44**, 154 (1999).
14. X. Irigoien *et al.*, *Limnol. Oceanogr.* **45**, 44 (2000).
15. S. H. Jónasdóttir *et al.*, *Mar. Ecol. Prog. Ser.* **172**, 305 (1998).
16. M. R. Reeve, M. A. Walter, *J. Exp. Mar. Biol. Ecol.* **29**, 211 (1977).
17. Materials and methods are available as supporting material on *Science* Online.
18. S. H. Jónasdóttir, T. Kiørboe, *Mar. Biol.* **125**, 743 (1996).
19. D. M. Checkley, *Limnol. Oceanogr.* **25**, 430 (1980).
20. F. Alonzo, P. Mayzaud, S. Razouls, *Mar. Ecol. Prog. Ser.* **209**, 231 (2001).
21. S. P. Colin, H. G. Dam, *Limnol. Oceanogr.* **47**, 1430 (2002).
22. T. Andersen, J. J. Elser, D. O. Hessen, *Ecol. Lett.* **7**, 884 (2004).
23. L. D. J. Kuijper, T. R. Anderson, S. A. L. M. Kooijman, *J. Plankton Res.* **26**, 213 (2004).
24. T. Kiørboe, *Mar. Ecol. Prog. Ser.* **55**, 229 (1989).
25. R. H. Jones, K. J. Flynn, T. R. Anderson, *Mar. Ecol. Prog. Ser.* **235**, 147 (2002).
26. M. R. Roman, A. L. Gauzens, *Limnol. Oceanogr.* **42**, 623 (1997).
27. W. Breteler, N. Schogt, M. Baas, S. Schouten, G. W. Kraay, *Mar. Biol.* **135**, 191 (1999).
28. We would like to thank E. Griffiths for her help in the preparation of algal cultures. Supported by a grant from the Natural Environment Research Council (UK) through the Marine Productivity thematic program.

Supporting Online Material
www.sciencemag.org/cgi/content/full/307/5714/1457/DC1
Materials and Methods
Figs. S1 and S2
References and Notes

22 November 2004; accepted 12 January 2005
10.1126/science.1107767

Life at Depth: *Photobacterium profundum* Genome Sequence and Expression Analysis

A. Vezzi,[1] S. Campanaro,[1] M. D'Angelo,[1] F. Simonato,[1] N. Vitulo,[1] F. M. Lauro,[2] A. Cestaro,[1] G. Malacrida,[1] B. Simionati,[1] N. Cannata,[1] C. Romualdi,[1] D. H. Bartlett,[2] G. Valle[1]*

Deep-sea life requires adaptation to high pressure, an extreme yet common condition given that oceans cover 70% of Earth's surface and have an average depth of 3800 meters. Survival at such depths requires specific adaptation but, compared with other extreme conditions, high pressure has received little attention. Recently, *Photobacterium profundum* strain SS9 has been adopted as a model for piezophily. Here we report its genome sequence (6.4 megabase pairs) and transcriptome analysis. The results provide a first glimpse into the molecular basis for life in the largest portion of the biosphere, revealing high metabolic versatility.

Ambient pressure has influenced the evolution and distribution of species in the oceans (*1*). Piezophiles have evolved in multiple lineages of the Bacteria and Archaea domains of life (*2*), and high-pressure–adapted vertebrates and invertebrates have also been characterized. To undertake a genome-wide analysis of life at high pressure, we sequenced the genome of *Photobacterium profundum* strain SS9 (hereafter called SS9), using the shotgun approach (*3*). SS9 was previously isolated at a depth of 2500 m (*4*). It was selected because it grows over a broad (90 MPa) pressure range, is amenable to genetic manipulation, and as a member of the family Vibrionaceae, is related to a number of piezosensitive microbes for which whole-genome sequence information is available for comparison.

The genome of SS9 shows a tripartite structure (*5*): a 4.1-Mbp major circular chromosome (chr. 1), a 2.2-Mbp minor circular chromosome (chr. 2), and an 80-kbp circular plasmid (Fig. 1 and table S1).

The presence of two circular chromosomes is common to other Vibrionaceae (*6*), but the SS9 chromosomes are about 25% larger than those of *Vibrio parahaemolyticus* and *Vibrio vulnificus* YJ016, the most closely related genomes to that of SS9 so far sequenced (*7*, *8*).

SS9 has the maximal number of ribosomal RNA (rRNA) operons so far identified in a bacterial genome, 14 on chr. 1 and 1 on chr. 2; this may reflect the ability to respond rapidly to favorable changes in growth conditions (*9*). The high intragenomic variation among these operons (5.13% and 2.56%, respectively, in 16*S* and 23*S* rRNA) is also consistent with the view that the various operons could have evolved to operate under particular physiological conditions (*10*).

The number of open reading frames (ORFs) unique to SS9 is unexpectedly high despite several Vibrionaceae genomes having been sequenced. This is particularly true for chr. 2, where 38.6% of the ORFs are unique, as compared with 18.7% for chr. 1. Transposons are also found at a higher frequency on chr. 2 (table S1), supporting the idea that whereas chr. 1 is more stable, containing the most "established" genes (*11*), chr. 2 is able to act as a "genetic melting pot." Moreover, many genes that are located on chr. 1, mainly those near the origin of replication, also are present on the large chromosome in other Vibrionaceae, although this is not true for genes on chr. 2 (fig. S1).

The SS9 genes have been functionally classified according to COG (Clusters of Orthologous Groups) (*12*) (table S2), Gene Ontology (*13*), and KEGG (Kyoto Encyclopedia of Genes and Genomes) (*14*). Owing to the high number of unknown genes on chr. 2, most functional COG categories are better represented on chr. 1 (fig. S2); this is especially evident for functional classes J, D, H, M, F, and O, which are involved in essential cellular processes. In contrast, class G (carbohydrate transport and metabolism) appears to be overrepresented on chr. 2, confirming that genes implicated in adaptation to the environment and to the available carbon sources are frequently found on chr. 2 (*7*, *11*).

An overview of the genome reveals features that may be related to the deep-sea environment. A notable omission from the SS9 genome are ORFs encoding light-activated photolyase genes, which is consistent with the absence of sunlight in the deep sea. A very uncommon trait is the presence of two complete operons for F_1F_0 ATP synthase, one on each chromosome (for the locus name, see table S3). SS9 contains three complete sets of cbb3 cytochrome oxidase genes; the one on chr. 2 was possibly acquired from an α-proteobacterium, along with an unusual diheme cytochrome c gene. These findings support the idea that modified electron and proton transport are necessary for metabolic activity at high pressure (*15*), as further discussed below. The reductases include those for both assimilatory and dissimilatory nitrate reduction, as well as those for tetrathionate, dimethylsulfoxide, fumarate, sulfite, and trimethylamine-N-oxide (TMAO).

To obtain a comprehensive picture of high-pressure adaptation, we used microarray technology to compare the transcriptional pro-

[1]CRIBI Biotechnology Centre and Department of Biology, Università di Padova, via Bassi 58/B, 35131 Padova, Italy. [2]Scripps Institution of Oceanography, University of California, San Diego, La Jolla, CA 92093–0202, USA.

*To whom correspondence should be addressed. E-mail: giorgio.valle@unipd.it

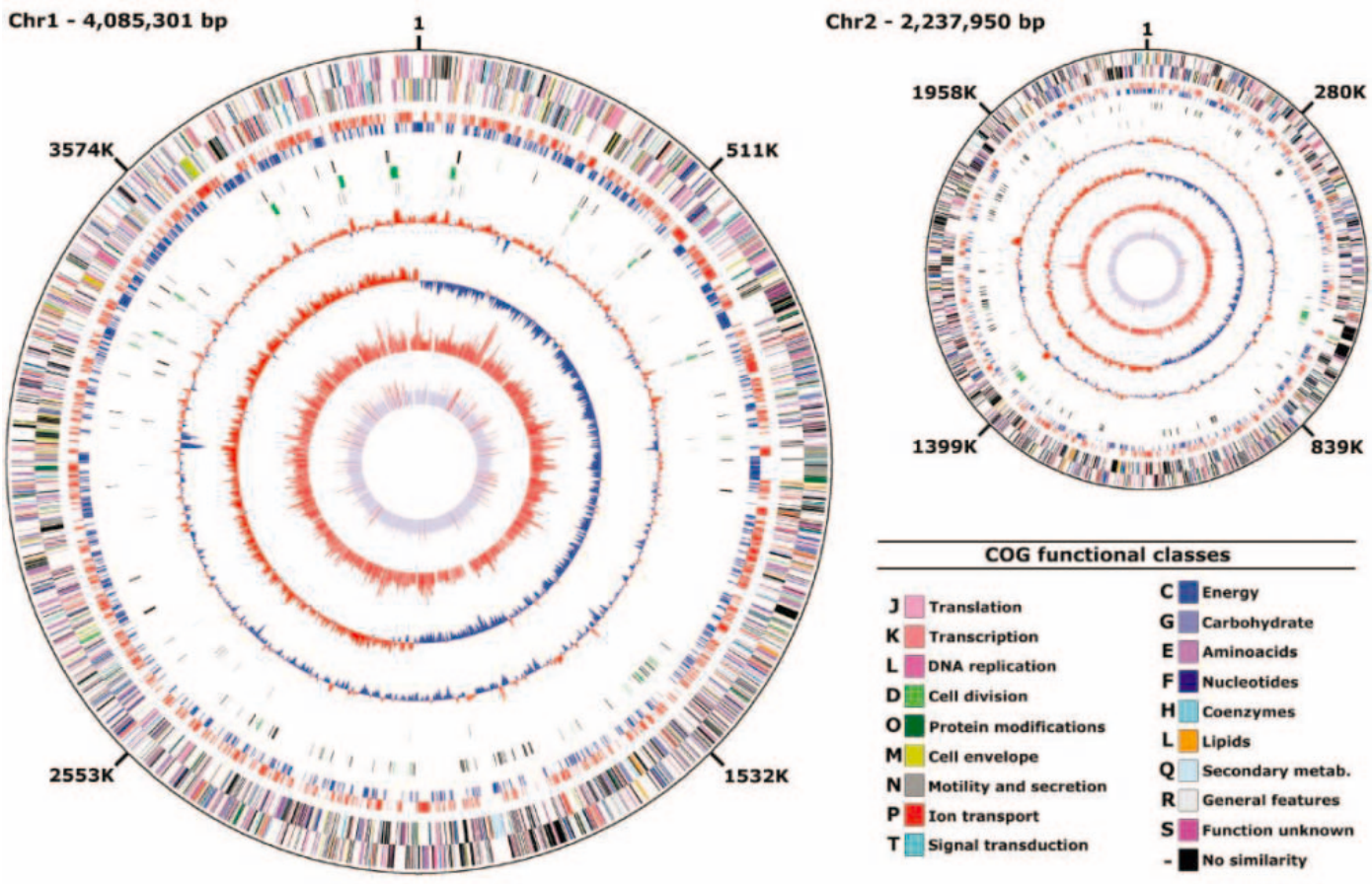

Fig. 1. Genomic organization of *P. profundum* strain SS9 chromosome 1 (left) and chromosome 2 (right). From the outside inward: The first and second circles show predicted protein-coding regions on the plus and minus strands (colors were assigned according to the color code of the COG functional classes); the third and fourth circles show *V. vulnificus* YJ016 orthologous genes in both strands; the fifth circle shows phage- (green) and transposon- (black) related genes; the sixth circle shows rRNA operons (green); the seventh circle shows tRNA (black); the eighth circle shows percentage G+C in relation to the mean G+C for the chromosome; the ninth circle shows GC skew; the 10th circle shows the mean fluorescence value of the microarray clones at 28 MPa; and the 11th circle shows CAI (scores above 0.5 units are shown in red).

file of SS9 grown at 45, 28, and 0.1 MPa. Because the results obtained at 45 and 28 MPa are very similar, we consider only the 28- and 0.1-MPa data (*5*) (table S4). The microarray experiments led to the identification of 260 differentially expressed genes that were grouped in 14 classes according to their Gene Ontology Biological Process (*13*). Comparison of the two different pressure conditions shows that most genes for amino acid transport, ion transport, protein folding, and glycolysis are up-regulated at 0.1 MPa (fig. S3).

The absolute intensity of fluorescence from the microarray analysis indicates that transcription is much more active on chr. 1 than on chr. 2. Almost all of the highly expressed genes are on chr. 1 (Fig. 1), whereas genes on chr. 2 are very poorly expressed (Fig. 1 and fig. S4). The highest spikes of expression level often correspond to high values of the codon adaptation index (CAI) (*16*). These results give further support to the hypothesis of a differential role for the two chromosomes.

Two of the highly expressed regions of chr. 2 are up-regulated at 28 MPa: one corresponding to a cluster of unknown genes and the other to the genes responsible for the Stickland reaction. So far, the complete Stickland reaction pathway has only been found in the Clostridiales and Spirochaetales (*17*), which are anaerobic bacteria. This pathway is responsible for amino acid fermentation using an amino acid reductase containing selenocysteine. The presence of a selenocysteinyl-tRNA (SeC) synthase gene, a key enzyme for the synthesis of selenoproteins, is further evidence that SS9 may also possess this mode of fermentation. It is notable that the Stickland reaction and TMAO reductase respiratory system are both up-regulated at high pressure, even though SS9 was grown under anaerobic conditions both at 0.1 and 28 MPa. A possible explanation for this finding is that at high pressure, the membrane-based cytochrome respiratory system is not fully functional (*2*) and thus requires a supplemental contribution from the above respiratory and fermentation pathways.

Complex carbohydrates are an important carbon source in oceanic abyssal environments as polymers sink down from shallower waters. We found that the regulation of metabolic pathways for the degradation of different polymers such as chitin, pullulan, and cellulose is controlled by pressure, being activated at 28 MPa and turned off at 0.1 MPa.

Confirmation that SS9 is a true piezophile comes from the observation that several stress-response genes are activated at atmospheric pressure. Indeed, four genes up-regulated at 0.1 MPa are involved in protein folding and in response to stress conditions: *htpG*, *dnaK*, *dnaJ*, and *groEL*. In *Escherichia coli*, the abundance of the proteins encoded by these genes increases after a high-pressure shock (*18*). This indicates that the proteins of this piezophilic bacterium are optimized for high pressure and require the help of these chaperones to fold correctly at 0.1 MPa. The response of SS9 to stress at 0.1 MPa is also marked by the overexpression of genes involved in DNA repair. Furthermore, there is transcriptional induction of the glycolytic pathway (fig. S5) and trehalose phosphotransferase system, which have

been shown to be up-regulated under stress conditions (*19*).

The transport of amino acids such as Trp, Lys, His, and Leu is reduced at high pressure, owing to the volume change of activation of the transport process (*20*). The finding that SS9 overexpresses amino acid transporters at 0.1 MPa is noteworthy, because the efficiency of these transporters should be higher at low pressure. These transporters may have evolved a particular protein structure to adapt to elevated pressure; therefore, their up-regulation at 0.1 MPa could compensate the reduction of functionality.

Although the deep sea represents the most common environment in the biosphere, adaptation to its prevailing conditions is still not well understood. Here we have shown that SS9 has specific metabolic, regulatory, and structural adaptations to deep-sea conditions. For example, biodegradation of relatively recalcitrant carbon sources is turned on at high pressure. In addition, the sensitivity of SS9 to low pressure is evident by the activation of different chaperones and DNA repair proteins at atmospheric pressure (*21*).

References and Notes

1. A. A. Yayanos, *Proc. Natl. Acad. Sci. U.S.A.* **83**, 9542 (1986).
2. D. H. Bartlett, *Biochim. Biophys. Acta* **1595**, 367 (2002).
3. Materials and methods are available as supporting material on *Science* Online.
4. Y. Nogi, N. Masui, C. Kato, *Extremophiles* **2**, 1 (1998).
5. The sequences reported here have been deposited in EMBL Nucleotide Sequence Database (accession nos. chr. 1, CR354531; chr. 2, CR354532; plasmid, CR377818). Array data have been submitted to European Bioinformatics Institute ArrayExpress database (accession no. A-MEXP-117).
6. E. S. Egan, M. K. Waldor, *Cell* **114**, 521 (2003).
7. K. Makino *et al.*, *Lancet* **361**, 743 (2003).
8. C. Y. Chen *et al.*, *Genome Res.* **13**, 2577 (2003).
9. J. A. Klappenbach, J. M. Dunbar, T. M. Schmidt, *Appl. Environ. Microbiol.* **66**, 1328 (2000).
10. B. M. Prüss, K. P. Francis, F. von Stetten, S. Scherer, *J. Bacteriol.* **181**, 2624 (1999).
11. J. F. Heidelberg *et al.*, *Nature* **406**, 477 (2000).
12. R. L. Tatusov *et al.*, *Nucleic Acids Res.* **29**, 22 (2001).
13. Gene Ontology Consortium, *Nucleic Acids Res.* **32**, D258 (2004).
14. M. Kanehisa, S. Goto, S. Kawashima, Y. Okuno, M. Hattori, *Nucleic Acids Res.* **32**, D277 (2004).
15. H. Kawano *et al.*, *Biosci. Biotechnol. Biochem.* **67**, 1983 (2003).
16. P. M. Sharp, W. H. Li, *Nucleic Acids Res.* **15**, 1281 (1987).
17. A. Graentzdoerffer, A. Pich, J. R. Andreesen, *Arch. Microbiol.* **175**, 8 (2001).
18. T. J. Welch, A. Farewell, F. C. Neidhardt, D. H. Bartlett, *J. Bacteriol.* **175**, 7170 (1993).
19. C. Varela, E. Agosin, M. Baez, M. Klapa, G. Stephanopoulos, *Appl. Microbiol. Biotechnol.* **60**, 547 (2003).
20. F. Abe, K. Horikoshi, *Mol. Cell. Biol.* **20**, 8093 (2000).
21. An interactive SS9 genome browser (fig. S6) maintained by the Università di Padova–Italy is accessible at http://SS9.cribi.unipd.it.

22. We thank G. Bertoloni for a stimulating discussion and G. Bortoletto, E. Nalesso, M. Del Favero, and S. Todesco for assistance. We are grateful to the Italian MIUR (grant FIRB/RBAU012RN8/RBNE01F5WT_007) and Fondazione CARIPARO for financial support. D.H.B. and F.M.L. are grateful to the National Science Foundation (NSF/MCB 02-37059) for financial support.

Supporting Online Material

www.sciencemag.org/cgi/content/full/307/5714/1459/DC1
Materials and Methods
Tables S1 to S4
Figs. S1 to S6
References

28 July 2004; accepted 4 January 2005
10.1126/science.1103341

A Functional Dosage Compensation Complex Required for Male Killing in *Drosophila*

Zoe Veneti,[1] Joanna K. Bentley,[1] Takao Koana,[2] Henk R. Braig,[3] Gregory D. D. Hurst[1]*

Bacteria that selectively kill males ("male-killers") were first characterized more than 50 years ago in *Drosophila* and have proved to be common in insects. However, the mechanism by which sex specificity of virulence is achieved has remained unknown. We tested the ability of *Spiroplasma poulsonii* to kill *Drosophila melanogaster* males carrying mutations in genes that encode the dosage compensation complex. The bacterium failed to kill males lacking any of the five protein components of the complex.

Certain isofemale lines of *Drosophila* only give rise to daughters following the death of male embryos (*1*). Male death is due to the presence of intracellular bacteria that pass from a female to her progeny and that selectively kill males during embryogenesis (*2*). These male-killing bacteria are found in a wide range of other insect species, and many different bacteria have evolved male-killing phenotypes (*3*). In some host species, male-killers drive the host population sex ratio to levels as high as 100 females per male (*4*) and alter the pattern of mate competition (*5*). However, the underlying processes that produce male-limited mortality are unclear (*6*). Here we examine the interaction between the male-killing bacterium *Spiroplasma poulsonii* and the sex determination pathway of *D. melanogaster* (*7*).

The primary signal of sex in *Drosophila* is the X-to-autosome ratio. This signal is permanently established in expression of *Sex-lethal* (*Sxl*) in females and its absence in males (*8*, *9*). This, in turn, effects three processes: germline sexual identity, somatic sexual differentiation, and dosage compensation, the process by which the gene expression titer on the X chromosome is equalized between two sexes despite their difference in X chromosome number. Mutations in the gene *tra* that convert XX individuals to male somatic sex do not induce female death (*7*). Our observations indicate germline formation and migration happen correctly in male embryos and that dying male embryos do not express *Sxl*. We, therefore, examined the requirement of the *Spiroplasma* for genes within the system of dosage compensation.

In *Drosophila*, the single X of males is hypertranscribed. This process of hypertranscription requires the formation of the dosage compensation complex (DCC) and its binding to (and modification of) the X chromosome (*10*). SXL in female *Drosophila* inhibits the production of MSL-2 protein, which is thus only present in male *Drosophila*. MSL-2 forms a complex with four other proteins, MSL-1, MSL-3, MLE, and MOF, which collectively form the DCC. MSL-1, MSL-3, MLE, and MOF are constitutively present in both males and females and are also supplied maternally. The complete DCC binds, with JIL-1, to the male X chromosome at various entry points, and, with the products of two noncoding RNAs, *RoX1* and *RoX2*, it affects the modification of the single X chromosome and its hypertranscription.

We examined the effect of mutations within the host DCC on the ability of the male-killer to function (*11*). The survival of male progeny beyond embryogenesis to L2/L3 (and in one case adult) was scored in the presence of different loss-of-function mutations within the dosage compensation system (normal male-killing occurs during embryogenesis) (*2*), in the presence and absence of infection. Because many genes within this group additionally show strong maternal effects (*12*), the effect of mutations was in each case tested by using both mothers that were heterozygous for the loss-

[1]Biology Department, University College London, Wolfson House, 4 Stephenson Way, London, NW1 2HE, UK. [2]Low-Dose Radiation Research Center, Central Research Institute of Electric Power Industry, Iwado-kita 2-11-1, Komae, Tokyo 201-8511. Japan. [3]School of Biological Sciences, University of Wales, Bangor, Gwynedd, LL57 2UW, UK.

*To whom correspondence should be addressed: E-mail: g.hurst@ucl.ac.uk

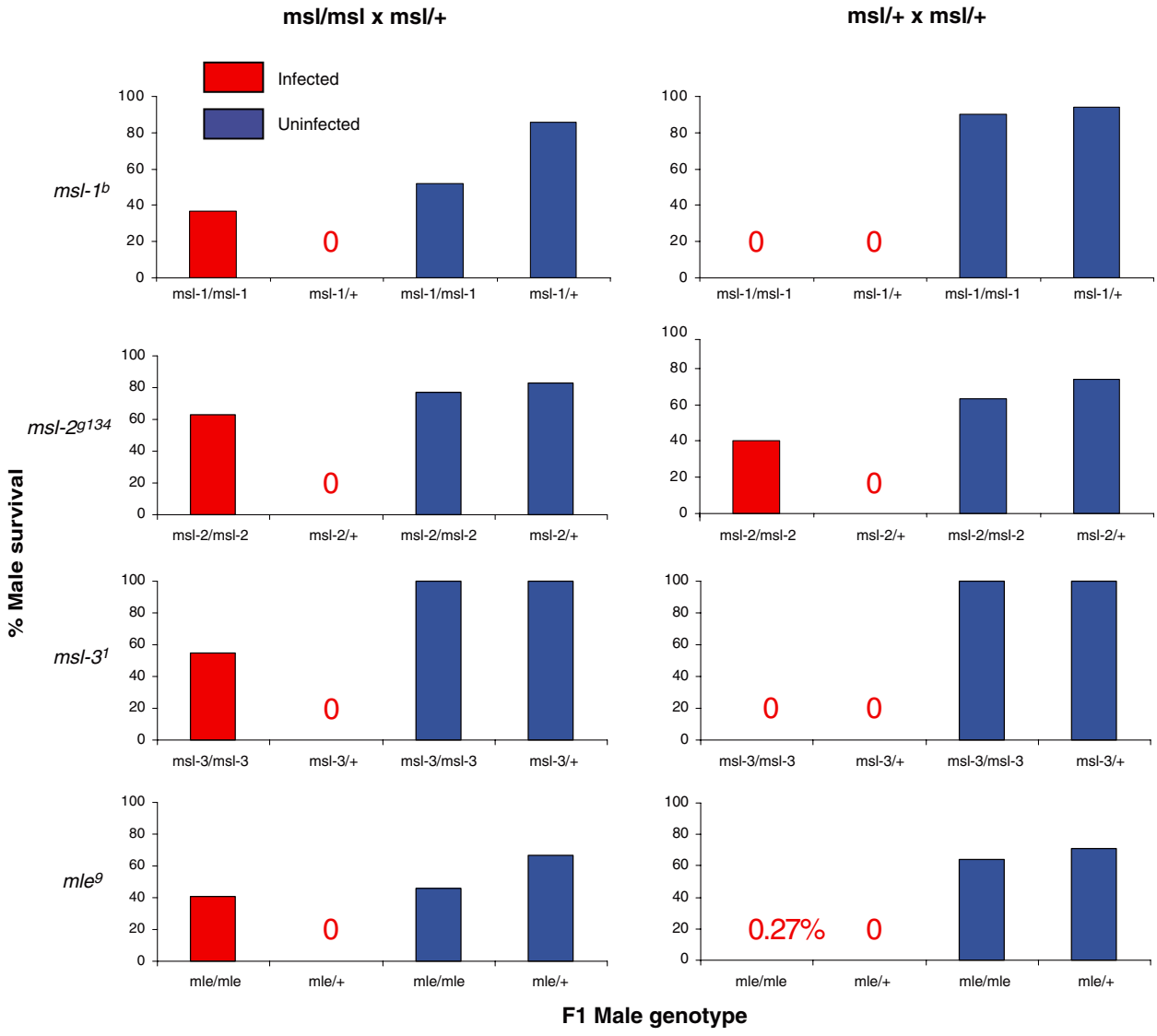

Fig. 1. Percentage survival through to day 5 of F_1 males of differing genotype with respect to loss-of-function mutations in the dosage compensation pathway in the presence (red) and absence (blue) of infection. Left-hand side graphs represent male survival rates in crosses where the female parents were homozygous for the loss-of-function mutations in question and the male parent heterozygous for it. Right-hand side graphs represent crosses where both male and female parents were heterozygous for the loss-of-function mutations. Percentage survival of males is taken relative to females of the same genotype within the cross; mean of at least eight independent crosses taken for each cross type.

Fig. 2. Percentage survival to day 5 of male progeny in crosses between females of different genotype with respect to the mutation *mof*^{1} (given above the bar) and wild-type males. *18H1* is a transgenic copy of *mof*$^+$ inserted on chromosome 2.

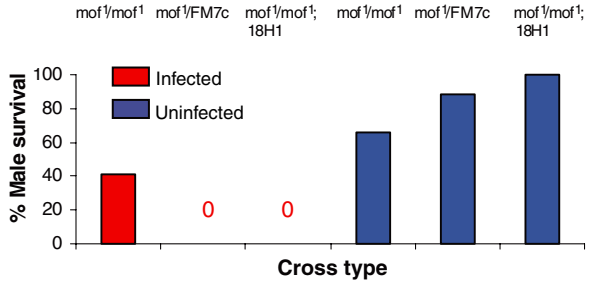

of-function mutation and mothers homozygous for it.

Uninfected males homozygous for loss-of-function mutations within the dosage compensation system generally survive to the third larval instar. We tested survival to the third larval instar for loss-of-function alleles of *msl-1* (alleles *msl-1*^{1} and *msl-1*^{b}), *msl-2* (*msl-2*^{g227} and *msl-2*^{g134}), *msl-3* (*msl-3*^{132}), *mle* (*mle*^{9}, *mle*^{1}), and *mof* (*mof*^{1}), and survival to adult for *mle*^{1}/*mle*^{6} transheterozygotes. In the case of all alleles of *msl-1*, *msl-3*, *mle*, and *mof*, a similar pattern is observed: Males homozygous or hemizygous for the loss-of-function mutation have appreciable survival in the presence of infection when their mother is also homozygous for the loss-of-function mutation (Figs. 1 and 2; tables S1–S4). In contrast, heterozygous male embryos that were siblings of the above (that will have a wild-type DCC) were always killed, as were all male embryos in the case where the mother was heterozygous (where maternal supply of these proteins enables dosage compensation to be initiated, although not maintained) (*12*). In the case of *mle*^{1}/*mle*^{6} transheterozygotes, male survival to adult was observed (table S1). For the case of *mof*, male-killing was restored to full efficiency when 18H1, a transgenic copy of *mof* (*13*), was added to the *mof*^{1} loss-of-function background. Within the above crosses, three observations make us sure the

Spiroplasma was fully operational. First, crosses involving heterozygous mothers, where male-killing was complete, were conducted concurrently with those using homozygous mothers, and the females in these crosses were siblings from the same vials. Second, in each cross and vial where homozygous males survived, heterozygous males (with wild-type function) still died. Finally, F_1 females derived from these crosses, when mated to wild-type males, produced a full, female-biased sex ratio.

In the case of *msl*-2, where there is no maternal supply of MSL-2, survival of homozygous sons was observed for both homozygous and heterozygous mothers for the case of the mutation *msl-2*^{g134} (Fig. 1). For the case of *msl-2* ^{g227}, no male progeny were observed from infected females (table S5). This mutation does not rescue males in our assay, probably because the two mutations have different effects on *msl-2* expression. The *msl-2*^{g134} allele prevents formation of MSL-2 protein, whereas *msl-2* ^{g227} potentially encodes the RING-finger element of a truncated MSL-2 protein (*14*).

Thus, absence or reduced function of any of the proteins of the DCC can reduce the efficiency of male killing, and a functional DCC is required for male killing by *S. poulsonii*. The fact that the genes mediating this process in *Drosophila* have been well studied can be exploited to yield further insights into the mechanism of male killing.

References and Notes

1. G. E. Magni, *Nature* **172**, 81 (1953).
2. S. J. Counce, D. F. Poulson, *J. Exp. Zool.* **151**, 17 (1962).
3. G. D. D. Hurst, F. M. Jiggins, M. E. N. Majerus, in *Insect Symbiosis*, K. Bourtzis, T. A. Miller, Eds. (CRC Press, Boca Raton, FL, 2003), pp. 177–197.
4. E. A. Dyson, G. D. D. Hurst, *Proc. Natl. Acad. Sci. U.S.A.* **101**, 6520 (2004).
5. F. M. Jiggins, G. D. D. Hurst, M. E. N. Majerus, *Proc. R. Soc. Lond. B. Biol. Sci.* **267**, 69 (2000).
6. G. D. D. Hurst, F. M. Jiggins, *Emerg. Infect. Dis.* **6**, 329 (2000).
7. B. Sakaguchi, D. F. Poulson, *Genetics* **48**, 841 (1963).
8. T. W. Cline, *Genetics* **107**, 231 (1984).
9. L. Sanchez, R. Nothiger, *EMBO J.* **2**, 485 (1983).
10. G. D. Gilfillan, I. K. Dahlaveen, P. B. Becker, *FEBS Lett.* **567**, 8 (2004).
11. See supporting online material.
12. A. Franke, A. Dernburg, G. J. Bashaw, B. S. Baker, *Development* **122**, 2751 (1996).
13. A. Hilfiker, D. Hilfiker-Kleiner, A. Pannuti, J. C. Lucchesi, *EMBO J.* **16**, 2054 (1997).
14. S. Zhou *et al.*, *EMBO J.* **14**, 2884 (1995).

15. We wish to thank M. Kuroda, A. Pomiankowski, and L. Hurst for comments on the manuscript and M. Kuroda, J. Luchessi, and J. Roote for kindly providing mutant stocks. We wish to thank The Biotechnology and Biological Sciences Research Council (Studentship to JB/Grant no.15/S15317 to GH/HB) for financial support.

Supporting Online Material

www.sciencemag.org/cgi/content/full/307/5714/1461/DC1
Materials and Methods
Tables S1 to S5
References and Notes

5 November 2004; accepted 8 January 2005
10.1126/science.1107182

Extensive DNA Inversions in the *B. fragilis* Genome Control Variable Gene Expression

Ana M. Cerdeño-Tárraga,[1] Sheila Patrick,[2]* Lisa C. Crossman,[1] Garry Blakely,[3] Val Abratt,[4] Nicola Lennard,[1] Ian Poxton,[5] Brian Duerden,[6] Barbara Harris,[1] Mike A. Quail,[1] Andrew Barron,[1] Louise Clark,[1] Craig Corton,[1] Jonathan Doggett,[1] Matthew T. G. Holden,[1] Natasha Larke,[1] Alexandra Line,[1] Angela Lord,[1] Halina Norbertczak,[1] Doug Ormond,[1] Claire Price,[1] Ester Rabbinowitsch,[1] John Woodward,[1] Bart Barrell,[1] Julian Parkhill[1]*

The obligately anaerobic bacterium *Bacteroides fragilis*, an opportunistic pathogen and inhabitant of the normal human colonic microbiota, exhibits considerable within-strain phase and antigenic variation of surface components. The complete genome sequence has revealed an unusual breadth (in number and in effect) of DNA inversion events that potentially control expression of many different components, including surface and secreted components, regulatory molecules, and restriction-modification proteins. Invertible promoters of two different types (12 group 1 and 11 group 2) were identified. One group has inversion crossover (*fix*) sites similar to the *hix* sites of *Salmonella typhimurium*. There are also four independent intergenic shufflons that potentially alter the expression and function of varied genes. The composition of the 10 different polysaccharide biosynthesis gene clusters identified (7 with associated invertible promoters) suggests a mechanism of synthesis similar to the O-antigen capsules of *Escherichia coli*.

Bacteroides fragilis is the major obligately anaerobic Gram negative bacterium isolated from abscesses, soft tissue infections, and bacteraemias that arise from contamination of normally uncolonized body sites by bacteria from the resident gastrointestinal (GI) microbiota. Putative virulence attributes of *B. fragilis* include attachment mechanisms, aerotolerance, extracellular enzyme production, and resistance to complement-mediated killing and phagocytosis [reviewed in (*1*)]. The lipopolysaccharide of *B. fragilis* triggers inflammatory events via the Toll-like receptor 2 (TLR2) and is likely to be involved in systemic inflammatory response syndrome caused by GI tract bacteria (*2*). *B. fragilis* itself only accounts for between 4 and 13% of the normal human fecal microbiota but is present in 63 to 80% of *Bacteroides* infections. In contrast, the related *B. thetaiotaomicron* accounts for between 15 and 29% of the fecal microbiota but is associated with only 13 to 17% of infection cases. *B. fragilis* is capable of a high amount of within-strain phase and antigenic variation of surface components. A single strain of *B. fragilis* may reversibly produce three different encapsulating surface structures: the large capsule and the small capsule, both visible by light microscopy, and an electron-dense layer (EDL) visible by electron microscopy (*3*). In addition, reversible within-strain antigenic variation of multiple antigenically distinct high molecular mass polysaccharides and other components is evident (*4*). Before the advent of the genome sequencing program, the potential mechanisms generating this variation were unknown. We determined the complete genome sequence of the nonenterotoxin-producing DNA homology group I *B. fragilis*, strain NCTC 9343.

The genome of *B. fragilis* NCTC 9343 contains a single circular chromosome of 5,205,140 base pairs (bp) predicted to encode

[1]Sanger Institute, Wellcome Trust Genome Campus, Hinxton, Cambridge, CB10 1SA, UK. [2]Department of Microbiology and Immunobiology, School of Medicine, Queen's University of Belfast, Grosvenor Road, Belfast, BT12 6BN, UK. [3]Institute of Cell and Molecular Biology, University of Edinburgh, Darwin Building, Kings Buildings, Edinburgh EH9 3JR, UK. [4]Department of Molecular and Cell Biology, University of Cape Town, Private Bag Rondebosch 7701, South Africa. [5]Division of Medical Microbiology, University of Edinburgh Medical School, Teviot Place, Edinburgh, EH8 9AG, UK. [6]Department of Medical Microbiology, University of Wales College of Medicine, Heath Park, Cardiff, CF14 4XN, UK.

*To whom correspondence should be addressed. E-mail: parkhill@sanger.ac.uk (J.P.); s.patrick@qub.ac.uk (S.P.)

4274 genes and a plasmid, pBF9343 (fig. S1 and table S1). During the assembly of shotgun data, particular regions could not be resolved because certain segments of the sequence were present in two alternative orientations. This indicated that specific inversions of these sequences occurred at a high frequency within the clonal growth of bacteria used for DNA isolation. These fragilis invertible (*fin*) regions can be grouped on the basis of the inverted repeat sequences that flank them. Twelve regions (table S2A, group 1) shown to be invertible or with sequence similarity are flanked by inverted repeats, designated fragilis inversion crossover (*fix*) sites, similar to those acted on by the *Salmonella* Hin DNA invertase (*5*). All of these invertible regions contain a consensus promoter, suggesting that they control the expression of downstream genes. Seven *fin* regions (average length of 226 bp) were found upstream of 7 of the 10 polysaccharide biosynthesis gene clusters (table S3), immediately suggesting a mechanism for the observed antigenic variation. The orientation of specific promoters can be correlated experimentally with expression of specific polysaccharides (*6*), an observation confirmed in independent experiments (*5*). The remaining five related *fin* regions in group 1 are 161 bp in length and are associated with a variety of other putative proteins (table S2A). We identified two serine site-specific DNA invertases similar to Hin in the genome, FinA (BF2779), chromosomally located but not near an invertible region, and FinB (pBF9343.01), on the plasmid. The role of FinA (Mpi) in the inversion of these segments has been demonstrated (*7*), and the plasmid-encoded FinB binds to *fix* sites (*5*). In total, the genome encodes 30 enzymes potentially capable of site-specific DNA inversion: 26 tyrosine recombinases (integrase family), 3 serine recombinases (resolvase-invertase family), and 1 Piv-like transposase-invertase (IS110 family).

A further 11 *fin* promoter regions (average length of 370 bp) are different from the *hin*-like group 1 regions and more heterogeneous in nature (table S2A, group 2). The inverted repeats that flank these regions and contain the sites of strand exchange (group 2 *fix* sites) are different from the *hix*-like regions, indicating that they are acted on by a different recombinase. These predominantly control the expression of a family of outer membrane proteins, and some might also drive the expression of divergent genes with diverse functions [Supporting Online Material (SOM) Text]. The use of DNA inversion by *B. fragilis* goes beyond the control of promoter sequences. Several more complex inversion events, or intergenic shufflons, that involve the inversion of complete and partial coding sequences were observed in the shotgun sequence. One example, whereby DNA inversion brings silent gene segments into an expression site, is the two-domain specificity protein of a type-I restriction-modification system (BF1839) (table S2B, IR-BB). Each domain in such proteins is responsible for recognizing half of the two-part DNA binding site. Just after the start codon and between the two domains of BF1839 are independent inverted repeats that are unrelated to group 1 or 2 *fix* sites, both of which are present in similar positions in the downstream convergent gene BF1842, which does not have an appropriate start codon (Fig. 1A). Independent recombination events between these inverted repeats would produce four different specificity proteins recognizing four different DNA sequences. Between these genes are two further gene cassettes, each of which encodes one C-terminal recognition domain. At the 5′ end of these cassettes are two further, different inverted repeats that allow either of the cassettes to be exchanged with the C-terminal domain of the adjacent gene (BF1838 or BF1842), increasing the number of potential recognition specificities to eight. Three potential recombinases encoded nearby (BF1833, 1843, and 1845) may be involved in this system. A similar, although less complex, variable restriction-modification system has been described in *Mycoplasma pulmonis* (*8*). Three further independent intergenic shufflons, acting on outer membrane proteins and a signal transduction system, were observed in the shotgun sequence (Fig. 1, table S2B, and SOM Text). Other intergenomic inversions (IR-Q, IR-R, and IR-S) (table S3) involve the inversion of complete coding sequences, often reorientating them with or against the apparent direction of transcription of surrounding genes. These may also affect the transcription levels of the genes within these regions.

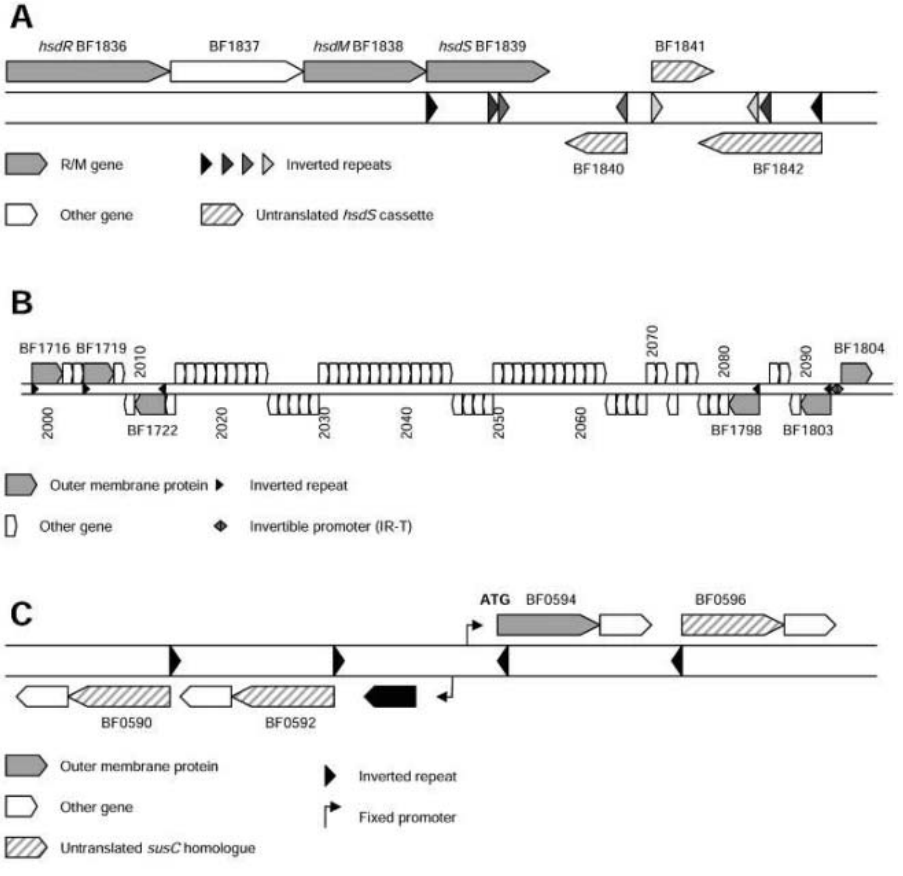

Fig. 1. Examples of invertible regions in the *B. fragilis* genome (*18*). (**A**) Restriction modification intergenic shufflon: restriction-modification (R/M) complex genes, gray boxes; other genes, open boxes; potential *hsdS* DNA binding modules, hatched boxes; different inverted repeats at the inversion ends, light gray triangles. (**B**) Inversion of large segments of DNA through large inverted repeats (black triangles) brings alternative outer membrane protein genes (gray boxes) downstream of an invertible promoter (gray diamond). (**C**) Local inversion through inverted repeats (black triangles) fuses silent alternative outer membrane protein gene cassettes (hatched boxes) to a fixed promoter and translation start.

Comparison of the *B. fragilis* genome with the recently sequenced *B. thetaiotaomicron* strain VPI 5482 (ATCC 29148) (*9*) reveals that there are no orthologous variable promoters or indeed operons driven by them. *B. thetaiotaomicron* does encode some variable systems (*9*), but they are unique to that

organism and considerably less numerous than those in *B. fragilis*. This enhanced potential for variation and other genomic differences (SOM Text) may explain in part why *B. fragilis* is isolated more frequently from infection than *B. thetaiotaomicron*.

Surface polysaccharides are involved in establishing abscess formation (*10*). Ten separate gene clusters potentially involved in polysaccharide synthesis are evident in the genome sequence (table S3). The polysaccharide gene clusters A to H have genes similar to *wzx* and *wzy* that are involved in transfer of linked sugar repeats across the cytoplasmic membrane and repeat unit polymerization, respectively, but are lacking in genes associated with the export of polymer across the outer membrane. This suggests that these gene clusters are similar to the *Escherichia coli* group 4 O-antigen capsules (*11*) and is in keeping with the characteristic heterogeneity of the polysaccharide chain length after SDS–polyacrylamide gel electrophoresis (PAGE) and the EDL phenotype (*12*). A gene with some similarity to *E. coli wzz* (BF1708) that determines chain length is located within polysaccharide gene cluster J. Variation in the expression of BF1708 may explain the varying reports of presence (*13*) or absence (*14*) of repeating O-antigen units after PAGE.

Phase variation controlled by DNA inversion events has been reported in several other bacteria. For example, *Salmonella typhimurium* regulates the expression of a flagellar protein by using a single invertible promoter (*15*), and *E. coli* plasmids use shufflons to express one of several variant pilus proteins (*16*). Different species of *Mycoplasma* have been shown to regulate the expression of a number of surface proteins by using invertible promoters (*17*) or to use a shufflon system to express variable surface proteins (*8*). However, in each of these cases, the use of these mechanisms is restricted to a single system or class of surface molecules. As described here, *B. fragilis* uses DNA inversion to control a larger number or greater breadth of systems than in any other organism described to date, including surface proteins, polysaccharides, and regulatory systems. This may be related to its niche as a commensal and opportunistic pathogen, because the resulting diversity in surface structures could increase both immune invasion and the ability to colonize novel sites.

Note added in proof: The genome sequence of another strain of *B. fragilis* has recently been published (*19*), and the analysis is in general agreement with that presented here.

References and Notes

1. S. Patrick, in *Molecular Medical Microbiology*, M. Sussman, Ed. (Academic Press, London, 2002), pp. 1921–1948.
2. C. Erridge, A. Pridmore, A. Eley, J. Stewart, I. R. Poxton, *J. Med. Microbiol.* **53**, 735 (2004).
3. S. Patrick, J. H. Reid, A. Coffey, *J. Gen. Microbiol.* **132**, 1099 (1986).
4. S. Patrick, D. Gilpin, L. Stevenson, *Infect. Immun.* **67**, 4346 (1999).
5. S. Patrick *et al.*, *Microbiology* **149**, 915 (2003).
6. C. M. Krinos *et al.*, *Nature* **414**, 555 (2001).
7. M. J. Coyne, K. G. Weinacht, C. M. Krinos, L. E. Comstock, *Proc. Natl. Acad. Sci. U.S.A.* **100**, 10446 (2003).
8. I. Chambaud *et al.*, *Nucleic Acids Res.* **29**, 2145 (2001).
9. J. Xu *et al.*, *Science* **299**, 2074 (2003).
10. A. O. Tzianabos, A. B. Onderdonk, B. Rosner, R. L. Cisneros, D. L. Kasper, *Science* **262**, 416 (1993).
11. C. Whitfield, I. S. Roberts, *Mol. Microbiol.* **31**, 1307 (1999).
12. D. A. Lutton *et al.*, *J. Med. Microbiol.* **35**, 229 (1991).
13. I. R. Poxton, R. Brown, *J. Gen. Microbiol.* **132**, 2475 (1986).
14. A. A. Lindberg, A. Weintraub, U. Zahringer, E. T. Rietschel, *Rev. Infect. Dis.* **12** (suppl. 2), S133 (1990).
15. M. Silverman, J. Zieg, M. Hilmen, M. Simon, *Proc. Natl. Acad. Sci. U.S.A.* **76**, 391 (1979).
16. A. Gyohda, N. Furuya, A. Ishiwa, S. Zhu, T. Komano, *Adv. Biophys.* **38**, 183 (2004).
17. A. Horino, Y. Sasaki, T. Sasaki, T. Kenri, *J. Bacteriol.* **185**, 231 (2003).
18. The sequence and annotation of the genome have been submitted to the DNA Data Bank of Japan, European Molecular Biology Laboratory, and GenBank databases with accession numbers CR626927 (chromosome) and CR626928 (pBF9343) and are available with further details from www.sanger.ac.uk/Projects/B_fragilis/.
19. T. Kuwahara *et al.*, *Proc. Natl. Acad. Sci. U.S.A.* **101**, 14919 (2004).

20. We acknowledge the support of the Wellcome Trust Sanger Institute core sequencing and informatics groups. S.P. thanks M. Larkin (Queen's University Environmental Science and Technology Research Centre, Queen's University of Belfast) for the use of the laboratory and advice on DNA extraction methods. Supported by the Wellcome Trust through its Beowulf Genomics initiative.

Supporting Online Material

www.sciencemag.org/cgi/content/full/307/5714/1463/DC1
Materials and Methods
SOM Text
Figs. S1 and S2
Tables S1 to S4

16 August 2004; accepted 30 December 2004
10.1126/science.1107008

Requirement for Caspase-8 in NF-κB Activation by Antigen Receptor

Helen Su,[1]* Nicolas Bidère,[1]* Lixin Zheng,[1] Alan Cubre,[1] Keiko Sakai,[1] Janet Dale,[2] Leonardo Salmena,[3] Razqallah Hakem,[3] Stephen Straus,[2] Michael Lenardo[1]†

Caspase-8, a proapoptotic protease, has an essential role in lymphocyte activation and protective immunity. We show that caspase-8 deficiency (CED) in humans and mice specifically abolishes activation of the transcription factor nuclear factor κB (NF-κB) after stimulation through antigen receptors, Fc receptors, or Toll-like receptor 4 in T, B, and natural killer cells. Caspase-8 also causes the αβ complex of the inhibitor of NF-κB kinase (IKK) to associate with the upstream Bcl10-MALT1 (mucosa-associated lymphatic tissue) adapter complex. Recruitment of the IKKα,β complex, its activation, and the nuclear translocation of NF-κB require enzyme activity of full-length caspase-8. These findings thus explain the paradoxical association of defective apoptosis and combined immunodeficiency in human CED.

The intracellular aspartate-specific cysteine protease caspase-8 initiates death receptor signaling for apoptosis (*1*). Recruitment into the death-signaling complex induces procaspase-8 oligomerization, followed by full processing into a highly active soluble tetramer (*2*, *3*). However, caspase-8 is also essential for lymphocyte activation and protective immunity in mice and humans (*4*, *5*). Patients with caspase-8 deficiency (CED) have defective apoptosis and immunodeficiency due to impaired activation of T, B, and natural killer (NK) lymphocytes (*4*).

Human peripheral blood leukocytes (PBLs) or mouse T cells treated with the pan-caspase inhibitor benzyloxycarbonylvalyl-alanyl–aspartic acid (*O*-methyl)–fluoro-methylketone (zVAD) have reduced antigen receptor–induced expression of interleukin-2 (IL-2) and its receptor subunit CD25 (*4*, *6*, *7*). Because nuclear factor κB (NF-κB) is required for IL-2 and CD25 gene transcription as well as lymphocyte activation (*8*, *9*), we examined this transcription factor in cells exposed to caspase inhibitor. NF-κB family members—Rel (c-*rel*), RelA (p65), RelB, NF-κB1 (p105/50), and NF-κB2 (p100/52)—regulate gene transcription as dimers (*8*, *9*).

[1]Laboratory of Immunology, National Institute of Allergy and Infectious Diseases, National Institutes of Health, Bethesda, MD 20892, USA. [2]Laboratory of Clinical Infectious Diseases, National Institute of Allergy and Infectious Diseases, National Institutes of Health, Bethesda, MD 20892, USA. [3]Ontario Cancer Institute, University of Toronto, Toronto, Ontario M5G 2C1, Canada.

*These authors contributed equally to this work.
†To whom correspondence should be addressed. E-mail: lenardo@nih.gov

Lymphocyte stimulation causes phosphorylation and degradation of inhibitor of κB (IκB) proteins, leading to NF-κB nuclear translocation and transcriptional activation. Nuclear translocation of p65 or p50, which constitute the NF-κB heterodimer, was detected 5 min after T cell receptor (TCR) stimulation in control PBLs but not in cells treated with zVAD (Fig. 1A and fig. S1, A to C) (*10*). The difference occurred despite CD28 costimulation, indicating a defect in TCR signaling (Fig. 1A). Consistent with the zVAD effect, the caspase-8-deficient Jurkat T cell line I9.2 exhibited almost no NF-κB nuclear translocation after TCR stimulation compared to that in parental A3 cells (fig. S1, D to G, and fig. S2A), with a corresponding decrease in NF-κB nuclear binding activity but no effect on the binding activity of the transcription factors OCT1 or TFIID (Fig. 1B). TCR stimulation of I9.2 cells failed to induce transcription from an NF-κB promoter–driven luciferase reporter construct (Fig. 1C). NF-κB was also defective in A3 or primary human $CD4^+$ cells in which caspase-8 was specifically knocked down using short hairpin RNAs (shRNAs) (fig. S3, A to C), A3 or mouse EL-4 T cells pretreated with zVAD (fig. S3, D to F, and fig. S4, A to D), and in caspase-8-deficient T cells from conditional knockout mice (fig. S4, E and F). These effects appeared to be selective for the TCR signaling pathway, because tumor necrosis factor–α (TNF-α)–induced NF-κB activation was not affected by zVAD or caspase-8 deficiency (Fig. 1 and figs. S1 to S4). Moreover, all other early activation events examined were essentially unaffected (fig. S5) (*10*). Together, these results suggest a selective role for caspase-8 in NF-κB activation.

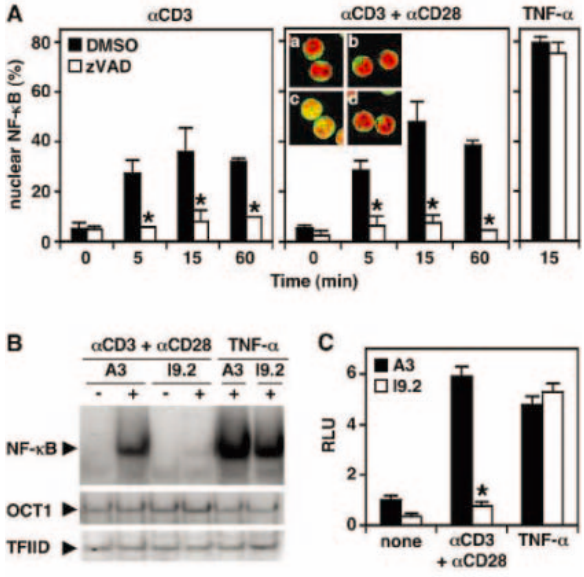

Fig. 1. Defective NF-κB translocation and transcriptional activation in CED T cells. (**A**) Quantitation of the fraction of cells by immunofluorescence confocal microscopy showing NF-κB p65 nuclear translocation. Results are shown as the mean ± SD for PBLs from three normal donors, with or without zVAD, and then stimulated with antibodies to CD3ε (anti-CD3ε) and anti-CD28 (1 μg/ml each), anti-CD3ε (1 μg/ml) alone, or TNF-α (10 ng/ml) as indicated. (Inset) Representative merged views of p65 (green), Hoechst (red), overlay (yellow) from unstimulated (a and b), or cells stimulated with anti-CD3ε and anti-CD28 (c and d), pretreated with dimethyl sulfoxide (DMSO) (a and c), or zVAD (b and d). (**B**) NF-κB gel shift of nuclear extracts prepared from A3 and I9.2 cells after 20 min of stimulation with anti-CD3ε and anti-CD28 (1 μg/ml each) (+), control (−), or TNF-α (10 ng/ml). OCT1 or TFIID gel shifts of the same nuclear extracts are shown. (**C**) Relative light units (RLU) of luciferase activity for an NF-κB luciferase reporter construct transfected into A3 or I9.2 cells and stimulated for 16 hours with anti-CD3ε, anti-CD28 (2 μg/ml each), and goat antibody to mouse immunoglobulin G (IgG) (5 μg per ml) or TNF-α (30 ng per ml) one day after transfection. Asterisk indicates $P < 0.05$ by the unpaired Student's *t* test for experimental compared to corresponding control.

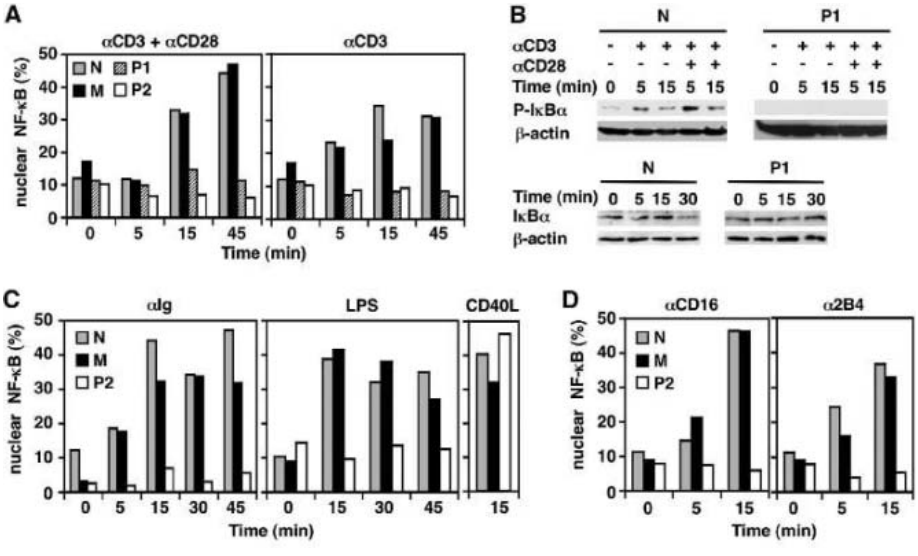

Fig. 2. Impaired NF-κB in lymphocytes from caspase-8-deficient humans. N, normal donor; M, healthy mother (+/*m*); P1, proband (*m*/*m*); P2, affected sibling (*m*/*m*). Genotype: +, normal; *m*, mutant. (**A**) Quantitation of the fraction of cells by immunofluorescence confocal microscopy showing NF-κB p65 nuclear translocation. T lymphocytes were stimulated with anti-CD3ε and anti-CD28 (1 μg/ml each) or anti-CD3ε (1 μg/ml) alone. (**B**) Lysates from stimulated T cells, immunoblotted for phosphorylated-IκBα (P-IκBα) and IκBα. (**C**) NF-κB p65 nuclear translocation in B cells stimulated with biotinylated anti-IgG (20 μg/ml) and streptavidin (20 μg/ml), lipopolysaccharide (LPS, 50 μg/ml), or CD40 ligand (CD40L, 2.5 μg/ml). (**D**) NF-κB p65 nuclear translocation in NK cells stimulated with anti-CD16 (20 μg/ml) or 2B4 (10 μg/ml) and goat antibody to mouse IgG (20 μg/ml).

We next examined NF-κB activation in PBLs from NIH CED family 66 (*4*). Early activation events in T cells were essentially normal, but NF-κB did not translocate to the nucleus after TCR stimulation in PBLs that were homozygous for CED (fig. S6, Fig. 2A, and fig. S7A). Notably, the heterozygous mother showed no such impairment, indicating that a single functional copy of the gene sufficed for NF-κB signaling.

Phosphorylation activates the IκB kinase (IKK) complex, composed of the two catalytic subunits IKKα and IKKβ and a regulatory subunit IKKγ (NEMO) (*8*, *9*). Active IKK phosphorylates IκBα, which marks IκBα for degradation, thereby liberating NF-κB for nuclear translocation and transcriptional activity. However, we saw no IκBα phosphorylation or degradation in TCR-stimulated PBLs from a CED patient (Fig. 2B and fig. S7I). Hence, caspase-8 was necessary for NF-κB activation after TCR stimulation.

We next evaluated NF-κB activation in B cells and NK cells. B cells from a CED patient failed to translocate NF-κB into the nucleus after B cell receptor (BCR) stimulation (Fig. 2C and fig. S7C). Ramos B cells, in which caspase-8 was knocked down using specific shRNAs, displayed a similar defect (fig. S7, F and G). NF-κB activation induced by lipopolysaccharide (LPS) requires signaling through Toll-like receptor 4 (TLR4). In B cells from a CED patient, but not an autoimmune lymphoproliferative syndrome patient bearing a Fas mutation (ALPS, Type Ia), NF-κB nuclear translocation was abrogated after LPS stimulation (Fig. 2C and fig. S7, C to E).

By contrast, NF-κB could be normally activated in CED B cells through CD40 (Fig. 2C and fig. S7C) (*11*). NK cells from CED patients failed to translocate NF-κB into the nucleus after FcγRIII or 2B4 (NK cell–activating receptor) stimulation (Fig. 2D and fig. S7H). NF-κB activation proceeds normally in caspase-8-deficient mouse embryo fibroblasts after TNF-α or Fas stimulation (*12*). Thus, CED impairs both adaptive immunoreceptor signaling and certain pathways of innate immunity that activate NF-κB.

Early TCR activation events link to NF-κB activation through protein kinase Cθ (PKCθ) activation (*13*, *14*). PKCθ phosphorylation recruits the CARMA1-Bcl10-MALT1 (CBM) complex to the immunological synapse (*15*, *16*). This complex of adapter molecules causes activation of the IKK complex. However, the CBM and IKK complexes do not appear to interact directly (*17*), and how the signal for NF-κB activation is conveyed between the two is not well understood (*15*, *16*, *18*). The amounts of active phosphorylated PKCθ were not altered by caspase-8 deficiency (fig. S5C). In normal Jurkat cells, IKKα phosphorylation occurred at 5 min after TCR stimulation, and IKKα,β and IκBα phosphorylation occurred maximally after 10 min, followed by IκBα degradation (Fig. 3A and fig. S8A). IKK phosphorylation coincided with the appearance of in vitro kinase activity using glutathione S-transferase (GST)–IκBα as a substrate (Fig. 3B). IKK phosphorylation, IκBα phosphorylation and degradation, and in vitro kinase activity were reduced in I9.2 cells (Fig. 3, A and B). Thus, caspase-8 acts between PKCθ and IKK in the NF-κB pathway.

We used coimmunoprecipitation and immunoblotting to show that TCR stimulation induced caspase-8 to associate with the Bcl10-MALT1 complex followed by recruitment of IKK (Fig. 3C). Formation of this complex coincided with IKK phosphorylation and activation at 10 min after stimulation. Absence of caspase-8 abrogated IKKα,β recruitment and activation by the CBM complex (Fig. 3, A and D). The adapter protein FADD associated with caspase-8 and Bcl10-MALT1 at an earlier time (5 min) but disappeared before the recruitment of IKK to form the holocomplex (Fig. 3E). Caspase-8 appears to act before IKK, because reconstituting I9.2 cells with constitutively active IKK restored NF-κB activation (fig. S8, B and C). Thus, caspase-8 is integral to the assembly and activation of the CBM-IKK complex in response to antigen receptors.

Our observation that zVAD blocks NF-κB activation after TCR stimulation suggests that caspase-8 enzymatic activity may be essential. Indeed, we found that wild-type caspase-8, but not the catalytically inactive C360S mutant (where Cys^{360} is replaced by Ser), enhanced NF-κB responses to TCR stimulation in transfected I9.2 cells (Fig. 3F). We next tested caspase-8 autoprocessing mutants (D210A, D374A, and D384A) by substituting alanines for aspartic acid residues (*10*). These mutants increased NF-κB activity in I9.2 cells after TCR stimulation, indicating that enzymatic activity, but not autoprocessing, was required (Fig. 3F and fig. S8F). Consistent with this conclusion, only full-length forms of caspase-8, which are known to be enzymatically active (*2*, *3*), were detected in the CBM complex (Fig. 3E). We therefore used a more sensitive probe, biotinylated-VAD (b-VAD), which bonds covalently to the catalytic cysteine of active caspases. Precipitation of b-VAD detected a small amount of enzymatically active full-length caspase-8 in lysates from unstimulated T cells (Fig. 3G). TCR stimulation caused activation of full-length caspase-8 and induced physical interaction with Bcl10 at times when IKK was recruited, phosphorylated, and active (Fig. 3G). Depletion of the b-VAD–bound species revealed that only a minor fraction (10 to 15%) of the total

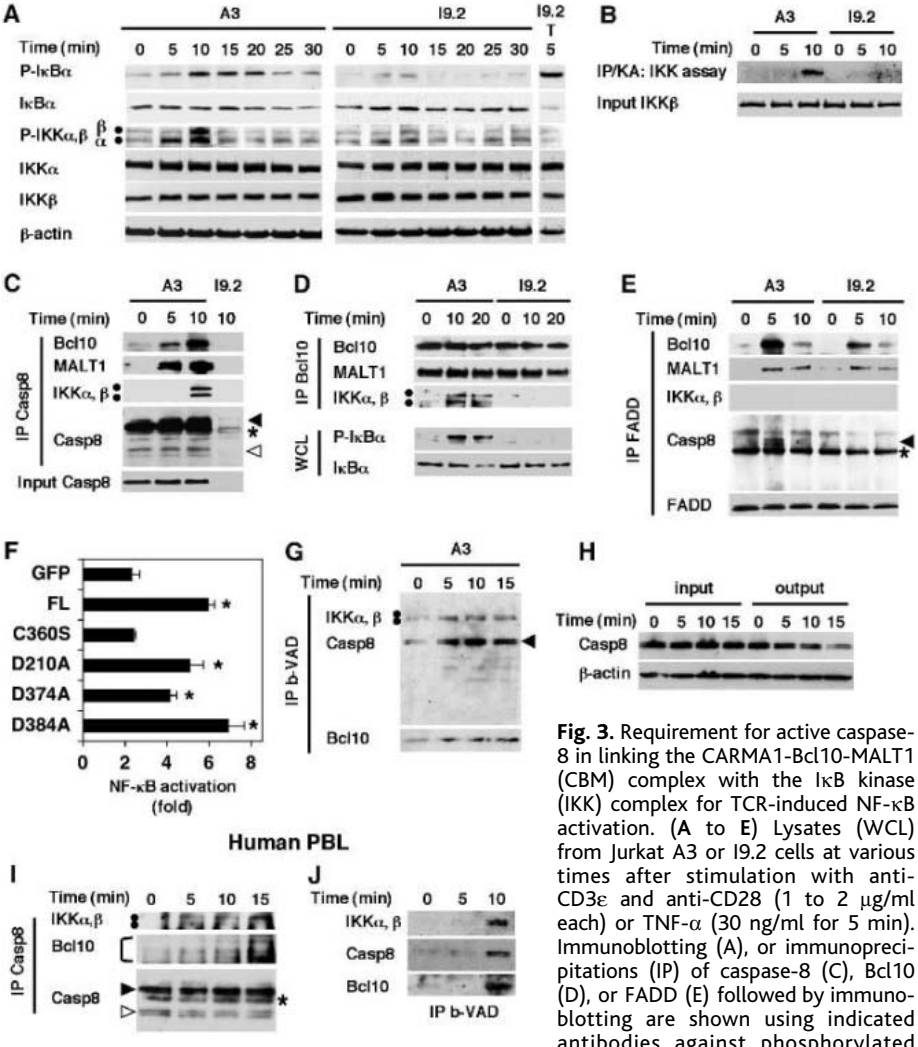

Fig. 3. Requirement for active caspase-8 in linking the CARMA1-Bcl10-MALT1 (CBM) complex with the IκB kinase (IKK) complex for TCR-induced NF-κB activation. (**A** to **E**) Lysates (WCL) from Jurkat A3 or I9.2 cells at various times after stimulation with anti-CD3ε and anti-CD28 (1 to 2 μg/ml each) or TNF-α (30 ng/ml for 5 min). Immunoblotting (A), or immunoprecipitations (IP) of caspase-8 (C), Bcl10 (D), or FADD (E) followed by immunoblotting are shown using indicated antibodies against phosphorylated IκBα (P-IκBα), IκBα, the α and/or β subunits of phosphorylated IKK (P-IKK), Bcl10, MALT1, caspase-8, or FADD. Solid arrowhead indicates full length (p54 and 52). Open arrowhead indicates partly processed (p43 and 41) forms of caspase-8. Asterisks indicate Ig heavy chain in immunoprecipitates. For (B), IKK in vitro kinase activity was assessed in coimmunoprecipitates of IKKγ by the ability to phosphorylate GST-IκBα. (**F**) Activity of an NF-κB luciferase reporter in I9.2 cells transfected with the indicated caspase-8 expression constructs. GFP, green fluorescence protein–expressing vector; FL, full-length wild-type caspase-8. Cells were stimulated for 24 hours with anti-CD3ε and anti-CD28 (2 μg/ml each) and goat antibody to mouse IgG (5 μg/ml) 2 days after transfection. Asterisks indicate $P < 0.001$ by the Student's t test compared to the GFP control. (**G**) Biotinylated-VAD (b-VAD) was incubated with protein lysates after TCR stimulation as in (F), then precipitated with streptavidin, and IKK, caspase-8, and Bcl10 proteins were detected by immunoblotting. (**H**) Lysates before (input) and after (output) precipitation of b-VAD–bound proteins, shown immunoblotted for full-length caspase-8 and β-actin. (**I** and **J**) Lysates from human PBLs were prepared at various times after stimulation with anti-CD3ε and anti-CD28 (1 μg/ml each). IP of caspase-8 (I) or using b-VAD (J) were followed by immunoblotting to detect IKKα,β, Bcl10, and caspase-8 proteins.

caspase-8 became enzymatically active after TCR stimulation (Fig. 3H and fig. S8G). Hence, NF-κB activation by antigen receptors requires enzyme activity of full-length caspase-8. In the NF-κB–activating holocomplex, caspase-8 appears to be bound, unprocessed, and only weakly activated, by contrast to caspase-8 in a death-inducing complex (*2*, *3*).

Caspase-8 now emerges both as a pivotal molecule for death-receptor signaling and as a selective signal transducer for NF-κB during the early genetic response to an antigen. This explains the requirement for caspase activity and caspase-8 for lymphocyte activation and c-*rel* responses after antigen receptor stimuli (*4*–*7*, *19*). Full-length, unprocessed, but active caspase-8 serves as a crucial link for the CBM and IKK complexes leading to NF-κB activation not only in lymphoid cell lines, but also in freshly isolated human lymphocytes (Fig. 3, I and J). After antigen receptor stimulation, MALT1-dependent recruitment of the ubiquitin ligase TRAF6 to the CBM complex may enhance regulatory polyubiquitination of IKKγ (*20*, *21*). IKKγ ubiquitination, but not phosphorylation of IKKα,β, occurred in the absence of caspase-8, indicating that ubiquitination may be necessary but not sufficient for IKK activation (fig. S8H).

CED patients manifest certain diagnostic criteria for ALPS, most notably impaired lymphocyte apoptosis (*22*). However, the combined T, B, and NK cell immunodeficiency is not seen in ALPS patients with Fas, Fas ligand, or caspase-10 mutations. Our findings reveal how a single protease regulates both lymphocyte proliferation and programmed death through different molecular forms. The molecular mechanism we have unveiled may be useful in understanding and treating other varieties of immunodeficiency and disordered lymphocyte homeostasis.

References and Notes

1. A. Ashkenazi, V. M. Dixit, *Science* **281**, 1305 (1998).
2. K. M. Boatright *et al.*, *Mol. Cell. Biol.* **11**, 529 (2003).
3. M. Donepudi, A. Mac Sweeney, C. Briand, M. G. Grutter, *Mol. Cell. Biol.* **11**, 543 (2003).
4. H. J. Chun *et al.*, *Nature* **419**, 395 (2002).
5. L. Salmena *et al.*, *Genes Dev.* **17**, 883 (2003).
6. N. J. Kennedy, T. Kataoka, J. Tschopp, R. C. Budd, *J. Exp. Med.* **190**, 1891 (1999).
7. A. Alam, L. Y. Cohen, S. Aouad, R. P. Sekaly, *J. Exp. Med.* **190**, 1879 (1999).
8. S. Ghosh, M. Karin, *Cell* **109**, S81 (2002).
9. Q. Li, I. M. Verma, *Nat. Rev. Immunol.* **2**, 725 (2002).
10. Materials and methods are available as supporting material on *Science* Online.
11. B. Zarnegar *et al.*, *Proc. Natl. Acad. Sci. U.S.A.* **101**, 8108 (2004).
12. E. E. Varfolomeev *et al.*, *Immunity* **9**, 267 (1998).
13. Z. Sun *et al.*, *Nature* **404**, 402 (2000).
14. X. Lin, A. O'Mahony, Y. Mu, R. Geleziunas, W. C. Greene, *Mol. Cell. Biol.* **20**, 2933 (2000).
15. M. Thome, *Nat. Rev. Immunol.* **4**, 348 (2004).
16. P. C. Lucas, L. M. McAllister-Lucas, G. Nunez, *J. Cell Sci.* **117**, 31 (2004).
17. P. C. Lucas *et al.*, *J. Biol. Chem.* **276**, 19012 (2001).
18. L. Yu, M. J. Lenardo, *Science* **302**, 1515 (2003).
19. M. Falk *et al.*, *J. Immunol.* **173**, 5077 (2004).
20. L. Sun, L. Deng, C. K. Ea, Z. P. Xia, Z. J. Chen, *Mol. Cell. Biol.* **14**, 289 (2004).
21. H. Zhou *et al.*, *Nature* **427**, 167 (2004).
22. M. C. Sneller *et al.*, *Blood* **89**, 1341 (1997).

23. Molecular interaction data have been deposited in the Bimolecular Interaction Network Database (BIND) with accession codes 196525, 196526, 196446, and 196449. We thank I. Stefanova for tyrosine phosphorylation experiments; V. Barr and L. Samelson for T cell spreading experiments; E. Lee and G. Wang for technical assistance; J. Blenis, R. Siegel, L. Van Parijs, V. Horejsi, A. Jain, V. Dixit, M. Peter, and Z. Liu for materials and reagents; D. Stephany, K. Holmes, and O. Schwartz for flow cytometry and microscopy assistance; F. Dugan and J. Davis for clinical assistance; L. Sun, Z. Chen, Z. Liu, and S. Feske for advice on IKK kinase assay and calcium flux; L. Yu and R. Siegel for helpful discussions; and R. Germain, L. Samelson, and J. Puck for critically reading the manuscript. H.S. is a fellow of the Cancer Research Institute. N.B. is supported by an Association pour la Recherche contre le Cancer (ARC) fellowship.

Supporting Online Material
www.sciencemag.org/cgi/content/full/307/5714/1465/DC1
Materials and Methods
SOM Text
Figs. S1 to S8
References

1 September 2004; accepted 4 January 2005
10.1126/science.1104765

Impaired Thermosensation in Mice Lacking TRPV3, a Heat and Camphor Sensor in the Skin

Aziz Moqrich,[1,2]* Sun Wook Hwang,[1]* Taryn J. Earley,[1] Matt J. Petrus,[2] Amber N. Murray,[1] Kathryn S. R. Spencer,[1] Mary Andahazy,[2] Gina M. Story,[1] Ardem Patapoutian[1,2]†

Environmental temperature is thought to be directly sensed by neurons through their projections in the skin. A subset of the mammalian transient receptor potential (TRP) family of ion channels has been implicated in this process. These "thermoTRPs" are activated at distinct temperature thresholds and are typically expressed in sensory neurons. TRPV3 is activated by heat (>33°C) and, unlike most thermoTRPs, is expressed in mouse keratinocytes. We found that TRPV3 null mice have strong deficits in responses to innocuous and noxious heat but not in other sensory modalities; hence, TRPV3 has a specific role in thermosensation. The natural compound camphor, which modulates sensations of warmth in humans, proved to be a specific activator of TRPV3. Camphor activated cultured primary keratinocytes but not sensory neurons, and this activity was abolished in TRPV3 null mice. Therefore, heat-activated receptors in keratinocytes are important for mammalian thermosensation.

Thermosensation is thought to be directly mediated by sensory neurons of the dorsal root ganglia (DRGs) that terminate as free nerve endings within the dermal and epidermal layers of the skin (*1*). Six members of the TRP family of ion channels are activated by distinct thresholds of temperature (*2*). The expression of most of these thermoTRPs in DRG neurons is consistent with a role in thermosensation. TRPV3 is activated by warm temperatures above 33°C and exhibits increased response at noxious higher temperatures (*3*–*5*). Mouse TRPV3 is distinct among thermoTRPs because it is expressed in keratinocytes but not in DRGs (*3*). TRPV4, a related innocuous heat-activated ion channel, is expressed in both DRGs and skin (*6*–*8*). The prevailing model that temperature is sensed directly by DRG neurons calls into question whether keratinocyte-derived TRPV3 is involved in thermosensation.

To specifically determine the in vivo function of TRPV3, we used a knockout construct to target the mouse gene encoding TRPV3 by deleting exons encoding the putative pore region and adjacent transmembrane segments five and six, essential domains of the ion channel (fig. S1A). Mice carrying two alleles of the TRPV3 mutation survived through adulthood at the expected Mendelian ratio (fig. S1B). The reverse transcription polymerase chain reaction (RT-PCR) was used to evaluate the expression of TRPV3 in the mutant mice. We used two sets of primers to evaluate TRPV3 transcripts, one pair spanning the deleted region and another preceding it (fig. S1, A and C) (*9*). TRPV3 transcript from the skin of homozygous knockout mice was not detected with the first pair of primers and was detected at low levels with the second pair (fig. S1C). In contrast,

[1]Department of Cell Biology, Scripps Research Institute, La Jolla, CA 92037, USA. [2]Genomics Institute, Novartis Research Foundation, San Diego, CA 92121, USA.

*These authors contributed equally to this work.
†To whom correspondence should be addressed. E-mail: ardem@scripps.edu

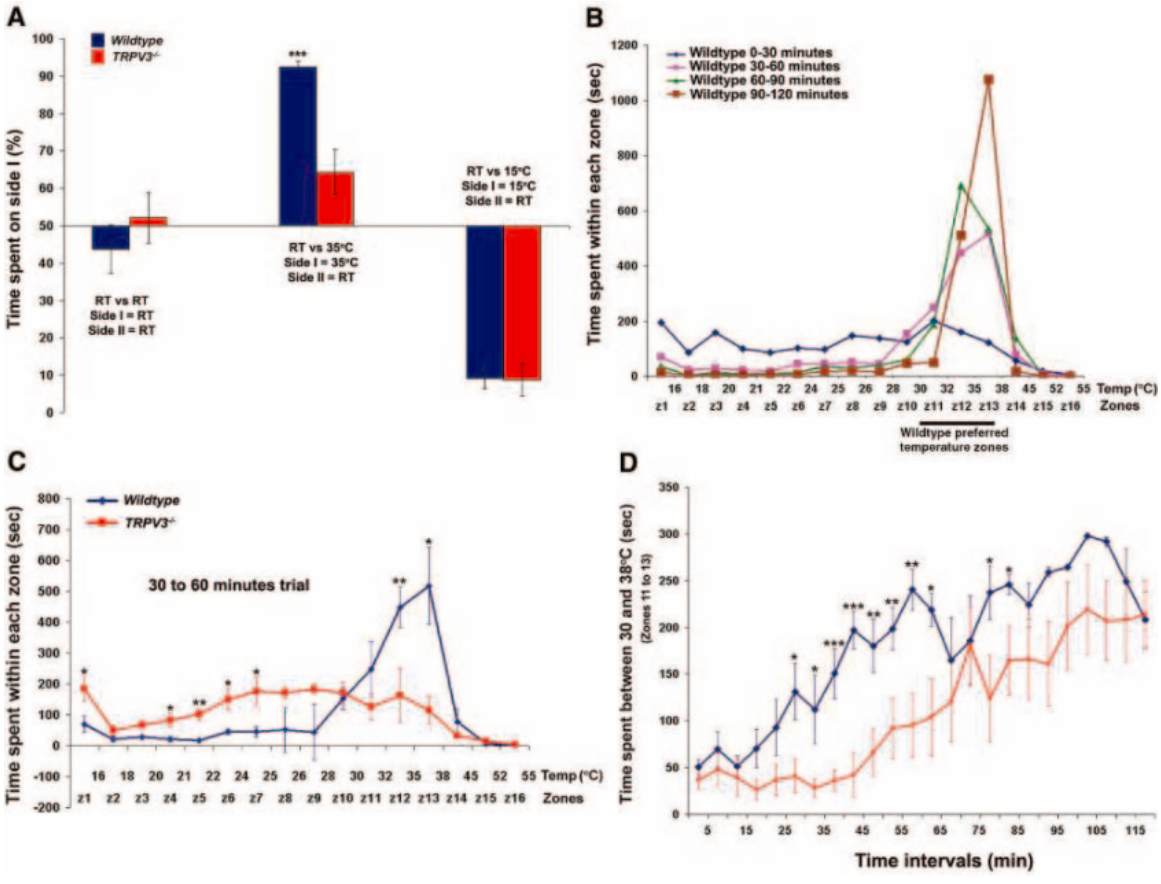

Fig. 1. Mice lacking TRPV3 have a profound deficit in sensing warm temperature in two novel thermotaxis assays. **(A)** Behavior of wild-type mice and TRPV3$^{-/-}$ littermates on the two-temperature choice test. **(B)** Behavior of wild-type mice on the gradient assay over a 2-hour trial, shown in 30-min intervals. **(C)** Behavior of wild-type and TRPV3$^{-/-}$ mice on the gradient from 30 to 60 min. **(D)** Time spent within the preferred zones (11 to 13) for wild-type and TRPV3$^{-/-}$ mice at each 5-min interval during the 2-hour trial. *$P < 0.05$, **$P < 0.01$, ***$P < 0.001$.

transcripts of F-actin and TRPV4 were present at normal levels in the knockout mice. Therefore, the deletion resulted in low levels of truncated TRPV3 transcript that does not encode critical pore and transmembrane domains, and there was no detectable compensatory up-regulation of TRPV4 expression in the presence of this mutation.

The mouse gene encoding TRPV3 is 9 kb away from the gene encoding TRPV1, the noxious heat and capsaicin–activated ion channel (*3*). However, the expression of TRPV1 in DRGs of wild-type and mutant mice appeared indistinguishable, which suggests that TRPV3 deletion results in no major effect on TRPV1 (fig. S1D). Indeed, 25% of neurons were positive for TRPV1 in both wild-type mice (550 of 2226) and TRPV3$^{-/-}$ mice (588 of 2342). We also tested TRPV3$^{-/-}$ mice for their behavioral response to capsaicin and found normal paw licking and/or shaking responses relative to wild-type littermates (fig. S1E). These results show that TRPV1 is expressed normally in TRPV3$^{-/-}$ mice.

We also determined whether the TRPV3 mutation caused anatomical aberrations in DRG projections. Calcitonin gene-related peptide (CGRP) marks DRG neurons that project to the skin. An antibody to CGRP applied to skin sections revealed that this subset of DRG neurons correctly projects to the epidermal-dermal layer in TRPV3$^{-/-}$ mice, corroborating results obtained with capsaicin injections (fig. S1, D and E). Collectively, the results show that TRPV3$^{-/-}$ mice lack functional TRPV3 without affecting TRPV1 and TRPV4 expression or overall DRG anatomy.

Mice carrying two alleles of the TRPV3 mutation appeared morphologically normal, with normal body weight, internal temperature, and open-field response profiles (fig. S2, A to C). The open-field assay demonstrates that TRPV3$^{-/-}$ mice do not have abnormalities in motor activity or anxiety (*10*). In some TRPV3$^{-/-}$ mice, a subtle and temporary hair irregularity in the abdominal area occurred around the third postnatal week. Because TRPV3 is expressed in keratinocytes, we investigated whether loss of TRPV3 caused anatomical skin defects. Newborn wild-type mice and their TRPV3$^{-/-}$ littermates excluded toluidine blue dye, which indicated that the epidermal barrier was intact (*9*, *11*). Light and electron microscopic examinations of the epidermis and dermis of TRPV3$^{-/-}$ mice showed no aberrations throughout development and adulthood (fig. S3, A to H) (*9*). The staining pattern obtained with a panel of keratinocyte markers also appeared normal in TRPV3$^{-/-}$ mice (fig. S3, G and H) (*9*). We also measured the thickness of the skin and found both the epithelial and dermal layers of TRPV3$^{-/-}$ mice to be similar to their wild-type littermates (fig. S3I). Together these results show that the anatomy of the skin is normal in TRPV3$^{-/-}$ mice.

Although behavioral tests in rodents for noxious heat are well described, there are few assays for responses to innocuous heat (30° to 42°C). Because TRPV3 is activated by warm temperatures, we established thermotaxis assays to analyze TRPV3$^{-/-}$ mice. In the first test, mice were presented with a choice of occupying a warm surface versus a room-temperature (RT) surface. When both plates were set to RT, wild-type and TRPV3$^{-/-}$ mice spent about 50% of the time on each side (Fig. 1A), a response profile not statistically different from a hypothetical mean of 300 s, or 50%, on side I (one-sample two-tailed t test, $P = 0.35$ for wild type, $P = 0.76$ for TRPV3$^{-/-}$, $n = 15$). We then tested 25 wild-type mice and 29 TRPV3$^{-/-}$ littermates in the 35°C (warm) versus RT preference test (Fig. 1A). Wild-type mice spent on average 92% of the time (554/600 s) on side I, demonstrating a strong behavioral bias toward innocuous warmth. TRPV3$^{-/-}$ littermates spent only 64% of the time (386/600 s) on side I. The difference in response times between wild-type and mutant mice was highly significant (two-sample two-tailed t test, $P = 7.3 \times 10^{-5}$). Nonetheless, TRPV3$^{-/-}$ mice still showed a slight bias toward the 35°C side as their response profile statistically deviated from a 300 s (50% on side I) hypothetical mean

(one-sample two-tailed t test, $P = 0.022$). This implies that other proteins, most likely TRPV4, are also involved in innocuous thermosensation (*8*, *12*). TRPV3$^{+/-}$ and TRPV1$^{-/-}$ mice behaved like wild-type mice in the 35°C versus RT test; hence, TRPV3 may have a specific role in this thermotaxis behavior (*9*). When side I of the apparatus was set to a cold temperature of 15°C, both wild-type mice and their TRPV3$^{-/-}$ littermates showed a robust avoidance (92% and 91%, respectively; $n = 18$) of the cooled side, suggesting a crucial role for TRPV3 in heat but not cold sensation.

In another thermotaxis assay, mice were allowed to move freely on a flat rectangular platform (10 cm by 97 cm) with a surface temperature gradient of 15°C to 55°C along the length. The compartment was divided into 16 virtual zones with distinct surface temperature ranges, and the amount of time spent in each zone was recorded. We focused our analysis on four consecutive 30-min intervals (total 2 hours). After some exploration, wild-type mice spent the majority of their time in zones 11 to 13 (temperatures of 30° to 38°C) (Fig. 1C). TRPV3$^{-/-}$ mice showed no significant bias for the preferred zones in the 30- to 60-min interval, a time when wild-type mice had already demonstrated a distinct preference (Fig. 1, B and C). However, after the first hour, the TRPV3$^{-/-}$ mice showed a temperature preference similar to that of wild-type mice (fig. S4, B and C). To highlight the timing of preference, we measured total time spent in the preferred zones (30° to 38°C) during 5-min intervals throughout the 2-hour period (Fig. 1D). Wild-type mice showed strong preference by 25 min, whereas TRPV3$^{-/-}$ mice were severely delayed, not showing preference until 60 min. Together, these experiments confirm an important role for TRPV3 in innocuous thermosensation and suggest that other factors are also involved (*8*, *12*).

TRPV3 is initially activated at warm temperatures (threshold of ~33°C) but also shows an increased response to noxious heat (45° to 48°C) (*3*). We performed two experiments to test the behavior of TRPV3 null mice in response to moderate and noxious heat temperatures. In the tail immersion assay, the distal part of the tail of a gently restrained mouse was immersed in a thermoregulated water bath, and the time to a reflexive tail flick was recorded. We observed delayed tail flick responses in TRPV3$^{-/-}$ mice at the temperatures tested, with significance achieved at 50°C and above (Fig. 2A). In the hot plate analgesia meter assay, mice were tested for onset of nociceptive behavior (hind paw lick or flick) at three different surface temperatures. Significant withdrawal latencies were observed in TRPV3$^{-/-}$ mice at the higher temperature of 55°C (Fig. 2B). Together, these results show that the response in TRPV3$^{-/-}$ mice to acute noxious heat was disrupted but not abolished. Indeed, the observed acute thermal nociceptive phenotype is similar to those reported for TRPV1$^{-/-}$ mice and suggests that these two TRPV-class ion channels have overlapping function in vivo (*13*, *14*).

In addition to an acute thermal phenotype, TRPV1$^{-/-}$ mice also show a strong deficit in thermal hyperalgesia (sensitization

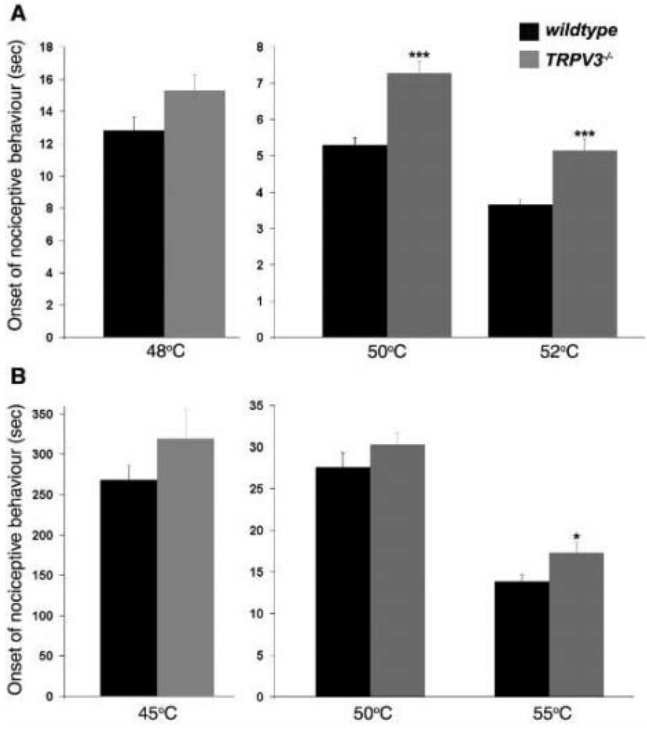

Fig. 2. Mice lacking TRPV3 are deficient in sensing acute noxious thermal stimuli. (**A**) Onset of nociceptive behavior for wild-type and TRPV3$^{-/-}$ mice in response to tail immersion ($n = 18$). Significant differences are observed at temperatures higher than 48°C. (**B**) Response latencies to hot plate (for wild type, $n = 25$ for 45°C, $n = 12$ for 50°C, and $n = 18$ for 55°C; for TRPV3$^{-/-}$, $n = 29$ for 45°C, $n = 12$ for 50°C, and $n = 18$ for 55°C). Significant difference is seen only at the highest temperature tested. *$P < 0.05$, ***$P < 0.001$.

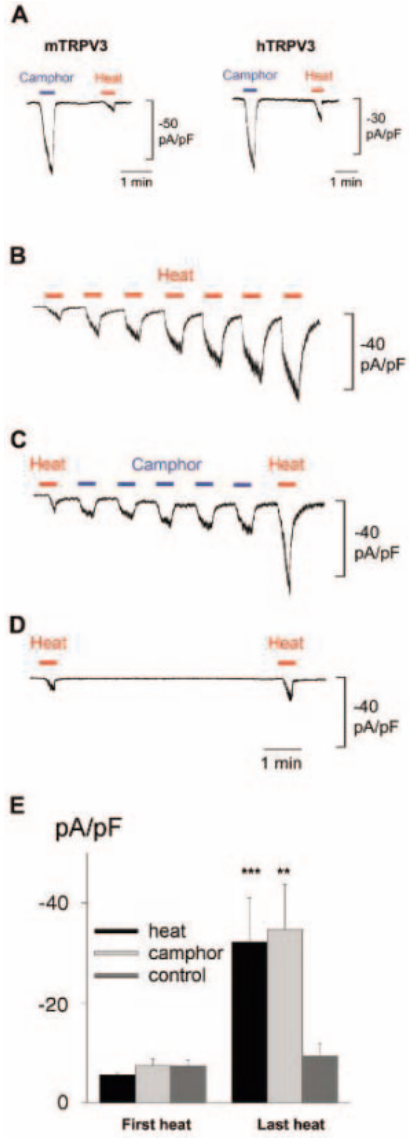

Fig. 3. Camphor activates and sensitizes TRPV3 in CHO cells. (**A**) Whole-cell currents in mouse and human TRPV3-expressing CHO cells were recorded in response to external application of camphor or a 37°C heat pulse. Camphor (2 mM) elicited large currents from TRPV3-expressing cells ($n = 6$ for mouse TRPV3, $n = 7$ for human TRPV3). (**B**) Repeated stimulation by heat alone sensitizes the TRPV3 current ($n = 11$). The last heat response was increased by 601 ± 157% (mean ± SE) over the initial heat response. (**C**) Camphor applications (500 μM) also sensitize TRPV3 responses to heat. The last-to-first heat responses were increased by 433 ± 71% ($n = 6$) [$P_{camphor} = 0.47$ in comparison to heat-induced sensitization in (B)]. (**D**) In the absence of camphor, a second heat pulse increases the first heat response by only 123 ± 19% ($n = 8$) [$P = 0.00015$ in comparison with (C), two-tailed Student's t test]. (**E**) Average of first and last heat currents from (B), (C), and (D). **$P < 0.005$, ***$P < 0.001$.

to noxious thermal stimuli) (*13*, *14*). To investigate the role of TRPV3 in hyperalgesia, we injected complete Freund's adjuvant (CFA) or bradykinin into a single hindpaw of wild-type and TRPV3$^{-/-}$ mice. Sensitivity was measured as the response latency to radiant heat stimulation in injected and noninjected hindpaws. Wild-type mice exhibited a significant decrease in the paw withdrawal latencies of the treated paw 24 hours after injection (n = 12, one-sample two-tailed t test, P = 0.00413 for wild type, P = 0.028642 for TRPV3$^{-/-}$). However, no significant differences were observed in the responses of wild-type and TRPV3$^{-/-}$ mice (fig. S5A). Bradykinin-induced thermal hyperalgesia was also indistinguishable between wild-type and TRPV3$^{-/-}$ mice (fig. S5B). Other nonthermal sensory tests also showed no deficits in TRPV3$^{-/-}$ mice. For example, normal responses to mechanical stimuli (acute or mechanical hyperalgesia) and to injections of formalin (a chemical noxious stimulus) were observed in TRPV3$^{-/-}$ mice (fig. S5, D and E).

Some of the thermoTRPs (TRPV1, TRPM8, and TRPA1) are receptors of sensory compounds that feel hot, cold, or burning (capsaicin, menthol, mustard oil, and cinnamaldehyde), consistent with a physiological role of these ion channels in thermosensation and pain (*2*, *15*, *16*). No sensory compound is known to activate TRPV3. Camphor is a botanical compound used in a variety of topical analgesics and decongestants. Application of camphor on human skin leads to sensitization to heat responses by an unknown mechanism (*17*). We tested the response of these ion channels to camphor. We found that 1 to 2 mM camphor activated Chinese hamster ovary (CHO) cells expressing human or mouse TRPV3 but not those expressing any of the other five thermoTRPs (Fig. 3A) (*9*). Activation of TRPV3 by 1 to 2 mM camphor is physiologically relevant, as this chemical is often used in balms at ~10% by weight (corresponding to concentrations of ~0.5 to 1 M).

The effect of camphor on human skin is best characterized as a sensitization to warm temperatures (*17*). We therefore assessed whether camphor sensitizes TRPV3 responses to warmth. We applied innocuous heat or camphor to TRPV3-expressing cells. Repeated heat pulses of 37°C sensitized TRPV3, as each additional stimulus gave a larger response (Fig. 3, B, D, and E) (*3*, *5*). TRPV3 sensitization to warmth also occurred in response to recurrent activation of the ion channel by camphor (Fig. 3, C and E).

Mouse TRPV3 is specifically expressed in skin keratinocytes (*3*). We therefore tested whether camphor could also activate and sensitize native TRPV3 in primary cultured keratinocytes. Eighty percent (n = 56 of 70) of cultured mouse keratinocytes showed gradually increasing current responses with repeated 37°C pulses. These currents were outwardly rectifying with a reversal potential E_{rev} near 0 mV, similar to the TRPV3 currents when heterologously expressed in CHO cells (Fig. 4A). The majority of cells (66%) were also sensitive to 2 to 10 mM camphor, and the responses to warm temperature (37°C) were robustly potentiated by treatment with camphor (Fig. 4B). Furthermore, 5 μM ruthenium red (a blocker of TRPV ion channels) completely blocked the camphor-induced currents at negative voltages (fig. S6A). Collectively, these recordings provide strong evidence that camphor activates and sensitizes native TRPV3 expressed in keratinocytes. In our experiments, TRPV3- and TRPV4-like responses are both readily observed in keratinocyte cultures (80% TRPV3-like and 30% TRPV4-like, with a 20% overlap). These data vary from a report that describes TRPV4-like heat responses but few TRPV3-like responses in a majority of keratinocytes (*8*). However, Chung *et al.*

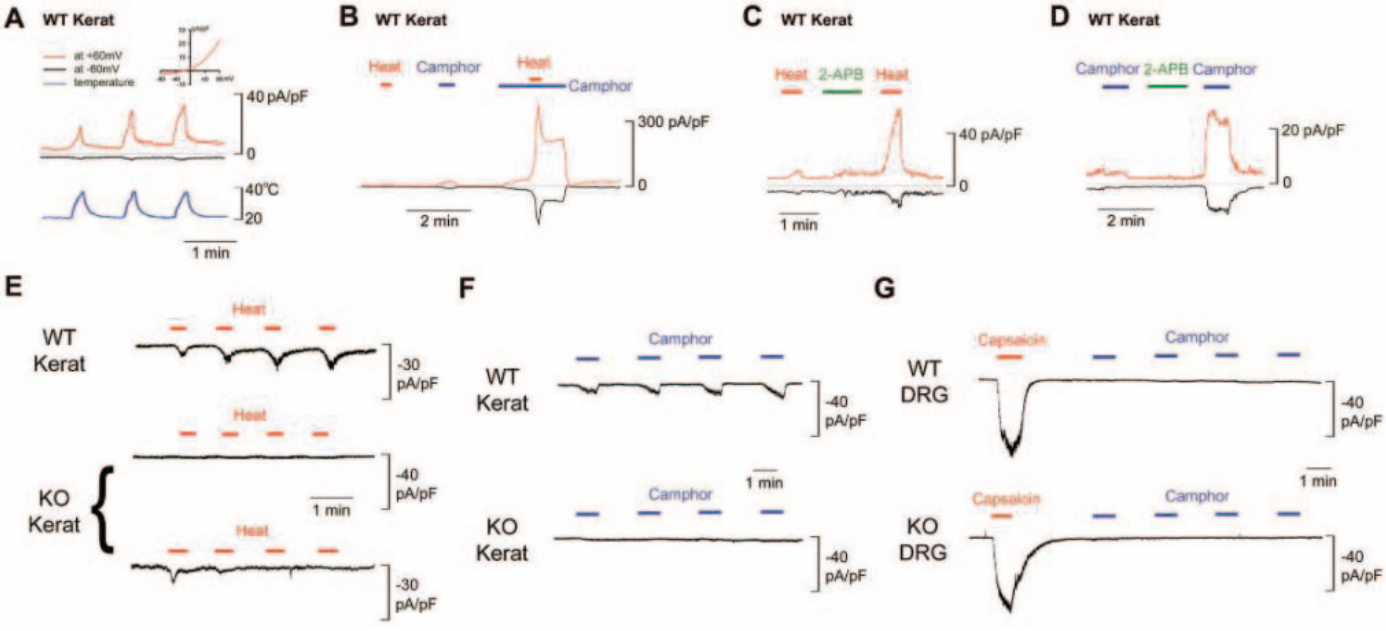

Fig. 4. Heat- and camphor-activated currents in wild-type and TRPV3$^{-/-}$ mice. (**A** to **D**) Camphor activates and sensitizes TRPV3 in cultured wild-type keratinocytes. (A) Repeated stimulation of heat gives rise to a TRPV3-like sensitizing current. Inset: Current response upon heat stimulation shows outwardly rectifying current-voltage relationship with E_{rev} near 0 mV. Dotted line, zero current level. (B) Camphor (5 mM) activates an outwardly rectifying current. The heat response of the same cell is greatly increased during application of 5 mM camphor (n = 10 of 16 tests, 569 ± 129%, P = 0.002). Application of 100 μM 2-APB sensitizes the response to heat (n = 5, 911 ± 331%, P = 0.0001) (C) and the response to 2 mM camphor (n = 5, 877 ± 181%, P = 0.003) (D), respectively. (**E**) Repeated stimulation by heat activates and sensitizes a TRPV3-like current in keratinocytes from wild-type littermates (upper trace, recorded at –60 mV, n = 22). Other cells show TRPV4-like response (n = 2), mixed response (n = 4), or no response (n = 1) (*9*). No response (middle trace, n = 16) or TRPV4-like rapidly desensitized current (bottom trace, n = 9) is observed in TRPV3$^{-/-}$ keratinocytes. TRPV3-like, TRPV4-like, or mixed currents were determined as described (*8*, *19*). (**F**) Keratinocytes from TRPV3$^{-/-}$ mice do not respond to 5 mM camphor (n = 34, bottom trace), whereas those from wild-type littermates show the normal camphor response (n = 7 of 9, upper trace). (**G**) Cultured DRG neurons from wild-type littermates or from TRPV3$^{-/-}$ mice do not respond to repeated application of 5 mM camphor (n = 43 and n = 14, respectively); 58% of wild-type mouse DRG neurons tested and 57% of those from TRPV3$^{-/-}$ mice show response to 0.5 μM capsaicin.

observed TRPV3 protein expression in a majority of keratinocytes and detected abundant TRPV3-like responses in the presence of 2-aminoethoxydiphenyl borate (2-APB), a compound that activates and sensitizes TRPV3 (*8*, *18*, *19*). Consistent with these reports, we observed that pretreatment with 100 μM 2-APB strongly potentiated heat and camphor responses in keratinocytes (Fig. 4, C and D), whereas camphor was not capable of sensitizing 2-APB responses (n = 3) (*9*). Together, these studies imply that TRPV3 is present in a majority of cultured keratinocytes.

We next compared the camphor- and heat-induced currents of wild-type and TRPV3$^{-/-}$ littermate keratinocytes. The majority of wild-type keratinocytes showed gradually increasing current responses with repeated 37°C pulses at –60 mV, whereas TRPV3$^{-/-}$ keratinocytes showed no responses or some responses with TRPV4-like desensitization (Fig. 4E) (fig. S6B). Responses to repeated application of 5 mM camphor were observed in wild-type but not TRPV3$^{-/-}$ keratinocytes (Fig. 4F). This suggests that TRPV3 is a heat receptor in keratinocytes, that it is the only receptor for camphor in these cells, and that camphor sensitivity is a specific functional marker for TRPV3. Unlike what was observed for keratinocytes, 5 mM camphor failed to evoke sensitizing current responses from capsaicin-sensitive or capsaicin-insensitive DRG neurons from either wild-type mice (n = 43) or TRPV3$^{-/-}$ mice (n = 14) (Fig. 4G).

The residual sensitivity to warm temperatures in TRPV3$^{-/-}$ mice may be due to partial compensation by TRPV4, the only other ion channel known to respond to innocuous heat in culture (*20*, *21*). Consistent with expression analysis, camphor activity was observed in keratinocytes but not in DRG neurons, even with high concentrations of camphor. Therefore, the acute thermosensory phenotype observed in TRPV3$^{-/-}$ mice suggests an important role of skin in temperature sensation. Keratinocytes are not known to "sense" temperature; instead, DRGs are thought to directly sense heat through free nerve endings (*1*). This conclusion is mainly based on the ability of dissected neurons to respond to temperature shifts and on the anatomical observation that no synapses are apparent between free nerve endings and keratinocytes (*22*, *23*). However, a recent study has observed a population of chemosensory cells that form synaptic contacts with trigeminal afferent nerve fibers within the nasal epithelium (*24*). Furthermore, nonsynaptic communication between keratinocytes and nerve fibers can be considered.

References and Notes

1. H. Hensel, *Monogr. Physiol. Soc.* **38**, 1 (1981).
2. A. Patapoutian, A. P. Peier, G. M. Story, V. Viswanath, *Nature Rev. Neurosci.* **4**, 529 (2003).
3. A. M. Peier *et al.*, *Science* **296**, 2046 (2002).
4. G. D. Smith *et al.*, *Nature* **418**, 186 (2002).
5. H. Xu *et al.*, *Nature* **418**, 181 (2002).
6. W. Liedtke *et al.*, *Cell* **103**, 525 (2000).
7. M. Suzuki *et al.*, *Neurosci. Lett.* **353**, 189 (2003).
8. M. K. Chung, H. Lee, A. Mizuno, M. Suzuki, M. J. Caterina, *J. Biol. Chem.* **279**, 21569 (2004).
9. A. Moqrich *et al.*, data not shown.
10. T. Miyakawa, M. Yamada, A. Duttaroy, J. Wess, *J. Neurosci.* **21**, 5239 (2001).
11. J. Reichelt, H. Büssow, C. Grund, T. M. Magin, *Mol. Biol. Cell* **12**, 1557 (2001).
12. H. Todaka, J. Taniguchi, J.-i. Satoh, A. Mizuno, M. Suzuki, *J. Biol. Chem.* **279**, 35133 (2004).
13. J. B. Davis *et al.*, *Nature* **405**, 183 (2000).
14. M. J. Caterina *et al.*, *Science* **288**, 306 (2000).
15. S. E. Jordt *et al.*, *Nature* **427**, 260 (2004).
16. M. Bandell *et al.*, *Neuron* **41**, 849 (2004).
17. B. G. Green, *J. Invest. Dermatol.* **94**, 662 (1990).
18. H. Z. Hu *et al.*, *J. Biol. Chem.* **279**, 35741 (2004).
19. M. K. Chung, H. Lee, A. Mizuno, M. Suzuki, M. J. Caterina, *J. Neurosci.* **24**, 5177 (2004).
20. A. D. Guler *et al.*, *J. Neurosci.* **22**, 6408 (2002).
21. H. Watanabe *et al.*, *J. Biol. Chem.* **277**, 13569 (2002).
22. N. Cauna, *J. Anat.* **115**, 277 (1973).
23. M. Hilliges, L. Wang, O. Johansson, *J. Invest. Dermatol.* **104**, 134 (1995).
24. T. E. Finger *et al.*, *Proc. Natl. Acad. Sci. U.S.A.* **100**, 8981 (2003).

25. We thank M. Bandell, B. Conti, H. Esendencia, P. Garrity, S. Kupriyanov, M. Mayford, A. Peier, L. Reijmers, M. Wood, and J. Watson for input and assistance; M. Caterina for sharing a detailed protocol on primary culture of keratinocytes; T. Bartfai for sharing the thermal gradient platform; and N. Hong, T. Jegla, U. Mueller, and L. Stowers for critical reading of the manuscript. Supported by National Institute of Neurological Disorders and Stroke grants R01NS046303 and R01NS42822. G.M.S. is a recipient of a National Research Service Award postdoctoral fellowship from NIH. A.P. is a Damon Runyon Scholar.

Supporting Online Material

www.sciencemag.org/cgi/content/full/307/5714/1468/DC1
Materials and Methods
Figs. S1 to S6
References

13 December 2004; accepted 4 January 2005
10.1126/science.1108609

OSBP Is a Cholesterol-Regulated Scaffolding Protein in Control of ERK1/2 Activation

Ping-yuan Wang, Jian Weng, Richard G. W. Anderson*

Oxysterol-binding protein (OSBP) is the founding member of a family of sterol-binding proteins implicated in vesicle transport, lipid metabolism, and signal transduction. Here, OSBP was found to function as a cholesterol-binding scaffolding protein coordinating the activity of two phosphatases to control the extracellular signal–regulated kinase (ERK) signaling pathway. Cytosolic OSBP formed a ~440-kilodalton oligomer with a member of the PTPPBS family of tyrosine phosphatases, the serine/threonine phosphatase PP2A, and cholesterol. This oligomer had dual specific phosphatase activity for phosphorylated ERK (pERK). When cell cholesterol was lowered, the oligomer disassembled and the level of pERK rose. The oligomer also disassembled when exposed to oxysterols. Increasing the amount of OSBP oligomer rendered cells resistant to the effects of cholesterol depletion and decreased the basal level of pERK. Thus, cholesterol functions through its interaction with OSBP outside of membranes to regulate the assembly of an oligomeric phosphatase that controls a key signaling pathway in the cell.

Depletion of membrane cholesterol markedly increases the level of pERK in the caveolae and cytosol fractions of cells (*1*). The level of pERK is increased further by simultaneously exposing the cells to epidermal growth factor (EGF), which suggests that cholesterol depletion inactivates a pERK phosphatase. Recently, we identified a cholesterol-regulated phosphatase that has dual specific activity for pERK (*2*). When cellular cholesterol levels are normal, this phosphatase works in tandem with the ERK kinase MEK-1 to regulate the level of pERK in the cell. The phosphatase is a heterooligomer of ~440 kD that derives its dual specific activity from two phosphatases. One is a member of the PTPPBS family of tyrosine phosphatases (*3*), and the other is the serine/threonine phosphatase PP2A (*2*). These two enzymes each depend on the activity of the other to coordinately remove phosphate from both the threonine and the tyrosine residues of pERK. Depletion of cell cholesterol results in the dissociation of PP2A from the PTPPBS member and a loss of dual specific pERK phosphatase activity. Thus, cholesterol appears to act directly or indirectly to control the formation of an oligomer of two phosphatases that together have functionality that neither has alone. Here, we present

Department of Cell Biology, University of Texas Southwestern Medical Center, Dallas, TX 75390–9039, USA.

*To whom correspondence should be addressed. E-mail: richard.anderson@utsouthwestern.edu

evidence that this oligomer is held together through interactions between cholesterol and the OSBP.

The cholesterol dependency of the oligomeric phosphatase complex was demonstrated using HeLa cells expressing a cDNA for the PTPPBS family member HePTP tagged with polyhistidine, myc, and an influenza hemagglutinin peptide (HA). Cells were transfected for 48 hours, incubated in the presence of methyl-β-cyclodextrin (CD) or CD plus cholesterol for 60 min (to remove or retain cholesterol, respectively), and the cytosol was used to purify the HePTP by nickel-nitrilotriacetic acid (Ni-NTA) agarose chromatography. The HA-HePTP-myc-his was eluted with increasing concentrations of imidazole. Peak elution occurred at an imidazole concentration of 80 to 160 mM (Fig. 1A). The HePTP isolated from cells exposed to CD plus cholesterol coeluted with the PP2A phosphatase, whereas PP2A was markedly reduced in fractions of HA-HePTP-myc-his isolated from cholesterol-depleted cells (Fig. 1A).

In transfected cells, lipid, probably cholesterol, was found in the HePTP/PP2A complex (Fig. 1B). HeLa cells expressing HA-HePTP-myc-his were labeled with [^{3}H]-cholesterol and [^{3}H]-palmitic acid. HA-HePTP-myc-his was isolated with Ni-NTA agarose beads and processed for thin-layer chromatography (TLC). Autoradiography showed a single band in the cytosol fraction that comigrated with cholesterol and was absent in CD-treated cells. A slower migrating radioactive band eluted from the Ni-NTA beads with imidazole. This band was also absent from CD-treated cells, which suggests that it was cholesterol. Fourteen different oxysterols that we tested failed to migrate to the same position (table S1). Furthermore, imidazole caused cholesterol to migrate anomalously on TLC (Fig. 1C), and cytosolic [^{3}H]-cholesterol migrated the same when exposed to imidazole (fig. S1). We did not detect any phospholipid or ceramide in the complex.

The presence of cholesterol suggested that the oligomeric phosphatase contained a sterol-binding protein. Initially, we thought the bound lipid that migrated slower on TLC plates (Fig. 1B) was an oxysterol, which prompted us to see whether the oligomer contained OSBP. We purified the oligomer from HeLa cells expressing HA-HePTP-myc-his and processed the sample for immunoblotting (Fig. 2A). The complex clearly contained endogenous OSBP and PP2A. Depleting cells of cholesterol caused the loss of both proteins from the complex. HA-HePTP-myc-his lacking a 15 amino acid segment called the kinase interaction motif (KIM) domain (ΔKIM-HePTP) (*4*) did not interact with endogenous OSBP (Fig. 2B).

Thus, OSBP may represent a cholesterol-binding component of the endogenous complex that we originally purified from HeLa cells (*2*). We used monoclonal antibody (mAb) OSBP to immunoblot the fractions from the columns used for purification (Fig. 2, C and D). Even though this antibody was not sensitive enough to detect OSBP in cytosol fractions, a strong signal was seen in fractions from both the Mono Q (Fig. 2C) and the gel filtration columns used to purify the oligomer (Fig. 2D). We could also co-immunoprecipitate endogenous OSBP from the gel-filtration fractions with α-PP2A immunoglobulin G (IgG). In addition, bacterially expressed OSBP bound [^{3}H]-cholesterol (Fig. 2E and fig. S2). Remarkably, the bound [^{3}H]-cholesterol was displaced by cholesterol but not by 25-hydroxycholesterol (Fig. 2E), which suggests that oxysterols and cholesterol bind to different sites on OSBP.

If OSBP interacts with HePTP, coexpressing the two should cause more oligomer to form because cells have excess PP2A (Fig. 3A). Cells were transiently transfected with either HA-HePTP-myc-his, OSBP, or the combination, and HA-HePTP-myc-his was purified. In cells expressing HA-HePTP-myc-his alone, the bound HA-HePTP-myc-his was enriched in endogenous OSBP relative to the unbound cytosol. Some $PP2A_B$ also coeluted, indicating the presence of oligomer. Little OSBP bound to Ni-NTA from cytosol of cells expressing OSBP alone. By contrast, cells coexpressing HA-HePTP-myc-his and OSBP had dramatically more bound OSBP and $PP2A_B$. The same result was obtained if the polyhistamine tag was put on OSBP instead of HePTP (fig. S3). OSBP lacking the pleckstrin homology (PH) domain (ΔPH-OSBP) was unable to oligomerize with HePTP and PP2A, whereas mutating the highly conserved valine 522, serine 523 signature region (VS-OSBP) to alanine had no effect (fig. S3).

We postulate that cholesterol bound to OSBP is what holds the oligomer together. If so, then the quantity of oligomer (cholesterol, HePTP, OSBP, and PP2A) present in cells should be a function of the amount of OSBP. We expressed the same amount of HA-HePTP-myc-his in two sets of cells expressing 10-fold different amounts of OSBP (Fig. 3B). The cells were labeled with [^{3}H]-cholesterol overnight before processing for purification of HA-HePTP-myc-his. Immunoblots showed that nearly equal amounts of HA-HePTP-myc-his were present. Markedly more OSBP and PP2A were present in fractions from cells expressing the higher amount of OSBP. Moreover, the fraction with the highest amount of OSBP contained 5 times as much radioactive lipid as the corresponding fraction from cells expressing low levels of OSBP. We conclude that OSBP

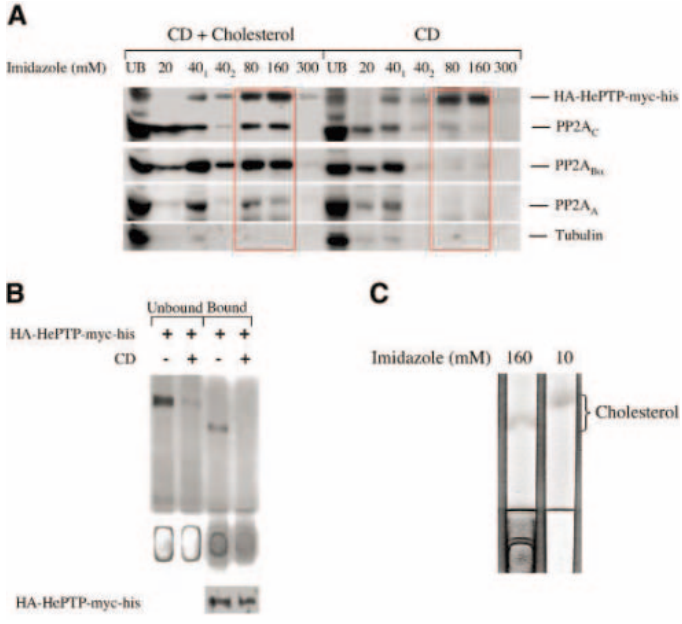

Fig. 1. Isolation of the cholesterol-regulated HePTP/PP2A oligomer using Ni-NTA chromatography. (**A**) HeLa cells expressing HA-HePTP-myc-his were incubated in the presence of 1% CD or a mixture of 1% CD and 200 μg/ml cholesterol for 1 hour at 37°C. The cells were washed and the cytosol isolated. Six milligrams of cytosol was mixed with Ni-NTA beads and incubated for 3 hours at 4°C. The beads were pelleted, loaded on a column, and washed with the indicated concentrations of imidazole. Sixty micrograms of the unbound (UB) protein and equal volumes of each eluate were processed for immunoblotting with antibodies that recognize the indicated proteins. (**B**) HeLa cells expressing HA-HePTP-myc-his were labeled with [^{3}H]-cholesterol and [^{3}H]-palmitic acid. Cytosol was prepared from cells that had been incubated in the presence or absence of 1% CD for 1 hour at 37°C. Equal amounts of cytosol (3 mg) were processed for isolation of the oligomer on Ni-NTA beads. Fifty microliters of the unbound fraction and 500 μl of the bound fraction were processed for lipid extraction. The lipids were separated by TLC and the radioactivity detected by autoradiography. A 50-μl sample of the bound fraction was also processed for immunoblotting to detect HA-HePTP-myc-his. (**C**) Fifty micrograms of unlabeled cholesterol was mixed with buffer B containing either 10 mM or 160 mM imidazole, extracted, and loaded onto a TLC plate, and the lipids were separated using the same condition as in (B). Cholesterol was visualized by iodine staining.

drives assembly of the two phosphatases plus cholesterol into an oligomeric complex.

OSBP is known as an oxysterol-binding protein (*5*), which raises the possibility that oxysterols affect oligomer assembly. Cytosol from HeLa cells expressing OSBP and HA-HePTP-myc-his was mixed with either 25-hydroxycholesterol or cholesterol before purifying the HA-HePTP-myc-his (Fig. 3C). The HA-HePTP-myc-his isolated from the cholesterol-treated cytosol contained both OSBP and PP2A, indicating the presence of the oligomeric phosphatase. By contrast, neither protein was associated with HA-HePTP-myc-his isolated from 25-hydroxycholesterol–treated cytosol. Previous studies have shown that incubating cells in the presence of 25-hydroxycholesterol increases pERK but not phosphorylated c-Jun N-terminal kinase (pJNK) (*6*, *7*). We found that exposing cytosol to 25-hydroxycholesterol inhibited pERK dephosphorylation activity (fig. S4).

Immunoprecipitates of either HePTP or PP2A have dual specific phosphatase activity for pERK (*2*). HeLa cells expressing OSBP-myc-his and HA-HePTP were processed to measure pERK phosphatase activity in OSBP immunoprecipitates (Fig. 4A). Dual specific phosphatase activity was measured by using immunoblotting to detect either the pY or the pT in a pERK2-GST (glutathione S-transferase) substrate. Incubation of pERK2-GST in the presence of immunoprecipitated OSBP caused a marked reduction in the level of both pY and pT. The presence of either vanadate or okadaic acid inhibited dephosphorylation of both residues. No phosphatase activity was detected when α-myc IgG was replaced with a nonimmune IgG. Thus, antibodies against tagged HePTP, OSBP, and untagged PP2A all immunoprecipitate the oligomeric phosphatase activity (*2*).

Further evidence that the three proteins in the complex interact functionally came from the chance observation that the pT-specific pERK mAb recognized OSBP in the immunoprecipitated oligomer (Fig. 4A). Vanadate reduced pT-specific mAb pERK binding, which suggests that it stimulated PP2A to dephosphorylate a phosphothreonine residue in OSBP. Indeed, vanadate-dependent loss of pT-specific mAb pERK immunoblotting of OSBP was blocked by okadaic acid (fig. S5B). We obtained the same results when mAb pThr was substituted for pT-specific mAb pERK (Fig. 4A). We observed the same phenomenon with purified endogenous oligomeric phosphatase. Thus, an interaction occurs in the oligomer between HePTP and PP2A that controls OSBP phosphorylation.

We also found that incubating cytosol in the presence of CD caused a loss of PP2A from the oligomer (fig. S5A), which indicates that removal of cholesterol from the cytosol causes a partial disassembly of the phosphatase. As expected, vanadate no longer stimulated dephosphorylation of pOSBP in immunoprecipitated complexes lacking PP2A (fig. S5B). These results suggest that cytosolic cholesterol is required for stability of the oligomer.

We could not be certain whether HePTP is the PTPPBS family member in the endogenous HeLa cell oligomeric phosphatase because of the lack of an appropriate antibody. Nevertheless, when we adjusted the amount of pERK phosphatase activity by increasing or decreasing the amount of OSBP, the level of endogenous pERK changed (Fig. 4, B and C). The level of pERK in both fractions was markedly lower in cells expressing wild-type and VS-OSBP compared with cells expressing ΔPH-OSBP (Fig. 4B). Because only OSBP and VS-OSBP interact with HePTP (fig. S3), increasing the amount of oligomeric phosphatase reduces endogenous pERK levels. Endogenous pERK phosphatase was reduced by RNA interference (RNAi) of OSBP mRNA (Fig. 4C). Cells were exposed to two small interfering RNAs (siRNAs) directed against different regions of the OSBP mRNA and one control siRNA directed against an irrelevant mRNA before processing for immunoblotting and reverse transcription polymerase chain reaction (RT-PCR). Reducing the mRNA for OSBP resulted in a marked increase in the amount of pERK in the cell.

Increasing the amount of oligomeric phosphatase blocked the effects of cholesterol depletion on pERK dephosphorylation. HeLa cells expressing HA-HePTP and OSBP, but not HA-HePTP alone, have elevated amounts of oligomeric phosphatase (Fig. 3A). Incubating either set of cells in the presence of the MEK-1 inhibitor PD98059 for 10 min to

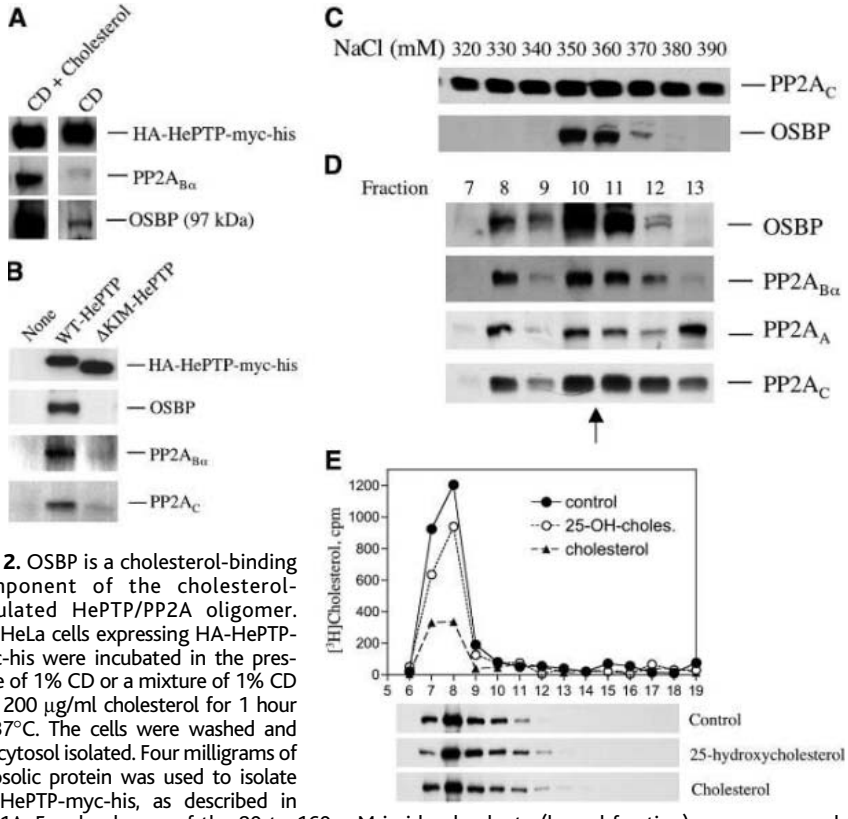

Fig. 2. OSBP is a cholesterol-binding component of the cholesterol-regulated HePTP/PP2A oligomer. (**A**) HeLa cells expressing HA-HePTP-myc-his were incubated in the presence of 1% CD or a mixture of 1% CD and 200 μg/ml cholesterol for 1 hour at 37°C. The cells were washed and the cytosol isolated. Four milligrams of cytosolic protein was used to isolate HA-HePTP-myc-his, as described in Fig. 1A. Equal volumes of the 80 to 160 mM imidazole eluate (bound fraction) were processed for immunoblotting. (**B**) HeLa cells expressing either nothing, HA-HePTP-myc-his, or HA-HePTP-myc-his lacking the KIM domain were processed to isolate his-tagged proteins as described using a 2-mg sample of cytosol. The protein from an equal volume of the bound fraction was processed for immunoblotting with the indicated antibodies. (**C**) HeLa cell cytosol (10 mg) was loaded on a Mono Q column and washed extensively with 250 mM NaCl as described (*2*). Fractions from the column were eluted with a linear 250 to 450 mM NaCl gradient. Equal volumes of the indicated fractions were processed for immunoblotting. (**D**) The 350 to 380 mM fractions were pooled and processed for purification by gel filtration as described (*2*). Fractions (1 ml) were collected and processed for immunoblotting. The peak fraction for ferritin (440 kD) is marked with an arrow. (**E**) A Ni-NTA–purified, bacterially expressed OSBP/[^{3}H]-cholesterol complex (500 μl) was mixed with either 4 μl of ethanol (filled circles) or 4 μl of ethanol containing 1 mg/ml of either cholesterol (triangles) or 25-hydroxycholesterol (open circles) (20 μM final concentration) and incubated overnight at 4°C. The samples were then separated by gel filtration and each fraction assayed either for radioactivity or OSBP using mAb α-V5.

block phosphorylation of ERK caused a marked reduction in the level of endogenous pERK (Fig. 4D). When cells expressing only HA-HePTP-his were depleted of cholesterol, the loss of pERK was markedly inhibited. By contrast, cholesterol depletion had little effect on endogenous pERK dephosphorylation in cells expressing both OSBP and HA-HePTP.

Although we cannot rule out the possibility that other proteins in the oligomeric complex mediate cholesterol regulation, assembly of the oligomeric pERK phosphatase

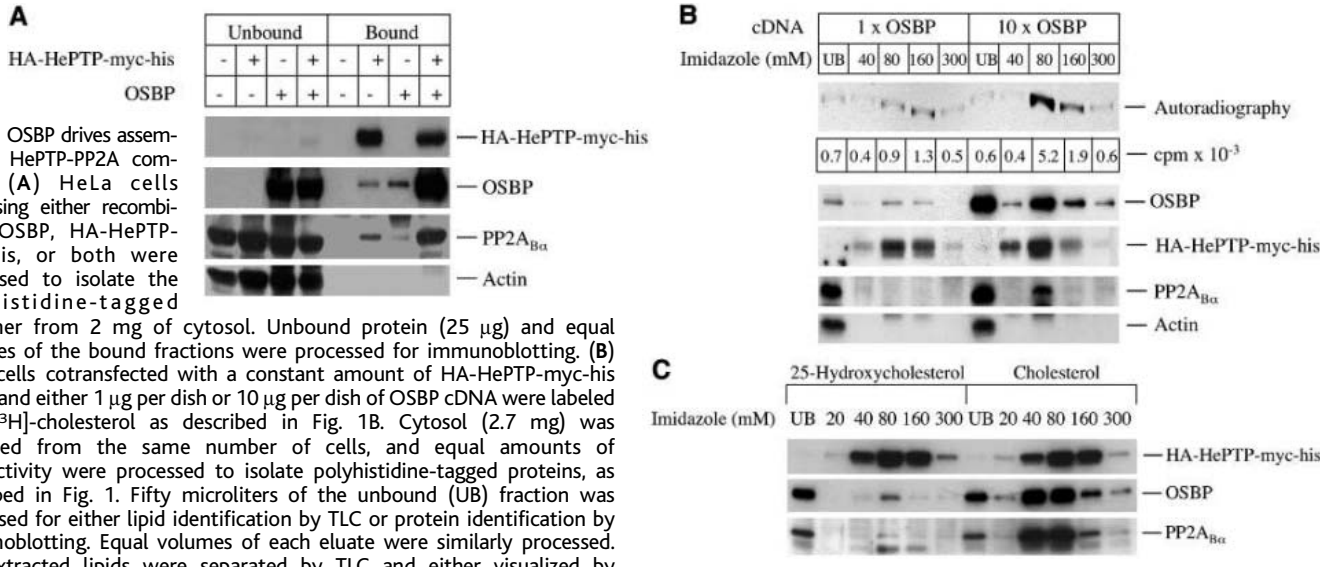

Fig. 3. OSBP drives assembly of HePTP-PP2A complex. (**A**) HeLa cells expressing either recombinant OSBP, HA-HePTP-myc-his, or both were processed to isolate the polyhistidine-tagged oligomer from 2 mg of cytosol. Unbound protein (25 μg) and equal volumes of the bound fractions were processed for immunoblotting. (**B**) HeLa cells cotransfected with a constant amount of HA-HePTP-myc-his cDNA and either 1 μg per dish or 10 μg per dish of OSBP cDNA were labeled with [^{3}H]-cholesterol as described in Fig. 1B. Cytosol (2.7 mg) was prepared from the same number of cells, and equal amounts of radioactivity were processed to isolate polyhistidine-tagged proteins, as described in Fig. 1. Fifty microliters of the unbound (UB) fraction was processed for either lipid identification by TLC or protein identification by immunoblotting. Equal volumes of each eluate were similarly processed. The extracted lipids were separated by TLC and either visualized by autoradiography or the band cut out and counted directly (cpm × 10^{-3}). (**C**) Cytosol (2 mg) from HeLa cells expressing HA-HePTP-myc-his and OSBP was mixed with Ni-NTA beads and incubated in the presence of either 20 μM 25-hydroxycholesterol or 20 μM cholesterol dissolved in ethanol for 3 hours at 4°C before being processed to isolate HA-HePTP-myc-his, as described in Fig. 1. A 25-μg sample of UB proteins and equal volumes of each eluate were processed for immunoblotting to detect the indicated proteins.

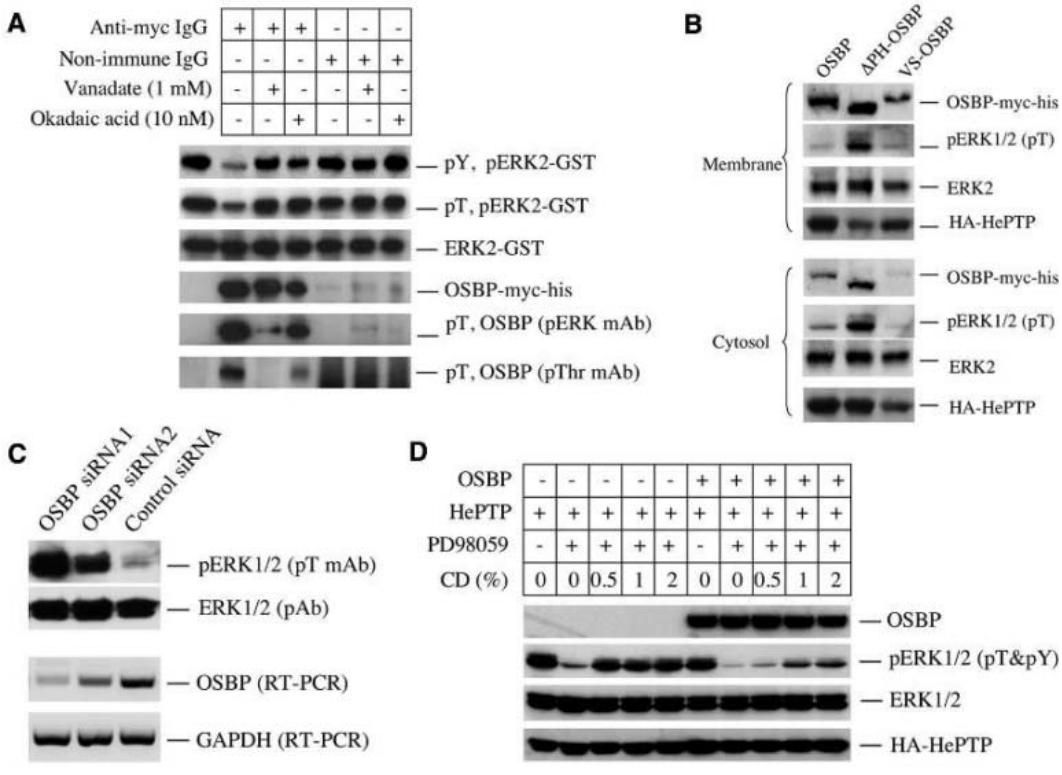

Fig. 4. OSBP oligomer regulates pERK phosphorylation. (**A**) Cytosol was isolated from HeLa cells expressing both OSBP-myc-his and HA-HePTP. Equal amounts of cytosol were processed for immunoprecipitation using either α-myc or nonimmune IgG. The beads were washed and resuspended in buffer C before adding 50 ng of pERK2-GST protein and the indicated inhibitors and incubated for 3 hours at 30°C. The reaction was stopped by adding 6 x SDS sample buffer to the mixture and processing the sample for immunoblotting using antibodies that detect the indicated protein. (**B**) HeLa cells coexpressing HePTP and either wild-type OSBP, ΔPH-OSBP, or VS-OSBP were fractionated into either a membrane fraction or a cytosol fraction and processed for immunoblotting (50 μg per lane) using the indicated antibodies. We used a sensitive pT α-pERK to detect activated ERK. (**C**) HeLa cells were incubated for 24 hours in the presence of two siRNAs directed against different regions of the OSBP mRNA and one directed against the mRNA for microsomal triglyceride transfer protein, and then the cells were washed and cultured for an additional 48 hours before being processed. Cell lysates were then tested for the level of OSBP and glyceraldehyde-phosphate dehydrogenase mRNA with RT-PCR or for the amount of pERK and ERK by immunoblotting. (**D**) HeLa cells expressing either HePTP alone or together with OSBP were cultured in six-well plates for 48 hours. The cells were washed and incubated in serum-free Dulbecco's modified Eagle's medium in the presence of 20 μM PD98059 to block MEK-1 for 10 min at 37°C before adding the indicated amount of CD and incubating an additional 15 min at 37°C. Cells were immediately dissolved in SDS sample buffer and processed for immunoblotting to detect the indicated protein or epitope.

appears to depend on a direct interaction between OSBP and sterols. OSBP belongs to a group of proteins that share in common a phosphoinositide-binding PH domain that can target the molecule to the Golgi apparatus (*8*), a FFAT motif that can target it to the endoplasmic reticulum (ER) (*9*), and a lipid-binding domain that binds specific lipids. These proteins are thought to be involved in the nonvesicular transfer of lipids between various membrane compartments (*10*). For example, CERT has recently been identified as a ceramide-binding protein that appears to use the PH and FFAT motifs to transfer ceramide between ER and Golgi-apparatus membranes (*11*). Although a nonvesicular lipid transport function has not been established for OSBP, it does move to the Golgi apparatus when cells are either depleted of cholesterol or exposed to oxysterols, which indicates that it has the ability to sense cellular sterol levels. Targeting to the Golgi apparatus depends on the PH domain (*12*). OSBP also can bind VAP in ER membranes (*13*). Ordinarily, most of the OSBP appears to be soluble in the cytoplasm in a conformation that masks the PH domain (*8*).

If OSBP is the cholesterol-sensing protein in the pERK phosphatase oligomer, then we imagine that when cholesterol binds to the lipid-binding domain in OSBP it undergoes a conformational change that masks the PH domain. In this configuration, OSBP is able to bind HePTP and PP2A to form a high-molecular-weight complex (fig. S6A). The molecules in the oligomer are precisely arranged so that they are able to interact in response to specific environmental cues. These interactions are critical for spatially organizing HePTP and PP2A so that they can work coordinately to remove both phosphates from pERK1/2 but not from other mitogen-activated protein kinases such as stress-activated protein kinase (*2*). Either oxysterol binding or cholesterol removal changes the conformation of OSBP so that the PH domain is exposed and the phosphatases dissociate (fig. S6B). Unmasking the PH domain causes OSBP to move to specific membrane compartments such as the Golgi apparatus, where it may reacquire cholesterol. Therefore, the pERK1/2 phosphatase activity conferred through OSBP is positively regulated by cholesterol and negatively regulated by oxysterols. One implication of this model is that other lipid-transfer proteins with pH domains and FFAT motifs may have lipid-specific scaffolding functions that regulate key signaling pathways.

References and Notes

1. T. Furuchi, R. G. Anderson, *J. Biol. Chem.* **273**, 21099 (1998).
2. P. Y. Wang, P. Liu, J. Weng, E. Sontag, R. G. Anderson, *EMBO J.* **22**, 2658 (2003).
3. K. A. Augustine *et al.*, *Anat. Rec.* **258**, 221 (2000).
4. R. Pulido, A. Zuniga, A. Ullrich, *EMBO J.* **17**, 7337 (1998).
5. M. K. Storey, D. M. Byers, H. W. Cook, N. D. Ridgway, *Biochem. J.* **336**, 247 (1998).
6. M. P. Ares *et al.*, *Atherosclerosis* **153**, 23 (2000).
7. J. H. Yoon, A. E. Canbay, N. W. Werneburg, S. P. Lee, G. J. Gores, *Hepatology* **39**, 732 (2004).
8. N. D. Ridgway, P. A. Dawson, Y. K. Ho, M. S. Brown, J. L. Goldstein, *J. Cell Biol.* **116**, 307 (1992).
9. C. J. Loewen, A. Roy, T. P. Levine, *EMBO J.* **22**, 2025 (2003).
10. S. Munro, *Nature* **426**, 775 (2003).
11. K. Hanada *et al.*, *Nature* **426**, 803 (2003).
12. A. Mohammadi *et al.*, *J. Lipid Res.* **42**, 1062 (2001).
13. J. P. Wyles, C. R. McMaster, N. D. Ridgway, *J. Biol. Chem.* **277**, 29908 (2002).

14. We thank C. Hall and M. Zhu for valuable technical assistance and B. Pallares for administrative assistance. We are indebted to E. Sontag for advice and reagents. This work was supported by NIH (HL 20948, GM 52016), the Perot Family Foundation, and the Cecil H. Green Distinguished Chair in Cellular and Molecular Biology. Molecular interaction data have been deposited in the Biomolecular Interaction Network Database with accession code 196938.

Supporting Online Material

www.sciencemag.org/cgi/content/full/307/5714/1472/DC1
Materials and Methods
Figs. S1 to S6
Table S1
References

19 November 2004; accepted 7 January 2005
10.1126/science.1107710

How Visual Stimuli Activate Dopaminergic Neurons at Short Latency

Eleanor Dommett,[1]* Véronique Coizet,[1]* Charles D. Blaha,[2]† John Martindale,[1] Véronique Lefebvre,[1] Natalie Walton,[1] John E. W. Mayhew,[1] Paul G. Overton,[1] Peter Redgrave[1]‡

Unexpected, biologically salient stimuli elicit a short-latency, phasic response in midbrain dopaminergic (DA) neurons. Although this signal is important for reinforcement learning, the information it conveys to forebrain target structures remains uncertain. One way to decode the phasic DA signal would be to determine the perceptual properties of sensory inputs to DA neurons. After local disinhibition of the superior colliculus in anesthetized rats, DA neurons became visually responsive, whereas disinhibition of the visual cortex was ineffective. As the primary source of visual afferents, the limited processing capacities of the colliculus may constrain the visual information content of phasic DA responses.

Sensory stimuli that are biologically salient because of their novelty, intensity, or reward value elicit a stereotyped phasic (short-latency <100 ms; short-duration ~100 ms) increase in firing rate of midbrain DA neurons in a variety of mammals (*1–3*). If not reinforced, responses to novel stimuli become habituated rapidly. The responses to rewarding stimuli also decline if stimuli can be predicted. When reward is signaled by an arbitrary stimulus, the phasic DA response shifts from the primary reward to the predicting stimulus. If, under these circumstances, a predicted reward fails to materialize, there is a brief pause in the ongoing activity of DA neurons. These findings have led to the influential suggestion that DA neurons provide the brain's reinforcement learning mechanisms with a "reward prediction error" signal that may be used to adjust future behavioral response probabilities (*4–6*). However, DA neurons exhibit robust responses to a wider class of stimuli than those unambiguously related to reward (*2*, *7*); this suggests that the phasic DA signal may have a broader role than reward alone (*8*). An important strategy for decoding the phasic DA signal would be to identify and then to elucidate the perceptual properties of the sensory pathways providing input to DA neurons. Surprisingly, very little is known about the source(s) of the short-latency phasic sensory input to DA neurons. A candidate structure is the superior colliculus, a retino-recipient nucleus in the dorsal midbrain with direct efferent projections to dopamine-containing regions of the ventral midbrain (*9*). The experimental rationale of the present study was based on a recent report (*10*) that, in the deep layers of the superior colliculus, which project directly to DA neurons (*9*), visual sensitivity is suppressed by anesthesia and can be restored temporarily by local injections of disinhibitory pharmacological agents.

Simultaneous electrophysiological recordings from the superior colliculus deep layers and electrophysiologically identified DA neurons in the substantia nigra (N = 18), or ventral tegmental area (N = 17), of anesthetized rats (*11*) revealed in all cases (N = 35)

[1]Department of Psychology, University of Sheffield, Sheffield, S10 2TP, UK. [2]Department of Psychology, Macquarie University, Sydney, NSW 2109, Australia.

*These authors contributed equally to this work.
†Present address: Department of Psychology, University of Memphis, Memphis, TN 38152–3230, USA.
‡To whom correspondence should be addressed. E-mail: P.Redgrave@sheffield.ac.uk

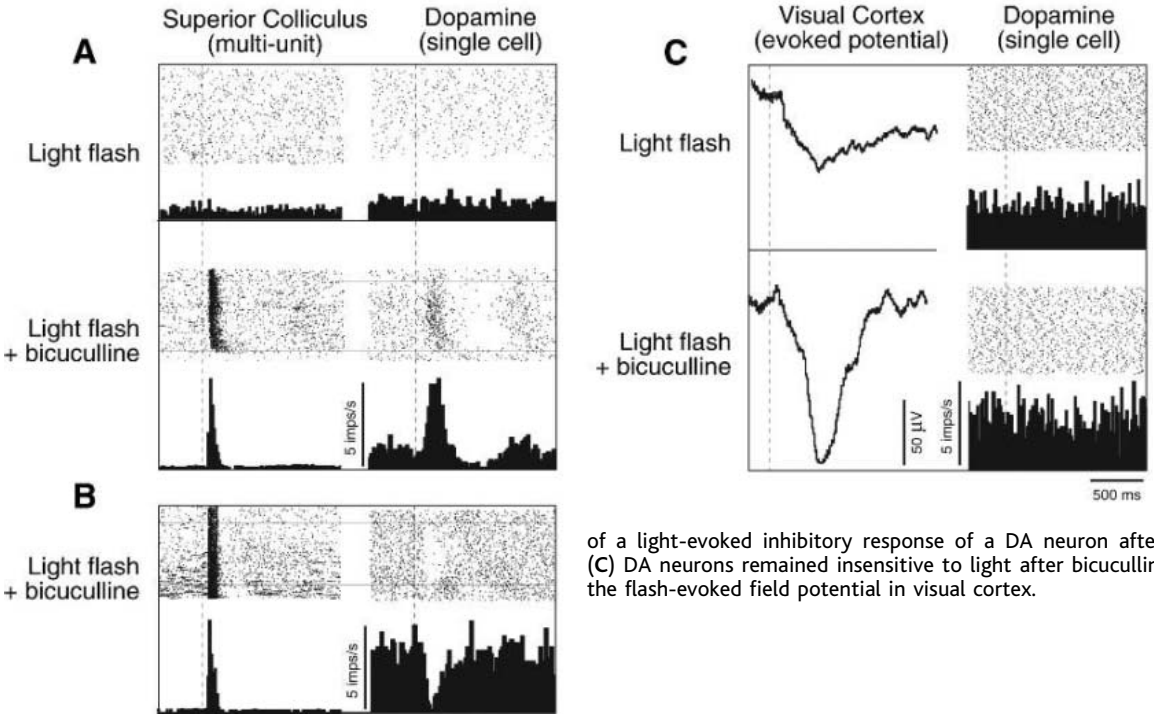

Fig. 1. Disinhibition of collicular deep layers induced phasic visual responses locally and in DA neurons. (**A**) Initially, raster displays and peri-stimulus histograms show that collicular neurons and a simultaneously recorded DA neuron were unresponsive to a regular (0.5 Hz) light flash (vertical dotted line) (top graphs). After a collicular microinjection of bicuculline, both local neurons and the DA neuron were excited at short latency by visual stimulation (bottom graphs). (**B**) Example of a light-evoked inhibitory response of a DA neuron after collicular disinhibition. (**C**) DA neurons remained insensitive to light after bicuculline-induced facilitation of the flash-evoked field potential in visual cortex.

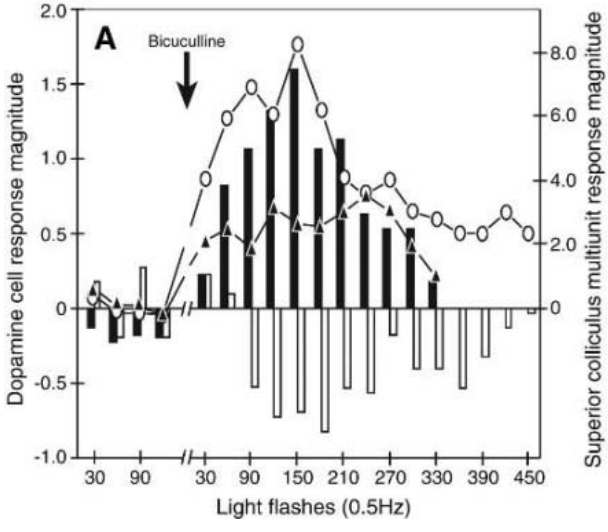

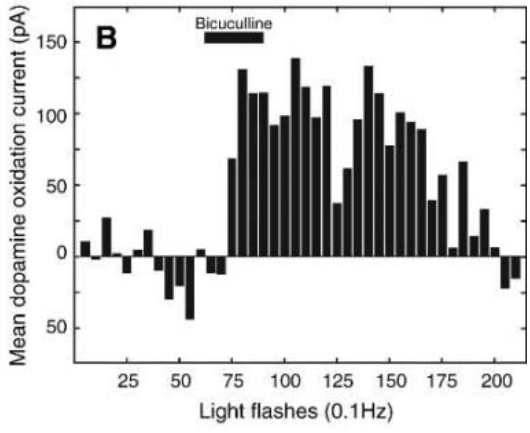

Fig. 2. Flash-evoked activation of collicular and DA responses fails to show habituation to predictable stimuli. (**A**) Measures of the response magnitude of an excited (black histogram) and inhibited (white histogram) DA cell, plus associated collicular multiunit activity (black and white symbols, respectively, and right scale), throughout a single trial. For each flash, the DA and collicular event count in the 300 ms preceding the stimulus was subtracted from the event count in the 300 ms post stimulus. Each bar/point represents the mean of 30 of these values, consecutively throughout the trial. (**B**) Electrochemical response magnitudes throughout the trial illustrated in Fig. 3A. After normalizing the baseline current to 0 at the time of stimulus onset, the oxidation current was recorded 200 ms after each light flash (see Fig. 3C left). Each bar represents the mean of five of these values, consecutively throughout the trial.

that neither the superior colliculus (Fig. 1A, top left) nor midbrain DA neurons (Fig. 1A, top right) responded to a whole-field light flash. However, after microinjection of the γ-aminobutyric acid type A ($GABA_A$) receptor blocker, bicuculline, into the superior colliculus (directly adjacent to the recording electrode), local neurons became sensitive to the light flash (Fig. 1A, bottom left, and 1B, left). Following the onset of collicular responses to the light stimulus, 30 out of 35 (85.7%) DA neurons also exhibited a clear short-latency response to the light. More than half of the light-activated DA neurons (17 out of 30; 56.6%) responded with an initial excitatory phase, of which nearly half were polyphasic (8 out of 17; 47.0%) (Fig. 1A, bottom right). In contrast, the ongoing activity of other DA neurons was initially suppressed (13 out of 30; 43.3%) (Fig. 1B, right), with about half (6 out of 13; 47.1%) exhibiting further excitatory components. The response latencies of neurons in the superior colliculus were reliably shorter (40.3 ± 3.1 ms) than those of corresponding DA neurons (113 ± 14.2 ms) (t = 5.4; df = 29; P < 0.001). Control experiments (N = 4) involving a comparable enhancement of visual processing in the striate cortex (Fig. 1C, left, produced by direct application of bicuculline to the cortical surface) left DA neurons unresponsive to the light stimulus (Fig. 1C, right).

We proceeded to consider factors that could differentiate the DA neurons by their initial excitatory or inhibitory reactions to the light. (i) Variables associated with the injections of bicuculline had no apparent effect. Analysis of histologically verified coordinates of the injection sites, and the

distribution of the neural activity marker c-Fos (*12*) (evoked by the direct excitatory action of bicuculline, fig. S1A), revealed no systematic differences between excited, inhibited, and nonresponsive DA neurons (*11*). (ii) Excitatory and inhibitory responses were observed in both the substantia nigra (9:5) and ventral tegmental area (8:8) (fig. S1B) ($\chi^2 = 0.63$; df = 1: $P > 0.05$). (iii) The difference in spontaneous firing rate in the 500 ms before each light flash for excited (1.41 ± 0.3 spikes) and inhibited neurons (2.0 ± 0.24 spikes) was not statistically reliable ($t = 1.485$; df = 28; $P = 0.173$). (iv) The mean spike widths of DA neurons exhibiting excitatory (4.17 ± 0.25 ms) and inhibitory (3.83 ± 0.23 ms) responses were not reliably different (fig. S1C) ($t = 0.972$; df = 28; $P = 0.339$). All but two (28 out of 30) of our putative DA neurons satisfied the recently proposed additional criterion for distinguishing DA neurons (duration to the first negative peak >1.1 ms) (*13*); the difference between the mean values of this parameter for excited (1.4 ± 0.09 ms) and inhibited (1.5 ± 0.07 ms) neurons was also not significant ($t = 0.292$; df = 28; $P = 0.773$). (v) No reliable differences were found between the mean latencies (excited = 121.18 ± 18.48 ms; inhibited = 105.38 ± 22.88 ms; $t = 0.543$; df = 28; $P = 0.592$) or response durations (excited = 189.41 ± 29.27 ms; inhibited = 192.46 ± 32.85 ms; $t = 0.69$; df = 28; $P = 0.945$) of light-responsive DA neurons. Differences in the initial response may therefore reflect differential activations of excitatory and inhibitory components of the tectonigral pathway (*9*) and their respective control of individual DA neurons.

An important aspect of our methodology was that the light stimulus was spatially and temporally predictable (every 2 s, for hundreds of trials). Measures of response magnitude throughout the experimental sessions (Fig. 2A) revealed no signs of the rapid habituation reported by others (*3*). Rather, the magnitude of the responses appeared more accurately to reflect the waxing and waning of bicuculline's effect in the superior colliculus (Fig. 2A).

Because the light stimulus evoked both excitatory and inhibitory DA neuronal responses, coupled with the observation that the release of dopamine from terminals is not always closely related to the electrophysiological activity of DA neurons (*14*), we conducted experiments using fixed potential amperometry (*15*, *16*) to measure light-evoked release of dopamine into target regions of the neostriatum. Without additional treatment, whole-field light flashes caused no detectable release of dopamine into the neostriatum of anesthetized rats (*11*). However, after local injections of bicuculline into the deep layers of the superior colliculus ($N = 23$), short-latency (mean 153.7 ± 25.1 ms), short duration (mean 331.4 ± 19.3 ms) electrochemical responses were recorded from the neostriatum in every case. Normally, this effect was evident only after signal averaging (Fig. 3, B and C). However, in some examples, each light flash evoked a clearly observable electrochemical response (Fig. 3A). In these cases, the magnitude of the electrochemical response to individual flashes also showed no evidence of rapid habituation to the temporally predictable stimuli (Fig. 2B). Injection of the selective dopamine reuptake blocker, nomifensine, in each case ($N = 4$) increased both the amplitude and duration of the light-induced electrochemical response (Fig. 3, A and B). Combined injections of the serotonergic and noradrenergic reuptake blockers, fluoxetine and desmethyl imipramine ($N = 2$), had no effect (Fig. 3C).

The present results provide complementary electrophysiological and electrochemical evidence for the phasic modulation of midbrain DA neurons by discrete visual stimuli. Light flashes only increased the phasic release of dopamine, whereas DA neurons showed both excitatory and inhibitory responses; these results may be partly explained by the supra-additive accumulation of dopamine in the forebrain when DA neurons switch to burst firing mode (*17*). However, phasic DA responses were observed only when neurons in the superior colliculus were released from inhibition associated with the anesthetic (*10*) and were themselves responsive to light stimuli. Comparable disinhibition of early cortical visual processing left DA neurones unresponsive (Fig. 1C), and later cortical processing capable of object recognition typically has latencies equal to or longer than those of DA neurones (*18*). In addition, other retino-recipient systems (e.g., pretectal and accessory optic nuclei) have been associated mainly with ocular reflexes or responses to photoperiod (*19*). Therefore, the superior colliculus could be the primary, if not exclusive, source of presaccadic information concerning the unexpected occurrence of biologically salient visual events.

In unanesthetized animals, neurons in the deep layers of the superior colliculus (*20*–*22*)

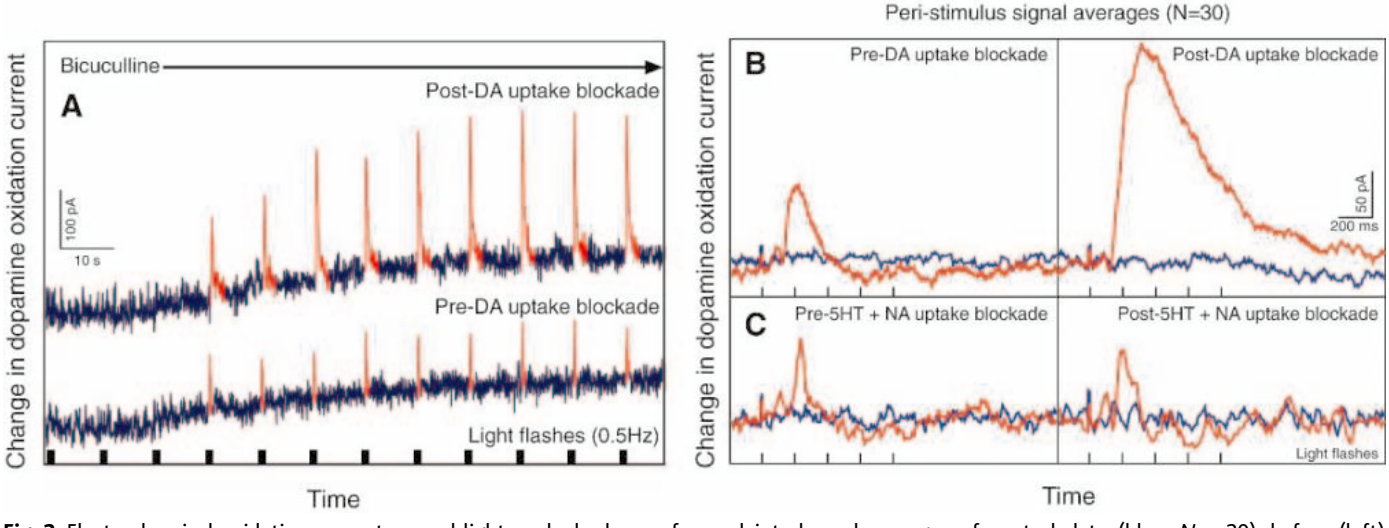

Fig. 3. Electrochemical oxidation currents reveal light-evoked release of dopamine into the striatum. (**A**) Onset of changes in striatal dopamine oxidation current induced by light flashes (red) during a collicular microinjection of bicuculline, before (bottom trace) and after pretreatment with nomifensine (20 mg/kg) (top trace). (**B**) Peristimulus averaging of light-evoked electrochemical responses (red, $N = 30$) and interleaved averages of control data (blue, $N = 30$), before (left) and after (right) pretreatment with nomifensine (20 mg/kg). (**C**) Averages of light-evoked responses (red, $N = 30$) and interleaved control data (blue, $N = 30$), before (left) and after (right) pretreatment with a combination of fluoxetine (20 mg/kg) and desmethyl imipramine (20 mg/kg).

and midbrain DA neurons (*3*) are both exquisitely sensitive to unexpected novel visual events, but they become habituated rapidly if stimuli become predictable or are not maintained by association with the primary reward (*3*, *20*). In the anesthetized preparation we used in these studies, visual sensitivity was observed only when the suppressive effects of anesthesia were relieved by local disinhibitory injections of bicuculline into the superior colliculus. Given that such disinhibition can block both the behavioral (*23*) and electrophysiological signs of habituation (Figs. 1, A and B, and 2), it is relevant that both measures of DA activation in the present study also showed consistent responses to predictable stimuli over hundreds of consecutive trials (Fig. 2). This suggests that the mechanisms responsible for mediating habituation (*24*) and reinforcement-related modulations of sensory processing in the superior colliculus (*25*) would be able to regulate the often-reported habituation and reward-related dishabituation of DA neurons to neutral visual stimuli (*3*).

In most vertebrate species, unpredicted visual events are represented by the superior colliculus in terms of a restricted range of stimulus dimensions according to a well-defined, spatially organized retinotopic map (*20*–*22*). In mammals, most visually responsive cells in the superior colliculus are transiently activated 40 to 60 ms after the appearance, disappearance, or movement of a stimulus within a specific region of the visual field. Collicular neurons respond poorly, if at all, to the contrast, velocity, wavelength, or geometric configuration of visual stimuli. Most experimental studies designed to evaluate the reward prediction error hypothesis of DA function [e.g. (*26*, *27*)] have used tasks that can be solved on the basis of luminance change and/or position of specific reward-related visual stimuli. It is interesting that both characteristics can be coded by neurons in the superior colliculus (*20*–*22*). It is likely, therefore, that the capacity of DA neurons to distinguish various classes of stimuli at short latency depends largely on presaccadic visual processing in the superior colliculus and the extent to which it can be modulated by associations with reinforcing stimuli.

References and Notes

1. A. S. Freeman, *Life Sci.* **36**, 1983 (1985).
2. J. C. Horvitz, *Neuroscience* **96**, 651 (2000).
3. W. Schultz, *J. Neurophysiol.* **80**, 1 (1998).
4. P. R. Montague, P. Dayan, T. J. Sejnowski, *J. Neurosci.* **16**, 1936 (1996).
5. W. Schultz, A. Dickinson, *Annu. Rev. Neurosci.* **23**, 473 (2000).
6. H. Nakahara, H. Itoh, R. Kawagoe, Y. Takikawa, O. Hikosaka, *Neuron* **41**, 269 (2004).
7. Y. Takikawa, R. Kawagoe, O. Hikosaka, *J. Neurophysiol.* **92**, 2520 (2004).
8. P. Redgrave, T. J. Prescott, K. Gurney, *Trends Neurosci.* **22**, 146 (1999).
9. E. Comoli *et al.*, *Nat. Neurosci.* **6**, 974 (2003).
10. H. Katsuta, T. Isa, *Neurosci. Res.* **46**, 73 (2003).
11. Materials and methods are available as supporting material on *Science* Online.
12. T. Herdegen, J. D. Leah, *Brain Res. Rev.* **28**, 370 (1998).
13. M. A. Ungless, P. J. Magill, J. P. Bolam, *Science* **303**, 2040 (2004).
14. P. A. Garris *et al.*, *Nature* **398**, 67 (1999).
15. D. J. Michael, R. M. Wightman, *J. Pharm. Biomed. Anal.* **19**, 33 (1999).
16. G. L. Forster, C. D. Blaha, *Eur. J. Neurosci.* **17**, 751 (2003).
17. F. G. Gonon, *Neuroscience* **24**, 19 (1988).
18. S. J. Thorpe, M. Fabre-Thorpe, *Science* **291**, 260 (2001).
19. A. J. Sefton, B. Dreher, in *The Rat Nervous System*, G. Paxinos, Ed. (Academic Press, San Diego, 1995), pp. 833–898.
20. R. H. Wurtz, J. E. Albano, *Annu. Rev. Neurosci.* **3**, 189 (1980).
21. D. L. Sparks, *Physiol. Rev.* **66**, 118 (1986).
22. B. E. Stein, M. A. Meredith, in *Electrophysiology of Vision*, A. G. Leventhal, Ed. (Macmillan Press, Hampshire, UK, 1991), pp. 85–110.
23. P. Redgrave, P. Dean, W. Souki, G. Lewis, *Psychopharmacology (Berl.)* **75**, 198 (1981).
24. K. E. Binns, T. E. Salt, *Vis. Neurosci.* **12**, 563 (1995).
25. T. Ikeda, O. Hikosaka, *Neuron* **39**, 693 (2003).
26. C. D. Fiorillo, P. N. Tobler, W. Schultz, *Science* **299**, 1898 (2003).
27. G. Morris, D. Arkadir, A. Nevet, E. Vaadia, H. Bergman, *Neuron* **43**, 133 (2004).

28. We thank P. Dayan, N. Daw, Y. Niv, and J. McHaffie, for their constructive suggestions. Supported by Wellcome Trust (P.R. and P.G.O.), Medical Research Council of the UK (P.R. and J.E.W.M.), Australian National Health and Medical Research Council (C.D.B.), and Macquarie University (P.R.).

Supporting Online Material
www.sciencemag.org/cgi/content/full/307/5714/1476/DC1
Materials and Methods
Fig. S1
References and Notes

2 November 2004; accepted 7 January 2005
10.1126/science.1107026

Chromatography Sorbents

A comprehensive line of chromatography sorbents is designed to simplify protein separation and purification for biotechnology drug discovery, development, and production. The integration of this broad range of chromatography media with Pall's extensive portofolio of membranes, protein purification technologies, and services, establishes Pall Life Sciences as a single-source provider of the full spectrum of scalable filtration and separation products.

Pall Corp For information 800-717-7255 www.pall.com

Manual Pipetting Aid

The WellAware Pipetting Aid increases the accuracy and speed of manual transfer between microplates and provides an alternative to automated liquid handling. Source and target microplates rest on the upward-facing screen of any standard LCD monitor while software guides the user by lighting up source and target wells and supplying text-to-speech audio cues. A variety of pipetting tasks can be facilitated, including cherry picking, plate transposition, plate reformatting, and serial dilution. The software runs on most laboratory computers and can accommodate 1- to 16-channel pipetting between standard 24- to 384-well microplates or tube racks.

BioTX Automation For information 877-Ask-BioTX www.biotxautomation.com

Microbial DNA

The WaterMaster DNA Purification Kit provides all the liquid reagents needed to purify microbial DNA from any water source after passage through a filter of the user's choice. DNA can be purified from bacteria and eukaryotes and can be used for restriction digests, polymerase chain reaction, subcloning, sequencing, or microarray analysis. The kit features a simple, gentle procedure with no toxic organic reagents or mechanical cell disruption. Because the method produces purified DNA in a low final volume, the DNA doesn't need to be concentrated.

Epicentre For information 800-284-8474 www.epicentre.com/watermaster.asp

Automated Viral Purification

The EZ1 Virus Mini Kit provides a fully automated procedure for simultaneous purification of viral DNA and RNA from serum, plasma, and cell-free body fluids, giving highly sensitive detection in downstream assays. The kit enables purification from a broad range of DNA and RNA viruses for life science applications. Automation on the BioRobot EZ1 workstation enables easy processing of 1 to 6 samples in parallel.

Qiagen For information 800-426-8157 www.qiagen.com

For more information visit GetInfo, *Science*'s new online product index at *http://science.labvelocity.com*

From the pages of GetInfo, you can:
- Quickly find and request free information on products and services found in the pages of *Science*.
- Ask vendors to contact you with more information.
- Link directly to vendors' Web sites.

Low-Volume Liquid Dispenser

The aliQuot low-volume liquid dispenser with automated stacker allows for the controlled dispensing of cells. The aliQuot's unique valve and manifold system eliminates the damage to cells associated with traditional pump and valve mechanisms, allowing for fast, automated cell dispensing while maintaining viability equivalent to that seen with manual procedures. The unique design also ensures that cells are dispensed evenly across the well. Compact in design, fitting easily into a standard laminar flow cabinet to maintain sterility, the aliQuot is suitable for rapidly and reproducibly dispensing liquid or suspensions in the 1 to 350 μl range into 96-, 384-, and 1536-well plates. Fitted with the automated stacker, it can be programmed to handle up to 30 microplates, including performing lid removal and replacement.

Genetix For information +44 1425 624600 www.genetix.com

Immersion Coolers

Three redesigned low-temperature coolers can be used to achieve low-temperature capability with nonrefrigerated circulators or boost the cooling capacity of refrigerated circulators. Designed to provide continuous cooling to temperatures as low as –100° C, VLT Series Immersion Coolers provide an economical alternative to dry ice and liquid nitrogen. They are suitable for use with solvent traps, freeze-point apparatus, impact testing, lyophilization, and other applications requiring low temperatures. They feature a digital temperature display and are available with or without temperature control. A rigid coil probe is standard on all units; flexible and cold finger probes are available as options on the VLT 100.

PolyScience For information 800-229-7569 www.polyscience.com

Thermal Cyclers

The Mastercycler ep system features fast speeds, high precision, user-friendliness, and reliability. There are three models to choose from: Mastercycler ep gradient for 96 × 0.2 ml tubes or 1 polymerase chain reaction (PCR) plate with a gradient range up to 20°C; Mastercycler ep gradient S, with a speed up to 6°C per second and a gradient range up to 24°C; and Mastercycler ep 384 for samples in a 384-well format. The instruments feature heated lids with integrated electronic sample protection technology for faster, more precise annealing and better block homogeneity. In the past few years, nucleic acid research has been developing dynamically, requiring new capabilities from PCR systems, and these instruments are designed to keep pace with these challenges with technological advances.

Eppendorf For information 800-645-3050 www.brinkmann.com

Literature

Active Motif's 2005 Catalog features products for studying the activation and regulation of transcription factors and signaling proteins, including DNA-binding and phospho-specific enzyme-linked immunosorbent assays; reagents for chromatin immunoprecipitation, gene splicing, and protein delivery; and a variety of antibodies, cell extracts, and recombinant proteins.

Active Motif For information 877-222-9543 www.activemotif.com

Newly offered instrumentation, apparatus, and laboratory materials of interest to researchers in all disciplines in academic, industrial, and government organizations are featured in this space. Emphasis is given to purpose, chief characteristics, and availability of products and materials. Endorsement by *Science* or AAAS of any products or materials mentioned is not implied. Additional information may be obtained from the manufacturer or supplier by visiting www.science.labvelocity.com on the Web, where you can request that the information be sent to you by e-mail, fax, mail, or telephone.

» advances in:

Biochips

Array of Applications

Stimulated by emerging tools and technologies, DNA microarrays have moved far beyond the laboratory. They now offer applications in areas as diverse as diagnostics, clinical profiling, and screening genetically modified organisms. BY PETER GWYNNE AND GARY HEEBNER

DNA microarrays enable researchers to analyze the expression of thousands of genes in a single experiment under tightly controlled conditions. First developed in the early 1990s, they initially provided a powerful tool for scientists trying to understand the fundamental aspects of cellular function and the genetic causes of disease.

In recent years, DNA microarrays have moved out of the research lab and into a wide variety of practical applications. "We have seen the evolution of microarrays from being primarily a gene expression tool to being used for many other types of applications," says Siobhan Pickett, director of genomic systems for **Molecular Devices**. "We all expected that this would happen eventually, because the microarray technology is just a tool. But it's really exciting to see how quickly and broadly that's been happening."

DNA microarrays, often known as chips or biochips, continue to find their most common application in studies of gene expression and detecting single nucleotide polymorphisms (SNPs). "In business as a whole, gene expression is still dominant," says Roland Green, chief technology officer and vice president of R&D for **NimbleGen Systems**. "However, we see the bulk of the growth in new applications such as ChIP and arrayCGH." Indeed, a profusion of new uses has emerged during the past two years. And growing numbers of users are finding that, in the words of Jochen Müller-Ibeler, product line manager for DNA microarrays at **Eppendorf**, "Microarrays are nice toys to play with."

This is the first of four supplements this year on biochips. The others will appear in the 6 July, 19 August, and 20 September issues of Science.

Inclusion of companies in this article does not indicate endorsement by either AAAS or Science*, nor is it meant to imply that their products or services are superior to those of other companies.*

EXPLOSION OF USES

What new uses have emerged? "There's been an explosion of applications of microarrays to comparative genomic hybridization [CGH]," says Wendy Price, business area manager for DNA arrays at **Invitrogen**. In that application, explains Jeremy Clarke, global product manager of **Genomic Solutions**, "You hybridize DNA from two sources against metaphase chromosomes. The mix is then hybridized against a large panel of DNA probes to look for regions of DNA gain or loss." Diagnostics has also benefited from microarrays. "Roche had the first approval for a diagnostic tool using microarrays," says Müller-Ibeler. "The diagnostic market is big and important for us." Another German company, **Greiner Bio-One**, takes a similarly optimistic view. "We are trying to push arrays into the diagnostic field, says Jörg Stappert, head of the firm's biochip group. "We are looking at lots of arrays to analyze for a few markers." MORE ›››

In this issue:

- DNA microarrays
- DNA preparation and labeling
- Microarray spotting
- Oligonucleotide synthesis
- Off-the-shelf vs. do-it-yourself DNA microarrays
- Scanners
- Analytical software
- Applications of DNA microarrays

» advances in: Biochips

DNA microarraying has also started to move into treatment technologies. "Clinical profiling is coming along," explains Sean Yu, vice president of operations at **SuperArray Bioscience**. "There are a number of clinical trials for the use of microarrays for prognosis or therapeutic guidance." **Affymetrix**, the company responsible for the first commercial DNA microarrays, recently participated in a program that identified the first gene linked to sudden infant death syndrome. "This is just one example of how DNA analysis microarrays are accelerating discovery and bridging the gap between basic scientific research and its impact on human health," says Affymetrix's chairman and CEO Stephen Fodor.

In addition, pharmaceutical firms have started to use microarray data to determine the success of clinical trials of new drugs. Beyond the clinic, the technology is finding application in food science and forensics. And basic research also benefits from the technology. "We're seeing a broad range of protein-based applications, including research on protein-protein interactions and antibody studies, that use both DNA and protein microarrays," Pickett says. "Researchers are also using DNA microarrays to study DNA-protein interactions."

NEW AND IMPROVED MICROARRAYING

The scope of the fresh uses depends in large part on the development of new and improved tools and technologies for microarraying. "People are more aware of the need to build better controls in their microarray experiments, especially when they are applied to diagnostics," says Price. Reusability has emerged as another key advance. "We are developing protocols to reuse microarrays three to five times," Green notes. "It's a matter of finding the right buffers and stripping the microarrays so that they don't pick up dirt. We think it will enable a new set of applications that were previously too expensive."

Certainly reusability improves the economics of microarraying investigations, particularly with expensive items such as NimbleGen's human genome 38-chip set. "We can use that array set five times; that makes it much more economical," Green continues. "I predict that this will be standard practice for many labs soon."

Vendors have also started to offer high throughput DNA microarrays. "Until now, it was one chip, one sample. Now it's moving into one chip, multiple samples," Stappert explains. "That will be important for drug screening. It's why we have started development of high throughput arrays. We are trying to push arrays into the diagnostic field, which needs lots of arrays to analyze for a few markers."

The development of so-called tiling arrays represents another advance critical to the development of new microarraying applications. "Tiling arrays use millions of DNA probes evenly spaced, or "tiled," across the genome, including coding and noncoding regions alike," Fodor explains. "These tiling arrays provide scientists with the only single tool available for genomewide analyses of many important biological functions, including transcription, transcription factor binding sites, sites of chromatin modification, sites of DNA methylation, and even chromosomal origins of replication."

Another key advance involves a new type of microarray. Several companies, including Affymetrix, **Agilent Technologies**, **Applied Biosystems**, and NimbleGen, now produce DNA microarrays that contain the entire human genome on a single chip.

USER-FRIENDLINESS AND LOW COST

Several companies have combined appropriate materials and solutions into kits for microarray fabrication and hybridization experiments. Those supplies lower the barrier against entry into microarraying for average scientists. **GE Healthcare**, for example, has added a range of chips and supplies to its CodeLink product line. The SensiChip line developed by **Zeptosens** and marketed by **Qiagen** features microarrays, reader, software, buffers, and a hybridization station.

SuperArray, meanwhile, aims to make microarrying more attractive in two ways. "To broaden into everyday uses such as clinical applications, you have to simplify the microarray and the data analysis," Yu says. "It's essential to simplify use and lower cost. A lot of our users are not expert in gene expression profiling, and so can't tell you what they are looking for. We'll help them start their microarray analysis."

Users of microarrays can also benefit from a choice between ready prepared and customized microarrays. "You have predefined and customized arrays, and low-density and high-density arrays," Eppendorf's Müller-Ibeler says. "It gives you more flexibility." SuperArray provides customizable features with its oligo arrays. "Researchers can start with general arrays and then customize them with our help for as low as $100 per array," Yu says. "We can do the customizing within two weeks."

TWO TYPES OF PREPARATION

Scientists can choose between two basic sources of DNA microarrays: ready-to-use versions that contain oligonucleotides synthesized directly on the chips, and more customizable forms that contain DNA spotted onto the chips.

Affymetrix uses photolithographic masks similar to those involved in making computer chips to prepare its high-density, ready-to-use microarrays. The masks control the light-sensitive removal of protective groups from hydroxyls in unmasked regions of the substrate, allowing the altered nucleotides to react with bases in the reaction solution and grow the DNA sequence.

The company has led the way in large-scale production of DNA microarrays with a broad range of offerings from its standard GeneChip System to custom services. It recently announced a high throughput microarray prototype that contains 96 individual arrays mounted onto a single plate. "Each array contains the same genomic information as our original human genome U133 arrays, but in approximately a five times smaller surface area," Fodor reports. "Soon each array on the 96-array

» advances in: Biochips

Source for Cell Signaling

If you want to learn about signal transduction, you'll find a good starting point in *Science*'s **STKE** (Signal Transduction Knowledge Environment) website. The site features original perspectives, reviews and protocols solicited by the site's editors, and the Connections Map database, which contains information on signaling components and relationships among them. STKE also contains links to full-text articles on signal transduction from journals distributed by 19 publishers. Users of the site can also participate in forums and download animated teaching resources. Finally, you can personalize the site to meet your own specific needs for information on signal transduction.

» http://www.stke.org

plate will contain over 1.4 million probes, able to measure the expression of approximately 40,000 human transcripts."

NimbleGen has developed maskless photolithographic technology that gives users more opportunity to adapt and reprogram their microarrays to their needs. "The Affymetrix system is good for high-volume printing runs, like making a newspaper," explains NimbleGen's Green. "Ours is more akin to using your laser printer to print reports that you've just written. The main benefit of our approach is that customers get to tailor the arrays to their experimental needs rather than vice versa – designing experiments to fit the arrays. Customers can design their arrays to answer their questions. Once they realize that, they start thinking about projects they never thought about before."

HITTING THE SPOT

The alternative to photolithographic methodology requires vendors or users to spot complementary DNA (cDNA) – produced from messenger RNA using the reverse transcriptase polymerase chain reaction – onto chips. Scientists who want to do their own spotting must first prepare their cDNA. To help them, companies such as **Ambion**, **BD Biosciences Clontech**, and **Promega** offer reagents and kits for isolating and purifying DNA and RNA. GE Healthcare, **Mirus Bio**, and **Roche Applied Science** have kits for labeling nucleic acid samples for fluorescent detection.

Users have a choice of approaches for spotting. The most common methods involve solid or split metal pins. Dipped into wells containing the DNA samples of interest, each of a set of pins picks up a small amount of the DNA, which it drops onto the chip's surface. "Solid pins have the advantage that, if you work with viscous substances like proteins, you don't have to worry about blockage," Genomic Solutions' Clarke says. "With split pins you can do several hundred spots with the same intake of substance." Suppliers such as GE Healthcare and **Hitachi Genetic Systems/MiraiBio** produce spotting robots for use with both types of pin. Genomic Solutions is launching a suite of products for the protein arraying market to address the requirements of these new protein printing applications.

The other main spotting technique, based on inkjet technology adapted from the printer industry, eliminates cross contamination of nucleotides by using separate print heads for each base. "There are two types of inkjet: solenoid valve and piezo-electric," Clarke says. "Both are relatively expensive, and you have to be very specific with your buffer set and to calibrate your surface very carefully. Solenoid technology delivers large spots, usually in the 20 nanoliter range, and is volumetrically controlled. Piezo delivers a very small spot, but you need tighter control." Companies such as **Arrayjet**, **GenHunter**, Genomic Solutions, and **PerkinElmer Life Sciences** use inkjet technology.

Some researchers prefer to produce their own DNA chips in their laboratories. For these do-it-yourselfers, who often lack the engineering expertise required to develop their own robotic systems and software, several companies focus on user-friendliness. "We offer very comprehensive training packages," Clarke says. "And we help our customers to develop solutions to their arraying needs even before the purchase. We also work with third parties on applications of our products."

LABELING, SCANNING, AND INTERPRETATION

The detection method that scientists use with DNA chips depends on the type of label they choose for their experiments. Fluorescence labeling, offered by Affymetrix, Genomic Solutions, Invitrogen, Molecular Devices, and other suppliers, has proved markedly more popular than the alternatives. "There have been radioactive tags, but I don't see any significant switch away from fluorescent labeling," says Pickett of Molecular Devices. However, Eppendorf will soon introduce a colorimetric method. "It's cheaper and easy to use," Müller-Ibeler explains. "You can incorporate it into your lab as a full system."

To detect fluorescent labels, researchers use confocal laser scanners tailored for use with DNA microarrays. "We make continuing gradual improvements to all aspects of our family of four GenePix scanners and GenePix Pro and Acuity software," Pickett says. "Changes in the level of automation and the precision of spot handling have made automated analysis possible and robust." Genomic Solutions supplies high-resolution, auto-focusing semi-confocal array readers that allow researchers to read arrays on uneven surfaces without having to worry about the best parameters to choose.

Invitrogen provides kits that help scientists handle fluorescence scanning from soup to nuts. "We have worked hard on improving reproducibility and accuracy in sample labeling to introduce more standardization in this portion of the workflow," Price says. Adds group leader Kate Rhodes: "Our SuperScript Plus kits have our superscript enzyme, very streamlined and simple protocols, including low elution volume purification, and very well matched fluor dyes to generate more true positives with greater accuracy."

The need for automated analysis stems from the huge volumes of data created by DNA microarrays with thousands of samples or spots. To avoid bottlenecks in storing and analyzing the data, some researchers start out by performing array experiments with the Affymetrix-style comprehensive chips and then downsize their efforts to focus on a specific family of genes. Suppliers such as Affymetrix, **Lion Biosciences**, Molecular Devices, **Spotfire**, and **Silicon Genetics** produce software packages for analyzing and interpreting data from DNA microarrays. Invitrogen offers its Vector Xpression software package for microarray MORE ›››

» advances in: Biochips

analysis. "It probably has more complete ability to do statistical analysis," Price says. "We'll probably focus less on it as a stand-alone effort and use it more as a component of our platform technologies, built into web based solutions."

ABUNDANCE OF APPLICATIONS

New applications of DNA microarrays abound. Perhaps the most far reaching involve medical sleuthing.

Two decades of research has shown an etiological relationship between certain human papillomaviruses (HPVs) and many cases of cervical cancer. Greiner Bio-One will introduce its PapilloCheck DNA microarray that types 24 HPVs. "It has much greater resolution than the present test systems," Stappert says. "With the current tests', you can only prove high risk or low risk. With our genotyping, you can get the details." The company plans to launch the system in Europe in summer or fall, and in the United States once the **U.S. Food and Drug Administration** approves it.

Affymetrix has contributed to an effort to discover a mutation that had eluded researchers for decades. Scientists at the **Translational Genomics Research Center** and the **Clinic for Special Children** used the company's mapping 10K arrays to discover the first gene linked to a form of sudden infant death syndrome. The research team used the arrays, each of which genotypes 10,000 single nucleotide polymorphisms, to analyze the DNA of just four infants and their family members. "Within five days," Fodor says, "the group identified the mutation that had so tragically affected certain Amish families."

Microarraying has also emerged in clinical trials. In a recent phase 3 trial, expression profiles helped researchers at **Novartis Pharmaceuticals** to predict that the company's Gleevec drug had a low probability of success in treating chronic myelogenous leukemia. And in a phase 2 trial, researchers at the **Dana-Farber Cancer Research Institute** applying Affymetrix's GeneChip arrays to myeloma patients treated with the **Millennium Pharmaceuticals** drug Velcade discovered a pattern of 30 genes that correlates with response or lack of response to the therapy.

FROM CANCER TO FOOD SAFETY

Eppendorf offers gene expression arrays, which it calls DualChips, for several conditions, including cancer, aging, and apoptosis. "And an inflammation array will come on the market this year," Müller-Ibeler says. In a collaboration with European Union institutes, the company is also developing a microarray system for diagnosing the safety of foods, most notably genetically modified organisms (GMOs). "It will come onto the market in the first half of this year," Müller-Ibeler says. "It will contain the most important features of the GMOs accepted in the European Union."

Applications in medicine and food safety represent only a start for microarray technology. The future plainly holds more advances in the design, function, utility, and additional applications of DNA microarrays.

Peter Gwynne (pgwynne767@aol.com) is a freelance science writer based on Cape Cod, Massachusetts, U.S.A. Gary Heebner (gheebner@cell-associates.com) is a marketing consultant with Cell Associates in St. Louis, Missouri, U.S.A.